UNIVERSITY OF OKLAHOMA

GRADUATE COLLEGE

PHOTOASSOCIATION AND ROVIBRATIONAL COOLING OF SODIUM CESIUM USING CHIRPED LASER PULSES AND STIMULATED RAMAN ADIABATIC PASSAGE

A DISSERTATION

SUBMITTED TO THE GRADUATE FACULTY

in partial fulfillment of the requirements for the

Degree of

DOCTOR OF PHILOSOPHY

By

STÉPHANE VALLADIER
Norman, Oklahoma
2015

PHOTOASSOCIATION AND ROVIBRATIONAL
COOLING OF SODIUM CESIUM USING
CHIRPED LASER PULSES AND
STIMULATED RAMAN ADIABATIC PASSAGE

A DISSERTATION APPROVED FOR THE
HOMER L. DODGE DEPARTMENT OF PHYSICS AND ASTRONOMY

BY

Dr. Gregory A. Parker, Chair

Dr. Michael A. Morrison, Co-Chair

Dr. Eric R. Abraham

Dr. Kieran J. Mullen

Dr. James P. Shaffer

Dr. Wai Tak Yip

To Victoria-Stéphanie Badino & Mireille Montet,
my great-grandmother and my grandmother;

To Élie & Hortense Granjeon,
my step grandparents;

To Régis & Thérèse Valladier,
my grandparents.

To my wife Marine
for your support, your love, and above all, your patience.

Acknowledgements

My first and foremost thanks go to my advisor and mentor for more than nine years, Prof. Michael A. Morrison. You opened my mind to scientific research, and constantly reminded me of the traps and pitfalls that plague the path, while the intellectual reward, even though hard to get, was definitely worth the trouble. For your help, guidance, advice, and above all, patience: *sincere thanks*, *Michael*. Next I want to thank Prof. Gregory A. Parker who agreed to advise me when Prof. Morrison officially retired. Greg, your insights, suggestions, and warnings when dealing with numerical intricacies were extremely valuable. Thanks for your help and support through the second half of this journey. For their experimental expertise, I convey my gratitude to Profs. Abraham and Shaffer, who kept me aware of the realities of the laboratory, sometimes easily forgotten by theorists. For accepting to jump on the wagon while it was already on the tracks, I very gratefully thank Prof. Yip. Finally, I dearly thank Prof. Mullen for his ongoing moral support and his help in making my last semester at the University of Oklahoma possible.

I do not think it possible to go through Graduate School without an entourage of true friends. I wish this list would be exhaustive, but sadly, I only have limited space, and can not thank all of you individually as well as you deserve. Nonetheless, my friendship and gratitude go in particular to Nassima Baamara, Marine Le Faucheur, Brad C. Wilcox, Tom Akin, Sara Barber, Sean Krzyzewski, Scarlet Norberg, and Shayne Cairns. To Bobby and Allison Fleshman, my thanks to you are "bigger in the inside than on the outside". To my colleague in this adventure, James Dizikes, for his friendship and patience with my crazyness, for the long discussions on Physics, for his support, for the tools you developed that helped me in this work, un grand merci.

Although I left home to get on this adventure, home never left me. Thanks to Bérengère and Pierre Quero for their unfaltering friendship, understanding, and electronic presence. Thanks to technology, my uncle Michel Valladier and his wife Annie were very often by my side, and have not the slightest idea of how much it meant to me. To my sister Diane Daunas for her unfaltering love, her moods that always cheered me up, and her help in motivating me, merci *Micropuce*. To my stepmother Éliane Granjeon, whose serenity and calm were inspiring and helpful beyond hope, thank you. To my mother Corinne Constant for her complete confidence in her son, her patience in waiting for the end of this long road, and the long hours spent a long time ago checking my homework, and always pushing me to give my best, *thank you*. To my father, Étienne Valladier. You ignited a hunger for knowledge in me that will never be satiated. I hope that I put as much care in this work as you have taught me to put in everything I do. I wish that you are as proud of this result as I am proud to have you as a father.

Et dans mes grandes mains tremblantes
où repose ma thèse terminée,
je haussais vers le ciel la gloire de mes parents
vers les volcans de mon Velay et les collines
de ma Provence.

—d'après Marcel Pagnol,
La gloire de mon Père

Stéphane Valladier
Burbank, California, 13th March, 2015

Remerciements

D'abord et avant tout mes remerciements s'adressent à mon directeur de thèse et mentor pendant plus de neuf ans, le Prof. Michael A. Morrison. Vous m'avez ouvert l'esprit à la recherche scientifique, et m'avez constamment mis en garde contre les pièges et trappes qui infestent le chemin, alors que la récompense intellectuelle, bien que difficile à obtenir, valait véritablement la peine. Pour votre aide, vos conseils, vos avis, et par dessus tout, votre patience: *sincères remerciements*, *Michael*. Ensuite je voudrais remercier le Prof. Gregory A. Parker qui accepta de me suivre quand le Prof. Morrison pris officiellement sa retraite. Greg, votre discernement, vos suggestions, et vos avertissements à propos des subtilités numériques furent d'une grande valeur. Merci de votre aide et de votre soutien pendant la deuxième moitié de ce parcours. Pour leur expertise dans le domaine expérimental, je transmets ma gratitude aux Profs. Abraham et Shaffer, qui m'ont rappelé les réalités du laboratoire, parfois facilement oubliées par les théoriciens. Pour avoir accepter de prendre le train en marche alors qu'il était déjà bien en route, je remercie très sincèrement le Prof. Yip. Enfin, je remercie très chèrement le Prof. Mullen pour son soutien moral sans faille et son aide pour avoir rendu possible mon dernier semestre à l'Université d'Oklahoma.

Je doute qu'il soit possible de traverser l'École Doctorale sans un solide entourage de véritables amis. J'aimerais que cette liste soit exhaustive, mais malheureusement, je n'ai que peu de place, et je ne pourrais jamais vous remercier tous autant que vous le méritez. Cependant, mon amitié et ma gratitude s'adressent en particulier à Nassima Baamara, Marine Le Faucheur, Brad C. Wilcox, Tom Akin, Sara Barber, Sean Krzyzewski, Scarlet Norberg, et Shayne Cairns. À Bobby et Allison Fleshman, ma gratitude pour vous est "plus grande

à l'intérieur qu'à l'extérieur". À mon collègue dans cette aventure, James Dizikes, pour son amitié et sa patience avec mes folies, pour les longues discussions de Physique, pour son soutien, pour les outils que tu as développés et qui m'ont aidés dans mon travail, un grand merci.

Bien qu'ayant quitté ma terre pour m'engager dans cette aventure, ma terre ne m'a jamais quitté. Merci à Bérengère et Pierre Quero pour leur amitié sans faille, leur compréhension, et leur présence électronique. Grâce à la technologie, mon oncle Michel Valladier et sa femme Annie furent souvent à mes côtés, et vous n'avez pas la moindre idée de ce que ça a représenté pour moi. À ma sœur Diane Daunas pour son amour sans faille, ses humeurs qui m'ont toujours remonté le moral, et son aide pour me motiver, merci *Micropuce*. À ma belle-mère Éliane Granjeon, dont la sérénité et le calme furent une source d'inspiration et d'aide au-delà de tout espoir, merci. À ma mère Corinne Constant pour sa confiance totale dans son fils, sa patience en attendant la fin de cette longue route, et les longues heures passées il y a longtemps à vérifier mes devoirs, et à toujours me pousser à donner le meilleur de moi-même, *merci*. À mon père, Étienne Valladier. Tu as allumé en moi une faim de connaissance qui ne sera jamais rassasiée. J'espère avoir mis autant de soin dans ce travail que tu m'as enseigné à en mettre dans tout ce que j'entreprenais. Je souhaite que tu sois aussi fier de ce résultat que je suis fier de t'avoir pour père.

Et dans mes grandes mains tremblantes
où repose ma thèse terminée,
je haussais vers le ciel la gloire de mes parents
vers les volcans de mon Velay et les collines
de ma Provence.

—d'après Marcel Pagnol,
La gloire de mon Père

Stéphane Valladier
Burbank, Californie, le 13 mars 2015

Table of Contents

List of Tables

List of Figures

Abstract

This dissertation presents the study of how two laser pulses can bind sodium and cesium atoms at ultracold temperature ($T = 200\mu K$) into an ultracold, polar, diatomic molecule with a definite quantum state. A single-channel scattering model represents the initial continuum state, and two different models represent the intermediate state: one excluding spin-orbit coupling effects in the intermediate state, the other accounting for such effects. We calculate the $A^1\Sigma^+ - b^3\Pi$ spin-orbit coupled wave functions using a basis expansion technique, and validate the results by comparing to experimentally obtained, spin-orbit coupled energy levels. The computation of photoassociation rates between the continuum state and the intermediate states reveals the crucial importance of spin-orbit coupling. Furthermore, this study shows how the spectral bandwidth (narrow *vs*. broad), the chirping (chirped *vs*. unchirped), the detunings, the intensities, and the pulse delay (intuitive *vs*. counter-intuitive sequence) of the lasers affect the transfer of population from the continuum scattering state to a comparatively low-lying ($v_X = 32, J_X = 0$) rovibrational state of the $X^1\Sigma^+$ ground electronic state of NaCs. The transfer process relies either on a sequence of π-pulses, or uses stimulated Raman adiabatic passage (STIRAP). Lasers with narrow spectral bandwidth (0.5 GHz) always yield a final population in $|X^1\Sigma^+, v_X = 32, J_X = 0\rangle$ higher than 95% in less than 4 ns.

Chapter 1

Introduction

1.1 Ultracold polar molecules

Since the successful realization of Bose-Einstein condensates [1], physicists endeavored to extend cooling techniques from atoms to molecules, hoping to reach the ultracold thermal regime of a few hundred microKelvin (μK).

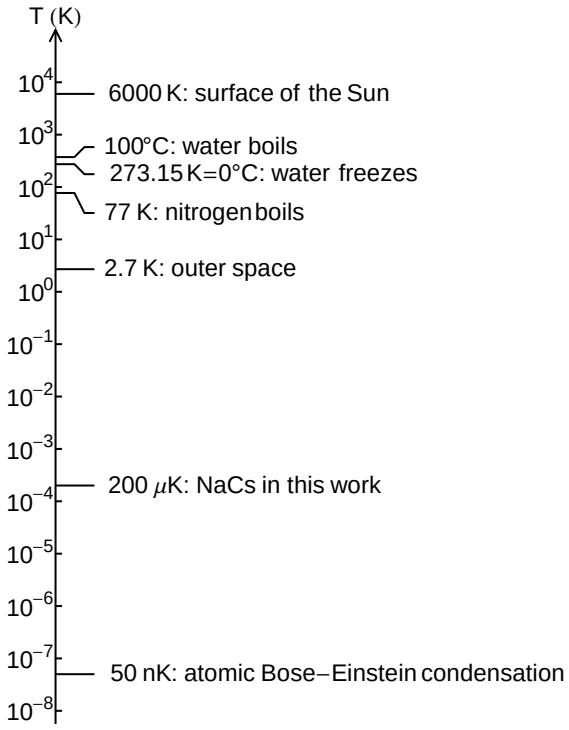

Figure 1.1: Common temperatures in Physics compared to the ultracold regime, $T \leq 1$mK.

Ultracold molecules are the nexus where high-precision measurement physicists, controlled-chemistry scientists, and experts in quantum information processing meet [2, 3]. Krems [4] mentions that thermal motion complicates the occurrence of bimolecular reaction controlled by external fields; molecular gases in the ultracold regime would not suffer from these complications, con-

sequently facilitating the reaction. The drastic reduction of thermal motion in the ultracold regime grants controls of new degrees of freedom only available to molecules.

Ultracold homonuclear[a] diatomic molecules widened the horizon of physical chemistry with photoassociation, a process where a laser light binds two atoms to form a molecule. Then the hope for ultracold polar *heteronuclear* diatomic molecules was on sight, along with many promises. Carr *et al*. [3] provide an extensive review of the fundamental science accessible with ultracold molecules, along with possible applications. For example, strong dipolar molecules are good candidates for testing fundamental symmetries, as they may be used to measure the electric dipole moment of the electron (eEDM) [5]. The existence of an eEDM would violate the parity and time-reversal symmetries, and could explain the matter/antimatter imbalance in the observed Universe. When an electron is bound to an atom, the effect of an external electric field on the eEDM is about 3 times smaller than when the electron is bound to a dipolar molecule. Thus dipolar molecules naturally increase the resolutions of the eEDM measurements. DeMille [6] proposed to use the strong dipole-dipole interaction between such molecules to build a quantum computer. A few years later, Rabl *et al*. [7] proposed a scheme to create quantum memory devices, paving the way to the next upgrade from current Solid State Drives (SSD) used in today's computers. Recently, Bomble *et al*. [8] simulated the execution of quantum algorithms using laser pulses on a register of ultracold NaCs molecules. Finally, Pupillo *et al*. [9] proposed to align strong dipolar molecules with an external field to create a floating lattice structure, capable to host a

[a] As soon as two atoms bond together, they form a molecule. If the two atomic nuclei in this *diatomic* molecule are identical, the molecule is *homonuclear*, *e.g*. O_2, the oxygen most lifeforms on Earth breath. If the two atomic nuclei are different, the molecule is *heteronuclear*. Carbon monoxide, CO, is a well known heteronuclear molecule: in the USA, many states require by law that homes be equipped with CO alarms, as the gas is highly toxic to humans.

different atomic or molecular species that would then form a lattice gas.

1.2 The photoassociation process

In order to use ultracold dipolar molecules, a scheme to create them is necessary. My research concerns a theoretical study of the photoassociation of the NaCs molecule from the continuum of the ground electronic Born-Oppenheimer (BO) state $X^1\Sigma^+$ to a superposition of rovibrational levels of the first excited BO state $A^1\Sigma^+$, and subsequent stabilization to one of the low-lying rovibrational levels of the $X^1\Sigma^+$ state—a process called rovibrational cooling. Photoassociation is triggered by a pulsed laser that excites the initial continuum state to a superposition of high-lying rovibrational levels of the $A^1\Sigma^+$ state. The subsequent wave packet propagates back and forth in the potential well of the $A^1\Sigma^+$ state. Eventually, spontaneous (or stimulated) emission can populate a low-lying rovibrational level of the $X^1\Sigma^+$ state. The overall process is sketched in Fig. 1.2.

The study also accommodates the strong spin-orbit coupling effects between the $b^3\Pi$ and the $A^1\Sigma^+$ electronic states, and reported by Zaharova *et al.* [10]. In the range of excitation energy usually used in photoassociation, these relativistic effects should not be ignored.

1.3 Context

Within the past decade, several groups achieved rovibrational cooling of diatomic molecules using various processes involving photoassociation. Luc-Koenig and Masnou-Seeuws [11] described rovibrational cooling of Cs_2 using chirped laser pulses for the photoassociation step, and relied either on

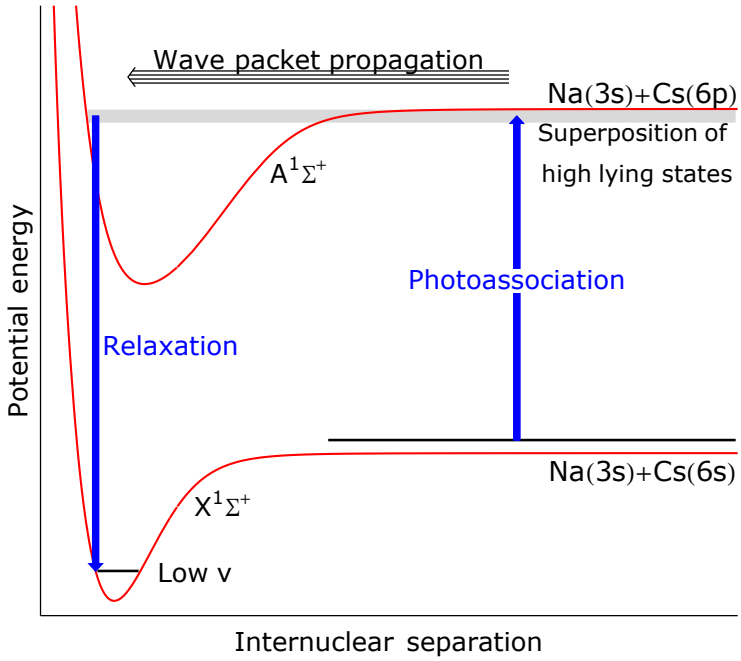

Figure 1.2: General photoassociation cooling process. The photoassociation laser transfers the colliding atoms from the continuum of the ground electronic state to a superposition of high-lying rovibrational states of the first excited Born-Oppenheimer (BO) electronic state. As the wave packet formed propagates to smaller internuclear separations, relaxation can occur either by spontaneous or stimulated emission.

spontaneous [12] or stimulated [13] emission for the relaxation step. Winkler *et al.* [14] transferred ultracold $^{87}Rb_2$ formed via a Feschbach resonance from a bound rovibrational state of the ground electronic state into a more deeply bound rovibrational state of that electronic state.

The group of Ye at JILA[a] [15] populated high-lying vibrational levels of the $X^1\Sigma^+$ state of $^{40}K^{87}Rb$ by preparing Feschbach molecules and then using STImulated Raman Adiabatic Passage (STIRAP [16, 17]) to transfer them to the destination state. Kerman *et al.* [18] reported on the formation of $^{85}Rb^{133}Cs$ molecules in deeply bound states of the $X^1\Sigma^+$ state using a continuous-wave laser for photoassociation and spontaneous emission for relaxation. Yet, preparing Feschbach molecules is technologically intricate and costly, and the relia-

[a]Formerly known as the Joint Institute for Laboratory Astrophysics.

bility of spontaneous emission to reach a chosen quantum state is questionable.

1.4 Why NaCs?

As mentioned above, one goal of ultracold physics is to form highly polar molecules. The sodium-cesium (NaCs) dimer has the second largest permanent electric dipole moment of all alkali dimers [Tbl. VI in 19]. This dipole moment is also fairly constant among the low-lying vibrational states in the ground electronic state of NaCs [19]. Żuchowski and Hutson [20, Tbl. II] showed that NaCs is quite insensitive to the reaction $2\mathrm{NaCs} \rightarrow \mathrm{Na}_2 + \mathrm{Cs}_2$: once the molecule is formed it is the least likely among other heteronuclear alkali dimer to dissociate when colliding with another molecule.

To my knowledge, only two groups are now doing research on NaCs: the Tiemann team at Hannover [21], and the Bigelow group at Rochester [22]. Therefore proposing a *new* photoassociation scheme for NaCs will contribute to the field of formation of ultracold alkali dimers.

1.5 Here's the menu

This manuscript unfolds in the following manner:

- **Chap.** 2 provides a non-exhaustive set of background topics and concepts necessary to understand the results at the end, and also the invaluable ingredients required to do the research. These include the basics of the 2- and 3- state problems of quantum mechanics, the potential energy curves for the electronic states of the molecule, and the electric dipole moment function that partially governs the transition between the relevant electronic states

- **Chap.** 3 defines the system I studied, details its relevant physical characteristics, and gives justifications for the models and approximations I used.

- **Chap.** 4 sets up the mathematical description of the system and the physical interactions that govern its behavior; then proceeds to derive the equations one needs to solve to actually discover *how* the system behaves.

- **Chaps.** 5 focuses on the probability density functions for the spin-orbit coupled channels, in particular the location of the peaks of probability depending on the energy of the coupled-channel bound state.

- **Chap.** 6 give the solutions to the equations obtained in Chap. 4, and finally,

- **Chap.** 7 summarizes the findings of this adventure, and suggests possible extension of this work.

Chapter 2

Background

"A beginning is the time for taking the most delicate care that the balances are correct."
—Frank Herbert, *Dune*

2.1 Lasers

This section summarizes some aspects of the mathematical modeling of lasers relevant to this work. Saleh and Teich [23, Chap. 3 & 15][a] provide in-depth information on the optical properties of laser apparati. For the purpose of this research, it suffices to remember that lasers are essentially sources of monochromatic electromagnetic fields. In this work, the term *laser* refers only to the time-dependent, propagating, monochromatic electromagnetic field, and never to its source. As a propagating E&M wave, laser fields are also space-dependent. I justify in Sec. 3.2.4 p. 63 why I can neglect this spatial dependence. Finally, only the electric part of the laser E&M field is considered. In this section, I focus on the *time*-dependence of the laser field.

In general, the laser field $\vec{\mathscr{E}}(t)$, polarized in the direction $\hat{\epsilon}$ is written as

$$\vec{\mathscr{E}}(t) = \mathscr{E}(t)\cos(\omega t)\hat{\epsilon} \tag{2.1}$$

where $\mathscr{E}(t)$ is the amplitude and ω the angular frequency of the photons in the laser field.

[a] See also references therein and Bransden and Joachain [24, Chap. 15].

In what follows, I examine special cases for the time dependence of $\mathscr{E}(t)$. Later on, I introduce chirped laser fields, where ω becomes time-dependent.

2.1.1 Continuous wave lasers

In a continuous wave (cw) laser, the amplitude of the field is constant:

$$\mathscr{E}(t) = \mathscr{E}_0 \qquad \text{so that} \qquad \vec{\mathscr{E}}(t) = \mathscr{E}_0 \cos(\omega t)\hat{\epsilon}. \tag{2.2}$$

Thus a cw laser is an electric field that points along the direction $\hat{\epsilon}$ perpendicular to the direction of propagation, with a single definite angular frequency ω. Mathematically, the cw laser field is on since the beginning of times, and remains on until the end of times. Physically, the cw laser field interacts with a system that never experiences the on-off transition regime of the laser.

The intensity $I(t)$ of an electromagnetic wave is the time-average[a] over one period T of the wave, of the magnitude of the Poynting vector $\vec{\pi}(t)$:

$$I(t) = \frac{1}{\mathrm{T}} \int_t^{t+\mathrm{T}} |\vec{\pi}(t')| \, \mathrm{d}t', \tag{2.3}$$

where $|\vec{\pi}(t')| = c\varepsilon_0 |\vec{\mathscr{E}}(t')|^2$. For a cw laser with amplitude $\mathscr{E}_0$, the intensity is the constant $I = \frac{1}{2} c\varepsilon_0 \mathscr{E}_0^2$.

Let's now examine a special case of lasers with time-dependent amplitudes: the Gaussian laser pulses.

[a] See [25, p. 454].

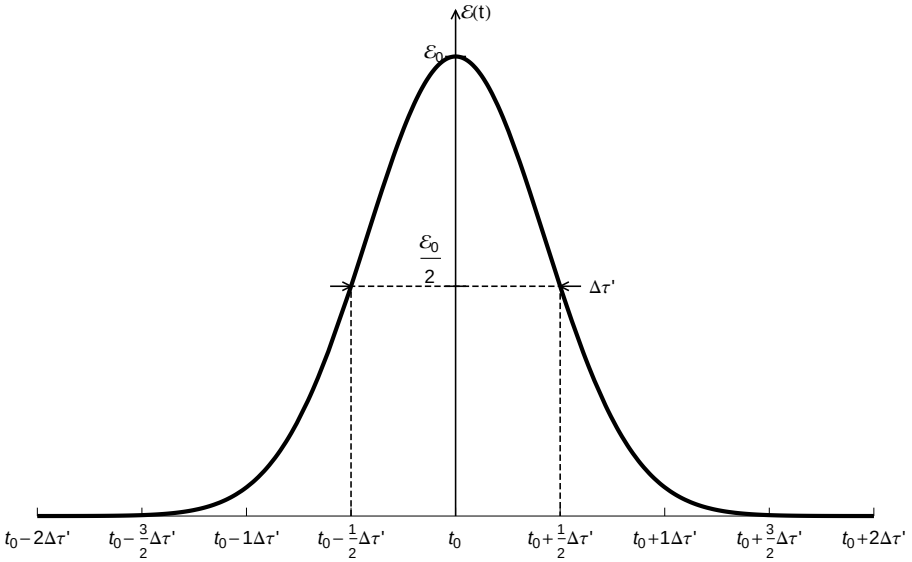

Figure 2.1: Gaussian electric field pulse *amplitude*. The horizontal dashed line indicates the Half Maximum height, while the two vertical dashed lines mark the Full Width at Half Maximum (FWHM) $\Delta\tau'$.

2.1.2 Gaussian laser pulses

In a pulsed laser, the amplitude $\mathscr{E}(t)$ is zero long before and long after the interaction of the laser with the system:

$$\lim_{t\to-\infty}\mathscr{E}(t)=\lim_{t\to+\infty}\mathscr{E}(t)=0$$

Typical pulsed lasers have a Gaussian amplitude—see Fig. 2.1—such that

$$\mathscr{E}(t)=\mathscr{E}_0\exp\left(-4\ln 2\left(\frac{t-t_0}{\Delta\tau'}\right)^2\right) \tag{2.4}$$

where the pulse has maximum amplitude $\mathscr{E}_0$ at $t=t_0$ and $\Delta\tau'$ is the Full Width at Half Maximum (FWHM) such that $\mathscr{E}(t\pm\frac{\Delta\tau'}{2})=\frac{\mathscr{E}_0}{2}$.

The intensity is still defined by Eq. (2.3), but a pulsed laser has a time-

dependent amplitude, so

$$
\begin{aligned}
I(t) &= \frac{1}{\mathrm{T}}\int_{t}^{t+\mathrm{T}} |\vec{\pi}(t')|\,\mathrm{d}t' = \frac{c\varepsilon_0}{\mathrm{T}}\int_{t}^{t+\mathrm{T}} |\vec{\mathscr{E}}(t')|^2\,\mathrm{d}t' \\
&= \frac{c\varepsilon_0}{\mathrm{T}}\int_{t}^{t+\mathrm{T}} |\mathscr{E}(t')|^2\cos^2(\omega t)\,\mathrm{d}t' \\
&= \frac{c\varepsilon_0\mathscr{E}_0^2}{\mathrm{T}}\int_{t}^{t+\mathrm{T}} \exp\left(-4\ln 2\left(\frac{t'-t_0}{\Delta\tau'}\right)^2\times 2\right)\cos^2(\omega t')\,\mathrm{d}t' \qquad (2.5)
\end{aligned}
$$

The integral in Eq. (2.5) has no analytic solution. However, if the period of the wave is shorter than the FWHM $\Delta\tau'$, the wave oscillates over one period without the envelope changing significantly, see Fig. 2.2. The exponential factor may then be considered constant in the interval $[0,\mathrm{T}]$, and thus taken out of the integral in Eq. (2.5) when $\mathrm{T} = \frac{2\pi}{\omega} \ll \Delta\tau'$:

$$
\begin{aligned}
I(t) &\underset{\omega\Delta\tau'\gg 2\pi}{\approx} c\varepsilon_0\mathscr{E}_0^2\exp\left(-4\ln 2\left(\frac{t-t_0}{\Delta\tau'}\right)^2\times 2\right)\frac{1}{\mathrm{T}}\int_{t}^{t+\mathrm{T}}\cos^2(\omega t')\,\mathrm{d}t' \\
I(t) &\underset{\omega\Delta\tau'\gg 2\pi}{\approx} \frac{c\varepsilon_0\mathscr{E}_0^2}{2}\exp\left(-4\ln 2\left(\frac{t-t_0}{\Delta\tau'/\sqrt{2}}\right)^2\right). \qquad (2.6)
\end{aligned}
$$

In this research, the angular frequency ω corresponds to the transition frequency between the quantum states involved. At least, ω is on the order of the $6^2S_{1/2} \rightarrow 6^2P_{1/2}$ transition frequency of Cesium [26]: $\omega \approx 2\pi\times 3.35\times 10^{14}\,\mathrm{Hz}$. The duration of the laser pulses in this research never exceeds $10\,\mathrm{ns} = 10^{-8}\,\mathrm{s}$, thus $\omega\Delta\tau \approx 2\pi\times 3.35\times 10^{14}\times 10^{-8} \gg 2\pi$, so Eq. (2.6) applies. Under such condition, the intensity is also Gaussian bell shaped, with peak value $I_0 = \frac{c\varepsilon_0\mathscr{E}_0^2}{2}$ at $t = t_0$ and FWHM $\Delta\tau = \Delta\tau'\sqrt{2}/2$.

The integral over time of the intensity represents the total energy per unit area provided by the pulse. Let's write $I(t)$ as $I(t) = I_0\exp\left(-\frac{(t-t_0)^2}{2\sigma^2}\right)$. The Gaussian function is such that 99.7% of the pulse energy is carried between $t_0-3\sigma$ and $t_0+3\sigma$. I can relate the standard deviation σ of the pulse intensity to the

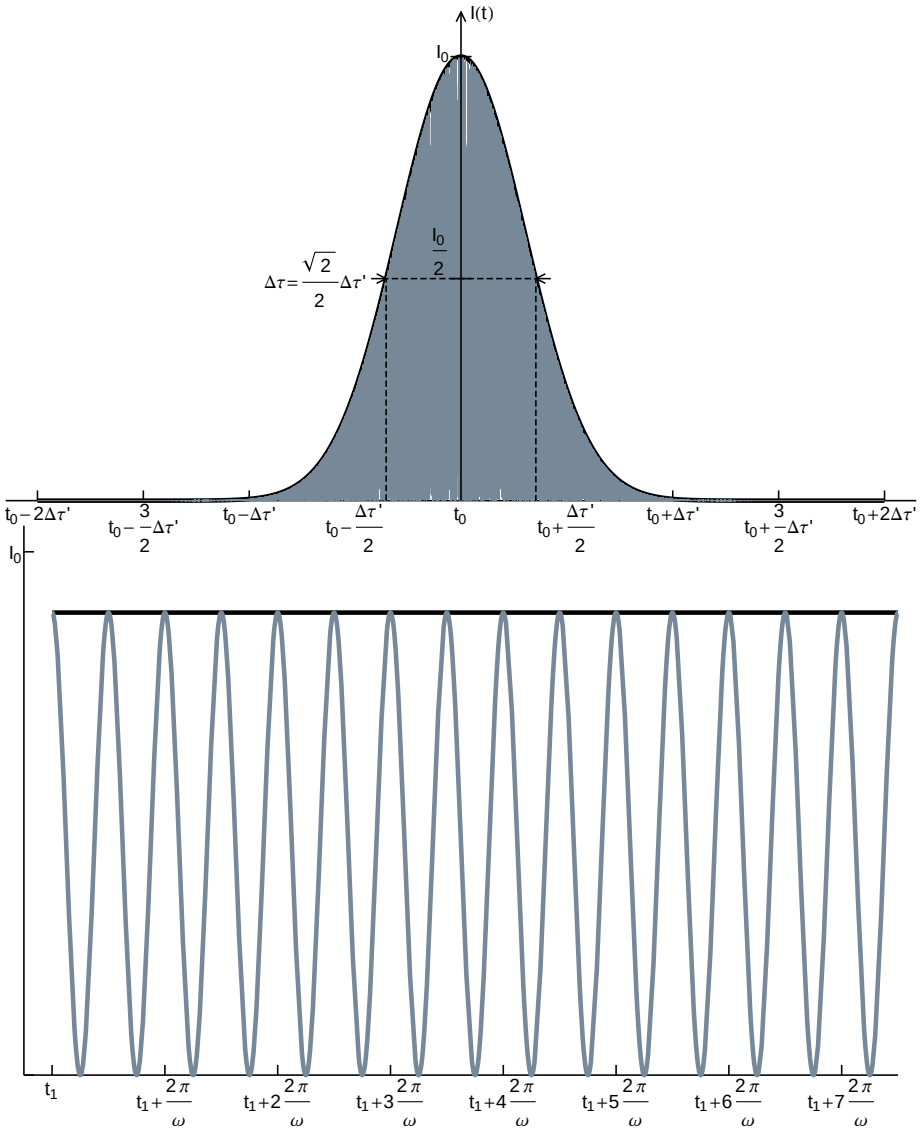

Figure 2.2: **Top**: Gaussian electric field pulse *intensity*. Solid thick black line: Gaussian envelope. The gray filling inside the envelope is actually the densely packed oscillations of the $\cos^2(\omega t)$ term in Eq. (2.5). These oscillations are magnified in the bottom panel. The horizontal dashed line indicates the Half Maximum height, while the two vertical dashed lines mark the Full Width at Half Maximum (FWHM), which is $\sqrt{2}/2$ smaller than the FWHM $\Delta\tau'$ of the original amplitude pulse of Fig. 2.1. **Bottom**: The period $2\pi/\omega$ of the wave is much smaller than the FWHM of the pulse. After 7 periods of the original wave, the height of the crests remains the same, thereby justifying the approximation that yields to Eq. (2.6). This figure uses $\omega = 2\pi \times 3.35 \times 10^{14}\,\mathrm{Hz}$ and $\Delta\tau' = 10\,\mathrm{ns}$. The time t_1 in the bottom panel is taken 500 000 wave periods after the peak at t_0.

FWHM $\Delta\tau'$ of the corresponding field amplitude pulse by identifying the relevant terms. Thus

$$3\sigma = \frac{3\Delta\tau'}{4\sqrt{\ln 2}} \approx 0.9\Delta\tau'. \tag{2.7}$$

Therefore, numerically, it is sufficient to consider that a process involving Gaussian pulses starts $\Delta\tau'$ before the pulse reaches its maximum, and is over after $\Delta\tau'$ has elapsed since the pulse's maximum.

Finally, since the FWHM of the Gaussian function $I(t)$ is the temporal bandwidth of the laser, what is the associated spectral bandwidth? First, the Fourier Transform of a Gaussian function is a Gaussian function, with different parameters. Using the information from [23, p. 1124], the time-dependent Gaussian intensity

$$I(t) = \frac{c\varepsilon_0\mathscr{E}_0^2}{2}\exp\left(-4\ln 2\left(\frac{t-t_0}{\Delta\tau}\right)^2\right)$$

with FWHM $\Delta\tau$, has Fourier Transform

$$\mathscr{F}[I(t)] = I(\omega) = \frac{c\varepsilon_0\mathscr{E}_0^2}{2}\frac{8\pi\ln 2}{\Delta\omega^2}\exp\left(-4\ln 2\left(\frac{\omega-\omega_0}{\Delta\omega}\right)^2\right).$$

The spectral bandwidth $\Delta\omega$, which is also the FWHM of $I(\omega)$, relates to the temporal bandwidth through

$$\Delta\omega = \frac{4\ln 2}{\Delta\tau}.$$

Thus the briefer the laser pulse, the broader its spectral bandwidth: the frequency resolution of the pulse decreases with its duration. Consider a very brief laser pulse, such that $\Delta\tau \approx 5\,\text{ps}$, then the spectral bandwidth is $\Delta\omega \approx 2\pi \times 8.8 \times 10^{10}\,\text{Hz}$. Suppose now the laser tuned to the transition between two quantum states $|1\rangle$ and $|2\rangle$, with resonant frequency ω_{12}, and all initial popula-

tion in state $|1\rangle$. If there exists a quantum state $|3\rangle$ with an energy within $\Delta\omega$ of state $|2\rangle$, then the laser may[a] transfer some population to state $|3\rangle$ rather than $|2\rangle$, an unintended consequence. In choosing the laser pulses's characteristics in this research, I must keep this issue in mind.

2.1.3 Chirped laser pulses

By definition, a laser pulse is chirped when its central frequency ω is time-dependent, $\omega = \omega(t)$. A pulse is *linearly chirped* when its central frequency $\omega(t)$ depends linearly on time, *i.e.* when there exists a real constant[b] $\mathcal{y}$ such that $\omega(t) = \omega_0 + \mathcal{y}t$, where $\mathcal{y}$ is the chirp rate. Linearly chirped pulses are *up-chirped* for $\mathcal{y} > 0$ (frequency increases with time) and *down-chirped* for $\mathcal{y} < 0$ (frequency decreases with time). A chirped Gaussian laser pulse field, polarized along $\hat{\epsilon}$ has therefore the mathematical form

$$\vec{\mathscr{E}}(t) = \mathscr{E}(t)\cos\left(\omega(t)t\right)\hat{\epsilon}, \tag{2.8}$$

with $\mathscr{E}(t)$ the Gaussian envelope defined in Eq. (2.4).

Figure 2.3 shows an example of a linearly up-chirped Gaussian laser pulse. I chose the values of ω_0 and $\mathcal{y}$ to exaggerate the features created by chirping.

As Fig. 2.4 shows, for the laser tuning frequency and chirp rate value relevant to the problem, the intensity of the laser is constant over several optical cycles. Thus, like in the unchirped case of the previous section, the temporal intensity still follows a Gaussian curve. As before, if the electric field has Gaussian envelope with FWHM $\Delta\tau'$, then the temporal intensity has FWHM

[a] The transition can be allowed by relevant selection rules, but actually ill-favored by detrimental transition dipole moments factors.

[b] Given how many symbols this dissertation requires, I am running out: the character $\mathcal{y}$ (read *roomen*) is a letter in the Elvish script invented by Tolkien [27, App. E].

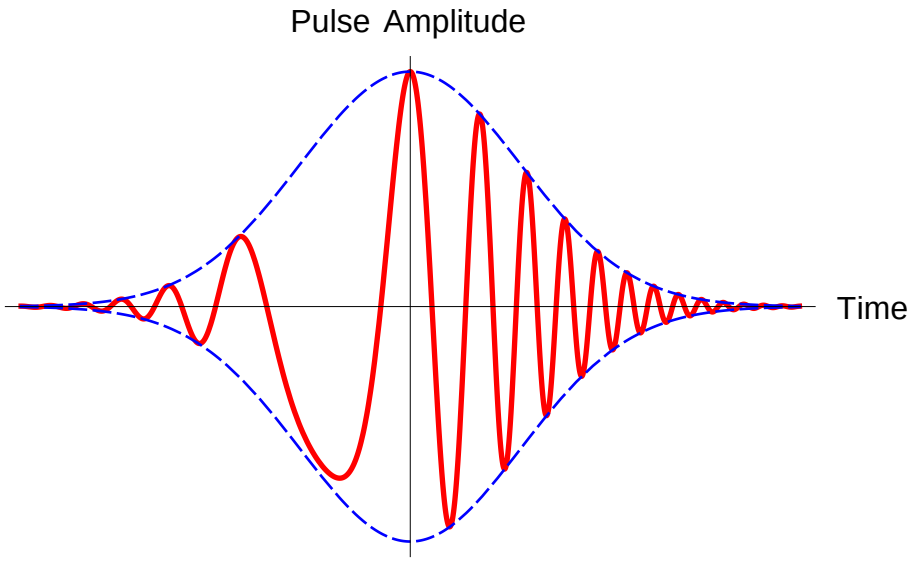

Figure 2.3: Linearly up-chirped Gaussian pulse: $\mathbf{e}^{-t^2}\cos((10+9t)t)$ is the pulse amplitude, with central frequency $\omega(t) = 10+9t$. The dashed lines indicate the pulse envelope.

$\Delta\tau = \Delta\tau'\sqrt{2}/2$:

$$I(t) = \frac{c\varepsilon_0\mathscr{E}_0^2}{2}\exp\left(-4\ln 2\left(\frac{t-t_0}{\Delta\tau}\right)^2\right). \tag{2.9}$$

The FWHM of the spectral intensity still defines the spectral bandwidth $\Delta\omega$ of the Gaussian chirped pulse. According to the results from Appendix A and using the notations of the current section[a],

$$\Delta\omega = \frac{4\ln 2}{\Delta\tau}\sqrt{1+\left(\mathcal{Y}\frac{\Delta\tau^2}{2\ln 2}\right)^2}. \tag{2.10}$$

For a chirped Gaussian pulse, the spectral bandwidth is a function of the temporal bandwidth and the chirp rate. Thus the choice of 2 parameters determines the third one.

[a]Dimensional reminder: the chirp rate $\mathcal{Y}$ has dimension of time^{-2}, and the FWHM $\Delta\tau$ has dimension of time, thus the sum in the square root in Eq. (2.10) is dimensionally consistent.

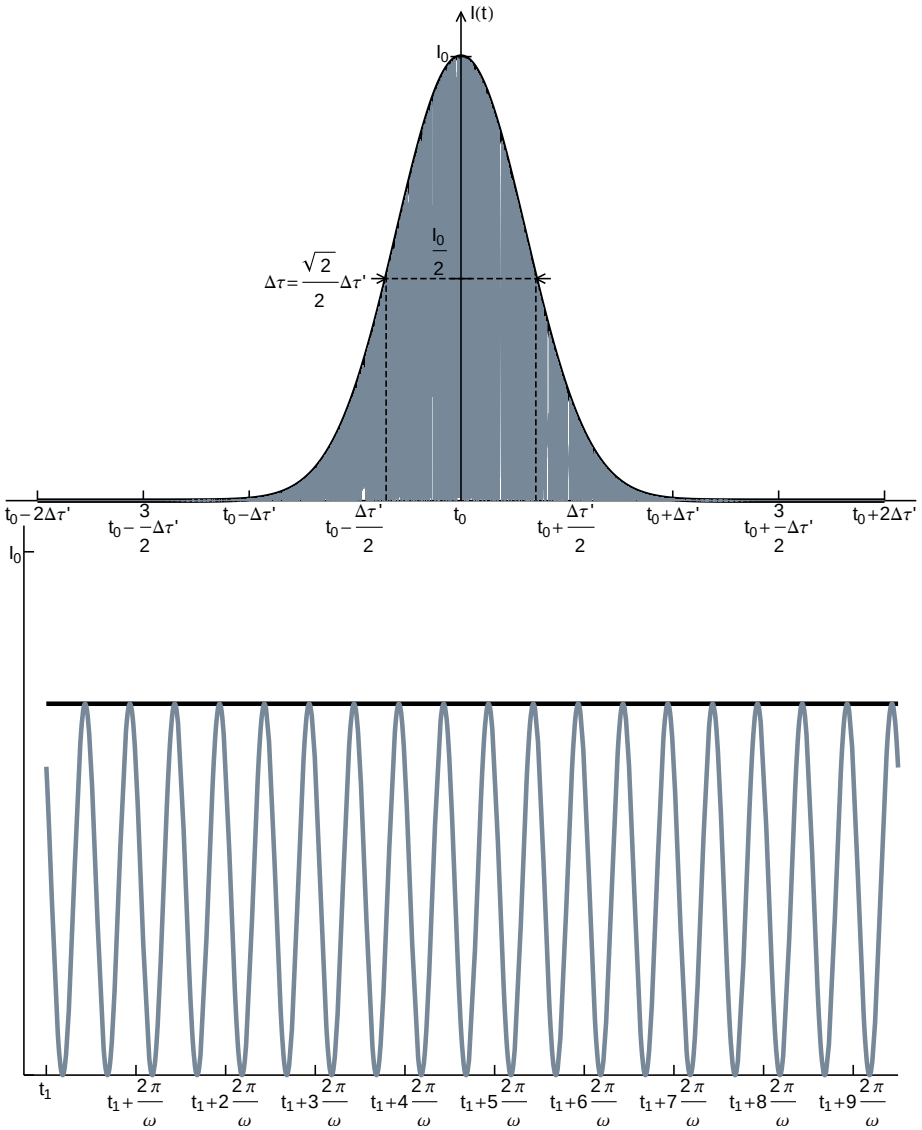

Figure 2.4: Linearly up-chirped Gaussian pulse intensity. The gray filling inside the envelope is actually the function $\mathbf{e}^{-4\ln 2\left(\frac{t-t_0}{\Delta\tau}\right)^2}\cos^2((\omega + \mathcal{Y}t)t)$ with $\Delta\tau = 3\,\text{ns}$, $\omega = 2\pi \times 335.048\,\text{THz}$, and $\mathcal{Y} = 2\pi \times 10\,\text{GHz/ns} = 6.28 \times 10^{-5}\,\text{ps}^{-2}$. For these values of the parameters, the intensity is constant over a few optical cycles, as the magnification in the bottom panel shows.

2.2 Adiabatic Theorem

Adiabaticity is a versatile concept in Physics, with different meanings in thermodynamics, statistical mechanics, molecular spectroscopy, and general quantum mechanics (see App. B). Here I limit the discussion of adiabaticity

in the context of the *adiabatic theorem* and adiabatic passage as presented by Messiah [28, Chap. XVII, §II.10, vol. 2], who derives the formal mathematical proof of the adiabatic theorem.

The **Adiabatic Theorem** states that if the system starts in an eigenket $|i(t_0)\rangle$ of the Hamiltonian $\widehat{\mathscr{H}}(t_0)$ at $t = t_0$, and if $\widehat{\mathscr{H}}(t)$ changes infinitely slowly with time, then at $t = t_1 > t_0$, the system will be in the eigenket $|i(t_1)\rangle$ of $\widehat{\mathscr{H}}(t_1)$ that derives from $|i(t_0)\rangle$ by continuity. Consequently, as time passes, the system makes no transition from $|i(t)\rangle$ to any other eigenket $|j(t)\rangle$ of $\widehat{\mathscr{H}}(t)$.

2.2.1 Adiabatic passage

Consider a total hamiltonian of the form $\widehat{\mathscr{H}}(t) = \widehat{\mathscr{H}_0} + \widehat{\mathscr{V}}(t)$, where $\widehat{\mathscr{V}}(t)$ represents a time-dependent interaction of the system with its environment. In the absence of $\widehat{\mathscr{V}}(t)$, the system is governed solely by $\widehat{\mathscr{H}_0}$.

By controlling the time variation of $\widehat{\mathscr{V}}(t)$, one controls how $\widehat{\mathscr{H}}(t)$ changes in time, and thus how its eigenstates $\{|j(t)\rangle\}_j$ evolve in time. In particular, one can control the evolution of the projection of the $|i(t)\rangle$s on the (time-independent) eigenkets of $\widehat{\mathscr{H}_0}$.

Let's now assume that at $t = t_0 = 0, \widehat{\mathscr{V}}(t_0) = 0$: the eigenstates of $\widehat{\mathscr{H}}(t_0)$ and $\widehat{\mathscr{H}_0}$ coincide since the two hamiltonian equal each others. Therefore, there exists an eigenket $|i(t_0)\rangle$ of $\widehat{\mathscr{H}}(t_0)$ that coincides at $t_0 = 0$ with a particular eigenket of interest $|\psi_0\rangle$ of $\widehat{\mathscr{H}_0}$. The point of adiabatic passage is to engineer $\widehat{\mathscr{V}}(t)$ so that at some later time t_1, $\widehat{\mathscr{V}}(t_1) = 0$ **and** $|i(t_1)\rangle$ now coincides with an eigenket $|\psi_1\rangle \neq |\psi_0\rangle$ of $\widehat{\mathscr{H}_0}$.

One may think of adiabatic passage as a rotation in Hilbert space of the time-dependent eigenkets $\{|j(t)\rangle\}_j$ of $\widehat{\mathscr{H}}(t)$. The rotation starts with the kets $|j(t)\rangle$'s coinciding with the eigenbasis of $\widehat{\mathscr{H}_0}$. As time passes, $\widehat{\mathscr{V}}(t)$ reorients the

kets $|j(t)\rangle$'s into another configuration relative to the fixed, time-independent eigenbasis of $\widehat{\mathscr{H}_0}$.

2.2.2 Condition for applicability of the adiabatic theorem

In adiabatic passage, the carrier state $|i(t)\rangle$ transfers population adiabatically from an initial state $|\psi_0\rangle$ to a final state $|\psi_1\rangle$. The transfer is adiabatic if the adiabatic theorem applies, *i.e.* the hamiltonian $\widehat{\mathscr{H}}(t)$ must vary slowly with time. How slow is sufficiently slow? This is what the adiabatic approximation answers.

Any rigorous implementation of the adiabatic approximation requires the determination of the eigensystem of $\widehat{\mathscr{H}}(t)$, *i.e.* that $\widehat{\mathscr{H}}(t)$ can be diagonalized, a condition satisfied by all hermitian operators[a]. The most general form of the adiabatic approximation appears in Messiah [28, pp. 753–754]. However, this form is impractical when engineering $\widehat{\mathscr{V}}(t)$ to achieve adiabaticity.

Noting that the adiabatic theorem is mostly used with the system at $t_0 = 0$ in a eigenket $|i(t_0)\rangle$ of $\widehat{\mathscr{H}}(t_0)$, the adiabatic approximation simplifies into [28]

$$\left|\frac{\alpha_{ji}(t)}{\omega_{ji}(t)}\right|^2 \ll 1, \qquad j \neq i, \tag{2.11}$$

where $\alpha_{ji}(t) = \left\langle j(t) \left| \frac{\partial}{\partial t} \right| i(t) \right\rangle$, and $\omega_{ji}(t) = \omega_j(t) - \omega_i(t)$ with $\hbar\omega_u(t)$ the eigenvalue of $\widehat{\mathscr{H}}(t)$ associated with $|u(t)\rangle$

$$\widehat{\mathscr{H}}(t)|u(t)\rangle = \hbar\omega_u(t)|u(t)\rangle, \qquad u = i, j. \tag{2.12}$$

[a] $\widehat{\mathscr{H}}(t)$ may not be hermitian, in which case the existence of its eigenelements must be proven by other means. Also the eigenvalues of $\widehat{\mathscr{H}}(t)$—if they exist—may not belong to $\mathbb{R}$. That's OK: rigorously, when $\widehat{\mathscr{H}}$ is time-dependent, its eigenvalues do not represent the possible energies of the system, and they might even be non-observable.

Let's show how the time-dependent potential $\widehat{\mathscr{V}}(t)$ comes into play a little more explicitly. First remember that the total time-dependent hamiltonian is $\widehat{\mathscr{H}}(t) = \widehat{\mathscr{H}_0} + \widehat{\mathscr{V}}(t)$, and differentiate Eq. (2.12) with respect to time for $u = i$:

$$\frac{\partial}{\partial t}\left(\widehat{\mathscr{H}}(t)|i(t)\rangle\right) = \frac{\partial}{\partial t}\left(\hbar\omega_i(t)|i(t)\rangle\right) \tag{2.13a}$$

$$\Leftrightarrow \frac{\partial\widehat{\mathscr{H}}}{\partial t}|i(t)\rangle + \widehat{\mathscr{H}}(t)\frac{\partial}{\partial t}|i(t)\rangle = \frac{\partial\hbar\omega_i(t)}{\partial t}|i(t)\rangle + \hbar\omega_i(t)\frac{\partial}{\partial t}|i(t)\rangle. \tag{2.13b}$$

Now, operate on the left with $\langle j(t)|$

$$\left\langle j(t)\left|\frac{\partial\widehat{\mathscr{H}}}{\partial t}\right|i(t)\right\rangle + \left\langle j(t)\left|\widehat{\mathscr{H}}(t)\frac{\partial}{\partial t}\right|i(t)\right\rangle = \frac{\partial\hbar\omega_i(t)}{\partial t}\langle j(t)|i(t)\rangle + \hbar\omega_i(t)\left\langle j(t)\left|\frac{\partial}{\partial t}\right|i(t)\right\rangle. \tag{2.13c}$$

Since $\widehat{\mathscr{H}}(t)$ is hermitian, $\langle j(t)|i(t)\rangle = \delta_{ij}$ and $\langle j(t)|\widehat{\mathscr{H}}(t) = \hbar\omega_j(t)\langle j(t)|$. Thus

$$\left\langle j(t)\left|\frac{\partial\widehat{\mathscr{H}}}{\partial t}\right|i(t)\right\rangle + \hbar\omega_j(t)\left\langle j(t)\left|\frac{\partial}{\partial t}\right|i(t)\right\rangle = \frac{\partial\hbar\omega_i(t)}{\partial t}\delta_{ij} + \hbar\omega_i(t)\left\langle j(t)\left|\frac{\partial}{\partial t}\right|i(t)\right\rangle \tag{2.13d}$$

$$\Leftrightarrow \left\langle j(t)\left|\frac{\partial}{\partial t}\right|i(t)\right\rangle = -\frac{1}{\hbar(\omega_j(t)-\omega_i(t))}\left\langle j(t)\left|\frac{\partial\widehat{\mathscr{H}}}{\partial t}\right|i(t)\right\rangle \tag{2.13e}$$

$$\Leftrightarrow \alpha_{ji} = -\frac{1}{\hbar\omega_{ji}}\left\langle j(t)\left|\frac{\partial\widehat{\mathscr{H}}}{\partial t}\right|i(t)\right\rangle \tag{2.13f}$$

$$\Leftrightarrow \alpha_{ji} = -\frac{1}{\hbar\omega_{ji}}\left\langle j(t)\left|\frac{\partial\widehat{\mathscr{V}}}{\partial t}\right|i(t)\right\rangle \tag{2.13g}$$

Therefore the adiabatic theorem is applicable when

$$\left|\frac{\left\langle j(t)\left|\frac{\partial\widehat{\mathscr{V}}}{\partial t}\right|i(t)\right\rangle}{\hbar\omega_{ji}^2(t)}\right|^2 \ll 1, \qquad j \neq i. \tag{2.14}$$

To verify that any process is adiabatic requires the knowledge of the time derivative of the operator $\widehat{\mathscr{V}}(t)$, and the eigenelements of the total time-dependent

hamiltonian $\widehat{\mathscr{H}}(t)$.

In the next section, I will exploit adiabatic passage in the 3-state problem, and derive the relevant adiabatic condition for that case.

2.3 Population transfer

2.3.1 The 2-state problem

This section defines the 2-state problem and presents some of its solution in certain cases. Cohen-Tannoudji *et al.* [29, chap. IV, p. 405] introduces the reader to the 2-state problem. The monograph by Shore [30] provides, to my knowledge, the most advanced, thorough, and complete treatment of the 2 and 3-state problems. I will focus on the latter in Sec. 2.3.2, but for the moment I shall concentrate on the former.

2.3.1.1 Presentation

Consider the 2 quantum states of Fig. 2.5. The states $|\mathsf{i}\rangle$ and $|\mathsf{f}\rangle$ are eigenstates of a time-*independent* hamiltonian $\widehat{\mathscr{H}_0}$: $\widehat{\mathscr{H}_0}|u\rangle = E_u|u\rangle, u = \mathsf{i},\mathsf{f}$. The goal in the 2-state problem is to tailor a time-*dependent* interaction $\widehat{\mathscr{V}}(t)$ to transfer an ensemble of particles initially in state $|\mathsf{i}\rangle$ to state $|\mathsf{f}\rangle$. For simplicity, I will assume that $\widehat{\mathscr{V}}(t)$ has no diagonal elements, and that all non zero matrix elements are real:

$$\left\langle \mathsf{i} \middle| \widehat{\mathscr{V}}(t) \middle| \mathsf{i} \right\rangle = \left\langle \mathsf{f} \middle| \widehat{\mathscr{V}}(t) \middle| \mathsf{f} \right\rangle = 0 \tag{2.15a}$$

$$\left\langle \mathsf{i} \middle| \widehat{\mathscr{V}}(t) \middle| \mathsf{f} \right\rangle = \left\langle \mathsf{f} \middle| \widehat{\mathscr{V}}(t) \middle| \mathsf{i} \right\rangle = \mathscr{V}_{if}(t) \neq 0. \tag{2.15b}$$

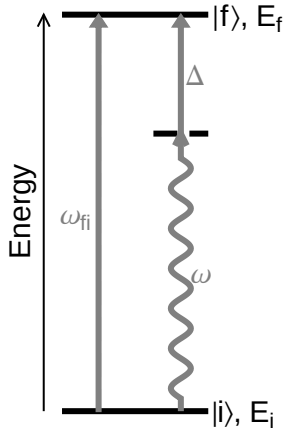

Figure 2.5: The 2-state problem: energy levels and states labels. The problem consists in transferring the system initially in state $|\mathsf{i}\rangle$ into state $|\mathsf{f}\rangle$ using a monochromatic coherent radiation with frequency ω. The detuning Δ is the difference between the radiation frequency and the energy separation between the 2 state: $\Delta = \omega_{\mathsf{fi}} - \omega$.

The system is described by a ket

$$|\Psi(t)\rangle = a_i(t)\,|\mathsf{i}\rangle + a_f(t)\,|\mathsf{f}\rangle, \tag{2.16}$$

where $\mathbb{P}_i(t) = |a_i(t)|^2$ represents the probability to find the system at time t in state $|\mathsf{i}\rangle$, and $\mathbb{P}_f(t) = |a_f(t)|^2$ represents the probability to find the system at time t in state $|\mathsf{f}\rangle$. Sometimes, one refers to $\mathbb{P}_i(t)$ as the *population* in state $|\mathsf{i}\rangle$, and to $\mathbb{P}_f(t)$ as the *population* in state $|\mathsf{f}\rangle$. The initial condition translates into $|\Psi(t=0)\rangle = |\mathsf{i}\rangle$, *i.e.* $\mathbb{P}_i(t=0) = 1$ and $\mathbb{P}_f(t=0) = 0$. From the Time-Dependent Schrödinger Equation using the descriptor of Eq. (2.16) and the properties of the interaction potential given by Eqs. (2.15), one obtains, in matrix form:

$$\mathsf{i}\,\hbar\frac{\mathrm{d}}{\mathrm{d}t}\begin{bmatrix} a_i \\ a_f \end{bmatrix} = \begin{bmatrix} E_i & \mathscr{V}_{if}(t) \\ \mathscr{V}_{if}(t) & E_f \end{bmatrix}\begin{bmatrix} a_i \\ a_f \end{bmatrix}. \tag{2.17}$$

Let's work on how to solve this equation.

2.3.1.2 Rotating wave approximation and solutions to the 2-state problem

The operator $\widehat{\mathscr{V}}(t)$ models the interaction between the electric dipole of the system and the electric field $\vec{\mathscr{E}}(t)$ of a monochromatic wave with frequency ω (see Eq. (2.1)). Thus, I may write

$$\mathscr{V}_{if}(t) = V_{if}\mathscr{E}(t)\cos(\omega t) = \hbar\Omega(t)\cos(\omega t), \tag{2.18}$$

so Eq. (2.17) now reads:

$$\mathbf{i}\hbar\frac{\mathrm{d}}{\mathrm{d}t}\begin{bmatrix} a_i \\ a_f \end{bmatrix} = \begin{bmatrix} E_i & \hbar\Omega(t)\cos(\omega t) \\ \hbar\Omega(t)\cos(\omega t) & E_f \end{bmatrix}\begin{bmatrix} a_i \\ a_f \end{bmatrix}. \tag{2.19}$$

Due to the oscillatory term $\cos(\omega t)$, this equation has no analytic solution [30, p. 231].

To pave the way towards a solution, let's perform the unitary transformation

$$\begin{bmatrix} a_i \\ a_f \end{bmatrix} = \begin{bmatrix} \mathbf{e}^{-\mathbf{i}E_i t/\hbar} & 0 \\ 0 & \mathbf{e}^{-\mathbf{i}(E_i-\hbar\omega)t/\hbar} \end{bmatrix}\begin{bmatrix} c_i \\ c_f \end{bmatrix} \tag{2.20}$$

The unitary transformation does not change the populations, $\mathbb{P}_i(t) = |a_i(t)|^2 = |c_i(t)|^2$ and $\mathbb{P}_f(t) = |a_f(t)|^2 = |c_f(t)|^2$. The new probability amplitudes c's satisfy

$$\mathbf{i}\hbar\frac{\mathrm{d}}{\mathrm{d}t}\begin{bmatrix} c_i \\ c_f \end{bmatrix} = \begin{bmatrix} 0 & \hbar\Omega(t)\cos(\omega t)\mathbf{e}^{-\mathbf{i}\omega t} \\ \hbar\Omega(t)\cos(\omega t)\mathbf{e}^{+\mathbf{i}\omega t} & E_f - E_i - \hbar\omega \end{bmatrix}\begin{bmatrix} c_i \\ c_f \end{bmatrix} \tag{2.21a}$$

$$\Leftrightarrow \mathbf{i}\hbar\frac{\mathrm{d}}{\mathrm{d}t}\begin{bmatrix} c_i \\ c_f \end{bmatrix} = \begin{bmatrix} 0 & \frac{\hbar\Omega(t)}{2}(1+\mathbf{e}^{-2\mathbf{i}\omega t}) \\ \frac{\hbar\Omega(t)}{2}(\mathbf{e}^{2\mathbf{i}\omega t}+1) & E_f - E_i - \hbar\omega \end{bmatrix}\begin{bmatrix} c_i \\ c_f \end{bmatrix}. \tag{2.21b}$$

Setting $\Omega(t)$ to a constant and $\omega = 0$ in the latter equation, renders the interac-

tion $\widehat{\mathscr{V}}$ time-*independent*. Then, Eq. (2.21b) has analytic solutions called Rabi oscillations [29, chap. IV.C.3, p. 412] with frequency $\frac{1}{\hbar}\sqrt{(E_f - E_i)^2 + 4|\hbar\Omega|^2}$.

When $\widehat{\mathscr{V}}(t)$ is time-dependent such that $\mathscr{V}_{if}(t) = V_{if}\mathscr{E}(t)\cos(\omega t)$, and the driving frequency ω is much greater than[a] $\frac{1}{\hbar}\sqrt{(E_f - E_i)^2 + 4|V_{if}\mathscr{E}_{\max}|^2}$, the behavior of interest for the probability amplitude occurs over many optical cycles [30, p. 236]. In this context, the **Rotating Wave Approximation (RWA)** [30, p. 236] assumes that the probability amplitudes $c_u(t), u = i, f$ do not change appreciably over an optical cycle of the driving field, and thus the rapidly oscillating term $\mathbf{e}^{2\mathbf{i}\,\omega t}$ in Eq. (2.21b) averages out over said optical cycle. In effect the RWA consists in the replacements

$$1 + \mathbf{e}^{2\mathbf{i}\,\omega t} \to 1$$
$$1 + \mathbf{e}^{-2\mathbf{i}\,\omega t} \to 1$$

It is useful to condense notations by defining the detuning Δ of the driving field from the resonance frequency, $\Delta = \frac{E_f - E_i}{\hbar} - \omega$. With the RWA, Eq. (2.21b) becomes

$$\frac{\mathrm{d}}{\mathrm{d}t}\begin{bmatrix} c_i \\ c_f \end{bmatrix} = -\frac{\mathbf{i}}{2}\begin{bmatrix} 0 & \Omega(t) \\ \Omega(t) & 2\Delta \end{bmatrix}\begin{bmatrix} c_i \\ c_f \end{bmatrix} \tag{2.22}$$

[a] The quantity $\mathscr{E}_{\max}$ is the maximum value of the electric field envelope $\mathscr{E}(t)$.

Δ (units of Ω)	0	1	2	3	4	5
$\mathbb{P}_f^{\max}$	1	0.5	0.2	0.1	0.0588	0.0385

Table 2.1: Rabi oscillations for a continuous wave laser: maximal population in the final state for various detunings. The maximal population in $|\mathsf{f}\rangle$ decreases as the detuning increases, according to $\mathbb{P}_f^{\max} = 1/\left(1+\left(\frac{\Delta}{\Omega}\right)^2\right)$.

2.3.1.3 Rabi oscillations for different detunings

For a continuous wave laser, Ω is time-independent. Then Eq. (2.22) has analytic solutions[a] for all values of the detuning Δ

$$c_i(t) = \frac{\mathbf{e}^{-\mathbf{i}\frac{\Delta}{2}t}}{\delta}\left(\delta\cos\left(\frac{\delta t}{2}\right)+\mathbf{i}\,\Delta\sin\left(\frac{\delta t}{2}\right)\right), \tag{2.23a}$$

$$c_f(t) = -\frac{\mathbf{i}\,\Omega}{\delta}\mathbf{e}^{-\mathbf{i}\frac{\Delta}{2}t}\sin\left(\frac{\delta t}{2}\right), \tag{2.23b}$$

where $\delta = \sqrt{\Delta^2+\Omega^2}$. The probability to find the system described by the ket $|\Psi(t)\rangle$ in state $|\mathsf{i}\rangle$ or state $|\mathsf{f}\rangle$ at time t, *i.e.* the populations $\mathbb{P}_i(t)$ and $\mathbb{P}_f(t)$, are therefore

$$\mathbb{P}_i(t) = |c_i(t)|^2 = \frac{1}{\delta^2}\left(\delta^2\cos^2\left(\frac{\delta t}{2}\right)+\Delta^2\sin^2\left(\frac{\delta t}{2}\right)\right), \tag{2.24a}$$

$$\mathbb{P}_f(t) = |c_f(t)|^2 = \left(\frac{\Omega}{\delta}\right)^2\sin^2\left(\frac{\delta t}{2}\right), \tag{2.24b}$$

In Fig. 2.6 p. 24, I plot Eqs. (2.24) for three values of the detuning Δ. The plots show that the population in each state oscillates with frequency $\delta = \sqrt{\Delta^2+\Omega^2}$, between extrema that also depend on the detuning (see Tbl. 2.1). As the detuning increases, so does the frequency of the oscillations, while the maximal population in state $|\mathsf{f}\rangle$ decreases. The population in the final state, $\mathbb{P}_f(t)$ is

[a] One may obtain these solutions by standard methods from calculus, in particular by diagonalizing the 2×2 matrix of Eq. (2.22).

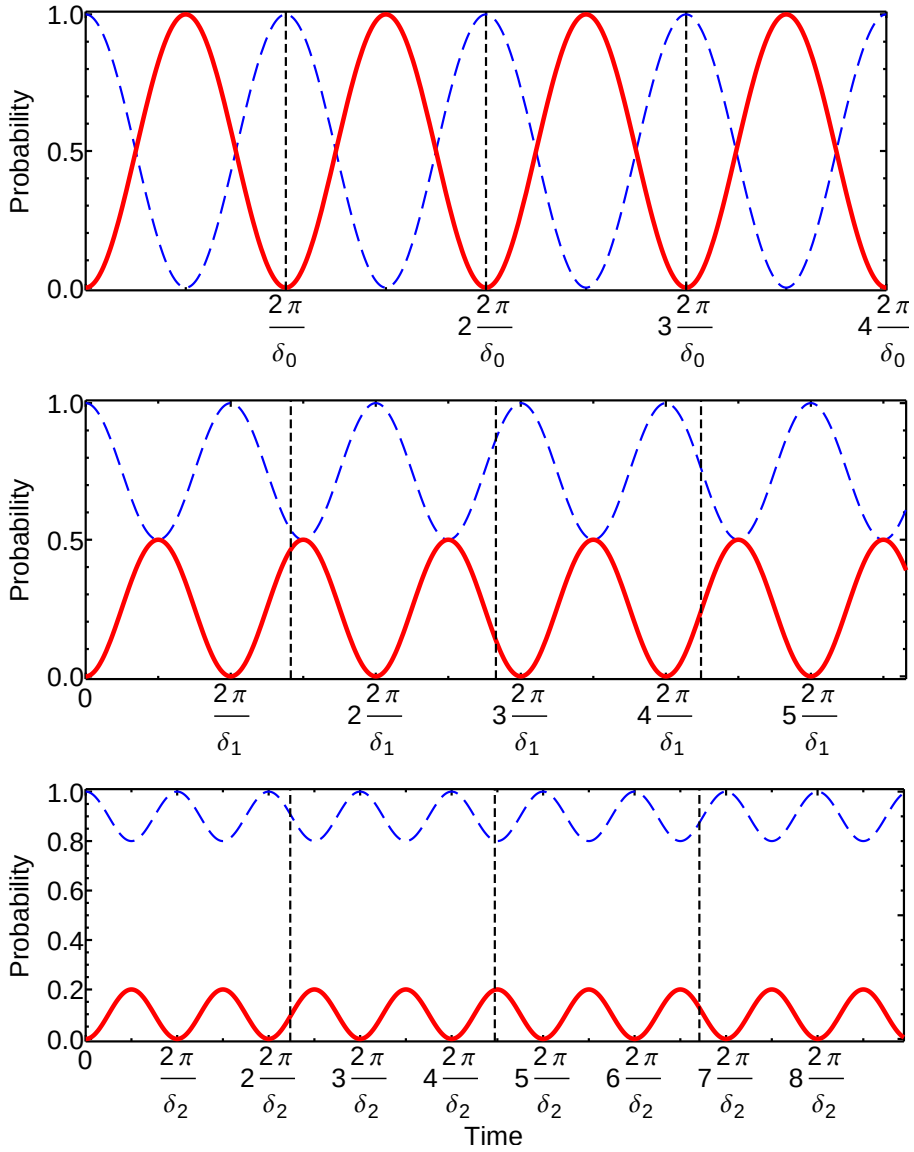

Figure 2.6: Rabi oscillations for 3 different detunings. Red solid curve: population in the final state $|\mathsf{f}\rangle$. Blue dashed curve: population in the initial state $|\mathsf{i}\rangle$. In each panel, the detuning is a multiple of Ω, $\Delta_k = k\Omega$, so $\delta_k = \sqrt{\Delta_k^2 + \Omega^2} = \Omega\sqrt{k^2+1}$. **Top panel**: zero detuning, $\Delta = 0$. **Middle panel**: $\Delta = \Omega$. **Bottom panel**: $\Delta = 2\Omega$. The vertical dashed lines mark the period for the on-resonance ($\Delta = 0$) case: as the detuning increases, the period of the oscillation decreases. Also, as the detuning increases, the maximum population that can be transferred in $|\mathsf{f}\rangle$ decreases, see also Tbl. 2.1.

maximal every half-period, that is when[a] $t = (2k+1)\frac{\pi}{\delta}, k \in \mathbb{N}$.

An important point to keep in mind: figure 2.6 shows oscillating *probabil-*

[a] $k \in \mathbb{N}$ since $t \geq 0$.

ities. If one performs a measurement on the system at any time t, then the possible outcomes of that measurement are given by Eqs. (2.24). For example, at zero detuning (top panel in Fig. 2.6), if the system is probed at $t = 2\frac{2\pi}{\delta_0}$, then there is a 100% chance that the system is in $|\mathsf{f}\rangle$. By the fifth postulate of quantum mechanics (Cohen-Tannoudji *et al*. [29, p. 221]), the system is then frozen into $|\mathsf{f}\rangle$. Probing the same system again at a later time—no later than the lifetime of $|\mathsf{f}\rangle$—will again yield $\mathbb{P}_f = 1$. Population oscillations plots can *not* be obtained in the lab like oscillations on an oscilloscope screen, every data point must be obtained individually and the experiment restarted.

Summary To achieve population transfer from $|\mathsf{i}\rangle$ to $|\mathsf{f}\rangle$ in the 2-state configuration with a continuous wave laser

1. the laser must be resonant with the transition $|\mathsf{i}\rangle \rightarrow |\mathsf{f}\rangle$, *i.e*. $\Delta = 0$,
2. the system must be probed at any time $t = (2k+1)\frac{\pi}{\Omega}, k \in \mathbb{N}$ to freeze the population in state $|\mathsf{f}\rangle$.

What happens with a pulsed laser?

2.3.1.4 Pulsed lasers in the 2-state problem: the necessity for π-pulses

When Ω is time-dependent, then for $\Delta = 0$ Eq. (2.22) has analytic solutions:

$$c_i(t) = \mathbf{i}\cos\left(\int_0^t \frac{\Omega(t')}{2}\,\mathrm{d}t'\right) \tag{2.25a}$$

$$c_f(t) = -\mathbf{i}\sin\left(\int_0^t \frac{\Omega(t')}{2}\,\mathrm{d}t'\right), \tag{2.25b}$$

which yields for the populations

$$\mathbb{P}_i(t) = \cos^2\left(\int_0^t \frac{\Omega(t')}{2}\,\mathrm{d}t'\right) \tag{2.26a}$$

$$\mathbb{P}_f(t) = \sin^2\left(\int_0^t \frac{\Omega(t')}{2}\,\mathrm{d}t'\right). \tag{2.26b}$$

The probability to find the system in $|\mathsf{f}\rangle$ is 1 at all instants t such that

$$\int_0^t \Omega(t')\,\mathrm{d}t' = (2k+1)\pi, \qquad k \in \mathbb{N}. \tag{2.27}$$

If $\Omega(t)$ is a pulse, lasting from $t = 0$ to $t = t_{\text{end}}$, then according to the above condition, the pulse successfully transferred population from $|\mathsf{i}\rangle$ to $|\mathsf{f}\rangle$ if

$$\int_0^{t_{\text{end}}} \Omega(t')\,\mathrm{d}t' = (2k+1)\pi, \qquad k \in \mathbb{N}. \tag{2.28}$$

The challenge is to achieve population transfer in a given amount of time: t_{end} is therefore a constraint on the problem. Furthermore, imposing *when* the process ends determines the FWHM of the pulse. If $\Delta\tau'$ is the FWHM of a Gaussian pulse, then at least 99.7% of the pulse energy is transferred to the system between $t_p - \Delta\tau'$ and $t_p + \Delta\tau'$ (see Sec. 2.1.2, p. 9). Therefore one may choose $\Delta\tau'$ such that $2\Delta\tau' = t_{\text{end}}$. The only parameter of the pulse left to satisfy the condition Eq. (2.28) is the pulse amplitude. In particular, a pulse that satisfies Eq. (2.28) for $k = 0$ is called a π-pulse.

Figure 2.7 shows the ideal case of a π-pulse and the corresponding population transfer. Figure 2.8 shows the case of a near-π-pulse and the corresponding population transfer. For the pulse in Fig. 2.8, $\int_0^{t_{\text{end}}} \Omega(t')\,\mathrm{d}t' = 3.15\pi$. Because the pulse does not satisfy Eq. (2.28), the population in the final state reaches 1 before the pulse is over, and then decreases to its final value. The

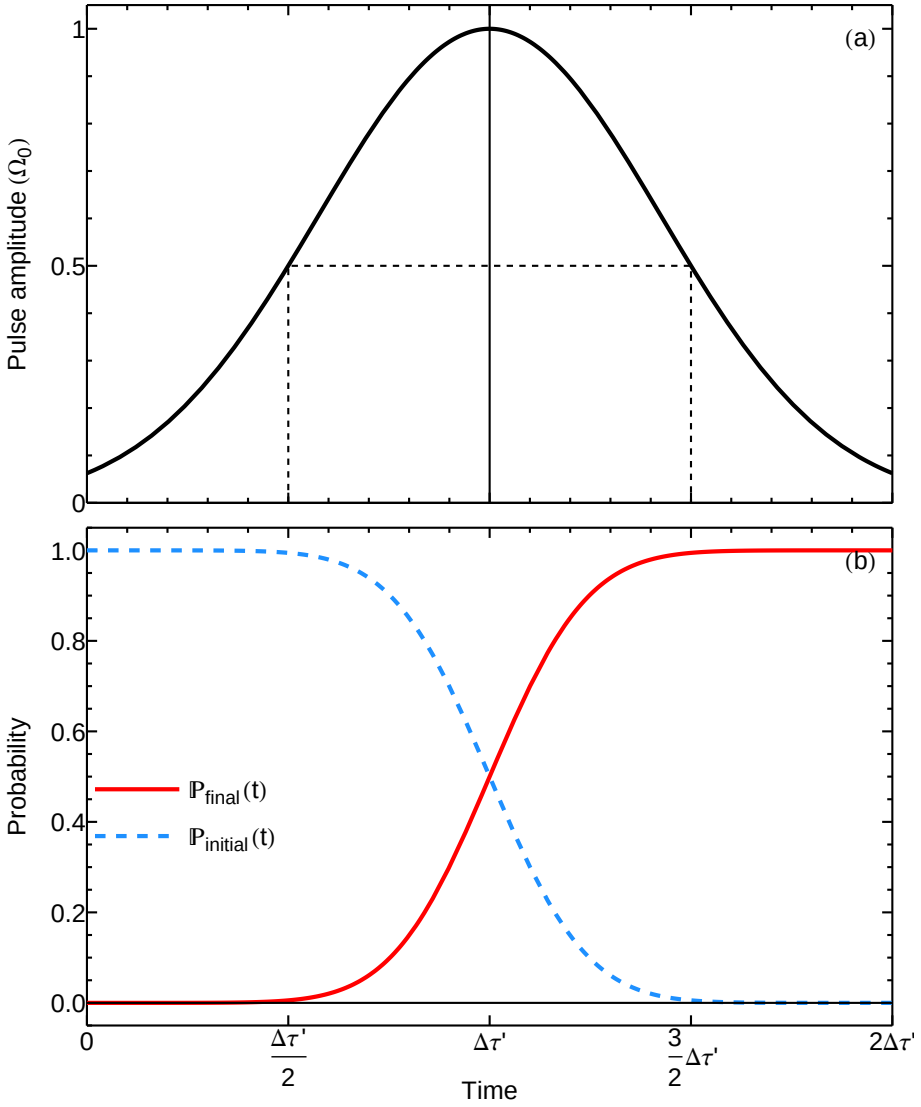

Figure 2.7: Population transfer for a π-pulse. (**a**): Solid curve, pulse amplitude $\Omega(t)$. The dashed lines mark the Full Width at Half Maximum. Note that the vertical axis is in units of Ω_0. (**b**): Probability in each state of the 2-state problem. The population passes smoothly and completely from the initial state $|i\rangle$ (blue dashed curve) to the final state $|f\rangle$ (red solid curve). The transfer effectively starts after $\Delta\tau'/2$, and is essentially over after $3\Delta\tau'/2$.

requirements of the π-pulse condition are quite constraining [16, p. 1005]. As Fig. 2.8 show, population is not fully transferred when the π-pulse condition is only approximately satisfied.

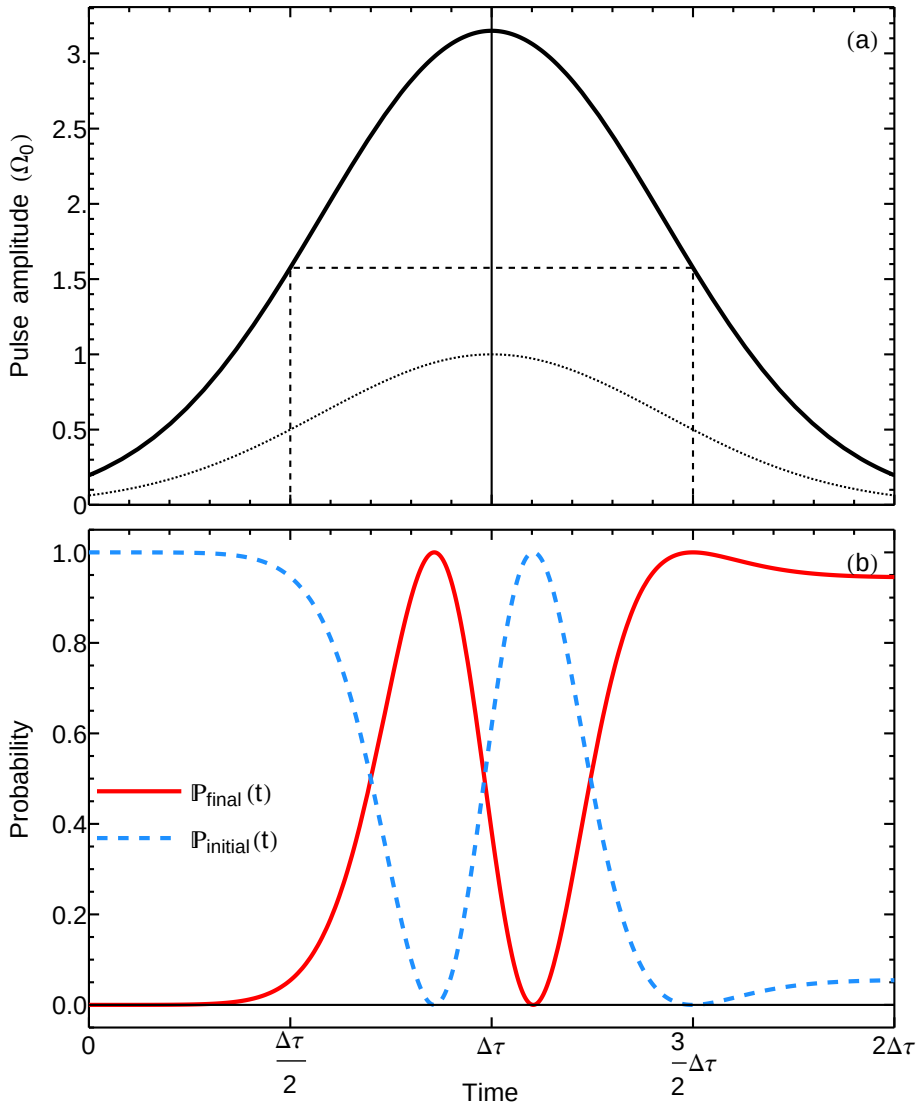

Figure 2.8: Population transfer for a *near-*π pulse. (**a**): Solid curve, pulse amplitude $\Omega(t)$. The dashed lines mark the Full Width at Half Maximum. Note that the vertical axis is in units of Ω_0. The dotted thin line represents the original π-pulse of Fig. 2.7. (**b**): Probability in each state of the 2-state problem. The population oscillates between the two states before reaching a steady value at the end of the process. However, because the pulse does not satisfy Eq. (2.28), the population in $|\mathsf{f}\rangle$ reaches 1 *before* the pulse is over, and then decreases to its final value.

2.3.2 The 3-state problem

In the previous section, the selection rules of the interaction $\widehat{\mathscr{V}}(t)$ determine the possibility of a transition $|i\rangle \to |f\rangle$. As $\widehat{\mathscr{V}}(t)$ represents the electric dipole-

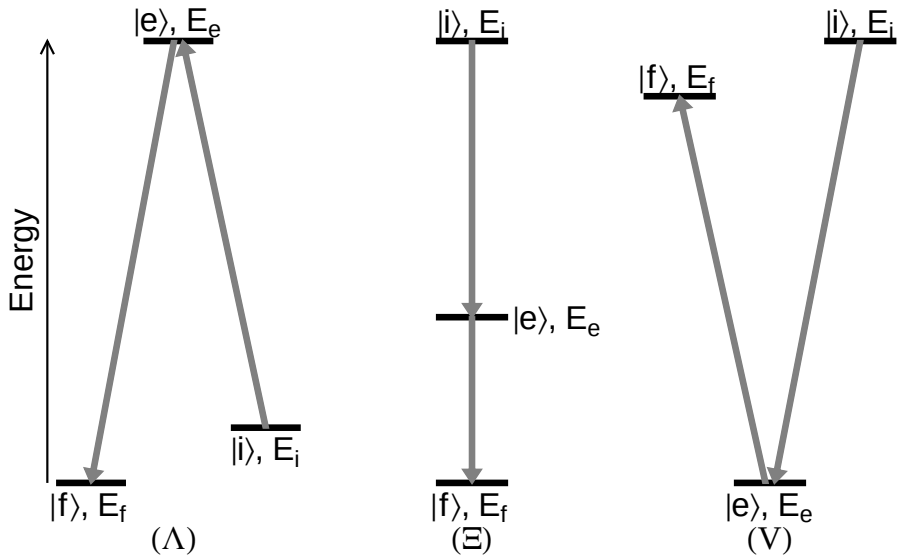

Figure 2.9: Possible ordering of energy in the 3-state problem. **Left** (Λ): Λ configuration, $E_f < E_i < E_e$. **Middle** (Ξ): Ξ configuration, $E_i < E_e < E_f$. **Right** (V): V configuration, $E_e < E_f < E_i$. The arrows indicate the expected sequence of the transfer. The diagrams are drawn for an overall *relaxation*: E_f is always below E_i. Swapping the indices f and i gives the diagram for an overall *excitation*.

electric field interaction, the strength of the transition $|i\rangle \rightarrow |f\rangle$ depends on the amplitude of the laser field and the magnitude of the electric dipole moment matrix element between $|i\rangle$ and $|f\rangle$. If selection rules forbid the transition altogether[a], then one can use an intermediate state $|e\rangle$, for which the transitions $|i\rangle \rightarrow |e\rangle$ and $|e\rangle \rightarrow |f\rangle$ are allowed by the operator $\widehat{\mathscr{V}}(t)$, as a stepping stone between $|i\rangle$ and $|f\rangle$. Whether $|i\rangle$ lies above or below $|f\rangle$ in energy, there are three possible ways to position $|e\rangle$ on the energy scale, as Fig. 2.9 shows.

2.3.2.1 Defining the problem

In the 3-state problem, two E&M fields are present: the pump field with frequency ω_P couples $|i\rangle$ & $|e\rangle$, while the Stokes field with frequency ω_S couples $|e\rangle$ to $|f\rangle$. If $\widehat{\mathscr{V}}(t)$ is the operator representing this interaction, we shall assume

[a] Or the matrix element $\left\langle i \left| \widehat{\mathscr{V}}(t) \right| f \right\rangle$ is so small that the amplitude of the corresponding laser is unrealistic.

that

$$\left\langle i \left| \widehat{\mathscr{V}} \right| i \right\rangle = \left\langle e \left| \widehat{\mathscr{V}} \right| e \right\rangle = \left\langle f \left| \widehat{\mathscr{V}} \right| f \right\rangle = \left\langle i \left| \widehat{\mathscr{V}} \right| f \right\rangle = 0.$$

I will further assume that all non-zero matrix element of $\widehat{\mathscr{V}}$ are real, and remember that they are time-dependent.

Furthermore, the Gaussian envelopes of each laser pulse do not coincide in time. In particular, the envelopes reach their peak values at different instants. Thus, the expression for the Gaussian pulse envelopes are

$$\mathscr{E}_i(t) = \mathscr{E}_i^0 \exp\left(-4\ln 2\left(\frac{(t-t_i)}{\Delta\tau_i}\right)^2\right), \qquad i = P, S, \tag{2.29}$$

where t_i is the instant when $\mathscr{E}_i(t)$ peaks. I also define the pulse delay $\eta = t_S - t_P$. When $\eta > 0 \Rightarrow t_S > t_P$, the pump pulse peaks *before* the Stokes pulse (intuitive sequence). When $\eta < 0 \Rightarrow t_S < t_P$, the pump pulse peaks *after* the Stokes pulse (counterintuitive sequence).

The descriptor of the system in the 3-state problem is

$$|\Psi(t)\rangle = c_i(t)\mathbf{e}^{-\mathbf{i}\,E_i t/\hbar}|i\rangle + c_e(t)\mathbf{e}^{-\mathbf{i}\,t(\omega_P + E_i/\hbar)}|e\rangle + c_f(t)\mathbf{e}^{-\mathbf{i}\,t(\omega_P - \omega_S + E_i/\hbar)}|f\rangle, \tag{2.30}$$

where the choice of phase factors sets the stage to use the RWA later. Plugging $|\Psi(t)\rangle$ into the Time-Dependent Schrödinger Equation yields equations for the probability amplitudes c's:

$$\mathbf{i}\,\hbar\frac{\mathrm{d}}{\mathrm{d}t}\begin{bmatrix} c_i \\ c_e \\ c_f \end{bmatrix} = \begin{bmatrix} 0 & \left\langle i \left| \widehat{\mathscr{V}} \right| e \right\rangle \mathbf{e}^{-\mathbf{i}\,t\omega_P} & 0 \\ \left\langle e \left| \widehat{\mathscr{V}} \right| i \right\rangle \mathbf{e}^{\mathbf{i}\,t\omega_P} & \hbar\Delta_P & \left\langle e \left| \widehat{\mathscr{V}} \right| f \right\rangle \mathbf{e}^{\mathbf{i}\,t\omega_S} \\ 0 & \left\langle f \left| \widehat{\mathscr{V}} \right| e \right\rangle \mathbf{e}^{-\mathbf{i}\,t\omega_S} & \hbar(\Delta_P - \Delta_S) \end{bmatrix}\begin{bmatrix} c_i \\ c_e \\ c_f \end{bmatrix}, \tag{2.31}$$

where I defined the detunings

$$\Delta_P = \frac{E_e - E_i}{\hbar} - \omega_P, \tag{2.32a}$$

$$\Delta_S = \frac{E_e - E_f}{\hbar} - \omega_S. \tag{2.32b}$$

As in the 2-state problem, the time dependence of $\left\langle i \left| \widehat{\mathscr{V}} \right| e \right\rangle$ and $\left\langle f \left| \widehat{\mathscr{V}} \right| e \right\rangle$ originates from an oscillatory part and a time-dependent envelope. However, each term has its own envelope and its own oscillation frequency[a]:

$$\left\langle i \left| \widehat{\mathscr{V}} \right| e \right\rangle = V_{ie}\mathscr{E}_P(t)\cos(\omega_P t) = \frac{\hbar\Omega_P(t)}{2}\left(\mathbf{e}^{\mathbf{i}\,\omega_P t} + \mathbf{e}^{-\mathbf{i}\,\omega_P t}\right) \tag{2.33a}$$

$$\left\langle f \left| \widehat{\mathscr{V}} \right| e \right\rangle = V_{fe}\mathscr{E}_S(t)\cos(\omega_S t) = \frac{\hbar\Omega_S(t)}{2}\left(\mathbf{e}^{\mathbf{i}\,\omega_S t} + \mathbf{e}^{-\mathbf{i}\,\omega_S t}\right) \tag{2.33b}$$

As in the 2-state problem, I assume that the Rabi frequencies $\Omega_P(t)$ and $\Omega_S(t)$ are real quantities. Now I insert Eqs. (2.33) into Eq. (2.31) and invoke the RWA to obtain:

$$\frac{\mathrm{d}}{\mathrm{d}t}\begin{bmatrix} c_i \\ c_e \\ c_f \end{bmatrix} = -\frac{\mathbf{i}}{2}\underbrace{\begin{bmatrix} 0 & \Omega_P(t) & 0 \\ \Omega_P(t) & 2\Delta_P & \Omega_S(t) \\ 0 & \Omega_S(t) & 2(\Delta_P - \Delta_S) \end{bmatrix}}_{\mathsf{H}(t)}\begin{bmatrix} c_i \\ c_e \\ c_f \end{bmatrix}. \tag{2.34}$$

Pulses in the intuitive sequence When[b] $\Delta_P = \Delta_S = 0$, if the pump pulse occurs before the Stokes pulse, and the pulses do not overlap significantly, the system undergoes Rabi oscillations between $|i\rangle$ & $|e\rangle$ while the pump pulse lasts. After the pump pulse is over, the Stokes pulse interacts with the system

[a] In reality, the system interacts with the superposition $\mathscr{E}_P(t) + \mathscr{E}_S(t)$. I give a mathematically and physically more rigorous approach in Sec. 4.3, p. 89. Thanks to the Rotating Wave Approximation, the full problem reduces to the situation described in the present section.

[b] The condition $\Delta_P = \Delta_S$ is equivalent to $\mathsf{E_f} - \mathsf{E_i} = \omega_P - \omega_S$, *i.e.* the energy separation between the two photons is in resonance with the transition from $|i\rangle$ to $|f\rangle$, hence the phrase *two-photon resonance*.

and triggers Rabi oscillations between $|e\rangle$ & $|f\rangle$. During this intuitive sequence, if the pump (first) pulse does not satisfy the π-pulse condition of Eq. (2.28), then the population in the intermediate state $|e\rangle$ at the end of the pump pulse, $\mathbb{P}_e(t_{\text{end}}^{\text{pump}})$, cannot reach 1, as in Fig. 2.8. Consequently, the Stokes (second) pulse, even if it satisfies Eq. (2.28) can only transfer into $|f\rangle$ *at best* the population $\mathbb{P}_e(t_{\text{end}}^{\text{pump}})$. Therefore, transferring population from $|i\rangle$ to $|f\rangle$ through $|e\rangle$ sequentially requires *both* pulses to satisfy the π-pulse condition [31].

STIRAP However, one may use adiabatic passage to successfully transfer population from $|i\rangle$ to $|f\rangle$ ([16, 30–32]). Fewell *et al.* [32] provide the analytic expressions for the time-dependent eigenstates of $\mathbf{H}(t)$ in Eq. (2.34) for any value of the detunings Δ_P and Δ_S. To gain insights relevant to this work, I confine the present discussion to the two-photon resonance case where $\Delta \equiv \Delta_P = \Delta_S$.

The eigenvalues of $\mathbf{H}(t)$ when $\Delta_P = \Delta_S = \Delta$ are

$$\omega_{\pm}(t) = \Delta \pm \sqrt{\Delta^2 + |\Omega_P(t)|^2 + |\Omega_S(t)|^2} \tag{2.35a}$$

$$\omega_0 = 0 \tag{2.35b}$$

Unless necessary, I will no longer indicate the time-dependence of $\omega_{\pm}(t)$, $\Omega_P(t)$, and $\Omega_S(t)$. I assumed above that the Rabi frequencies were real quantities, thus the modulus bars $|\cdot|$ in the definition of the eigenvalues are unnecessary[a]. The corresponding time-dependent eigenkets are:

$$|\Psi_+(t)\rangle = \frac{\Omega_P}{\sqrt{\omega_+(\omega_+ - \omega_-)}}|i\rangle + \frac{\omega_+}{\sqrt{\omega_+(\omega_+ - \omega_-)}}|e\rangle + \frac{\Omega_S}{\sqrt{\omega_+(\omega_+ - \omega_-)}}|f\rangle \tag{2.36a}$$

$$|\Psi_-(t)\rangle = \frac{\Omega_P}{\sqrt{\omega_-(\omega_- - \omega_+)}}|i\rangle + \frac{\omega_-}{\sqrt{\omega_-(\omega_- - \omega_+)}}|e\rangle + \frac{\Omega_S}{\sqrt{\omega_-(\omega_- - \omega_+)}}|f\rangle \tag{2.36b}$$

[a] Reminder: if $\Omega \in \mathbb{R}$, then $|\Omega|^2 = \Omega^2$. But if $\Omega \in \mathbb{C}$, then $|\Omega|^2 \neq \Omega^2$, since $|\Omega|^2$ is always real, while Ω^2 can be complex.

$$|\Psi_0(t)\rangle = \frac{\Omega_S}{\sqrt{-\omega_-\omega_+}}|i\rangle - \frac{\Omega_P}{\sqrt{-\omega_-\omega_+}}|f\rangle \tag{2.36c}$$

Since $-\omega_-\omega_+ = \Omega_P(t)^2 + \Omega_S(t)^2$, all of the square roots above are real quantities.

The eigenket $|\Psi_0\rangle$ is the key to adiabatic passage: if the system starts in $|\Psi_0(t = t_0)\rangle$, and $\mathbf{H}(t)$ varies slowly with time, then at a later time $t_1 > t_0$, the system will be in $|\Psi_0(t = t_1)\rangle$. Since $|\Psi_0\rangle$ has no component along $|e\rangle$, the probability to find the system in $|e\rangle$ always remains 0: the state $|e\rangle$ is *never* populated.

In the case of the 3-state problem, an interesting analogy helps to visualize adiabatic passage. Since $\mathbf{H}(t)$ is hermitian, the three eigenkets $\{|\Psi_+\rangle, |\Psi_-\rangle, |\Psi_0\rangle\}$ are orthonormal, just like $\{|i\rangle, |e\rangle, |f\rangle\}$. Remember how to change from cartesian coordinates to spherical polar coordinates: the unit vectors of Fig. 2.10 are related by[a]

$$\hat{r} = \cos\theta\,\hat{\mathcal{Z}} + \sin\theta\cos\varphi\,\hat{X} + \sin\theta\sin\varphi\,\hat{Y} \tag{2.37a}$$

$$\hat{\theta} = -\sin\theta\,\hat{\mathcal{Z}} + \cos\theta\cos\varphi\,\hat{X} + \cos\theta\sin\varphi\,\hat{Y} \tag{2.37b}$$

$$\hat{\varphi} = -\sin\varphi\,\hat{X} + \cos\varphi\,\hat{Y} \tag{2.37c}$$

The Hilbert space spanned by $\{|i\rangle, |e\rangle, |f\rangle\}$—or equivalently by $\{|\Psi_0\rangle, |\Psi_+\rangle, |\Psi_-\rangle\}$—is isomorphic to the familiar, everyday, 3 dimensional space $\mathbb{R}^3$. Thus by direct analogy, I can establish the following mapping

$$|i\rangle \leftrightarrow \hat{Y} \qquad \Psi_+ \leftrightarrow \hat{r} \tag{2.38a}$$

$$|e\rangle \leftrightarrow \hat{\mathcal{Z}} \qquad \Psi_- \leftrightarrow \hat{\theta} \tag{2.38b}$$

$$|f\rangle \leftrightarrow \hat{X} \qquad \Psi_0 \leftrightarrow \hat{\varphi} \tag{2.38c}$$

[a] Exceptionally, the hats on the letters do *not denote operators*, they are just a standard mathematical notation.

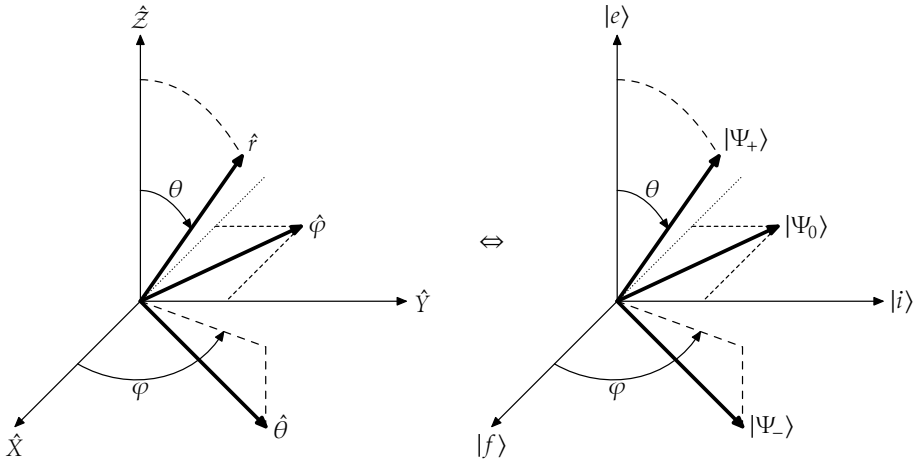

Figure 2.10: Spherical polar coordinates and 3D Hilbert space. **Left**: Angular spherical polar coordinates (θ, φ), along with the cartesian basis $(\hat{X}, \hat{Y}, \hat{Z})$ and the spherical polar basis $(\hat{r}, \hat{\theta}, \hat{\varphi})$ of $\mathbb{R}^3$. The vector $\hat{\varphi}$ is always parallel to the $(\hat{X}, \hat{Y})$ plane. The vectors $\hat{r}$ & $\hat{\theta}$ are in the meridian plane defined by the azimuth φ. On this figure, $\hat{\theta}$ is *below* the $(\hat{X}, \hat{Y})$ plane. The dotted line extends the $\hat{X}$-axis behind the $(\hat{Y}, \hat{Z})$ plane. **Right**: The kets $(|f\rangle, |i\rangle, |e\rangle)$ of the 3D Hilbert space correspond one to one with the vectors $(\hat{X}, \hat{Y}, \hat{Z})$ of $\mathbb{R}^3$. Likewise, $(|\Psi_+\rangle, |\Psi_-\rangle, |\Psi_0\rangle)$ correspond to $(\hat{r}, \hat{\theta}, \hat{\varphi})$. When $\varphi = 0, |\Psi_0\rangle = |i\rangle$; when $\varphi = \pi/2, |\Psi_0\rangle = -|f\rangle$. For all values of $\theta, |\Psi_0\rangle$ is always in the $(|f\rangle, |i\rangle)$ plane of the Hilbert space, thus $|\Psi_0\rangle$ never has a component along $|e\rangle$.

and define the angles θ and φ such that:

$$\cos\varphi = \frac{\Omega_S}{\sqrt{-\omega_-\omega_+}} \qquad \sin\varphi = \frac{\Omega_P}{\sqrt{-\omega_-\omega_+}} \qquad \tan\varphi = \frac{\Omega_P}{\Omega_S} \tag{2.39a}$$

$$\cos\theta = \sqrt{\frac{\omega_+}{\omega_+ - \omega_-}} \qquad \sin\varphi = \sqrt{\frac{\omega_-}{\omega_- - \omega_+}} \tag{2.39b}$$

Consequently,

$$|\Psi_+\rangle = \cos\theta\,|e\rangle + \sin\theta\cos\varphi\,|f\rangle + \sin\theta\sin\varphi\,|i\rangle \tag{2.40a}$$

$$|\Psi_-\rangle = -\sin\theta\,|e\rangle + \cos\theta\cos\varphi\,|f\rangle + \cos\theta\sin\varphi\,|i\rangle \tag{2.40b}$$

$$|\Psi_0\rangle = -\sin\varphi\,|f\rangle + \cos\varphi\,|i\rangle \tag{2.40c}$$

I may now interpret adiabatic passage as the rotation in Hilbert space of $|\Psi_0\rangle$ from $|i\rangle$ to $-|f\rangle$ when φ varies from 0 to $\pi/2$.

We should now examine closely the properties of Eq. (2.39a). The angle φ varies from 0 to $\pi/2$ if the ratio Ω_P/Ω_S varies from 0 at $t = t_0$ to $+\infty$ at $t = t_{\text{end}}$. When the Gaussian pump pulse $\Omega_P(t)$ peaks *before* the Gaussian Stokes pulse $\Omega_S(t)$ ($t_P < t_S$), then at the beginning of the process, $\Omega_P(t) \underset{t\ll t_P}{\gg} \Omega_S(t)$, so $\tan\varphi \underset{t\ll t_P}{\gg} 1$, *i.e.* $\varphi \underset{t\ll t_P}{\to} \pi/2$ and $|\Psi_0\rangle \underset{t\ll t_P}{\approx} -|f\rangle$. When the pulse sequence is over, that is for $t \gg t_S > t_P$, then

$$\Omega_P(t) \underset{t\gg t_S}{\ll} \Omega_S(t) \quad \Rightarrow \quad \tan\varphi \underset{t\gg t_S}{\ll} 1 \quad \Rightarrow \quad \varphi \underset{t\gg t_S}{\to} 0 \quad \Rightarrow \quad |\Psi_0\rangle \underset{t\gg t_S}{\approx} |i\rangle$$

On the contrary, when the Stokes pulse peaks *before* the pump pulse ($t_S > t_P$),

$$\begin{aligned}
&\Omega_P(t) \underset{t\ll t_S}{\ll} \Omega_S(t) \Rightarrow \quad \tan\varphi \underset{t\ll t_S}{\ll} 1 \Rightarrow \quad \varphi \underset{t\ll t_S}{\to} 0^+ \Rightarrow \quad |\Psi_0\rangle \underset{t\ll t_S}{\approx} |i\rangle \\
&\Omega_P(t) \underset{t\gg t_P}{\gg} \Omega_S(t) \Rightarrow \quad \tan\varphi \underset{t\gg t_P}{\gg} 1 \Rightarrow \quad \varphi \underset{t\gg t_P}{\to} \frac{\pi}{2}^+ \Rightarrow \quad |\Psi_0\rangle \underset{t\gg t_P}{\approx} -|f\rangle
\end{aligned}$$

Thus, only when the Stokes pulse *precedes* the pump pulse—*counterintuitive* sequence—does the state $|\Psi_0\rangle$ effectively rotate—in Hilbert space—from $|i\rangle$ to $-|f\rangle$. Bergmann *et al.* [16, §V.B, p. 1011] define the effective Rabi frequency $\Omega_{\text{eff}}(t) = \sqrt{\Omega_P^2(t) + \Omega_S^2(t)}$ and state

> "For optimum delay, the mixing angle should reach an angle of $\pi/4$ when Ω_{eff} reaches its maximum value."

For Gaussian pulses of identical width $\Delta\tau$ and identical height Ω_0, the requirement of [16] yields the optimal pulse delay

$$\eta = -\frac{\Delta\tau}{2\sqrt{\ln 2}} \approx -0.6\Delta\tau$$

as reported in [31] (see also Appendix C).

With the counterintuitive sequence, the passage is adiabatic if the adiabatic

condition Eq. (2.14) is satisfied , *i.e.* if

$$\left|\left\langle \Psi_{\pm} \left| \frac{\mathrm{d}}{\mathrm{d}t} \right| \Psi_0 \right\rangle\right|^2 \ll |\omega_{\pm} - \omega_0|^2 \tag{2.41}$$

Using the time-dependent colatitude $\theta(t)$ and azimuth $\varphi(t)$ of Eq. (2.39)

$$\frac{\mathrm{d}}{\mathrm{d}t}|\Psi_0\rangle = -\dot{\varphi}\cos\varphi\,|f\rangle - \dot{\varphi}\sin\varphi\,|i\rangle. \tag{2.42}$$

Thus,

$$\begin{aligned}
\left\langle \Psi_{+} \left| \frac{\mathrm{d}}{\mathrm{d}t} \right| \Psi_0 \right\rangle &= -\dot{\varphi}\cos\varphi\sin\theta\cos\varphi - \dot{\varphi}\sin\varphi\sin\theta\sin\varphi \\
&= -\dot{\varphi}\sin\theta \\
\left\langle \Psi_{-} \left| \frac{\mathrm{d}}{\mathrm{d}t} \right| \Psi_0 \right\rangle &= -\dot{\varphi}\cos\varphi\cos\theta\cos\varphi - \dot{\varphi}\sin\varphi\cos\theta\sin\varphi \\
&= -\dot{\varphi}\cos\theta
\end{aligned}$$

Since $\forall t\ |\cos\theta(t)| \leq 1$ and $|\sin\theta(t)| \leq 1$, naturally $|\dot{\varphi}g(\theta(t))|^2 \leq |\dot{\varphi}|^2, g = \cos, \sin$.
Using Eq. (2.39) and the procedure from Appendix D,

$$\frac{\mathrm{d}\varphi}{\mathrm{d}t} = \frac{1}{1 + \left(\frac{\Omega_P}{\Omega_S}\right)^2} \frac{\mathrm{d}}{\mathrm{d}R}\left(\frac{\Omega_P}{\Omega_S}\right) \tag{2.43a}$$

$$= \frac{\Omega_S^2}{\Omega_S^2 + \Omega_P^2} \cdot \frac{\dot{\Omega}_P\Omega_S - \Omega_P\dot{\Omega}_S}{\Omega_S^2} \tag{2.43b}$$

$$= \frac{\dot{\Omega}_P\Omega_S - \Omega_P\dot{\Omega}_S}{\Omega_S^2 + \Omega_P^2} \tag{2.43c}$$

Therefore the transfer from $|i\rangle$ to $|f\rangle$ using the state $|\Psi_0\rangle$ is adiabatic as long as,

at all times,

$$\left(\frac{\dot{\Omega}_P\Omega_S - \Omega_P\dot{\Omega}_S}{\Omega_S^2 + \Omega_P^2}\right)^2 \ll 2\Delta^2 + \Omega_P^2 + \Omega_S^2 - \sqrt{\Delta^2 + \Omega_P^2 + \Omega_S^2} \tag{2.44}$$

If at some instant t during the interaction between the external radiation and the sample, the adiabatic condition is not satisfied, then some population may pass from $|\Psi_0\rangle$ into either $|\Psi_+\rangle$ or $|\Psi_-\rangle$, and thus the state $|e\rangle$ may be temporarily populated. Fewell *et al.* [32] discuss more thoroughly the consequences of the adiabatic condition not being satisfied (see [32, p. 301]).

To close this section, Fig. 2.11 shows the components squared of $|\Psi_0\rangle$ along $|i\rangle$ and $|f\rangle$ as time passes when the lasers are in the counterintuitive sequence. The population transfer occurs mainly between the peaks of the two pulses. The time required to achieve complete transfer is thus on the order of two laser width plus the pulse delay, $2\Delta\tau + \eta$.

2.4 Spin-orbit coupling

Spin-orbit coupling is a relativistic effect [29]: in atoms, the electrons orbit around the nucleus thanks to the electric field of the protons. According to special relativity, this orbiting motion creates a magnetic field in the reference frame of the electron. The magnetic field then couples with the spin of the electron, hence the name spin-orbit coupling.

There are two ways to account for the spin-orbit effect in quantum mechanics: a classical approach consists in including the spin-orbit interaction hamiltonian in the Time-Dependent Schrödinger Equation, while the Dirac approach consists in imposing that the equation(s) describing the dynamics of the particles have relativistic invariance. In the latter case, the spin-orbit coupling term

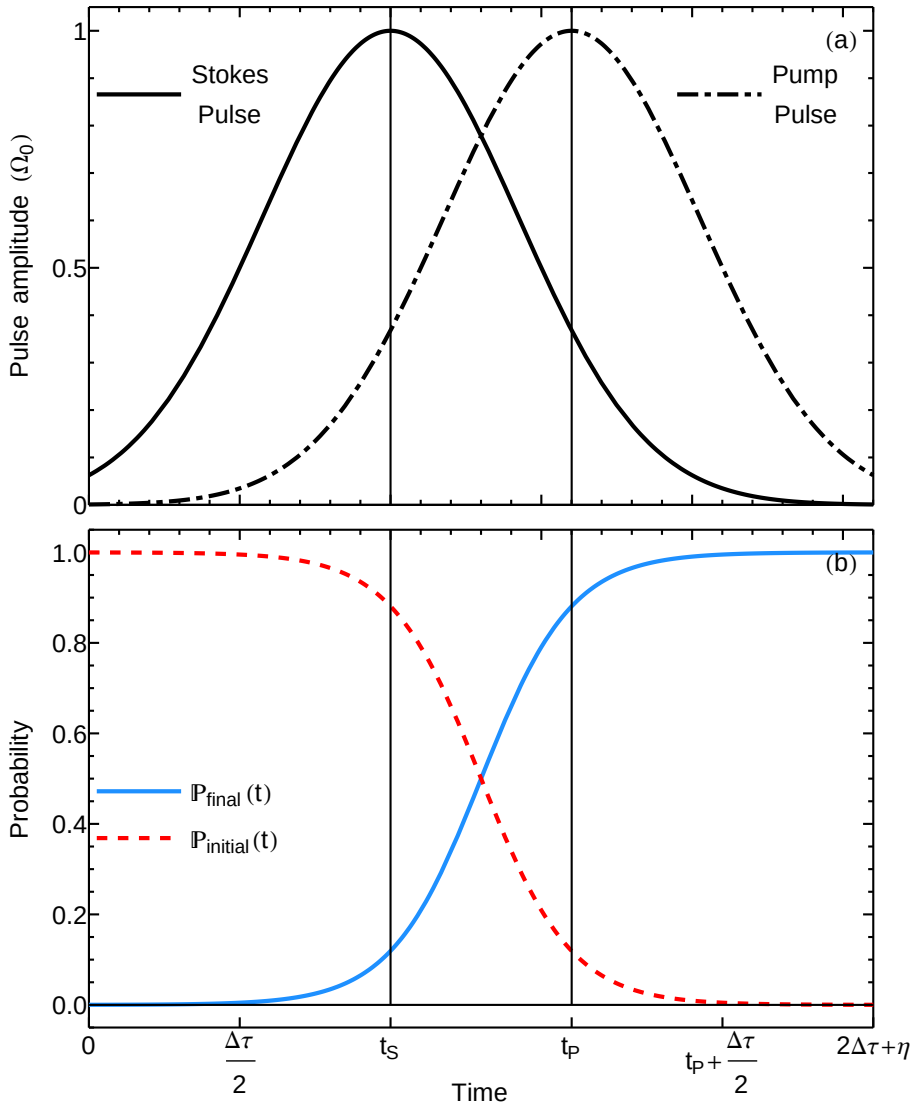

Figure 2.11: Ideal adiabatic passage in the 3-state problem. **Top** (**a**): Rabi pulses in the counterintuitive sequence. **Bottom** (**b**): Components squared of the adiabatic state $|\Psi_0\rangle$ along the states $|i\rangle$ (dashed red line) and $|f\rangle$ (solid blue line).

naturally comes out of a power series expansion in v/c of the Dirac hamiltonian [29, chap. XII], and is part of the more general fine-structure effects.

van Vleck [33] derived the full expression for the spin-orbit hamiltonian in diatomic molecules. Lefebvre-Brion and Field [34, §3.4, p. 181] discuss extensively the van Vleck result and the corresponding selection rules between molecular electronic states. Katô [35, Eq. (52 p. 3215)] derives in more de-

tails what electronic states actually couple through the spin-orbit interaction in molecules. In particular, the spin-orbit interaction couples only electronic states dissociating to the same asymptote.

2.5 Ingredients for the research

The goal of this research is to photoassociate, at ultracold temperature, a sodium atom with a cesium atom, and then transfer the resulting molecule to a low-lying rovibrational state in the $X^1\Sigma^+$ electronic state of NaCs.

Two types of physical quantities are mandatory for the research: the potential energy curves (PECs), and the transition electric dipole moment.

2.5.1 Potential energy curves

There are three PECs involved in this problem: the $X^1\Sigma^+$ ground electronic state, and the spin orbit-coupled $A^1\Sigma^+$ and $b^3\Pi$ electronic states. Here I present the origin of the data, and how I combined it to construct physically valid PECs, all plotted in Fig. 2.12 on p. 40.

2.5.1.1 $X^1\Sigma^+$ ground electronic state

For the $X^1\Sigma^+$ electronic state, I used the piecewise analytic expression obtained by Docenko *et al.* in their experimental work on the $X^1\Sigma^+$ and $a^3\Sigma^+$ electronic states of NaCs [21]. Three different pieces make up the potential $V_X(R)$. First, at small internuclear separations $0 < R < R_{SR}$, the potential model is

$$V_{SR}^X(R) = A_{SR} + \frac{B_{SR}}{R^3}. \tag{2.45a}$$

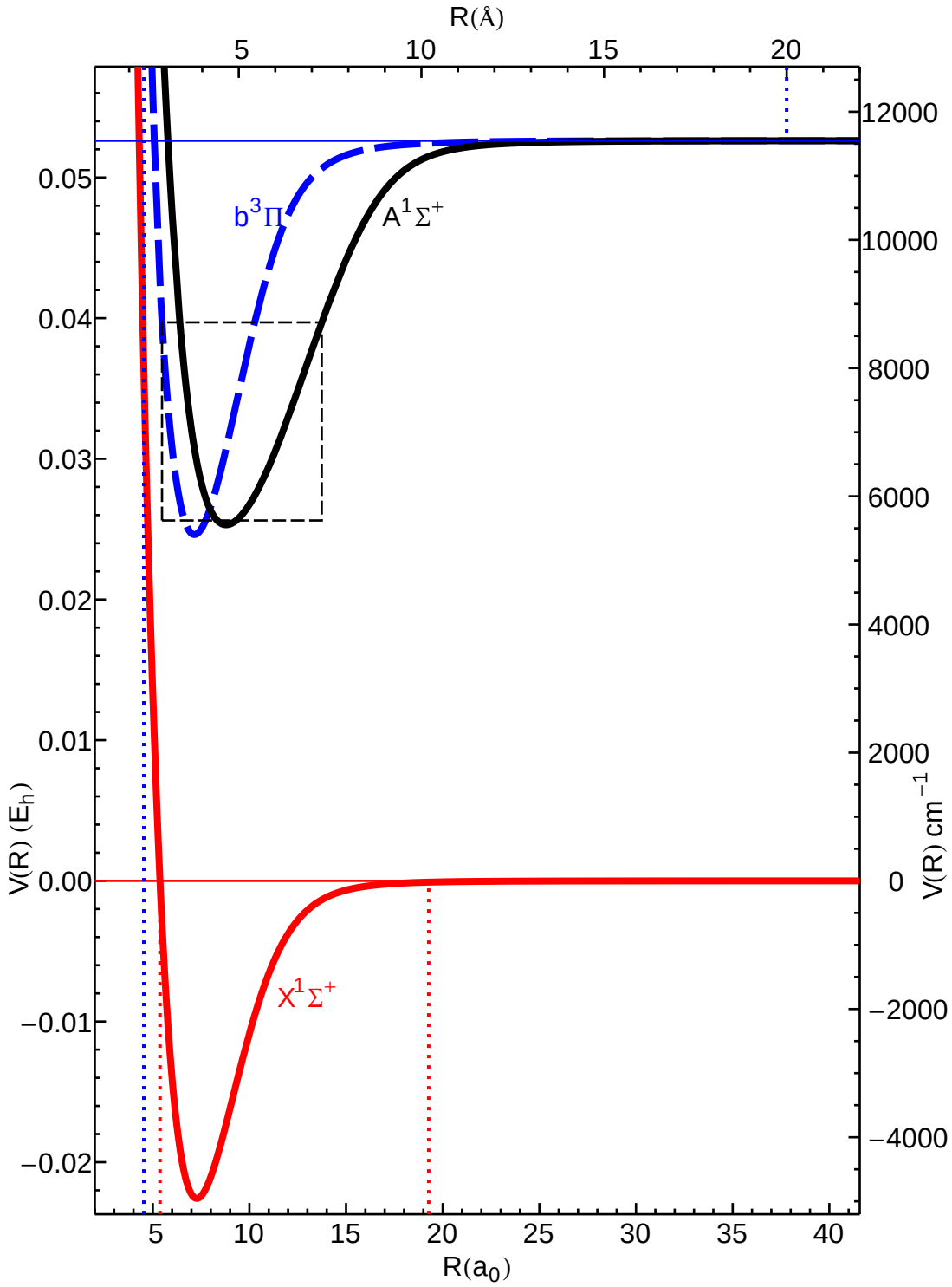

Figure 2.12: Potential energy curves for the $X^1\Sigma^+$, $A^1\Sigma^+$, and $b^3\Pi$ electronic states of NaCs. **Solid horizontals**: potential asymptotes, the $A^1\Sigma^+$ and $b^3\Pi$ states share the same asymptote. ***Red* (inner) dotted verticals**: R_{SR} and R_{LR} for the $X^1\Sigma^+$ state. ***Blue* (outer) dotted verticals**: R_{SR} and R_{LR} for the $A^1\Sigma^+$ and $b^3\Pi$ states. **Dashed rectangle**: range of energies and internuclear separations covered in the experiment of [10].

Between $R = R_{SR}$ and $R = R_{LR}$, Docenko *et al.* use the modified Dunham expression [36, chap. 4]

$$V^X_{WR}(R) = \sum_{i=0}^{n} a_i \left(\frac{R - Rm}{R + bR_m} \right)^i . \tag{2.45b}$$

Finally at large internuclear separations $R > R_{LR}$,

$$\begin{aligned} V^X_{LR}(R) = & \quad V^X_{disp}(R) \quad + V_{ex}(R) \\ & = -\frac{C^X_6}{R^6} - \frac{C^X_8}{R^8} - \frac{C^X_{10}}{R^{10}} - A_{ex} R^{\gamma} \mathbf{e}^{-\beta R}. \end{aligned} \tag{2.45c}$$

In general, electronic state potentials behave as $V_{disp}(R) = V_\infty - \sum_n C_n/R^n$; however NaCs is a heteronuclear neutral molecule, and I am only interested in electronic states where the sodium atom is always in an S state, therefore according to LeRoy [37, p. 117], $\forall n \leq 5, C^X_n = 0$ in $V^X_{disp}(R)$. Note also that the dissociation asymptote of the $X^1\Sigma^+$ state serves as the origin of the energy scale—the zero of energy—thus $V^X_\infty = 0$. Umanski and Voronin [38] provide detailed information on the exchange energy $V_{ex}(R)$.

Figure 2.12 shows the $X^1\Sigma^+$ state PEC, obtained by plugging in Eqs. (2.45) the parameters of Tbl. 2.2 (reproduced from [21]).

2.5.1.2 Excited electronic states, $A^1\Sigma^+$ and $b^3\Pi$

Zaharova *et al.* [10] published parameters for an extended Morse oscillator (EMO) model of the $A^1\Sigma^+$ and $b^3\Pi$ electronic states of NaCs. However, the EMO does not have the physically appropriate $\sum_n C_n/R^n$ behavior [37, 39] for values of the internuclear separation R much larger than the equilibrium internuclear separation of the respective potentials. Although the EMO does not represent correctly the long range interactions in the diatomic molecule, the predictions from this model agree with experimental data for the range of

Short range, $R \leq 2.8435$ Å		Well range, 2.8435 Å $< R <$ 10.20 Å	
A	$-0.121078258 \times 10^5\,\mathrm{cm}^{-1}$	b	-0.4000
B	$0.278126476 \times 10^6\,\mathrm{cm}^{-1}\,\text{Å}^3$	R_m	0.85062906 Å
Long range $R \geq 10.20$ Å		a_0	$-4954.2371\,\mathrm{cm}^{-1}$
		a_1	$0.8986226306643612\,\mathrm{cm}^{-1}$
C_6^X	$1.555214 \times 10^7\,\mathrm{cm}^{-1}\,\text{Å}^6$	a_2	$0.1517322178913964 \times 10^5\,\mathrm{cm}^{-1}$
C_8^X	$4.967239 \times 10^8\,\mathrm{cm}^{-1}\,\text{Å}^8$	a_3	$0.1091020582856565 \times 10^5\,\mathrm{cm}^{-1}$
C_{10}^X	$1.971387 \times 10^{10}\,\mathrm{cm}^{-1}\,\text{Å}^{10}$	a_4	$-0.2458305372316654 \times 10^4\,\mathrm{cm}^{-1}$
A_{ex}	$2.549087 \times 10^4\,\mathrm{cm}^{-1}\,\text{Å}^{\gamma}$	a_5	$-0.1608232170898541 \times 10^5\,\mathrm{cm}^{-1}$
γ	5.12271	a_6	$-0.8705012336065982 \times 10^4\,\mathrm{cm}^{-1}$
β	$2.17237\,\text{Å}^{-1}$	a_7	$0.2188049902097992 \times 10^5\,\mathrm{cm}^{-1}$
		a_8	$-0.3002538575091348 \times 10^6\,\mathrm{cm}^{-1}$
		a_9	$-0.7869349638160045 \times 10^6\,\mathrm{cm}^{-1}$
		a_{10}	$0.3396165699038170 \times 10^7\,\mathrm{cm}^{-1}$
		a_{11}	$0.7358409786704151 \times 10^7\,\mathrm{cm}^{-1}$
		a_{12}	$-0.2637478410890963 \times 10^8\,\mathrm{cm}^{-1}$
		a_{13}	$-0.4458510225166618 \times 10^8\,\mathrm{cm}^{-1}$
		a_{14}	$0.1351336683376161 \times 10^9\,\mathrm{cm}^{-1}$
		a_{15}	$0.1762627710924772 \times 10^9\,\mathrm{cm}^{-1}$
		a_{16}	$-0.4756878196167457 \times 10^9\,\mathrm{cm}^{-1}$
		a_{17}	$-0.4474883319488960 \times 10^9\,\mathrm{cm}^{-1}$
		a_{18}	$0.1216000437881570 \times 10^{10}\,\mathrm{cm}^{-1}$
		a_{19}	$0.7460756868876818 \times 10^9\,\mathrm{cm}^{-1}$
		a_{20}	$-0.2291733580271494 \times 10^{10}\,\mathrm{cm}^{-1}$
		a_{21}	$-0.8708937018502138 \times 10^9\,\mathrm{cm}^{-1}$
		a_{22}	$0.3095441526749659 \times 10^{10}\,\mathrm{cm}^{-1}$
		a_{23}	$0.8199544778493311 \times 10^9\,\mathrm{cm}^{-1}$
		a_{24}	$-0.2806754517994001 \times 10^{10}\,\mathrm{cm}^{-1}$
		a_{25}	$-0.6963731313587832 \times 10^9\,\mathrm{cm}^{-1}$
		a_{26}	$0.1516535916964652 \times 10^{10}\,\mathrm{cm}^{-1}$
		a_{27}	$0.4445582751072266 \times 10^9\,\mathrm{cm}^{-1}$
		a_{28}	$-0.3669908996749862 \times 10^9\,\mathrm{cm}^{-1}$
		a_{29}	$-0.1352434762493831 \times 10^9\,\mathrm{cm}^{-1}$

Table 2.2: Parameters of the analytic representation for the potential energy curve of the $X^1\Sigma^+$ state in NaCs. Reproduced from [21].

energies that Zaharova *et al.* studied (see dashed box in Fig. 2.12 on p. 40).

In ultracold photoassociation, a laser binds the scattering atoms into a high-lying rovibrational state of an excited electronic state of the molecule [40]. The long-range tail of the PEC controls the shape of the radial wave function of such high-lying state. Therefore, an alternative to the EMO model is necessary at large values of R.

Furthermore, the rightmost (respectively[a] leftmost) R boundaries of the EMO model in Fig. 2.12 are not large (*resp.* small) enough to switch to the long-range dispersion (*resp.* short range) form at these values of R.

Upon request, Professor Andrey Stolyarov[b] kindly sent me in 2009 his *ab initio* data for the $A^1\Sigma^+$ and $b^3\Pi$ electronic states of NaCs. Stolyarov's data has the appropriate long range behavior:

$$V^q_{ab\ initio}(R) \underset{R\gg R^q_e}{\approx} V^q_\infty - \frac{C^q_6}{R^6} - \frac{C^q_8}{R^8} - \frac{C^q_{10}}{R^{10}} \qquad j = A^1\Sigma^+ \text{ or } b^3\Pi, \tag{2.46}$$

where j stands either for the $A^1\Sigma^+$ or the $b^3\Pi$ electronic state, R^q_e is the equilibrium separation of state j, and V^q_∞ its asymptotic value. I extracted the dispersion coefficients from the Stolyarov data using the procedure below.

As the nuclei approach each others from large internuclear separation, more dispersion terms become necessary to describe the long-range tail of the potential. Starting with the asymptotic value V^q_∞, the model must first include a R^{-6} term, then R^{-8}, then R^{-10}, and finally the exchange term.

Since the Stolyarov data stops at $R = 20$ Å, I initially modeled the potential tail with $V^q_\infty - C^q_6/R^6$. This model has two parameters; to obtain statistically meaningful parameters through a least-squares regression, I need at least 5

[a] It is common practice to abbreviate *respectively* as *resp.*, a convention I will use from this point on.

[b] Department of Chemistry, Moscow State University, Moscow, Russia.

data points. Among the $n = 95$ data points contained in the Stolyarov set, I picked the last 5: R_{n-4}, R_{n-3}, R_{n-2}, R_{n-1}, R_n, and determined V_∞^q & C_6^q using *Mathematica*® least-squares regression.

To obtain converged values of the parameters, I added the next data point when decreasing R, R_{n-5}, and re-ran the regression. When adding points to the regression successively in this fashion, the parameters remained rather stable, until adding new points caused a significant divergence of the parameters from their previously stable value. This divergence signals the necessity for the next term in the long-range expression. Consequently, I restarted the procedure above, with $V_\infty^q - C_6^q/R^6 - C_8^q/R^8$.

Bussery *et al.* [41] and Marinescu and Sadeghpour [42] calculated *ab initio* values of C_6 and C_8 for NaCs in the $A^1\Sigma^+$ and $b^3\Pi$ states. I retained the results from the regression that yielded a 95% confidence interval for C_6 that contained the *ab initio* value of [42]. I never included C_{10} in the regression model: I used C_{10} to enforce smoothness of the piecewise potential I constructed (see below). The asymptotic value V_∞^q is necessary to run the regression, however, I discarded the fitted value, and used V_∞^q to ensure continuity of the piecewise potential.

Table 2.3 gives the value of C_6 and C_8 from the retained regression results.

Equipped with the Stolyarov data and the dispersion coefficients, and influenced by the work of [21], I constructed a piecewise model potential that exploits the EMO of [10].

For R values below the leftmost Stolyarov data point, R_{SR}, I used the decaying exponential suggested in [43, chap. 5]

$$V_{\mathrm{SR}}^q(R) = B_{\mathrm{SR}}^q \mathbf{e}^{-\alpha_{\mathrm{SR}}^q R} \qquad j = A^1\Sigma^+ \text{ or } b^3\Pi. \tag{2.47}$$

$q =$	$A^1\Sigma^+$	$b^3\Pi$
R^q_{SR} (Å)	2.4	2.4
B^q_{SR} (cm^{-1})	473510.3635544896	$1.7618018556402298 \times 10^6$
α^q_{SR} ($Å^{-1}$)	1.36381214805273	2.0587811904165627
R^q_{LR} (Å)	20	20
V^q_∞ (cm^{-1})	16501.744076327697	16501.817004117052
C^q_6 ($E_h a_0{}^6$)	17797.95844	8258.463614
C^q_8 ($E_h a_0{}^8$)	5.080016549×10^6	232117.7941
C^q_{10} ($E_h a_0{}^{10}$)	-3.424611835×10^9	-1.443415004×10^9

Table 2.3: Parameters for the short-range form $V^q_{SR}(R) = B^q_{SR}\mathbf{e}^{-\alpha^q_{SR}R}$ and the long-range form $V^q_{LR}(R) = V^q_\infty - \frac{C^q_6}{R^6} - \frac{C^q_8}{R^8} - \frac{C^q_{10}}{R^{10}}$ of the $A^1\Sigma^+$ and $b^3\Pi$ electronic states potential energy curves of NaCs.

For R values above the rightmost Stolyarov data point, R_{LR}, I describe the PEC with the dispersion potential of Eq. (2.46). Between R_{SR} and R_{LR}, I use the Stolyarov data. Yet I substitute the EMO model for the Stolyarov data in the applicable range of R values (see dashed rectangle in Fig. 2.12 p. 40), and use a spline interpolation to smoothly connect the experimental potential to the *ab initio* data points. Imposing continuity of $V^q(R)$ and $\frac{\mathrm{d}V^q}{\mathrm{d}R}$ at $R = R_{SR}$ yields B^q_{SR} and α^q_{SR}. The same constraints at $R = R_{LR}$ give the values of V^q_∞ and C^q_{10}.

The $A^1\Sigma^+$ and the $b^3\Pi$ states should have the same asymptotic value: the fine structure average energy E^{Cs}_{avg} of the cesium atom between the $6^2P_{1/2}$ and the $6^2P_{3/2}$ excited atomic states. Using the data tables from Steck [26], where the energies are measured from the ground atomic state $6^2S_{1/2}$,

$$E^{Cs}_{avg} = \frac{\sum_{j=1/2}^{3/2}(2j+1)E^{Cs}_j}{\sum_{j=1/2}^{3/2}(2j+1)} = 11547.6274568\,\mathrm{cm}^{-1}. \tag{2.48}$$

The parameters $V_\infty^{A^1\Sigma^+}$ and $V_\infty^{b^3\Pi}$ can be used to bring the asymptotic value of each potential to 0, and then E_{avg}^{Cs} can be added to each potential so that they dissociate to the correct value.

2.5.2 Electric dipole moment for NaCs between $X^1\Sigma^+$ and $A^1\Sigma^+$ electronic states

In this section, I discuss the adjustments I made to the electric transition dipole moment function between the $X^1\Sigma^+$ and the $A^1\Sigma^+$ electronic states of NaCs, reported by Aymar and Dulieu [44]. The knowledge of this function is mandatory for the calculation in my research, as will become clear in Sec. 4.2.2, p. 80.

The electric transition dipole moment function $\mathscr{D}_{AX}(R)$ from [44] is involved in the calculation of matrix elements[a] $\left\langle A,1,v_A \left| \mathscr{D}_{AX}(R) \right| X,J,v_X \right\rangle$, which I perform using numerical techniques. The three integrands are discretized over three different meshes of R-values. In particular, Aymar and Dulieu [44] provide data for $\mathscr{D}_{AX}(R)$ on a mesh much sparser than the grid I used with LEVEL [45] to obtain the converged wave functions $\chi_{v_X}^{XJ}(R)$ and $\chi_{v_A}^{A1}(R)$. Also, the data from [44] for $\mathscr{D}_{AX}(R)$ extend from $R_{min} = 3.2\,a_0$ up to $R_{max} = 30.8\,a_0$. Yet, the largest right classical turning points are $38.3\,a_0$ for the $X^1\Sigma^+$ state, and $60.7\,a_0$ for the $A^1\Sigma^+$ state, *i.e.* beyond R_{max}. Therefore, I need to interpolate $\mathscr{D}_{AX}(R)$ between the existing *ab initio* data points of [44]; and using the last data points as stepping stones, I need to extend $\mathscr{D}_{AX}(R)$ beyond R_{max}.

From $R = 0$ to R_{min}, all wave functions I calculated are essentially zero. There is no need to know $\mathscr{D}_{AX}(R)$ in this region.

From R_{min} to R_{max}, I interpolated the data with splines of order 2. A lower

[a] The notation for the vibrational kets will become clear in chap. 4. Bear with me.

interpolation order yields a non smooth curve at $R = 28\,a_0$, an un-physical behavior. A higher interpolation order creates an artificial dip between the data points at $R = 28\,a_0$ and $R = 29.8\,a_0$.

For $R > R_{\max}$, I was first inclined to use the asymptotic model published by Kim *et al.* [46, Eq. (5), p. 58]

$$\mathscr{D}_{AX}^{\mathrm{LR}}(R) = \mathscr{D}_{\infty}\left(1 + \frac{2\alpha}{R^3}\right) \tag{2.49}$$

where $\mathscr{D}_{\infty}$ is the transition dipole moment of the Cesium atom between its $6^2S_{1/2}$ and $6^2P_{1/2}$ atomic states. Kim *et al.* [46] use $\mathscr{D}_{\infty} = 3.23\,\mathrm{e}\,a_0$; however, the data from [44] seems to decrease at long range to the value [26] $\mathscr{D}_{\infty} = 3.1869 \pm 5.9 \times 10^{-3}\,\mathrm{e}\,a_0$, which I retain for my fitting procedure.

Let's transform Eq. (2.49) into

$$\ln\left(\frac{\mathscr{D}_{AX}}{\mathscr{D}_{\infty}} - 1\right) = \ln(2\alpha) - 3\ln R. \tag{2.50}$$

If the plot of $\{(\ln R, \ln\left(\frac{\mathscr{D}_{AX}}{\mathscr{D}_{\infty}} - 1\right))\}$ is a straight line, then the vertical intercept yields $\ln(2\alpha)$ and the slope of the line should be -3. Figure 2.13 shows that even for large values of R, the data does not fit a straight line. Several fits failed to converge on a value for the slope. Thus, the expression of Eq. (2.49) appears inappropriate for the data set from [44].

Instead, I came up with an expression that uses a decaying exponential

$$\mathscr{D}_{AX}^{\mathrm{LR}}(R) = \mathscr{D}_{\infty}\left(1 + \mathrm{e}^{-c_1 R}\right). \tag{2.51}$$

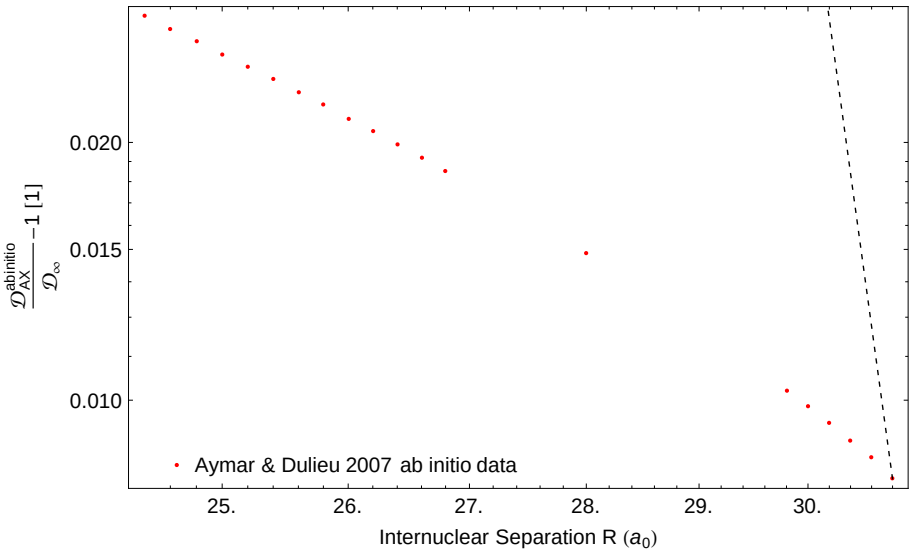

Figure 2.13: Log-log plot of the modified data from [44], $\{(\ln R, \ln\left(\frac{\mathscr{D}_{AX}}{\mathscr{D}_\infty} - 1\right))\}$. The slope of the dashed line is -3, as expected if the data fitted the model from [46]. Obviously, the *ab initio* data from [44] does *not* follow the dashed line, *i.e.* the model of Eq. (2.49): a different model is necessary.

Again, the equation may be recast as

$$\ln\left(\frac{\mathscr{D}_{AX}}{\mathscr{D}_\infty} - 1\right) = -c_1 R. \tag{2.52}$$

Figure 2.14 is a plot of $\ln\left(\frac{\mathscr{D}_{AX}}{\mathscr{D}_\infty} - 1\right)$ *vs.* R. The plot is not a straight line: I need to improve the model with a power of R to account for the curvature of the plot. Therefore I fitted the data set $\{(R, \ln\left(\frac{\mathscr{D}_{AX}}{\mathscr{D}_\infty} - 1\right))\}$ to $-c_1 R - c_2 R^k$ for values of k ranging from 2 to 12. I obtained a correlation coefficient $r^2 = 0.9999995033$ and the residuals shown in Fig. 2.14 when setting $k = 8$ and using the data from Aymar and Dulieu [44] from $R = 26.8\,a_0$ to $R = 30.8\,a_0$—the last data point. Thus, the long range model of Eq. (2.51) for the electric transition dipole

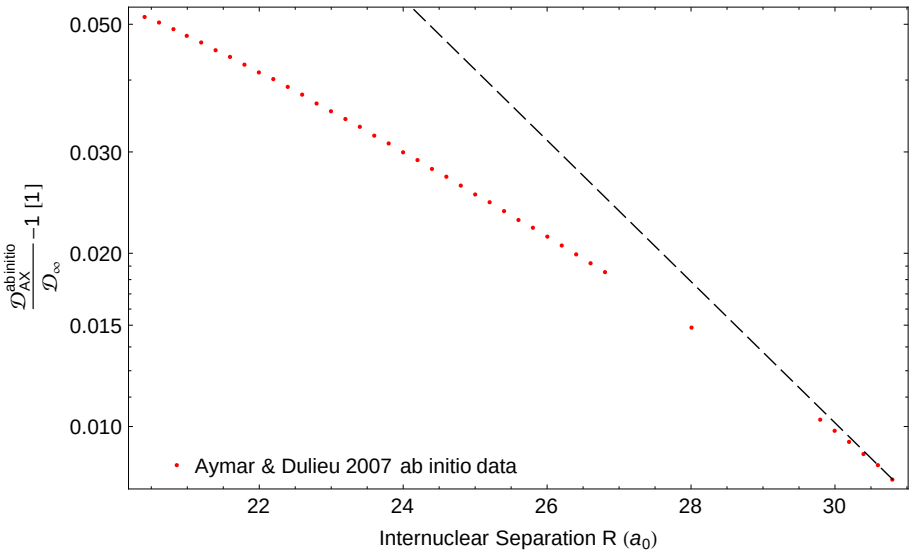

Figure 2.14: Semilog plot of the modified data from [44], $\{(R, \ln\left(\frac{\mathscr{D}_{AX}}{\mathscr{D}_{\infty}} - 1\right))\}$. Only the vertical axis is on a logarithmic scale. The dashed line suggests that the data does not fit a straight line on this semilog plot: an additional power of R is required in the model to account for the curvature of the data.

moment of NaCs between the $A^1\Sigma^+$ and the $X^1\Sigma^+$ electronic states is:

$$\mathscr{D}_{AX}^{\mathrm{LR}}(R) = \mathscr{D}_{\infty}\left(1 + \mathbf{e}^{-c_1 R - c_2 R^8}\right), \tag{2.53}$$

with $\mathscr{D}_{\infty} = 3.1869\, e\, a_0$

$$c_1 = 0.1443298701\, a_0^{-1}$$

$$c_2 = 4.482932805 \times 10^{-13}\, a_0^{-8}$$

Figure 2.16 shows a summary of this section: the data points from Aymar and Dulieu [44], the interpolated curve, the long range model of Eq. (2.51), and the R-value where the switch occurs from the interpolated curve to the long range model.

I have collected enough information on the concepts necessary to my research. Let's now move on to the physics description of the system I studied and the interactions that it experiences.

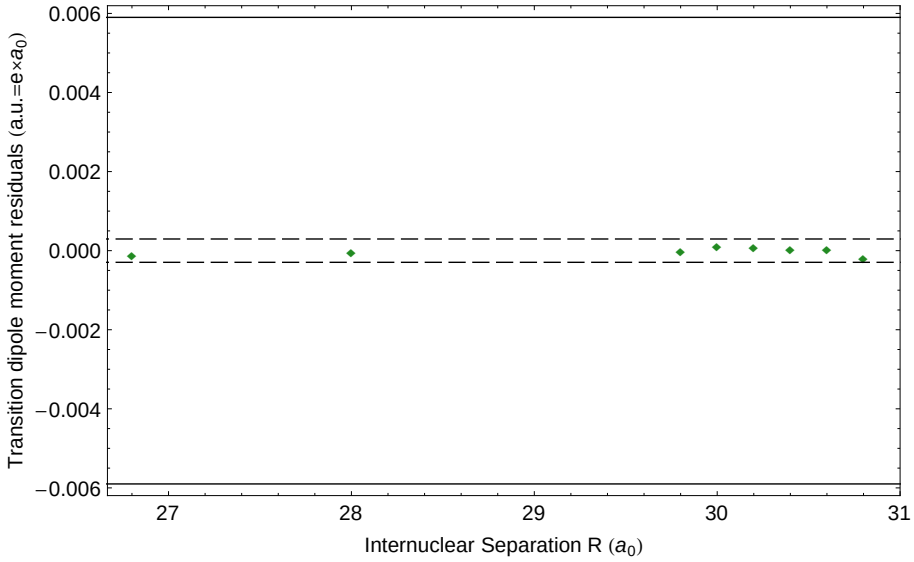

Figure 2.15: Linear fit residuals between the electric transition dipole moment long-range model of Eq. (2.51) and the data from [44]. Horizontal solid line: uncertainty in $\mathscr{D}_\infty$ reported in [26]. Horizontal dashed line: 0.05×uncertainty in $\mathscr{D}_\infty$ from [26]. The residuals are confined between the dashed lines, showing the quality of the fit.

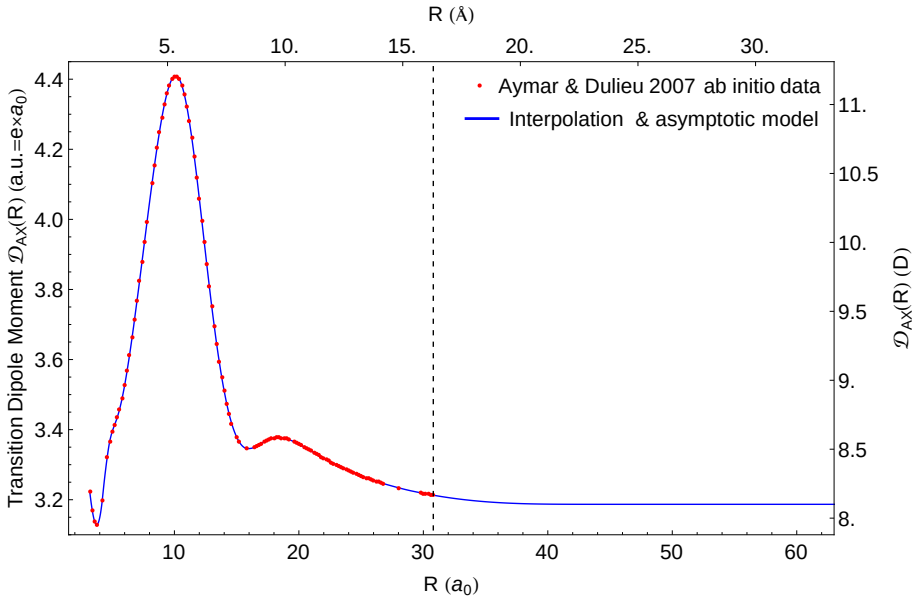

Figure 2.16: Complete electric transition dipole moment function $\mathscr{D}_{AX}(R)$. The vertical dashed line marks the switch from the interpolated curve to the long range model of Eq. (2.51).

Chapter 3

Physics

3.1 The system

The system I study is the ultracold pair of ^{23}Na ($Z_{\mathrm{Na}} = 11$) and ^{133}Cs ($Z_{\mathrm{Cs}} = 55$) scattering bosons[a] along with the molecule they form through photoassociation. This section provides some physical information about the system that will become highly relevant in the next chapter.

How cold is ultracold? As of this writing, there are two research groups performing experiments on NaCs: the Tiemann team at Hannover [21], and the Bigelow group at Rochester [22, 47–49]. Only the Bigelow group reported studies of ultracold NaCs at temperature $T = 200\mu K$, which is the temperature of the system in my study.

The study of any system in quantum mechanics requires the definition of a reference frame. The *laboratory* frame consists of three arbitrary, mutually orthogonal directions in space, and an arbitrary point in space to serve as an origin. The *space-fixed* (SF) frame has the same axes as the laboratory frame, but is centered at the center of mass of the system under study. In the particular case of this research, I attach the SF frame to the center of mass of the nuclei of the diatomic molecule. The *body-fixed* (BF) frame is also attached to the center of mass of the molecule, with coordinate axes chosen to take advantage of the symmetries of the molecule.

In a diatomic molecule, the electrons experience the electric field of the two nuclei, which has cylindrical symmetry about the line joining the two nuclei—

[a] An atom is a boson if the total number of its protons, neutrons, and electrons is even (Bransden and Joachain [24, p. 114]).

the *internuclear axis*. Thus, in a diatomic molecule, the internuclear axis defines the $\hat{z}$ axis of the BF frame. As the diatomic molecule is cylindrically symmetric, the direction of the $\hat{x}$ and $\hat{y}$ axes in the BF frame is arbitrary.[a]

Figure 3.1 shows the SF and BF frames for NaCs, and defines the colatitude θ and the azimuth φ. These two angles determine the orientation of the BF frame with respect to the SF frame. Bernath [50, p. 208] discusses the transformation from the laboratory frame to the SF frame for a diatomic molecule. A more thorough discussion appears in [51, chap. 2]. Bransden and Joachain [24, App. 9] treat the transformation from the SF frame to the BF frame. This research considers the system in the SF frame, where only the relative motion of the atoms matters. The reduced mass μ of the nuclei becomes relevant and is defined as

$$\mu = \frac{M_{\mathrm{Na}} M_{\mathrm{Cs}}}{M_{\mathrm{Na}} + M_{\mathrm{Cs}}} = 32.54570 \times 10^{-27} \text{ kg} \tag{3.1}$$

In each reference frame, different bases can be used to locate a point in space or to define a vector. Consider a point P a distance d away from the center of mass in Figure 3.1. In the SF frame, the cartesian coordinates of P are $(X, Y, \mathcal{Z})$, with $X^2 + Y^2 + \mathcal{Z}^2 = d^2$, while the spherical polar coordinates are (d, θ, φ). The two sets are related by the familiar relations

$$\begin{aligned} X &= d \sin\theta \cos\varphi, \\ Y &= d \sin\theta \sin\varphi, \\ \mathcal{Z} &= d \cos\theta. \end{aligned}$$

The *spherical basis*, which is useful when treating rotation in quantum mechan-

[a] In SF_6 for example, the 6 fluorine atoms are the vertices of a regular octahedron centered on the sulfur atom. Thus, in the corresponding BF frame, the $\hat{x}$, $\hat{y}$, $\hat{z}$, directions are completely determined by the shape of the SF_6 molecule.

ics, uses the $\ell = 1$ spherical harmonics quantized along the $\hat{\mathcal{Z}}$-axis of the SF frame [52, p. 63]:

$$Y_{\ell=1,m}(\theta,\varphi) = Y_{1m}(\theta,\varphi) = \left(\frac{3}{4\pi}\right)^{1/2} \frac{1}{d} \begin{cases} -\frac{1}{\sqrt{2}}(X + \mathbf{i}\, Y) & m = +1 \\ \mathcal{Z} & m = 0 \\ \frac{1}{\sqrt{2}}(X - \mathbf{i}\, Y) & m = -1 \end{cases}$$

The coordinates of P are then labeled according to the value of the index m of the spherical harmonics: (P_{-1}, P_0, P_{+1}). In particular, P_0 is the coordinate of P along the quantization axis $\hat{\mathcal{Z}}$ in the spherical basis. Similarly, any vector $\vec{u}$ with components $(u_X^{\mathrm{SF}}, u_Y^{\mathrm{SF}}, u_{\mathcal{Z}}^{\mathrm{SF}})$ in the SF frame's cartesian basis has components $(u_{-1}^{\mathrm{SF}}, u_0^{\mathrm{SF}}, u_{+1}^{\mathrm{SF}})$ in the corresponding spherical basis of the SF frame, where again u_0^{SF} is the component of $\vec{u}$ along the quantization axis $\hat{\mathcal{Z}}$ in the spherical basis. In the BF frame, the polar axis is the internuclear axis $\hat{z}$. The cartesian components of $\vec{u}$ are $(u_x^{\mathrm{BF}}, u_y^{\mathrm{BF}}, u_z^{\mathrm{BF}})$ and the corresponding spherical components are $(u_{-1}^{\mathrm{BF}}, u_0^{\mathrm{BF}}, u_{+1}^{\mathrm{BF}})$, where u_0^{BF} is the component of $\vec{u}$ along the internuclear axis $\hat{z}$. The transformation between the SF spherical basis and the BF spherical basis is extensively discussed in Rose [52] and Morrison and Parker [53].

Although the mixture of atoms is at $200\mu K$, *the temperature is sufficiently high for Maxwell-Boltzmann statistics to correctly model the probability distribution of energy* [54, pp. 170 & 222]. Indeed, the critical temperature T_c for Bose-Einstein condensation to occur is [54]

$$T_c = \left(\frac{n}{\zeta(3/2)}\right)^{2/3} \frac{2\pi\hbar^2}{m k_B}, \tag{3.2}$$

where n is the density of particles, m the mass of the boson, and ζ the Riemann

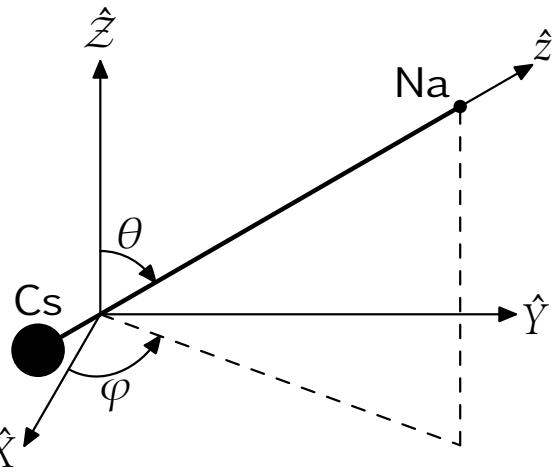

Figure 3.1: Definition of angles θ and φ in the *space*-fixed frame $(\hat{X}, \hat{Y}, \hat{Z})$ attached to the center of mass of the nuclei. The $\hat{z}$ axis is the internuclear axis, and defines the *body*-fixed frame. The cesium atom being heavier than the sodium atom, the center of mass of the diatomic molecule is closer to Cs than to Na.

zeta function. The typical densities of atoms in ultracold traps is $n \approx 10^{11}\,\mathrm{cm}^{-3}$ [47], so that $T_c(\mathrm{Na}) \approx 0.015\,\mu K$ and $T_c(\mathrm{Cs}) \approx 0.0026\,\mu K$, respectively 1.3×10^3 and 77×10^3 times below the trapping temperature.

Figure 3.2 shows the Maxwell-Boltzmann probability distribution of energy for the gaseous mixture of NaCs at $T = 200\mu K$. The most probable scattering energy is $E_{\mathrm{p}} = \frac{k_B T}{2} \approx 0.317 \times 10^{-9}\, E_h \approx 2.086\,\mathrm{MHz} \approx 6.96 \times 10^{-5}\,\mathrm{cm}^{-1}$. This is the scattering energy I am using for the initial state of my problem.

Furthermore, let me show that in a gas at temperature T_0 obeying Maxwell-Boltzmann statistics, approximately 99.95% of the particles have energy between 0 and $\varepsilon = 9k_B T_0$. Thus, using $\mathbb{P}(E)$ to denote the Maxwell-Boltzmann probability distribution of energy, let's determine ε such that $\int_0^{\varepsilon} \mathbb{P}(E)\,\mathrm{d}E \approx 99.95\%$:

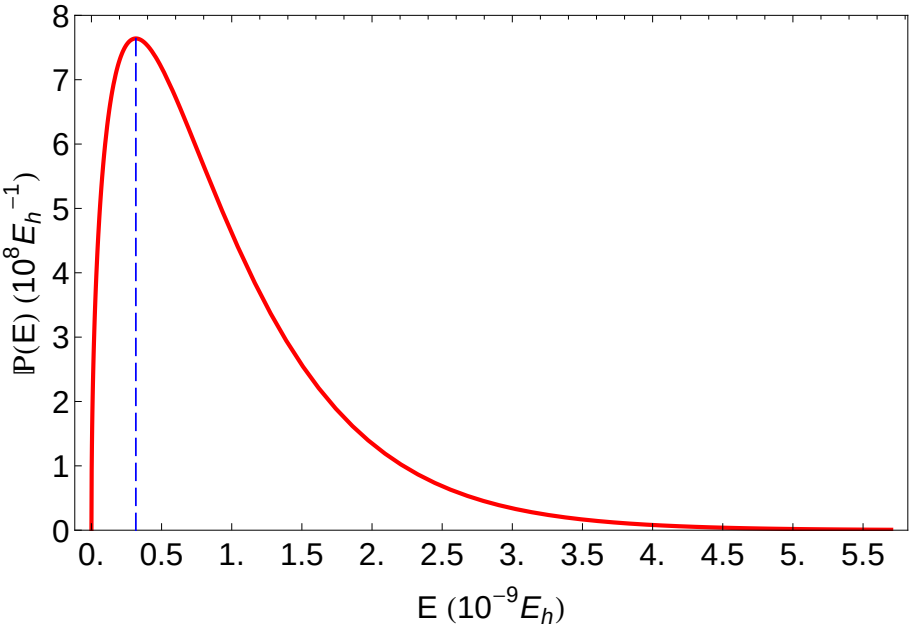

Figure 3.2: **Solid red:** Maxwell-Boltzmann distribution $\mathbb{P}(E) = \frac{2}{\sqrt{\pi}} \frac{\sqrt{E}}{(k_B T)^{3/2}} \mathbf{e}^{-\frac{E}{k_B T}}$ at $T = 200\mu K$. **Dashed blue:** most probable scattering energy $E_\mathrm{p} = \frac{k_B T}{2} \approx 0.317 \times 10^{-9}\, E_h \approx 2.086\,\mathrm{MHz} \approx 6.96 \times 10^{-5}\,\mathrm{cm}^{-1}$.

$$\int_0^\varepsilon \mathbb{P}(E)\,\mathrm{d}E = \int_0^\varepsilon \frac{2}{\sqrt{\pi}} \frac{1}{k_B T_0} \left(\frac{E}{k_B T_0}\right)^{1/2} \exp\left(-\frac{E}{k_B T_0}\right) \mathrm{d}E, \tag{3.3a}$$

$$= \frac{2}{\sqrt{\pi}} \int_0^{x_\varepsilon} 2x^2 \mathbf{e}^{-x^2}\,\mathrm{d}x, \tag{3.3b}$$

$$= \frac{2}{\sqrt{\pi}} \left(\left[-x\mathbf{e}^{-x^2}\right]_0^{x_\varepsilon} + \int_0^{x_\varepsilon} \mathbf{e}^{-x^2}\,\mathrm{d}x \right), \tag{3.3c}$$

$$= \mathrm{Erf}(x_\varepsilon) - \frac{2}{\sqrt{\pi}}\, x_\varepsilon\, \mathbf{e}^{-(x_\varepsilon)^2}, \tag{3.3d}$$

with $\mathrm{Erf}(x_\varepsilon) = \frac{2}{\sqrt{\pi}} \int_0^{x_\varepsilon} \mathbf{e}^{-x^2}\,\mathrm{d}x$. Tabulating the right-hand side of Eq. (3.3d) in *Mathematica*® shows that $x_\varepsilon = 3$, *i.e.* $\varepsilon = 9 k_B T_0$, yields $\int_0^\varepsilon \mathbb{P}(E)\,\mathrm{d}E \approx 99.95\%$.

Since the NaCs gas is trapped at a temperature $T = 200\mu K$, 99.95% of the atoms in the gas scatter off of each other with a relative kinetic energy at most equal to $\varepsilon = 9 k_B T = 1\,800\mu K$, according to the preceding paragraph. Should the particles be treated relativistically? The total relativistic energy $E_\mathrm{rel}^\mathrm{total}$ of

the scatterers is

$$E_{\text{rel}}^{\text{total}} = E_{\text{rest}} + \varepsilon \Leftrightarrow \frac{\mu c^2}{\sqrt{1-\frac{v^2}{c^2}}} = \mu c^2 + \varepsilon \quad \Leftrightarrow \quad \frac{v}{c} = \frac{\sqrt{1+2\mu c^2/\varepsilon}}{1+\mu c^2/\varepsilon}, \tag{3.4}$$

$$i.e. \quad v = 4.1 \times 10^{-9} c \tag{3.5}$$

with the numbers given. Since the speed of the particles is very much smaller than the speed of light, the kinetic energy of the nuclei in the problem can therefore be treated non-relativistically.

3.2 The interactions

I account for three interactions internal to the system, and one between the system and its environment. This section introduces the mathematical form of each operator representing a given interaction, along with basic notations for the relevant operators

3.2.1 Coulomb interactions

The NaCs system involves 2 nuclei, $Z_{\text{Na}} = 11$ electrons from the sodium atom, and $Z_{\text{Cs}} = 55$ electrons for the cesium atom. The Coulomb interaction causes mutual attraction between nuclei and electrons, and mutual repulsion between electrons and between nuclei.

The distances between particles (see Fig. 3.3) are the only variable quantities in the Coulomb interaction. The corresponding total potential energy $V(r,R)$, where r represents the collection of all r_{jCs}, r_{iNa}, and r_{ij} defined in Fig. 3.3, is

$$\widehat{\mathscr{V}}(r,R) = \widehat{\mathscr{V}}_{nn}(R) + \widehat{\mathscr{V}}_{ne}(r,R) + \widehat{\mathscr{V}}_{ee}(r). \tag{3.6}$$

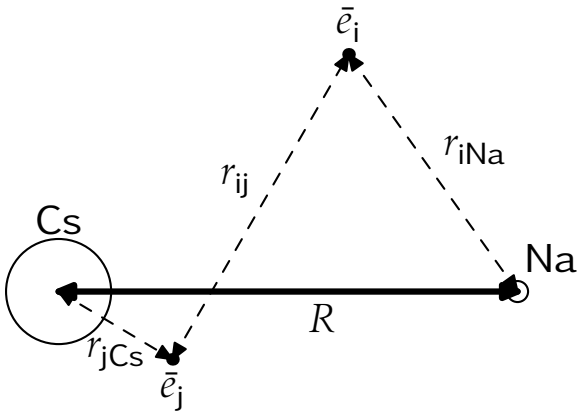

Figure 3.3: Definition of distances between particles experiencing the Coulomb interaction. The size difference of the circles represents the difference in charge and mass of the nuclei. Typically, the motion of the electrons is much faster than that of the nuclei: the dashed lines would stretch, shrink, and reorient much faster than the solid thick line can stretch or shrink.

The operator $\widehat{\mathscr{V}}_{ne}(r,R)$ represents the nucleus-electron Coulomb attraction energy

$$\widehat{\mathscr{V}}_{ne}(r,R) = -\sum_{i=1}^{N}\left(\frac{Z_{Na}e^2}{r_{iNa}} + \frac{Z_{Cs}e^2}{r_{iCs}}\right), \tag{3.7}$$

with $N = 66$ the total number of electrons in the molecule. The operator $\widehat{\mathscr{V}}_{ee}(r)$ represents the electron-electron Coulomb repulsion energy

$$\widehat{\mathscr{V}}_{ee}(r,R) = \sum_{\substack{i=1\\ j>i}}^{N}\frac{e^2}{r_{ij}} = \frac{1}{2}\sum_{i=1}^{N}\sum_{\substack{j=1\\ j\neq i}}^{N}\frac{e^2}{r_{ij}} \tag{3.8}$$

where the extra subscript below the sums guarantees that no electron interacts with itself. Likewise, the 1/2 prefactor removes the superfluous term obtained when expanding the double sum. Finally, $\widehat{\mathscr{V}}_{nn}(R)$ is the nucleus-nucleus Coulomb repulsion

$$\widehat{\mathscr{V}}_{nn}(R) = \frac{Z_{Na}Z_{Cs}e^2}{R}. \tag{3.9}$$

3.2.2 Rotations in molecules

With the definitions of Fig. 3.1, the total kinetic energy operator of the nuclei is defined as:

$$\widehat{\mathcal{T}_n}(\vec{R}) \equiv \underbrace{-\frac{\hbar^2}{2\mu}\frac{1}{R^2}\frac{\partial}{\partial R}\left(R^2\frac{\partial}{\partial R}\right)}_{\widehat{\mathcal{T}}(R)} + \underbrace{\frac{1}{2\mu R^2}\left[-\hbar^2\left(\frac{1}{\sin\theta}\frac{\partial}{\partial\theta}\left(\sin\theta\frac{\partial}{\partial\theta}\right)+\frac{1}{\sin^2\theta}\frac{\partial^2}{\partial\varphi^2}\right)\right]}_{\widehat{\vec{\mathcal{R}}}^2(\theta,\varphi)} \tag{3.10}$$

where $\widehat{\mathcal{T}}(R)$ accounts for the vibrations of the nuclei along the internuclear axis, and $\widehat{\vec{\mathcal{R}}}$ is the angular momentum operator representing the rotation of the nuclei about their center of mass.

Attempting to form a Complete Set of Commuting Observables (CSCO, see Cohen-Tannoudji *et al.* [29]), one can express $\widehat{\vec{\mathcal{R}}}^2$ in terms of as many angular momenta of the system as possible that commute with the complete molecular hamiltonian (§3.1.2.3 p. 96 and §3.2.1.1 p. 107-108 of [34]):

$$\widehat{\vec{\mathcal{R}}}^2 = (\widehat{\vec{\mathcal{J}}} - \widehat{\vec{\mathcal{L}}} - \widehat{\vec{\mathcal{S}}})^2 \tag{3.11a}$$

$$\begin{aligned} &= \widehat{\vec{\mathcal{J}}}^2 - \widehat{\vec{\mathcal{J}}}_z^2 + \widehat{\vec{\mathcal{S}}}^2 - \widehat{\vec{\mathcal{S}}}_z^2 + (\widehat{\vec{\mathcal{L}}}^2 - \widehat{\vec{\mathcal{L}}}_z^2) \\ &\quad - \{(\widehat{\vec{\mathcal{J}}}^+\widehat{\vec{\mathcal{L}}}^- + \widehat{\vec{\mathcal{J}}}^-\widehat{\vec{\mathcal{L}}}^+) + (\widehat{\vec{\mathcal{J}}}^+\widehat{\vec{\mathcal{S}}}^- + \widehat{\vec{\mathcal{J}}}^-\widehat{\vec{\mathcal{S}}}^+) - (\widehat{\vec{\mathcal{L}}}^+\widehat{\vec{\mathcal{S}}}^- + \widehat{\vec{\mathcal{L}}}^-\widehat{\vec{\mathcal{S}}}^+)\}, \end{aligned} \tag{3.11b}$$

Let $\widehat{\mathscr{A}}$ be any vector operator appearing in Eq. (3.11b), then $\widehat{\mathscr{A}_z}$ denotes the projection operator of $\widehat{\mathscr{A}}$ along the internuclear axis $\hat{z}$, and $\widehat{\mathscr{A}^\pm} = \widehat{\mathscr{A}_x} \pm \mathbf{i}\,\widehat{\mathscr{A}_y}$ is the raising (+)/lowering (-) operator corresponding to $\widehat{\mathscr{A}}$. The operator $\widehat{\vec{\mathcal{J}}}$ is the total angular momentum of the molecule, exclusive of nuclear spin; $\widehat{\vec{\mathcal{L}}}$ is the total electronic orbital angular momentum, and $\widehat{\vec{\mathcal{S}}}$ is the total electronic spin angular momentum. The associated quantum numbers are summarized in Tbl. 3.1.

Operator	$\widehat{\vec{\mathscr{J}}}^2$	$\widehat{\vec{\mathscr{L}}}^2$	$\widehat{\vec{S}}^2$	$\widehat{\vec{\mathscr{J}}}_Z$	$\widehat{\vec{\mathscr{J}}}_z$	$\widehat{\vec{\mathscr{L}}}_z$	$\widehat{\vec{S}}_z$
Quantum number	J	undefined	S	M	$\Omega = \lvert\Lambda + \Sigma\rvert$	Λ	Σ

Table 3.1: Molecular quantum numbers associated with various angular momenta. The number Λ is actually the *absolute value* of the quantum number for $\widehat{\vec{\mathscr{L}}}_z$ (see Herzberg [55]). The cylindrical symmetry of a diatomic molecule prevents $\widehat{\vec{\mathscr{L}}}^2$ to commute with other operators: its associated quantum number is undefined.

The operator $\widehat{\vec{\mathscr{J}}}^2$ always commutes with the molecular hamiltonian when nuclear spins are not conisdered, and thus is always part of any CSCO one attempts to construct. Lefebvre-Brion and Field [34] define the eigenkets of $\widehat{\vec{\mathscr{J}}}^2$, which are also eigenkets of $\widehat{\vec{\mathscr{J}}}_z^2$, using Wigner $\mathcal{D}$-functions and an appropriate choice of Euler angles (see [34, §2.3.3]):

$$\left\langle \frac{\pi}{2}\theta\varphi \middle| JM\Omega \right\rangle = \left(\frac{2J+1}{4\pi}\right)^{1/2} \mathcal{D}^J_{\Omega M}(\frac{\pi}{2},\theta,\varphi). \tag{3.12}$$

The mathematically curious reader may use the definitions of Wigner $\mathcal{D}$-functions from Edmonds [56, chap. 4] to prove that:

$$\langle JM\Omega \,|\, J'M'\Omega' \rangle = \delta_{JJ'}\delta_{MM'}\delta_{\Omega\Omega'} \tag{3.13a}$$

$$\begin{aligned}\langle JM\Omega \,|\cos\theta|\, J'M'\Omega' \rangle &= (-1)^{\Omega+M}(2J+1)^{1/2}(2J'+1)^{1/2} \\ &\times \begin{pmatrix} 1 & J' & J \\ 0 & \Omega' & -\Omega \end{pmatrix}\begin{pmatrix} 1 & J' & J \\ 0 & M' & -M \end{pmatrix}\delta_{MM'}\delta_{\Omega\Omega'}\end{aligned} \tag{3.13b}$$

where $\begin{pmatrix} j_1 & j_2 & j_3 \\ m_1 & m_2 & m_3 \end{pmatrix}$ is a Wigner 3-j symbol, and δ_{ab} is the Kronecker delta.

The cylindrical symmetry of a diatomic molecule prevents $\widehat{\vec{\mathscr{L}}}^2$ from com-

muting with other operators. Thus, the eigenstates of $\widehat{\overrightarrow{\mathscr{L}}}^2$ are not eigenstates of other operators. Therefore, the quantum number L can neither label the electronic wave functions nor the molecular wave functions. If L were a good quantum number, then the action of $\widehat{\overrightarrow{\mathscr{L}}}^2$ on the molecular ket would produce a term of the form $Y = L(L+1)$. With the help of the van Vleck pure precession hypothesis[a], one may approximate the value of Y without knowing L, which remains undefined. In particular, Zaharova *et al.* [10, p. 012508-6] used the van Vleck pure precession hypothesis to approximate Y for the Hund's case (a) $A^1\Sigma^+$ and $b^3\Pi$ electronic states of NaCs, setting:

$$\left\langle A^1\Sigma^+ \left| \widehat{\overrightarrow{\mathscr{L}}}^2 \right| A^1\Sigma^+ \right\rangle = \left\langle b^3\Pi \left| \widehat{\overrightarrow{\mathscr{L}}}^2 \right| b^3\Pi \right\rangle = 2. \tag{3.14}$$

Docenko *et al.* [21] do not account explicitly for the $\widehat{\overrightarrow{\mathscr{L}}}^2$ term in the model they use to determine the $X^1\Sigma^+$ electronic potential energy curve from experiment. The $X^1\Sigma^+$ state dissociates to atomic states $Na(3^2S)$+$Cs(6^2S)$, where the orbital angular momentum of each atom is 0. Angular momentum algebra [52, chap. III] shows that the only value of L that would be possible were L defined, would be $L = 0$, and so the orbital angular momentum would have zero magnitude. Using this estimate and the van Vleck pure precession hypothesis, I can set

$$\left\langle X^1\Sigma^+ \left| \widehat{\overrightarrow{\mathscr{L}}}^2 \right| X^1\Sigma^+ \right\rangle = 0. \tag{3.15}$$

The terms between curly braces in the second row of Eq. (3.11b) produce off-diagonal rotational couplings (see Sec. 3.1.2.3 p. 98 and Sec. 3.2.1.1 p. 107-108

[a] The van Vleck pure precession hypothesis states [57, p. 488, last paragraph] that the total electronic orbital angular momentum has constant magnitude, precesses uniformly about the internuclear axis, and the moment of inertia of the diatomic molecule is independent of Ω, the quantum number representing the projection of the total angular momentum of the molecule along the internuclear axis.

in [34]), which only connect electronic states that dissociate to the same asymptote. Katô [35, p. 3216] provides the non zero matrix elements for these off-diagonal couplings. For NaCs dissociating to the Na(3^2S)+Cs(6^2S) asymptote, only the $X^1\Sigma^+$ and the $a^3\Sigma^+$ electronic states are possible. Using Eqs. (62–64) from [35], the off-diagonal rotational couplings of Eq. (3.11b) between $X^1\Sigma^+$ state and $a^3\Sigma^+$ are zero. For NaCs dissociating to the Na(3^2S)+Cs(6^2P) asymptote, the only non-zero coupling that could occur through the operators between curly braces in Eq. (3.11b), is between the $A^1\Sigma^+$ and the $B^1\Pi$ electronic states. Following the experimental conclusion of [10, p. 012508-3], I neglect this coupling altogether.

3.2.3 Spin-orbit interactions

Although Van Vleck [33] (see also [34, Eq. 3.4.1 p. 181]) derived the full form of the spin-orbit hamiltonian $\widehat{\mathscr{H}_{\mathrm{SO}}}$ for diatomic molecules, the form

$$\widehat{\mathscr{H}_{\mathrm{SO}}} = \sum_i \hat{a}_i \widehat{\vec{\ell}_i} \cdot \widehat{\vec{s}_i} \tag{3.16}$$

suffices to determine which electronic states are coupled by the spin-orbit interaction. In Eq. (3.16), the sum runs only over electrons in open shells, and $\widehat{\vec{s}_i}$ is the spin angular momentum of the i-th electron. The definition of the operator $\hat{a}_i \widehat{\vec{\ell}_i}$ is

$$\hat{a}_i \widehat{\vec{\ell}_i} = \sum_K \frac{\alpha^2}{2} \frac{Z_{\mathrm{eff,K}}}{r_{iK}^3} \times \widehat{\vec{\ell}_{iK}} \tag{3.17}$$

where $Z_{\mathrm{eff,K}}$ is the effective charge of nucleus K experienced by the i-th electron, r_{iK} is the distance between nucleus K and electron i, and $\widehat{\vec{\ell}_{iK}}$ is the orbital anuglar momentum of the i-th electron about nucleus K.

The relevant electronic states in my research are $X^1\Sigma^+$, $A^1\Sigma^+$, and $b^3\Pi$. Us-

ing the notations and procedures in [35], I retrieved the results below. The spin-orbit operator only couples electronic states that dissociate to the same asymptote, so

$$\left\langle X^1\Sigma^+ \left| \widehat{\mathscr{H}_{SO}} \right| A^1\Sigma^+ \right\rangle = \left\langle X^1\Sigma^+ \left| \widehat{\mathscr{H}_{SO}} \right| b^3\Pi \right\rangle = 0 \tag{3.18a}$$

The $X^1\Sigma^+$ state and $a^3\Sigma^+$ dissociate to the same asymptote. However, the spin-orbit operator couples Σ states only when they behave differently under a reflection through a plane containing the internuclear axis, *i.e*.

$$\left\langle \Sigma^+ \left| \widehat{\mathscr{H}_{SO}} \right| \Sigma^+ \right\rangle = 0, \qquad \left\langle \Sigma^- \left| \widehat{\mathscr{H}_{SO}} \right| \Sigma^- \right\rangle = 0,$$
$$\left\langle \Sigma^- \left| \widehat{\mathscr{H}_{SO}} \right| \Sigma^+ \right\rangle \neq 0, \qquad \left\langle \Sigma^+ \left| \widehat{\mathscr{H}_{SO}} \right| \Sigma^- \right\rangle \neq 0.$$

In particular,

$$\left\langle X^1\Sigma^+ \left| \widehat{\mathscr{H}_{SO}} \right| a^3\Sigma^+ \right\rangle = 0. \tag{3.18b}$$

By the same symmetry argument, the spin-orbit operator cannot have diagonal matrix element for Σ states,

$$\left\langle X^1\Sigma^+ \left| \widehat{\mathscr{H}_{SO}} \right| X^1\Sigma^+ \right\rangle = \left\langle A^1\Sigma^+ \left| \widehat{\mathscr{H}_{SO}} \right| A^1\Sigma^+ \right\rangle = 0. \tag{3.18c}$$

However, the ${}^3\Pi_{\Omega=0}$ electronic state *has* diagonal matrix elements, since for this state $\Sigma = -1$ and $\Lambda = 1$:

$$\eta(R) \equiv -\left\langle b^3\Pi_0 \left| \widehat{\mathscr{H}_{SO}} \right| b^3\Pi_0 \right\rangle. \tag{3.18d}$$

The spin-orbit interaction indeed lifts the 3-fold ($\Omega = 0, 1, 2$) degeneracy of the $b^3\Pi$ state.

The only off-diagonal matrix element of the spin-orbit hamiltonian relevant to the current work is

$$\sqrt{2}\xi(R) \equiv -\left\langle \mathrm{A}^1\Sigma^+ \middle| \widehat{\mathscr{H}_{\mathrm{SO}}} \middle| \mathrm{b}^3\Pi \right\rangle \tag{3.18e}$$

The experimental work of Zaharova *et al.* [10] provides the functions $\eta(R)$ and $\xi(R)$ of Eqs. (3.18d & 3.18e).

3.2.4 Light matter interaction

The interaction between light and matter is a crucial process in the Universe in general. On Earth for example, the planet's flora absorbs sunlight to fuel photosynthesis, thereby extracting carbon from atmospheric CO_2, and releasing the dioxygen breathed my most lifeforms.

Maxwell's equations describe light as a propagating electromagnetic (E&M) wave. Einstein's discovery of the photoelectric effect revealed the existence of the quantum of light, the photon. A **Semi-Classical Model (SCM)** of the light-matter interaction describes a system of particles with quantum mechanics, while representing the external E&M field classically[a]. The SCM is valid if the number of photons in the interacting E&M field is far greater than the number of photons that the system may absorb or emit (see [24, chap. 4, p. 183] and Bohm [58, chap. 18, §15]).

What is the minimum number of photons carried by the field in this work? Gaussian laser pulses with a peak intensity I_0 and temporal full width at half

[a] Sometimes, such model is dubbed the semi-classical approximation. However, in the literature, the semi-classical approximation may refer to the WKB (Wentzel, Kramers, Brillouin) approximation, unrelated to how the E&M field is modeled.

maximum (FWHM)[a] $\Delta\tau$ carry a total energy per unit area of (chap. 2)

$$E_{/\text{area}} = \frac{I_0 \Delta\tau}{2}\sqrt{\frac{\pi}{\ln 2}}.$$

The lasers in this work have a peak intensity I_0 at least equal to $100\,\text{kW.cm}^{-2}$ and a temporal FWHM $\tau \approx 550\,\text{ps}$ (see Chap. 6). The experiment reported in [47] suggests that the NaCs sample occupies a spherical volume at least equal to $0.001\,\text{cm}^3$. The smallest area of the sample that the laser illuminates is the circular cross section of that spherical volume, *i.e.* a surface area on the order of $A = 0.024\,\text{cm}^2$. Therefore the laser beam supplies the sample with a minimum total energy of

$$E_{/\text{area}} \times A \approx 3.25 \times 10^{11}\ E_h \approx 2.14 \times 10^{18}\,\text{GHz} \approx 7.13 \times 10^{16}\ \text{cm}^{-1}.$$

The least energetic photons carried by the laser beams have an energy of approximately $0.051\ E_h \approx 3.3 \times 10^5\,\text{GHz} \approx 11.2 \times 10^3\ \text{cm}^{-1}$, corresponding to the transition from the asymptote of the $X^1\Sigma^+$ state to that of the $A^1\Sigma^+$ state (see Fig. 2.12). The most energetic photons have an energy of approximately $0.076\ E_h \approx 5 \times 10^5\,\text{GHz} \approx 16.7 \times 10^3\,\text{cm}^{-1}$, corresponding to the transition from the asymptote of the $A^1\Sigma^+$ state to the bottom of the $X^1\Sigma^+$ state potential well. Thus, dividing the total energy of the laser field by the energy of a given transition shows that the field carries 10^{12}–10^{15} photons. The NaCs sample contains 10^8–10^9 atomic pairs: if all atomic pairs absorb (emit) one photon from the pump (Stokes) laser pulse, then the sample absorbs (emits) a maximum of 10^9 photons *i.e.* 0.1% of the minimum number of photons in the field. Therefore the quantization of the E&M field would be excessive: I can treat the number

[a] This is the same $\Delta\tau$ as in chap. 2, *i.e.* the FWHM of the *intensity* of the laser, not its amplitude.

of photons emitted or absorbed classically, and the use of the **Semi-Classical Model** is justified.

Cohen-Tannoudji *et al.* [29, Compl. A_{XIII}, pp. 1306–1308] provide the complete hamiltonian for a system interacting with a—classical—electromagnetic field [a], and examine the relative importance of each term in this hamiltonian. In particular, when the wavelength λ of the external E&M field is much greater than the spatial extension of the atom/molecule system, the **Long Wavelength Approximation (LWA)** applies [29, Compl. A_{XIII}]: the electric field's spatial dependence is negligible over the spatial extension of the system.

Let's find an estimate for the maximum spatial extension of NaCs in this project. The photoassociation reaction tends to occur [40, p. 499] at internuclear separations on the order of the van der Waals radius[b] [40, p. 499]

$$R_{\mathrm{vdW}} = \frac{1}{2}\left(\frac{2\mu C_6}{\hbar^2}\right)^{1/4}$$

of the initial electronic state of the photoassociation reaction. In this research, photoassociation starts above the asymptote of the $X^1\Sigma^+$ and ends among the high-lying states of the $A^1\Sigma^+$ state. For the $X^1\Sigma^+$ state,

$$R_{\mathrm{vdW}} \approx 61.61\, a_0 \approx 32.6\,\text{Å}.$$

After the photoassociation reaction, the NaCs molecule is in a high-lying state of the $A^1\Sigma^+$ state, and the corresponding vibrational wave function decays exponentially to zero in the classically forbidden region. Let $R_{\mathrm{A}}^{+}(v_{\max})$ be the right classical turning point of NaCs in the highest vibrational wave function

[a] see also [24, chap. 4]

[b] The coefficient C_6 is the factor of $1/R^6$ in the long-range dispersion form of the potential energy curve under consideration (see chap. 2.5.1).

$\phi^{\mathrm{A}}_{v_{\max}}(R)$ of the $\mathrm{A}^1\Sigma^+$ state. The probability $\mathbb{P}$ that the internuclear separation of the molecule be greater than $R_{\max} = 1.2R^+_{\mathrm{A}}(v_{\max})$ is[a]

$$\mathbb{P} = \int_{R_{\max}}^{+\infty} |\phi^{\mathrm{A}}_{v_{\max}}(R)|^2 \, \mathrm{d}R \approx 9\%.$$

Thus the spatial extension of the NaCs molecule in this research is smaller than $R_{\max} \approx 67.15\, a_0 > R_{\mathrm{vdW}}$. Since the wave number of the laser fields in this project never exceeds $k \approx 17\,000\,\mathrm{cm}^{-1}$

$$kR_{\max} \approx 6 \times 10^{-3} \ll 1,$$

so I can apply the LWA.

Within the context of the LWA, the **Electric Dipole Approximation (EDA)** retains only the electric dipole term in the multipole expansion of the vector potential of the field. The operator $\widehat{\mathscr{V}}_{\mathrm{int}}(t)$ representing the interaction between the electric field $\vec{\mathscr{E}}(t)$ and the system is therefore

$$\widehat{\mathscr{V}}_{\mathrm{int}}(t) = -\widehat{\vec{\mathscr{D}}} \cdot \vec{\mathscr{E}}(t) \tag{3.19}$$

where $\widehat{\vec{\mathscr{D}}}$ is the operator for the total electric dipole moment of the NaCs molecule. In the space-fixed frame centered on the center of mass of the nuclei (Fig. 3.1 p. 54), the total electric dipole moment is

$$\vec{\mathscr{D}} = e\left(Z_{\mathsf{Na}}\vec{R}_{\mathsf{Na}} + Z_{\mathsf{Cs}}\vec{R}_{\mathsf{Cs}} - \sum_{j=1}^{Z_{\mathsf{Na}}+Z_{\mathsf{Cs}}} \vec{r}_j\right),$$

where $\vec{R}_{\mathsf{Na}}$, $\vec{R}_{\mathsf{Cs}}$, and $\vec{r}_j$ are the position vectors, of respectively the sodium

[a] The probability that the internuclear separation of the molecule will be greater than $R_{\max}$ when the molecule has wave function $\phi^{\mathrm{A}}_{v_{\max}-1}(R)$ is approximately 0.7%.

atom, the cesium atom, and the j-th electron. One may introduce the internuclear separation vector[a] $\vec{R} = \vec{R}_{\mathrm{Na}} - \vec{R}_{\mathrm{Cs}}$ to write the total electric dipole moment as

$$\vec{\mathscr{D}} = e\left(\left(\frac{Z_{\mathrm{Na}}M_{\mathrm{Cs}} - Z_{\mathrm{Cs}}M_{\mathrm{Na}}}{M_{\mathrm{Cs}} + M_{\mathrm{Na}}}\right)\vec{R} - \sum_{j=1}^{Z_{\mathrm{Na}}+Z_{\mathrm{Cs}}} \vec{r}_j\right).$$

The polarization of the laser field determines the dipole selection rules applicable to the problem: linear polarization gives $\Delta M = 0$, while circular polarization imposes $\Delta M = \pm 1$. To gain physical insights into the process, while keeping the number of molecular states involved in the problem to a minimum, I chose lasers linearly polarized along the laboratory-fixed $\hat{Z}$ axis (Fig. 3.1), so only the $\Delta M = 0$ selection rule applies.

3.3 Born-Oppenheimer Approximation

Compared to atoms, diatomic molecules have the additional freedom of vibrating along their internuclear axis, and rotating about their center of mass. In their seminal paper, Born and Oppenheimer [59] showed that the dynamics of the electrons are approximately separable from the dynamics of the nuclei since the electrons are much lighter (see also [34, pp. 89-90], [60, §VI], [59, 61, 62]). To approximate the total energy of the molecule E_T, one starts by considering the electronic energy E_{el}, then one adds the contribution of the vibrational motion, E_v, and finally the weaker contribution from the rotational motion of the nuclei, E_{rot} (Lefebvre-Brion and Field [34, p. 90]):

$$E_T \approx E_{\mathrm{el}} + E_v + E_{\mathrm{rot}}$$

The separation of the molecular dynamics into an electronic and a nuclear

[a] Remember: the center of mass of the nuclei is such that $M_{\mathrm{Na}}\vec{R}_{\mathrm{Na}} + M_{\mathrm{Cs}}\vec{R}_{\mathrm{Cs}} = \vec{0}$

contributions constitutes the **Born-Oppenheimer Approximation** (BOA). This decoupling has 2 consequences:

1. For a given set α of quantum numbers describing the state of the electrons (see below), the wave function of the molecule can be written as a product of two wave functions, one for the nuclei and one for the electrons

$$\psi^{\mathrm{BO}}_{\alpha,v} = \chi_v(R,\theta,\varphi)\,\Phi^{el}_{\alpha}(\vec{r};R), \tag{3.20a}$$

   where $\vec{r}$ denotes the set of coordinates of all electrons, and the semi-colon indicates that R is a parameter

2. The internuclear separation R being a *parameter*[a] for the electronic wave function, the radial part $\widehat{\mathscr{T}_n}(R)$ of the nuclear kinetic energy operator $\widehat{\mathscr{T}_n}$ does *not* act on the electronic wave function

$$\left\langle \Phi^{el}_{\alpha} \,\middle|\, \widehat{\mathscr{T}_n}(R) \,\middle|\, \Phi^{el}_{\alpha'} \right\rangle = \langle \Phi^{el}_{\alpha} | \Phi^{el}_{\alpha'} \rangle\, \widehat{\mathscr{T}_n}(R) = \delta_{\alpha\alpha'}\widehat{\mathscr{T}_n}(R)\,. \tag{3.20b}$$

In the Born-Oppenheimer Approximation, the electronic wave function $|\Phi^{el}_{\alpha}\rangle$ is an eigenfunction of the hamiltonian

$$\widehat{\mathscr{H}_{\mathrm{el}}}(\vec{r};\,R) + \widehat{\mathscr{V}_{nn}} = \widehat{\mathscr{T}_e} + \widehat{\mathscr{V}_{ee}} + \widehat{\mathscr{V}_{ne}} + \widehat{\mathscr{V}_{nn}} \tag{3.21}$$

where $\widehat{\mathscr{T}_e}$ is the kinetic energy operator for all electrons. The R-parameterized eigenvalue corresponding to $|\Phi^{el}_{\alpha}\rangle$ is the *Born-Oppenheimer potential energy* $V^{\mathrm{BO}}_{\alpha}(R)$, such that

$$(\widehat{\mathscr{H}_{\mathrm{el}}} + \widehat{\mathscr{V}_{nn}})\;|\Phi^{el}_{\alpha}\rangle = V^{\mathrm{BO}}_{\alpha}(R)\,|\Phi^{el}_{\alpha}\rangle \tag{3.22}$$

In the above, since $|\Phi^{el}_{\alpha}\rangle$ is an eigenstate of $\widehat{\mathscr{H}_{\mathrm{el}}} + \widehat{\mathscr{V}_{nn}}$, the set of quantum num-

[a] As opposed to a *variable*.

bers α corresponds to Λ, S, Σ, which are good quantum numbers for this particular operator. Yet, the Born-Oppenheimer Approximation can be written for other sets of quantum numbers α: for example, if the electronic ket $|\Phi_\alpha^{el}\rangle$ is an eigenstate of $\widehat{\mathscr{H}_{\text{el}}} + \widehat{\mathscr{V}_{nn}} + \widehat{\mathscr{H}_{\text{SO}}}$, then only the quantum number Ω is appropriate to label the electronic states. *Important*: to distinguish electronic states that have the same quantum numbers, α always contains an extra label that is not necessarily a quantum number. Thus the $X^1\Sigma^+$ state differs from the $A^1\Sigma^+$ state, although for both of them $\Lambda = 0,\ S = 0,\ \Sigma = 0$; and α for the $X^1\Sigma^+$ state is $\alpha_X = \{X, \Lambda = 0,\ S = 0,\ \Sigma = 0\}$, while α for the $A^1\Sigma^+$ state is $\alpha_A = \{A, \Lambda = 0,\ S = 0,\ \Sigma = 0\}$.

The Born-Oppenheimer potential energies relevant to this problem were presented in Sec. 2.5.1. The Born-Oppenheimer Approximation will come in handy in chap. 4, when deriving equations for the populations in the various rovibrational states of NaCs involved.

Speaking of chap. 4, now that I have presented the basic Physics of the problem, let's move on and do some maths.

Chapter 4

Mathematics

4.1 The model

4.1.1 The Hamiltonian

With all the interactions listed in chap. 3, and following the recommendations of [34], the total hamiltonian governing the mixture of sodium and cesium atoms exposed to the external laser electric field $\vec{\mathscr{E}}(t)$ is

$$\widehat{\mathscr{H}}(t) = \widehat{\mathscr{T}}(R) + \frac{\widehat{\vec{\mathscr{R}}}^2}{2\mu R^2} + \widehat{\mathscr{V}}_{nn} + \underbrace{\widehat{\mathscr{V}}_{ne} + \widehat{\mathscr{V}}_{ee} + \widehat{\mathscr{T}}_e}_{\widehat{\mathscr{H}}_{\text{el}}} + \widehat{\mathscr{H}}_{\text{SO}} \underbrace{- \widehat{\vec{\mathscr{D}}} \cdot \widehat{\vec{\mathscr{E}}}(t)}_{\widehat{\mathscr{V}}_{\text{int}}(t)}, \tag{4.1}$$

where

$\widehat{\mathscr{T}}$ – translational kinetic energy operator for the nuclei,
$\frac{\widehat{\vec{\mathscr{R}}}^2}{2\mu R^2}$ – rotational kinetic energy operator for the nuclei,
$\widehat{\mathscr{V}}_{nn}$ – nucleus-nucleus Coulomb interaction,
$\widehat{\mathscr{V}}_{ne}$ – nucleus-electron Coulomb interaction,
$\widehat{\mathscr{V}}_{ee}$ – electron-electron Coulomb interaction,
$\widehat{\mathscr{T}}_e$ – kinetic energy operator for the electrons,
$\widehat{\mathscr{H}}_{\text{SO}}$ – spin-orbit interaction,
$\widehat{\vec{\mathscr{D}}}$ – electric dipole operator.

Equation 4.1 also recalls the definition of the electronic hamiltonian $\widehat{\mathscr{H}}_{\text{el}}$, necessary when using the Born-Oppenheimer Approximation, and of the light-matter interaction term $\widehat{\mathscr{V}}_{\text{int}}(t)$.

Two different lasers act on the system, the pump pulse and the Stokes pulse. Thus the total electric field $\vec{\mathscr{E}}(t)$ is the sum of the pump field and the Stokes field

$$\vec{\mathscr{E}}(t) = \overrightarrow{\mathscr{E}_P}(t) + \overrightarrow{\mathscr{E}_S}(t) \tag{4.2}$$

The hamiltonian $\widehat{\mathscr{H}}(t)$ governs 2 nuclei and a total of $Z_{\mathsf{Na}} + Z_{\mathsf{Cs}} = 11 + 55 = 66$ electrons, and is written in the space-fixed frame.

In this research, unless otherwise specified, the origin of the energy scale—the zero of energy—is taken at the asymptote of the $X^1\Sigma^+$electronic state.

4.1.2 Descriptor of the system

All the interactions in the system being accounted for in chapter 3, I must choose a way to describe the system. There are two possibilities: either use a wave function or a density operator. The treatment via the density operator is ideal to treat the initial condition [29, Comp. E_{III}] (*i.e.* a gaseous mixture in thermal equilibrium at ultracold temperature $T = 200\mu K$), but requires to solve the quantum Liouville-von Neumann equation [63–65]. If the density operator is expressed in a basis of the relevant Hilbert space of dimension N, then solving the quantum Liouville-von Neumann equation means solving N^2 coupled partial differential equations [63, 64]. When using a wave function formalism, solving the problem means solving the Time-Dependent Schrödinger Equation, *i.e.* only N coupled partial differential equations.

The density operator would also allow for the appropriate treatment of spontaneous emission, which I am not considering in my problem. A relevant time scale involved in the problem is the lifetime τ of the cesium atom in the $6^2P_{1/2}$ atomic state. If the light-matter interaction lasts longer than τ, than the cesium atom could have decayed back to its ground atomic state. Ac-

cording to Steck [26], the lifetime of Cs:$6^2P_{1/2}$ is $\tau = 34.791(90)\,\mathrm{ns}$. Since the laser pulses I use in this research last at most 3 ns, the laser pulses will be over before any relaxation of the cesium atom can occur. Also, according to Tbl. 3 of Zaharova *et al.* [10], the lifetime for the transitions from vibrational states of the $A^1\Sigma^+$ state to the vibrational states of the $X^1\Sigma^+$ state are greater than 40 ns, also longer than the duration of the pulsed lasers sequence. Therefore it is legitimate to neglect spontaneous emission.

Furthermore, there exists a way to express the initial condition for the system in the density operator formalism using a linear combination of projectors over wave packets [66, p. 013412-3]. In general, a wave packet is a superposition of bound states and stationary continuum states. To facilitate my understanding of the underlying physics, I will simply use a wave packet. Doing so, I only have to solve the Time-Dependent Schrödinger Equation, that is N coupled partial differential equations.

Therefore I describe the system with a time-dependent ket $|\Psi(t)\rangle$. The corresponding wave function is $\langle R,\theta,\varphi,\vec{r}\,|\Psi(t)\rangle = \Psi(R,\theta,\varphi,\vec{r},t)$:

$$\Psi(R,\theta,\varphi,\vec{r},t) = \sum_{\alpha}\sum_{J=0}^{\infty}\sum_{M=-J}^{J}\frac{1}{R}\Gamma^{\alpha}_{JM\Omega}(R,t)\langle\frac{\pi}{2}\theta\varphi|JM\Omega\rangle\Phi^{\mathrm{el}}_{\alpha}(\vec{r};R). \tag{4.3}$$

In Eq. (4.3), R is the internuclear separation, the angles θ and φ define the orientation of the internuclear axis in the space-fixed frame (see Fig. 3.3), and $\vec{r}$ denotes the set of coordinates of all electrons. I defined the angular wave function $\langle\frac{\pi}{2}\theta\varphi|JM\Omega\rangle$ in Eq. (3.12) on p. 59. The R-parameterized wave function $\Phi^{\mathrm{el}}_{\alpha}(\vec{r};R)$ corresponds to the Born-Oppenheimer electronic state $|\Phi^{\mathrm{el}}_{\alpha}\rangle$ defined in Sec. 3.3 on p. 67. Finally the reduced radial wave function $\Gamma^{\alpha}_{JM\Omega}(R,t)$ (see Eq. (4.4) below) is a linear combination of the vibrational and stationary scattering wave functions of the Born-Oppenheimer potential energy curve that

corresponds to the tensor product state $|JM\Omega\rangle \otimes |\Phi_\alpha^{\text{el}}\rangle$.

Rigorously, Eq. (4.3) should contain a sum over Ω. However, the choice of a particular Hund's case for the electronic states $|\Phi_\alpha^{\text{el}}\rangle$'s determines what quantum numbers make up the set α. In all Hund's cases, J and M are always good quantum numbers For Hund's cases (b), (d), (e), and (e') [34, p. 103], Ω is not part of α, and so Eq. (4.3) should contain an extra $\sum_{\Omega=-J}^{J}$. For Hund's case (c), the only good quantum number that makes up α is Ω. Thus in Hund's case (c) the summation $\sum_\alpha$ reduces to $\sum_{\Omega=-J}^{J}$. Finally in Hund's case (a), the set[a] α is Λ, S, Σ, and so $\sum_\alpha$ becomes $\sum_{\Lambda\geq 0}\sum_{S\geq 0}\sum_{\Sigma=-S}^{S}$. Since $\Omega = \Lambda + \Sigma$, an extra summation over the allowed values of Ω would be superfluous.

The reduced radial wave function $\Gamma^\alpha_{JM\Omega}(R,t)$ is a superposition of rovibrational and energy normalized stationary continuum wave functions of the electronic state α with rotational quantum numbers J, M, Ω:

$$\Gamma^\alpha_{JM\Omega}(R,t) = \sum_v a_v^{\alpha JM\Omega}(t)\langle R|\alpha JM\Omega, v\rangle + \int_{E_\alpha^\infty}^{+\infty} a_E^{\alpha JM\Omega}(t)\langle R|\chi_E^{\alpha JM\Omega}\rangle \, \mathrm{d}E \qquad (4.4)$$

where the $\langle R|\alpha JM\Omega, v\rangle$s are the rovibrational wave functions in electronic state α with vibrational quantum number v and rotational quantum numbers J, M, Ω, E_α^∞ is the asymptotic value of the potential energy for electronic state α (with the potential energy curves of Fig. 2.12, $E_X^\infty = 0$), and $\langle R|\chi_E^{\alpha JM\Omega}\rangle$s are the energy-normalized stationary scattering wave functions with energy E above the asymptote of the electronic state α with rotational quantum number J, M, Ω. The point of this research is to derive and solve differential equations satisfied by

[a] Given the above remarks, the whole set of quantum numbers in Hund's case (a) is $\{J, \Omega, \Lambda, S, \Sigma\}$. The quantum number Ω appears in the preceding set despite the redundancy originating from $\Omega = \Lambda + \Sigma$ (see [34, pp. 94 & 103]). Lefebvre-Brion and Field [34] do not include the quantum number M in any of their Hund's case basis sets since their book does not cover "problems involving laboratory-fixed electromagnetic fields" (p. 103).

the coefficients a's in Eq. (4.4).

Equipped with a proper descriptor for the system, I can now translate the initial physical condition into a mathematical statement.

4.1.3 The initial conditions

At $t = 0$, when no laser has yet illuminated the sample, the system is simply a pair of atoms scattering above the asymptote of the $X^1\Sigma^+$ electronic state, for which $\Omega = 0$. Thus

$$\forall \alpha \neq X^1\Sigma^+,\ \forall \{J, M, \Omega\},\ \Gamma^{\alpha}_{JM\Omega}(R, t = 0) = 0. \tag{4.5}$$

The corresponding initial conditions on the expansion coefficients that appear in Eq. (4.4) are thus

$$\forall \alpha \neq X^1\Sigma^+,\ \forall \{J, M, \Omega\},\ a_v^{\alpha JM\Omega}(t = 0) = 0, \tag{4.6a}$$

$$a_E^{\alpha JM\Omega}(t = 0) = 0. \tag{4.6b}$$

Equation (4.3) contains a sum over all possible quantum numbers J. For the system at $T = 200\,\mu K$, what values are available to the quantum numbers $J, M,$ and Ω above the asymptote of the $X^1\Sigma^+$ state? Let's first examine what partial waves are accessible to the system at this temperature ([40, p. 499], [67], [68, p. 198], [69, p. 56]).

Figure 4.1 shows the potential energy curves for the $X^1\Sigma^+$ state $V_X(R) + \frac{\ell(\ell+1)}{2\mu R^2}$ with $\ell = 0$ and $\ell = 1$. The horizontal long-dashed green line in Fig. 4.1 represents the scattering energy chosen in Sec. 3.1. Clearly the initial scattering energy is not sufficient to overcome the $\ell = 1$ centrifugal barrier. Therefore only the s-wave ($\ell = 0$) is relevant to my problem.

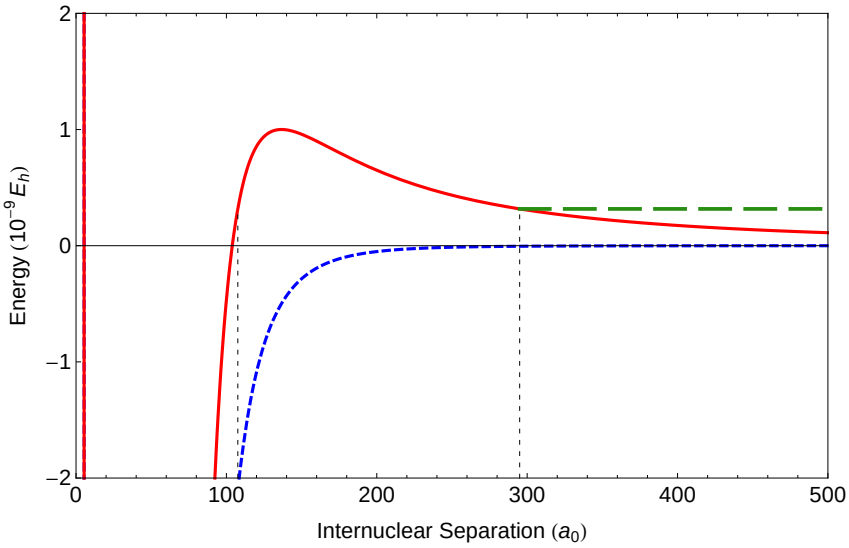

Figure 4.1: **Short dashed blue:** $X^1\Sigma^+$ electronic state of NaCs with $\ell = 0$. **Solid red:** $X^1\Sigma^+$ electronic state of NaCs with $\ell = 1$. **Long dashed green:** chosen scattering energy $E \approx 3.2\times10^{-10}\,E_h$. The chosen scattering energy is below the $\ell = 1$ rotational barrier of the $X^1\Sigma^+$ electronic state (solid red curve). The vertical thin dashes denote the width $\Delta R \approx 187.4\,a_0$ of the rotational barrier at E.

Angular momentum coupling rules between the s-wave and the $X^1\Sigma^+$ electronic state give the possible values of the quantum numbers J and M. To obtain the possible states $|JM\rangle$, I need (a) to couple the states $|L\Lambda\rangle$ with the kets $|S\Sigma\rangle$, (b) to rotate the quantization axis from the body-fixed internuclear axis z to the space-fixed axis $\mathcal{Z}$—which is the quantization axis for the partial waves—and finally, (c) I need to couple the electronic angular momentum $\vec{\mathscr{L}} + \vec{\mathcal{S}}$ with the angular momentum for the rotations of the nuclei $\vec{\mathscr{R}}$ to obtain the total angular momentum of the molecule $\vec{\mathscr{F}}$. First, remember that the van Vleck pure precession hypothesis (Sec. 3.2.2) suggests $L = 0$ for the $X^1\Sigma^+$ state, for which $\Lambda = 0, S = 0$, and $\Sigma = 0$. Let's define the total *electronic* angular momentum $\vec{\mathscr{J}}_a \equiv \vec{\mathscr{L}} + \vec{\mathcal{S}}$. The rules of angular momenta coupling ([29, chap. X],

[52, chap. III]) give:

$$|L\Lambda\rangle|S\Sigma\rangle = \sum_{J_a=|L-S|}^{L+S} \langle LS\Lambda\Sigma|J_a\Omega\rangle|J_a\Omega\rangle, \tag{4.7}$$

where $\langle LS\Lambda\Sigma|J_a\Omega\rangle$ is the Clebsch-Gordan coefficient, and[a] $\Omega = \Lambda + \Sigma$ is the projection of $\overrightarrow{\mathscr{J}_a}$ on the body-fixed internuclear $\hat{z}$-axis. For the $X^1\Sigma^+$ state, according to the above:

$$|L=0,\Lambda=0\rangle|S=0,\Sigma=0\rangle = \sum_{J_a=0}^{0} \langle 0000|J_a0\rangle|J_a,\Omega=0\rangle \tag{4.8a}$$

$$= \langle 0000|00\rangle|J_a=0,\Omega=0\rangle \tag{4.8b}$$

$$= |J_a=0,\Omega=0\rangle, \tag{4.8c}$$

since the Clebsch-Gordan coefficient $\langle 0000|00\rangle$ equals 1. The partial wave $|\ell m_\ell\rangle$ is quantized along the space-fixed $\hat{\mathcal{Z}}$-axis. To correctly couple $|J_a\Omega\rangle$ and $|\ell m_\ell\rangle$, I must first rotate the quantization axis of $|J_a\Omega\rangle$ from the internuclear body-fixed $\hat{z}$-axis to the space-fixed $\hat{\mathcal{Z}}$-axis. Using the passive convention (see Morrison and Parker [53]),

$$|J_a\Omega\rangle_{\mathrm{BF}} = \sum_{M_{J_a}=-J_a}^{J_a} \mathcal{D}^{J_a\,*}_{\Omega M_{J_a}}(\varphi,\theta,0)|J_aM_{J_a}\rangle_{\mathrm{SF}}. \tag{4.9}$$

[a] This Ω is the same as in Tbl. 3.1.

Thus in the present case,

$$|J_a = 0, \Omega = 0\rangle_{\mathrm{BF}} = \sum_{M_{J_a}=0}^{0} \mathcal{D}^{0\,*}_{0M_{J_a}}(\varphi, \theta, 0)\,|0M_{J_a}\rangle_{\mathrm{SF}} \tag{4.10a}$$

$$= \mathcal{D}^{0\,*}_{00}(\varphi, \theta, 0)\,|J_a = 0, M_{J_a} = 0\rangle_{\mathrm{SF}} \tag{4.10b}$$

$$= |J_a = 0, M_{J_a} = 0\rangle_{\mathrm{SF}} \tag{4.10c}$$

since the Wigner $\mathcal{D}^{0\,*}_{00}$ function equals 1. Now I can couple $|J_a = 0, M_{J_a} = 0\rangle$ with the only partial wave $|\ell m_\ell\rangle$ accessible to the system, the s-wave $|\ell = 0, m_\ell = 0\rangle$. Using angular momentum algebra as in Eq. (4.7) with $M = M_{J_a} + m_\ell$,

$$|J_a M_{J_a}\rangle|\ell m_\ell\rangle = \sum_{J=|J_a-\ell|}^{J_a+\ell} \langle J_a M_{J_a} \ell m_\ell | JM\rangle |JM\rangle \tag{4.11a}$$

$$|J_a = 0, M_{J_a} = 0\rangle|\ell = 0, m_\ell = 0\rangle = \sum_{J=0}^{0} \langle 0000 | J, M = 0\rangle |J, M = 0\rangle \tag{4.11b}$$

$$|J_a = 0, M_{J_a} = 0\rangle|\ell = 0, m_\ell = 0\rangle = |J = 0, M = 0\rangle\,. \tag{4.11c}$$

Consequently, the s-wave above the asymptote of the $X^1\Sigma^+$ state only allows the rotational quantum numbers $J = 0$, and $M = 0$. For the $X^1\Sigma^+$ state, $\Omega = 0$ regardless of the accessible partial waves, since Ω originates from the coupling of $\vec{\mathscr{L}}$ and $\vec{\mathcal{S}}$. Going back to the reduced radial wave function, the initial conditions for $\Gamma^{X^1\Sigma^+}_{JM0}$ are

$$\Gamma^{X^1\Sigma^+}_{000}(R, t = 0) \neq 0, \qquad \text{and} \qquad \forall J \neq 0,\ \Gamma^{X^1\Sigma^+}_{JM0}(R, t = 0) = 0. \tag{4.12}$$

The above intial condition for $\Gamma^{X^1\Sigma^+}_{JM0}$ yields for the corresponding expansion

coefficients of Eq. (4.4)

$$\forall J \neq 0,\, a_v^{X^1\Sigma^+ JM0}(t=0) = 0, \tag{4.13a}$$

$$a_E^{X^1\Sigma^+ JM0}(t=0) = 0. \tag{4.13b}$$

At $t = 0$, the system is unbound, so the vibrational components of $\Gamma_{000}^{X^1\Sigma^+}$ must be zero:

$$\forall v, a_v^{X^1\Sigma^+ 000}(t=0) = 0. \tag{4.14}$$

In order to keep the derivation that follows as general as possible[a], I only outline some properties that the coefficient $a_E^{X^1\Sigma^+ 000}$ must have at $t = 0$. At $t = 0$, I consider that the system is in the stationary scattering state $|\chi_{E_p}^{X^1\Sigma^+ 000}\rangle$ with energy $E_p =\approx 0.317 \times 10^{-9}\, E_h \approx 2.086\,\text{MHz} \approx 6.96 \times 10^{-5}\,\text{cm}^{-1}$. To reflect this fact, $a_E^{X^1\Sigma^+ 000}(t=0)$ must be a function of energy, very sharply peaked about $E = E_p$. Also, since all Γ's must be normalized for all values of t, $a_E^{X^1\Sigma^+ 000}(t=0)$ must satisfy:

$$\int_{E_{X^1\Sigma^+}^{\infty}}^{+\infty} \left| a_E^{X^1\Sigma^+ 000}(t=0) \right|^2 \mathrm{d}E = 1. \tag{4.15}$$

No operator in the definition Eq. (4.1) of $\widehat{\mathscr{H}}(t)$ acts on the quantum number M, *except* the light-matter interaction term $\widehat{\mathscr{V}}_{\text{int}}(t)$. So for all operators in $\widehat{\mathscr{H}}(t)$ *except* $\widehat{\mathscr{V}}_{\text{int}}(t)$, $\Delta M = 0$. The polarization of the laser light determines which selection rule on M does $\widehat{\mathscr{V}}_{\text{int}}(t)$ allow. I picked linearly-polarized light, so the selection rule on M for the light-matter interaction term is $\Delta M = 0$ (see Sec. 3.2.4). Likewise, no operator in $\widehat{\mathscr{H}}(t)$ acts on the quantum number Ω, *except* $\widehat{\vec{\mathscr{R}}}^2$ (see Eq. (3.11b). So for all operators in $\widehat{\mathscr{H}}(t)$ *except* $\widehat{\vec{\mathscr{R}}}^2$, $\Delta\Omega = 0$. In Eq. (3.11b), only $\widehat{\vec{\mathscr{J}}}^{\pm}\widehat{\vec{\mathscr{L}}}^{\mp}$ and $\widehat{\vec{\mathscr{J}}}^{\pm}\widehat{\vec{\mathscr{S}}}^{\mp}$ give rise to the selection rule $\Delta\Omega = \pm 1$.

[a] Later in this chapter (p. 92), I will discretize the integral over the continuum. One benefit is the simplification of the initial condition on the coefficient $a_E^{X^1\Sigma^+ 000}(t=0)$.

However, I argued below Eq. (3.15) on p. 60 that the effects of $\widehat{\vec{\mathscr{J}}}^{\pm}\widehat{\vec{\mathscr{L}}}^{\mp}$ and $\widehat{\vec{\mathscr{J}}}^{\pm}\widehat{\vec{\mathcal{S}}}^{\mp}$ are negligible in my study. Therefore, the effective hamiltonian in this research has selection rules $\Delta M = 0$ and $\Delta\Omega = 0$: M and Ω remain constant during the process. Both quantum numbers start as 0, and keep the same value throughout the whole process. Thus, ***I will no longer specify the quantum numbers M and Ω, and remember that they are always equal to zero, unless they are needed for clarity.***

4.2 Equations for the reduced radial wave functions

4.2.1 Method of solution

The system described by the wave function Eq. (4.3) and subject to the hamiltonian Eq. (4.1), evolves according to the Time-Dependent Schrödinger Equation

$$\mathbf{i}\hbar\frac{\partial}{\partial t}|\Psi(t)\rangle = \widehat{\mathscr{H}}(t)|\Psi(t)\rangle, \tag{4.16}$$

subject to the initial conditions Eqs. (4.5 & 4.12), or equivalently Eqs. (4.6), (4.13), (4.14), & (4.15). To solve the problem, notice that the Hamiltonian $\widehat{\mathscr{H}}(t)$ can be split into the time-*dependent* term $\widehat{\mathscr{V}}_{\text{int}}(t)$, and the time-*independent* term $\widehat{\mathscr{H}_0} = \widehat{\mathscr{T}}(R) + \frac{\widehat{\vec{\mathscr{R}}}^2}{2\mu R^2} + \widehat{\mathscr{V}}_{nn} + \widehat{\mathscr{H}}_{\text{el}} + \widehat{\mathscr{H}}_{\text{SO}}$. The idea here is to first find a basis of eigenfunctions of $\widehat{\mathscr{H}_0}$ in the extended Hilbert space $\mathcal{L}^2(\mathbb{R}^N)$, which accounts for the R-dependence of the descriptor $\Psi(R,\theta,\varphi,\vec{r},t)$. Then expanding the Γ's over such basis of $\widehat{\mathscr{H}_0}$ will yield equations for the time-dependent expansion coefficients a's of Eq. (4.4).

In the course of the derivation, the features of the total electric field $\vec{\mathscr{E}}(t)$ become incrementally relevant:

1. the polarization of the light is crucial when deriving equations for the Γ's, as it determines the selection rules for the quantum numbers J, M, and Ω between the electronic states (Eq. (4.18));

2. the range of frequencies to which the lasers are tuned comes into play (see paragraph below Eq. (4.23)), and allows me to neglect certain dipole moment functions;

3. the general time-dependence of the tuning frequency—the chirp—enters the stage and leads to Eq. (4.42);

4. finally, the time-dependence of the lasers' *envelope* appears at the very end in Eq. (4.52) and Eq. (4.79), where the chirps are taken linear.

As explained in Sec. 2.1, non-chirped lasers are a limiting case of chirped lasers, and continuous-wave lasers are limiting cases of pulsed lasers. Thus the final equations Eq. (4.52) and Eq. (4.79) are valid for chirped and non-chirped, pulsed and continuous-wave lasers[a].

4.2.2 Derivation

The first step, covered in this section, is to obtain equations for the reduced radial wave functions Γ's.

Plugging Eq. (4.3) into the Time-Dependent Schrödinger Equation Eq. (4.16)

[a] Dear reader, if you wish to include more features in this research, your best starting point is Eq. (4.17), especially if you want to use a different total electric field $\vec{\mathscr{E}}(t)$, or include rotational perturbations embedded in $\widehat{\mathscr{R}}^{\pm}$. If you want to include phenomena like hyperfine structure or E&M field quantization, you need to redefine your total hamiltonian and your descriptor, and thus go back to Eq. (4.1) and Eq. (4.3). Finally, if you intend to use this work to make brownies, learn Elvish, or acquire supernatural powers, I am afraid you grabbed the wrong grimoire.

using the hamiltonian of Eq. (4.1) yields

$$
\begin{aligned}
&\forall \alpha,\ J,\ M,\ \Omega,\\
&\quad \mathbf{i}\hbar\frac{\partial}{\partial t}\Gamma^{\alpha}_{JM\Omega} = \left(-\frac{\hbar^2}{2\mu}\frac{\partial^2}{\partial R^2} + \frac{\hbar^2}{2\mu R^2}(J(J+1)-\Omega^2)\right)\Gamma^{\alpha}_{JM\Omega}\\
&\qquad\qquad + \frac{\hbar^2}{2\mu R^2}\sum_{\alpha'}\left\langle \Phi^{el}_{\alpha}\left|\widehat{\vec{\mathscr{L}}}^2 - \widehat{\vec{\mathscr{L}}}^2_z + \widehat{\vec{\mathscr{S}}}^2 - \widehat{\vec{\mathscr{S}}}^2_z\right|\Phi^{el}_{\alpha'}\right\rangle\Gamma^{\alpha'}_{JM\Omega}\\
&\qquad + \sum_{\alpha'}\sum_{J'}\sum_{M'}\frac{1}{2\mu R^2}\langle JM\Omega|\left\langle \Phi^{el}_{\alpha}\left|\widehat{\vec{\mathscr{R}}}^{\pm}\right|\Phi^{el}_{\alpha'}\right\rangle|J'M'\Omega'\rangle\Gamma^{\alpha'}_{J'M'\Omega'}\\
&\qquad\qquad + \sum_{\alpha'}\left\langle \Phi^{el}_{\alpha}\left|\widehat{\mathscr{H}_e} + \widehat{\mathscr{H}_{\mathrm{SO}}}\right|\Phi^{el}_{\alpha'}\right\rangle\Gamma^{\alpha'}_{JM\Omega}\\
&\qquad\qquad - \sum_{\alpha'}\sum_{J'}\sum_{M'}\langle JM\Omega|\left\langle \Phi^{el}_{\alpha}\left|\widehat{\vec{\mathscr{D}}}\cdot\widehat{\vec{\mathscr{E}}}(t)\right|\Phi^{el}_{\alpha'}\right\rangle|J'M'\Omega'\rangle\Gamma^{\alpha'}_{J'M'\Omega'}
\end{aligned}
\tag{4.17}
$$

where $\widehat{\vec{\mathscr{R}}}^{\pm} = \widehat{\vec{\mathscr{L}}}^{+}\widehat{\vec{\mathscr{S}}}^{-} + \widehat{\vec{\mathscr{L}}}^{-}\widehat{\vec{\mathscr{S}}}^{+} - \widehat{\vec{\mathscr{J}}}^{+}\widehat{\vec{\mathscr{L}}}^{-} - \widehat{\vec{\mathscr{J}}}^{-}\widehat{\vec{\mathscr{L}}}^{+} - \widehat{\vec{\mathscr{J}}}^{+}\widehat{\vec{\mathscr{S}}}^{-} - \widehat{\vec{\mathscr{J}}}^{-}\widehat{\vec{\mathscr{S}}}^{+}$ is neglected in what follows, as explained at the end of Sec. 3.2.2. The sum over electronic states $\sum_{\alpha'}$ runs over all electronic states possible[a], including the state α. Thus the light-matter interaction term, the last term in Eq. (4.17), represents electric dipole transitions *within the same* electronic state and *between different* electronic states. The lasers are linearly polarized along the space-fixed $\hat{\mathcal{Z}}$-axis, thus $\widehat{\vec{\mathscr{E}}}(t) = \mathscr{E}(t)\cdot\hat{\mathcal{Z}}$. Also the amplitude of the total laser field $\mathscr{E}(t)$ depends neither on the angular nor the electronic coordinates but only on time, so I can

[a] The possible electronic states are ionization states, dissociative states, and electronic states that support bound vibrational states.

factor it out of all the summation terms:

$$
\begin{aligned}
&\forall \alpha,\ J,\ M,\ \Omega, \\
&\quad \mathbf{i}\hbar\frac{\partial}{\partial t}\Gamma^{\alpha}_{JM\Omega} = \left(-\frac{\hbar^2}{2\mu}\frac{\partial^2}{\partial R^2} + \frac{\hbar^2}{2\mu R^2}(J(J+1)-\Omega^2)\right)\Gamma^{\alpha}_{JM\Omega} \\
&\qquad\qquad + \frac{\hbar^2}{2\mu R^2}\sum_{\alpha'}\left\langle \Phi^{el}_{\alpha}\left|\widehat{\widehat{\mathscr{L}}}^2 - \widehat{\widehat{\mathscr{L}}}^2_z + \widehat{\widehat{\mathscr{S}}}^2 - \widehat{\widehat{\mathscr{S}}}^2_z\right|\Phi^{el}_{\alpha'}\right\rangle\Gamma^{\alpha'}_{JM\Omega} \\
&\qquad\qquad + \sum_{\alpha'}\left\langle \Phi^{el}_{\alpha}\left|\widehat{\mathscr{H}_e} + \widehat{\mathscr{H}_{\mathrm{SO}}}\right|\Phi^{el}_{\alpha'}\right\rangle\Gamma^{\alpha'}_{JM\Omega} \\
&\qquad\qquad - \mathscr{E}(t)\sum_{\alpha'}\sum_{J'}\sum_{M'}\langle JM\Omega|\left\langle \Phi^{el}_{\alpha}\left|\widehat{\widehat{\mathscr{D}}}\cdot\hat{\mathscr{Z}}\right|\Phi^{el}_{\alpha'}\right\rangle|J'M'\Omega'\rangle\Gamma^{\alpha'}_{J'M'\Omega'}
\end{aligned}
\tag{4.18}
$$

Without choosing a basis for the electronic states α's, I cannot pursue the derivation. Lefebvre-Brion and Field [34, §3.2, p. 99] extensively discuss the various Hund's coupling cases, each of them providing a convenient set of quantum numbers to identify the electronic states. Zaharova *et al.* [10] reported Hund's case (a) potentials and spin-orbit coupling functions for NaCs, suggesting to continue the derivation using Hund's case (a) basis, where the appropriate quantum numbers necessary to identify the electronic states are Λ, S, and Σ (defined in Tbl. 3.1)[a]. I can now specify the sum over electronic states $\sum_{\alpha'}$ in the previous equations using the replacement rule

$$
\sum_{\alpha'} \quad \rightarrow \quad \sum_{\Lambda'\geq 0}\sum_{S'\geq 0}\sum_{\Sigma'=-S'}^{+S'}
$$

The general electronic state ket $|\Phi^{\mathrm{el}}_{\alpha}\rangle$ becomes $|\alpha\Lambda S\Sigma\rangle$, where the label α prevents confusion between different electronic states with identical sets of quan-

[a] At very large R values, Hund's case (a) is usually *not* the most appropriate basis to use to represent the electronic states. Which Hund's case is most appropriate for a given situation depends on the range of energies studied, and what physical interactions dominate the system in this range of energies. Using potential energy curves, a given range of energies corresponds to one (or more) range of internuclear separation. In this research, there is no ideal Hund's case. The Hund's case (a) is a convenient stepping stone to do the research.

tum numbers: $|X000\rangle$ characterizes the $X^1\Sigma^+$electronic state, while $|A000\rangle$ characterizes the $A^1\Sigma^+$ state. Also, the electronic hamiltonian $\widehat{\mathscr{H}_e}$ is diagonal in the Hund's case (a) basis and its eigenvalues are the Born-Oppenheimer potential energies

$$\left\langle \alpha\Lambda S\Sigma \left| \widehat{\mathscr{H}_{\text{el}}} + \widehat{\mathscr{V}_{nn}} \right| \alpha\Lambda S\Sigma \right\rangle = V_\alpha^{\text{BO}}(R). \tag{4.19}$$

Furthermore in Hund's case (a) basis, the operator $\widehat{\vec{\mathscr{L}}}^2 - \widehat{\vec{\mathscr{L}}}_z^2 + \widehat{\vec{\mathscr{S}}}^2 - \widehat{\vec{\mathscr{S}}}_z^2$ is diagonal (Lefebvre-Brion and Field [34, §3.1.2.3]) and the R-dependent quantity $\frac{\hbar^2}{2\mu R^2}\left\langle \alpha\Lambda S\Sigma \left| \widehat{\vec{\mathscr{L}}}^2 \right| \alpha\Lambda S\Sigma \right\rangle$ is usually merged with $V_\alpha^{\text{BO}}(R)$ or approximated using the van Vleck pure precession hypothesis (see p. 60).

The next step in the derivation is to determine the matrix element of the electric dipole moment $\langle JM\Omega|\left\langle \alpha\Lambda S\Sigma \left| \widehat{\vec{\mathscr{D}}}\cdot\hat{z} \right| \alpha'\Lambda'S'\Sigma' \right\rangle|J'M'\Omega'\rangle$. Katô [35, p. 3209] derived the general expression to transform the electric dipole moment components in the spherical basis [52, p. 63 and following] from the molecule-fixed coordinates $\{\widehat{\mathscr{D}}_{-1}^{\text{BF}}, \widehat{\mathscr{D}}_0^{\text{BF}}, \widehat{\mathscr{D}}_{+1}^{\text{BF}}\}$ to the laboratory fixed coordinates $\{\widehat{\mathscr{D}}_{-1}^{\text{SF}}, \widehat{\mathscr{D}}_0^{\text{SF}}, \widehat{\mathscr{D}}_{+1}^{\text{SF}}\}$. Again the lasers in this research are linearly polarized along the $\hat{z}$-axis, so I only need the matrix elements of[a] $\widehat{\vec{\mathscr{D}}}\cdot\hat{z} = \widehat{\mathscr{D}}_0^{\text{SF}} = \widehat{\mathscr{D}}_Z$:

$$\begin{aligned}
&\langle JM\Omega|\left\langle \alpha\Lambda S\Sigma \left| \widehat{\mathscr{D}}_Z \right| \alpha'\Lambda'S'\Sigma' \right\rangle|J'M'\Omega'\rangle \\
&\qquad\qquad \equiv \langle JM\Omega|\left\langle \alpha\Lambda S\Sigma \left| \widehat{\mathscr{D}}_0^{\text{SF}} \right| \alpha'\Lambda'S'\Sigma' \right\rangle|J'M'\Omega'\rangle \\
&= \sum_{t=0,\pm1} (-1)^t \left\langle \alpha\Lambda \left| \widehat{\mathscr{D}}_t^{\text{BF}} \right| \alpha'\Lambda' \right\rangle \delta_{SS'}\delta_{\Sigma\Sigma'} \\
&\qquad\qquad \times(-1)^{M'-\Omega'}[(2J+1)(2J'+1)]^{1/2} \begin{pmatrix} J' & J & 1 \\ -M' & M & 0 \end{pmatrix} \begin{pmatrix} J' & J & 1 \\ -\Omega' & \Omega & -i \end{pmatrix}
\end{aligned} \tag{4.20}$$

The only electronic states involved in the problem are the $X^1\Sigma^+$, the $A^1\Sigma^+$, and

[a] In the following equations, t is just a dummy summation index that doe snot represent *any* physical quantity.

the $b^3\Pi$ states. Electric dipole transitions may only occur between states with the same spin multiplicity [35], as the Kronecker delta $\delta_{SS'}$ in Eq. (4.20) shows, so the only possible transitions are $X^1\Sigma^+ \leftrightarrow X^1\Sigma^+$, $X^1\Sigma^+ \leftrightarrow A^1\Sigma^+$, $A^1\Sigma^+ \leftrightarrow A^1\Sigma^+$, and $b^3\Pi \leftrightarrow b^3\Pi$. One necessary condition for $\begin{pmatrix} J' & J & 1 \\ -\Omega' & \Omega & -t \end{pmatrix}$ to differ from 0 is $\Omega - \Omega' - t = 0$. Since $\Omega = \Omega' = 0$ for all electronic states involved, only the $t = 0$ spherical component $\widehat{\mathscr{D}}_0^{\mathrm{BF}} = \widehat{\mathscr{D}}_z$ of the dipole moment has non-zero 3-j symbols prefactors in Eq. (4.20), which reduces it to

$$\begin{aligned}\langle JM0|\left\langle \alpha\Lambda S\Sigma \left|\widehat{\mathscr{D}}_{\mathcal{Z}}\right| \alpha'\Lambda'S'\Sigma'\right\rangle |J'M'0\rangle = (-1)^{M'}\mathscr{D}_{\alpha\alpha'}(R) \\ \times[(2J+1)(2J'+1)]^{1/2}\begin{pmatrix} J' & J & 1 \\ -M' & M & 0 \end{pmatrix}\begin{pmatrix} J' & J & 1 \\ 0 & 0 & 0 \end{pmatrix}\delta_{SS'}\delta_{\Sigma\Sigma'}\end{aligned} \tag{4.21}$$

where $\mathscr{D}_{\alpha\alpha'}(R) = \left\langle \alpha\Lambda \left|\widehat{\mathscr{D}}_z\right| \alpha'\Lambda' \right\rangle$ is the transition dipole moment function, which depends only on the internuclear separation R as all other coordinates have been integrated over.

The Wigner 3-j symbol $\begin{pmatrix} J' & J & 1 \\ -M' & M & 0 \end{pmatrix}$ is non-zero if the selection rules $\Delta J = \pm 1$ and $\Delta M = 0$ are satisfied. Hence the only surviving terms in Eq. (4.21) are

$$\begin{aligned}\langle JM0|\left\langle \alpha\Lambda S\Sigma \left|\widehat{\mathscr{D}}_{\mathcal{Z}}\right| \alpha'\Lambda'S\Sigma\right\rangle |J+1,M0\rangle = (-1)^{M}[(2J+1)(2J+3)]^{1/2}\mathscr{D}_{\alpha\alpha'}(R) \\ \times\begin{pmatrix} J+1 & J & 1 \\ -M & M & 0 \end{pmatrix}\begin{pmatrix} J+1 & J & 1 \\ 0 & 0 & 0 \end{pmatrix}\end{aligned} \tag{4.22a}$$

and

$$\langle JM0|\left\langle \alpha\Lambda S\Sigma \left| \widehat{\mathscr{D}_z} \right| \alpha'\Lambda' S\Sigma \right\rangle |J-1,M0\rangle = (-1)^M[(2J+1)(2J-1)]^{1/2}\mathscr{D}_{\alpha\alpha'}(R) \times \begin{pmatrix} J-1 & J & 1 \\ -M & M & 0 \end{pmatrix}\begin{pmatrix} J-1 & J & 1 \\ 0 & 0 & 0 \end{pmatrix}. \quad (4.22b)$$

Inserting Eqs. (4.22) in Eq. (4.18), remembering that only $\Omega = 0$ is relevant, yields

$$\begin{aligned} &\forall\ J,\ M,\ \alpha \in \{X, A, b\}, \\ &\qquad \mathbf{i}\hbar\frac{\partial}{\partial t}\Gamma^{\alpha}_{JM0} = \left(-\frac{\hbar^2}{2\mu}\frac{\partial^2}{\partial R^2} + \frac{\hbar^2}{2\mu R^2}J(J+1) + V^{\mathrm{BO}}_{\alpha}(R)\right)\Gamma^{\alpha}_{JM0} \\ &\qquad\qquad + \frac{\hbar^2}{2\mu R^2}\left(\left\langle \alpha\Lambda S\Sigma \left| \widehat{\vec{\mathscr{L}}^2} \right| \alpha\Lambda S\Sigma \right\rangle - \Lambda^2 + S(S+1) - \Sigma^2\right)\Gamma^{\alpha}_{JM0} \\ &\qquad\qquad + \sum_{\alpha'}\left\langle \alpha\Lambda S\Sigma \left| \widehat{\mathscr{H}_{\mathrm{SO}}} \right| \alpha'\Lambda' S'\Sigma' \right\rangle \Gamma^{\alpha'}_{JM0} \\ &+(-1)^{M+1}\mathscr{E}(t)\sqrt{2J+1}\sum_{\alpha'}\mathscr{D}_{\alpha\alpha'}(R)\left[\sqrt{2J+3}\begin{pmatrix} J+1 & J & 1 \\ -M & M & 0 \end{pmatrix}\begin{pmatrix} J+1 & J & 1 \\ 0 & 0 & 0 \end{pmatrix}\Gamma^{\alpha'}_{J+1M0}\right. \\ &\qquad\qquad \left. + \sqrt{2J-1}\underbrace{\begin{pmatrix} J-1 & J & 1 \\ -M & M & 0 \end{pmatrix}\begin{pmatrix} J-1 & J & 1 \\ 0 & 0 & 0 \end{pmatrix}}_{\text{only } \neq 0 \text{ if } J\neq 0 \text{ and } M\neq \pm J}\Gamma^{\alpha'}_{J-1M0}\right]. \end{aligned} \quad (4.23)$$

Within the same electronic state, an external electric field might trigger electric-dipole allowed transitions. However, neither the pump nor the Stokes laser are resonant with any transition *within* the $X^1\Sigma^+$, the $A^1\Sigma^+$, or the $b^3\Pi$ state. Thus the interaction of the electric field $\vec{\mathscr{E}}(t)$ with the permanent electric-dipole moments $\mathscr{D}_{XX}$, $\mathscr{D}_{AA}$, and $\mathscr{D}_{bb}$ is negligible compared to the interaction between $\vec{\mathscr{E}}(t)$ and $\mathscr{D}_{AX}$ (Eq. (4.24)). I can discard from Eq. (4.23) all terms that

involve $\mathscr{D}_{XX}$, $\mathscr{D}_{AA}$, or $\mathscr{D}_{bb}$. Let's define for later

$$\mathscr{D}_{AX}(R) \equiv \left\langle A0 \left| \widehat{\mathscr{D}}_z \right| X0 \right\rangle. \tag{4.24}$$

Note that $\mathscr{D}_{XA}(R) = \left\langle X0 \left| \widehat{\mathscr{D}}_z \right| A0 \right\rangle = \mathscr{D}_{AX}(R)$ as the expectation value of $\widehat{\mathscr{D}}_z$ must be a real quantity.

Let's get more specific. As explained in Sec. 4.1.3, the system starts in the $X^1\Sigma^+$ state with $J = M = \Omega = 0$. I drop the subscripts M and Ω, given my remark at the end of Sec. 4.1.3, and I use the equations for the matrix elements of $\widehat{\mathscr{H}}_{\mathrm{SO}}$ given in Sec. 3.2.3

$$\begin{aligned} \mathbf{i}\hbar\frac{\partial}{\partial t}\Gamma_0^{X^1\Sigma^+} = &\left(-\frac{\hbar^2}{2\mu}\frac{\partial^2}{\partial R^2} + \frac{\hbar^2}{2\mu R^2}\times 0 + V^{\mathrm{BO}}_{X^1\Sigma^+}(R)\right)\Gamma_0^{X^1\Sigma^+} \\ &+ \frac{\hbar^2}{2\mu R^2}\left(\left\langle X000 \left| \widehat{\vec{\mathscr{J}}}^2 \right| X000 \right\rangle - 0^2 + 0(0+1) - 0^2\right)\Gamma_0^{X^1\Sigma^+} \\ &- \mathscr{E}(t)\mathscr{D}_{XA}(R)\sqrt{3}\begin{pmatrix} 1 & 0 & 1 \\ 0 & 0 & 0 \end{pmatrix}\begin{pmatrix} 1 & 0 & 1 \\ 0 & 0 & 0 \end{pmatrix}\Gamma_1^{A^1\Sigma^+}. \end{aligned} \tag{4.25a}$$

The van Vleck pure precession hypothesis (see footnote on p. 60) suggests that the expectation value of $\widehat{\vec{\mathscr{J}}}^2$ for the $X^1\Sigma^+$ state is zero. Let's simplify the notation and set:

$$V_X(R) = V^{\mathrm{BO}}_{X^1\Sigma^+}(R) \tag{4.25b}$$

The linearly polarized pump laser takes the system to the $A^1\Sigma^+$ state with

$J = 1$:

$$\begin{aligned}
\mathbf{i}\hbar\frac{\partial}{\partial t}\Gamma_1^{\mathrm{A}^1\Sigma^+} &= \left(-\frac{\hbar^2}{2\mu}\frac{\partial^2}{\partial R^2} + \frac{\hbar^2}{2\mu R^2}\times 2 + V^{\mathrm{BO}}_{\mathrm{A}^1\Sigma^+}(R)\right)\Gamma_1^{\mathrm{A}^1\Sigma^+} \\
&\quad + \frac{\hbar^2}{2\mu R^2}(2 - 0^2 + 0(0+1) - 0^2)\Gamma_1^{\mathrm{A}^1\Sigma^+} \\
&\quad - \sqrt{2}\xi(R)\Gamma_1^{\mathrm{b}^3\Pi} \\
&\quad -\mathscr{E}(t)\mathscr{D}_{AX}(R)\sqrt{3}\left[\sqrt{5}\begin{pmatrix} 2 & 1 & 1 \\ 0 & 0 & 0 \end{pmatrix}^2\Gamma_2^{\mathrm{X}^1\Sigma^+} + \sqrt{1}\begin{pmatrix} 0 & 1 & 1 \\ 0 & 0 & 0 \end{pmatrix}^2\Gamma_0^{\mathrm{X}^1\Sigma^+}\right].
\end{aligned} \tag{4.25c}$$

where I used the van Vleck pure precession hypothesis Eq. (3.14) from Sec. 3.2.2 on p. 58. Remember that the wave functions Γ's are linear combinations of the vibrational wave functions and the stationary scattering wave functions available in the electronic state $|\Phi_\alpha^{\mathrm{el}}\rangle$.

An even permutation of its columns does not modify any Wigner 3-j symbol, and the ones above have values

$$\begin{pmatrix} 2 & 1 & 1 \\ 0 & 0 & 0 \end{pmatrix} = \sqrt{\frac{2}{15}} \quad \text{and} \quad \begin{pmatrix} 0 & 1 & 1 \\ 0 & 0 & 0 \end{pmatrix} = -\frac{1}{\sqrt{3}}.$$

The linearly polarized Stokes pulse brings the system down from the $\mathrm{A}^1\Sigma^+$, $J = 1$ to $\mathrm{X}^1\Sigma^+$ with $J = 0$ or $J = 2$. The reduced radial wave function $\Gamma_0^{\mathrm{X}^1\Sigma^+}$ already describes the time-dependent distribution of probability in $\mathrm{X}^1\Sigma^+$, $J = 0$, while the reduced radial wave function $\Gamma_2^{\mathrm{X}^1\Sigma^+}$, along with the equation below, describes the time-dependent distribution of probability in $\mathrm{X}^1\Sigma^+$, $J = 2$:

$$\begin{aligned}
\mathbf{i}\hbar\frac{\partial}{\partial t}\Gamma_2^{\mathrm{X}^1\Sigma^+} &= \left(-\frac{\hbar^2}{2\mu}\frac{\partial^2}{\partial R^2} + \frac{\hbar^2}{2\mu R^2}\times 6 + V_X(R)\right)\Gamma_2^{\mathrm{X}^1\Sigma^+} \\
&\quad -\mathscr{E}(t)\mathscr{D}_{XA}(R)\sqrt{5}\left[\sqrt{7}\begin{pmatrix} 3 & 2 & 1 \\ 0 & 0 & 0 \end{pmatrix}^2\Gamma_3^{\mathrm{A}^1\Sigma^+} + \sqrt{3}\begin{pmatrix} 1 & 2 & 1 \\ 0 & 0 & 0 \end{pmatrix}^2\Gamma_1^{\mathrm{A}^1\Sigma^+}\right].
\end{aligned} \tag{4.25d}$$

The Stokes laser is tuned to allow transitions from $A^1\Sigma^+$, $J = 1$ back to $X^1\Sigma^+$, $J = 0$. Technically all repopulation processes between the $X^1\Sigma^+$ state and the $A^1\Sigma^+$ state, changing J values by 1 every time, must be included in the set of equations. However, I will notice later that for lasers with a narrow spectral bandwidth (0.5 GHz), *neither* the pump-dump nor the STIRAP process populate $X^1\Sigma^+$, $J = 2$. For lasers with a broader spectral bandwidth (10 GHz) a small amount of repopulation occurs, but mainly back into the excited state. Therefore, I neglect all population recycling processes[a] that would transfer population out of $X^1\Sigma^+$, $J = 2$.

The spin-orbit operator couples the $J = 1$ $b^3\Pi$ state to the $J = 1$ $A^1\Sigma^+$ state as already seen in Eq. (4.25c), and the relevant reduced radial wave function satisfies

$$\begin{aligned} \mathrm{i}\hbar\frac{\partial}{\partial t}\Gamma_1^{b^3\Pi} = &\left(-\frac{\hbar^2}{2\mu}\frac{\partial^2}{\partial R^2} + \frac{\hbar^2}{2\mu R^2}\times 2 + V^{\mathrm{BO}}_{b^3\Pi}(R)\right)\Gamma_1^{b^3\Pi} \\ &+ \frac{\hbar^2}{2\mu R^2}\times 2\,\Gamma_1^{b^3\Pi} - \eta(R)\,\Gamma_1^{b^3\Pi} - \sqrt{2}\xi(R)\,\Gamma_1^{A^1\Sigma^+}. \end{aligned} \tag{4.25e}$$

The $b^3\Pi$ is not dipole-coupled to any other electronic states involved in the problem, as explained earlier, hence the absence of a light-matter interaction term in the previous equation.

To avoid cluttering the equations that follow, I define the shorthands

$$\Gamma_0^{X^1\Sigma^+} = \Gamma_0^X \qquad \Gamma_2^{X^1\Sigma^+} = \Gamma_2^X$$
$$\Gamma_1^{A^1\Sigma^+} = \Gamma_1^A \qquad \Gamma_1^{b^3\Pi} = \Gamma_1^b$$

[a] These processes are physically and mathematically allowed but since no population enters $X^1\Sigma^+$, $J = 2$ *ever*, said processes do not actually occur.

which all depend only on the internuclear separation R and time t, and

$$V^{\mathrm{BO}}_{\mathrm{A}^1\Sigma^+}(R) = V_A(R) \qquad\qquad V^{\mathrm{BO}}_{\mathrm{b}^3\Pi}(R) = V_b(R).$$

Equation (4.26) on p. 90 uses the above shorthands and summarizes Eqs. (4.25) in matrix form.

Equation (4.26) looks like a 4×4 system of *coupled*, *partial*, *differential* equations, which is not a trivial thing to solve. One goal of this research is to study the influence of the spin-orbit coupling on the population transfer process. To make an actual comparison, I need to first study the effect of ignoring spin-orbit coupling on the process, then include the coupling, and examine how the conclusions change.

In Sec. 4.3, I derive the general equations for the probability amplitudes in each rovibrational and stationary scattering states, when the model *ignores* spin-orbit coupling. Section 4.4 achieves the same goal as Sec. 4.3, but the equations I obtain for the same probability amplitudes *account for* spin-orbit coupling. Interestingly, although the physical content of the coefficients in the equations is different, both sets have the same mathematical structure.

4.3 Neglecting spin-orbit

In this section, I neglect altogether the spin-orbit function in Eq. (4.26), then I derive equations for the probability amplitudes a's of Eq. (4.4). Since the $\mathrm{b}^3\Pi$ electronic state is initially unoccupied, and I neglect all couplings to it, the $\mathrm{b}^3\Pi$

$$
i\hbar\frac{\partial}{\partial t}\begin{bmatrix}\Gamma_0^X\\ \Gamma_2^X\\ \Gamma_1^A\\ \Gamma_1^b\end{bmatrix} = \begin{bmatrix} -\frac{\hbar^2}{2\mu}\frac{\partial^2}{\partial R^2} + V_X(R) & 0 & -\frac{\sqrt{3}}{3}\mathscr{E}(t)\mathscr{D}_{AX}(R) & 0 \\ 0 & -\frac{\hbar^2}{2\mu}\left(\frac{\partial^2}{\partial R^2} - \frac{6}{R^2}\right) + V_X(R) & -2\frac{\sqrt{15}}{15}\mathscr{E}(t)\mathscr{D}_{AX}(R) & 0 \\ -\frac{\sqrt{3}}{3}\mathscr{E}(t)\mathscr{D}_{AX}(R) & -2\frac{\sqrt{15}}{15}\mathscr{E}(t)\mathscr{D}_{AX}(R) & -\frac{\hbar^2}{2\mu}\left(\frac{\partial^2}{\partial R^2} - \frac{4}{R^2}\right) + V_A(R) & -\sqrt{2}\xi(R) \\ 0 & 0 & -\sqrt{2}\xi(R) & -\frac{\hbar^2}{2\mu}\left(\frac{\partial^2}{\partial R^2} - \frac{4}{R^2}\right) + V_b(R) - \eta(R) \end{bmatrix}\begin{bmatrix}\Gamma_0^X\\ \Gamma_2^X\\ \Gamma_1^A\\ \Gamma_1^b\end{bmatrix} \tag{4.26}
$$

state becomes irrelevant to the dynamics, and Eq. (4.26) reduces to:

$$\mathrm{i}\hbar\frac{\partial}{\partial t}\begin{bmatrix}\Gamma_0^X\\ \Gamma_2^X\\ \Gamma_1^A\end{bmatrix}=\begin{bmatrix}-\frac{\hbar^2}{2\mu}\frac{\partial^2}{\partial R^2}+V_X(R) & 0 & -\frac{\sqrt{3}}{3}\mathscr{E}(t)\mathscr{D}_{AX}(R)\\ 0 & -\frac{\hbar^2}{2\mu}\left(\frac{\partial^2}{\partial R^2}-\frac{6}{R^2}\right)+V_X(R) & -2\frac{\sqrt{15}}{15}\mathscr{E}(t)\mathscr{D}_{AX}(R)\\ -\frac{\sqrt{3}}{3}\mathscr{E}(t)\mathscr{D}_{AX}(R) & -2\frac{\sqrt{15}}{15}\mathscr{E}(t)\mathscr{D}_{AX}(R) & -\frac{\hbar^2}{2\mu}\left(\frac{\partial^2}{\partial R^2}-\frac{4}{R^2}\right)+V_A(R)\end{bmatrix}\begin{bmatrix}\Gamma_0^X\\ \Gamma_2^X\\ \Gamma_1^A\end{bmatrix}. \tag{4.27}$$

The reduced radial wave functions Γ's may be expanded over the basis of vibrational wave functions of the corresponding electronic state[a]

$$\Gamma_0^X(R,t)=\sum_{v_X=0}^{N_{X0}-1}a_{v_X}^{X0}(t)\langle R|X,0,v_X\rangle+\int_0^{+\infty}a_E^{X0}(t)\langle R|\chi_E^{X0}\rangle\,\mathrm{d}E, \tag{4.28a}$$

$$\Gamma_2^X(R,t)=\sum_{v_X=0}^{N_{X2}-1}a_{v_X}^{X2}(t)\langle R|X,2,v_X\rangle, \tag{4.28b}$$

$$\Gamma_1^A(R,t)=\sum_{v_A=0}^{N_{A1}-1}a_{v_A}^{A1}(t)\langle R|A,1,v_A\rangle. \tag{4.28c}$$

where $N_{\alpha J}$ is the number of vibrational states in electronic state α with rotational quantum number J. Also, the vibrational wave function $\langle R|\alpha,J,v_\alpha\rangle$ has vibrational energy $E_{v_\alpha}^{\alpha J}$.

No laser in the problem is tuned to such a frequency that the continuum of the $\mathrm{A}^1\Sigma^+$ state or the $\mathrm{X}^1\Sigma^+$ $J=2$ state might be populated, whence the absence of an integral over energies in Eqs. (4.28b & 4.28c).

To facilitate the derivation—and later the solution—of equations for the probability amplitudes, let's discretize the integral over continuum energies in Eq. (4.28a). First, I shall limit the range of integration from 0 to ε, since this range covers 99.95% of the continuum states accessible to the system at $T=200\mu K$ (see p. 55). Next, I consider the most general discretization—or quadrature—possible, *i.e.* the range of continuum energies needs not be evenly

[a] Remember: M and Ω are not specified because they remain zero throughout the process.

divided, and the discretization consists in the replacement

$$\int_0^{+\infty} a_E^{X0}(t)\langle R|\chi_E^{X0}\rangle \,\mathrm{d}E \quad \rightarrow \quad \sum_{i=1}^{N_E} a_{E_i}^{X0}(t)\langle R|\chi_{E_i}^{X0}\rangle \Delta E_i, \tag{4.29}$$

where the i-th interval of energy as width ΔE_i, and there are N_E such intervals. A little caveat: the *continuum* stationary scattering kets $|\chi_E^{X0}\rangle$ are mutually orthogonal in the *Dirac* sense[a]

$$\langle \chi_E^{X0}|\chi_{E'}^{X0}\rangle = \delta(E-E'), \tag{4.30}$$

whereas the *discretized* stationary scattering kets $|\chi_{E_i}^{X0}\rangle$ are mutually orthogonal in the *Kronecker* sense

$$\langle \chi_{E_i}^{X0}|\chi_{E_j}^{X0}\rangle = \delta_{E_iE_j}. \tag{4.31}$$

I should remind the reader that in the transition dipole moment matrix elements (TDMMEs) $\langle \ldots|\mathscr{D}_{AX}|\ldots\rangle$ that appear below, the brackets $\langle ...\rangle$ represent an integration over the internuclear separation R, and all TDMMEs are real numbers.

Let's substitute the expansions Eq. (4.28a) and Eq. (4.28c) in the first row of Eq. (4.27), multiply on the left by $\langle X, 0, v_X|R\rangle$, integrate from $R = 0$ to $R = +\infty$, and use orthonormalization of the wave functions. Then the probability amplitudes of the vibrational bound states of the $X^1\Sigma^+$ state, $J = 0$, are such

[a] In photoassociation processes, stationary scattering wave functions must be energy normalized. Thus, the energy density of states is automatically accounted for in the wave function when taking matrix elements of the light-matter interaction term [70, p. 224], and so the probability of free-bound transition per unit time, obtained by Fermi's Golden Rule, has the appropriate dimension (see [71, p. S1022], Friedrich [72, Eq. (2.137) p. 122])

that[a]

$$\forall v_X \in [\![0, N_{X0} - 1]\!],$$
$$\mathbf{i}\hbar \frac{\mathrm{d}}{\mathrm{d}t} a_{v_X}^{X0}(t) = E_{v_X}^{X0} a_{v_X}^{X0} - \sum_{v_A=0}^{N_{A1}-1} \frac{\sqrt{3}}{3} \mathscr{E}(t) \langle X, 0, v_X \,|\, \mathscr{D}_{AX} \,|\, A, 1, v_A \rangle a_{v_A}^{A1}(t), \tag{4.32}$$

and for the discrete scattering states

$$\forall j \in [\![1, N_E]\!],$$
$$\mathbf{i}\hbar \frac{\mathrm{d}}{\mathrm{d}t} a_{E_j}^{X0}(t) = E_j^{X0} a_{E_j}^{X0} - \sum_{v_A=0}^{N_{A1}-1} \frac{\sqrt{3}}{3} \mathscr{E}(t) \left\langle \chi_{E_j}^{X0} \,|\, \mathscr{D}_{AX} \,|\, A, 1, v_A \right\rangle a_{v_A}^{A1}(t) \tag{4.33}$$

Given the expansion Eq. (4.28a), the quantity $|a_E^{X0}(t)|^2 \,\mathrm{d}E$ is the probability density to find the system in the continuum of the $\mathrm{X}^1\Sigma^+$ state with scattering energy between E and $E + \mathrm{d}E$. However, the quantity $|a_{E_j}^{X0}\sqrt{\Delta E_j}|^2$ is the probability to find the system in the stationary scattering state with wave function $\langle R | \chi_{E_j}^{X0} \rangle$. For convenience, I define

$$\forall j \in [\![1, N_E]\!], \qquad \alpha_{E_j}^{X0} \equiv a_{E_j}^{X0} \sqrt{\Delta E_j}. \tag{4.34}$$

After multiplying Eq. (4.33) by $\sqrt{\Delta E_j}$, I obtain

$$\forall j \in [\![1, N_E]\!],$$
$$\mathbf{i}\hbar \frac{\mathrm{d}}{\mathrm{d}t} \alpha_{E_j}^{X0}(t) = E_j^{X0} \alpha_{E_j}^{X0} - \sum_{v_A=0}^{N_{A1}-1} \frac{\sqrt{3}}{3} \mathscr{E}(t) \sqrt{\Delta E_j} \left\langle \chi_{E_j}^{X0} \,|\, \mathscr{D}_{AX} \,|\, A, 1, v_A \right\rangle a_{v_A}^{A1}(t). \tag{4.35}$$

The probability amplitudes of the rovibrational states of the $\mathrm{X}^1\Sigma^+$ state,

[a] As usual, $\forall v \in [\![a, b]\!]$ means that v can be any *integer* between a and b with $(a, b) \in \mathbb{R}^2$.

$J = 2$, satisfy

$$\begin{aligned}
&\forall v_X \in [\![0, N_{X2} - 1]\!], \\
&\mathrm{i}\hbar \frac{\mathrm{d}}{\mathrm{d}t} a_{v_X}^{X2}(t) = E_{v_X}^{X2} a_{v_X}^{X2} - \sum_{v_A=0}^{N_{A1}-1} 2\frac{\sqrt{15}}{15} \mathscr{E}(t) \langle X, 2, v_X \,|\mathscr{D}_{AX}|\, A, 1, v_A \rangle a_{v_A}^{A1}(t).
\end{aligned} \tag{4.36}$$

The last set of equations, for the probability amplitudes of the rovibrational states of the $\mathrm{A}^1\Sigma^+$ state, originates from the last row in Eq. (4.27) when using the expansions of Eq. (4.28):

$$\begin{aligned}
&\forall v_A \in [\![0, N_{A1} - 1]\!], \\
&\mathrm{i}\hbar \frac{\mathrm{d}}{\mathrm{d}t} a_{v_A}^{A1}(t) = E_{v_A}^{A1} a_{v_A}^{A1} - \sum_{v_X=0}^{N_{X2}-1} 2\frac{\sqrt{15}}{15} \mathscr{E}(t) \langle A, 1, v_A \,|\mathscr{D}_{AX}|\, X, 2, v_X \rangle a_{v_X}^{X2}(t) \\
&\qquad\qquad - \sum_{v_X=0}^{N_{X0}-1} \frac{\sqrt{3}}{3} \mathscr{E}(t) \langle A, 1, v_A \,|\mathscr{D}_{AX}|\, X, 0, v_X \rangle a_{v_X}^{X0}(t) \\
&\qquad\qquad - \sum_{j=1}^{N_E} \frac{\sqrt{3}}{3} \mathscr{E}(t) \left\langle A, 1, v_A \,|\mathscr{D}_{AX}|\, \chi_{E_j}^{X0} \right\rangle \sqrt{\Delta E_j} \alpha_{E_j}^{X0}(t).
\end{aligned} \tag{4.37}$$

Equation (4.39) on p. 95 collects Eqs. (4.32), (4.35), (4.36), and (4.37) in matrix form. All diagonal blocks in Eq. (4.39) are themselves diagonal, while all off-diagonal blocks are not diagonal. To avoid cluttering the matrix, I specify only the generic term in each block, and I also define the shorthands

$$\begin{aligned}
{}^{A1}_{v_A}\mathscr{D}^{X0}_{v_X} &= -\langle A, 1, v_A \,|\mathscr{D}_{AX}|\, X, 0, v_X \rangle = -\langle X, 0, v_X \,|\mathscr{D}_{XA}|\, A, 1, v_A \rangle, && \text{(4.38a)} \\
{}^{A1}_{v_A}\mathscr{D}^{X2}_{v_X} &= -\langle A, 1, v_A \,|\mathscr{D}_{AX}|\, X, 2, v_X \rangle = -\langle X, 2, v_X \,|\mathscr{D}_{XA}|\, A, 1, v_A \rangle, && \text{(4.38b)} \\
{}^{A1}_{v_A}\mathscr{D}^{X0}_{E_j} &= -\left\langle A, 1, v_A \,|\mathscr{D}_{AX}|\, \chi_{E_j}^{X0} \right\rangle \sqrt{\Delta E_j} = -\left\langle \chi_{E_j}^{X0} \,|\mathscr{D}_{XA}|\, A, 1, v_A \right\rangle \sqrt{\Delta E_j}. && \text{(4.38c)}
\end{aligned}$$

To prepare the application of the Rotating Wave Approximation (Sec. 2.3.1.2,

$$
\begin{array}{c|c|c|

p. 21), let's perform a unitary transformation by defining new probability amplitudes c's such that:

$$c^{X0}_{E_j}(t)\mathbf{e}^{-\mathbf{i}\zeta_E(t)} = \alpha^{X0}_{E_j}(t), \qquad c^{A1}_{v_A}(t)\mathbf{e}^{-\mathbf{i}\zeta_A(t)} = a^{A1}_{v_A}(t), \tag{4.40a}$$

$$c^{X0}_{v_X}(t)\mathbf{e}^{-\mathbf{i}\zeta_X(t)} = a^{X0}_{v_X}(t), \qquad c^{X2}_{v_X}(t)\mathbf{e}^{-\mathbf{i}\zeta_X(t)} = a^{X2}_{v_X}(t), \tag{4.40b}$$

where the phases ζ are defined in terms of an *arbitrary* energy E_0 and the chirped frequencies of the pump (P) and Stokes (S) lasers

$$\zeta_E(t) = \frac{E_0 t}{\hbar}, \quad \zeta_X(t) = \frac{E_0 t}{\hbar} + (\omega_P(t) - \omega_S(t))t, \quad \zeta_A(t) = \frac{E_0 t}{\hbar} + \omega_P(t)t. \tag{4.41}$$

The laser frequencies are time-dependent since the lasers in this study are ultimately chirped. To keep the derivation as generic as possible I do *not yet* specify a particular way of chirping. The quantity E_0 serves to simplify the matrix obtained at the end of the derivation. For example when using only one state in the discretization of the continuum, one should choose E_0 as the most probable continuum energy according to the appropriate statistical distribution, here Maxwell-Boltzmann (see Sec. 3.1 and Fig. 3.2 p. 55 therein).

After performing the unitary transformation defined above, the new probability amplitudes c's satisfy Eq. (4.42) on page 97. In order for the matrix to fit in the page, I defined

$$\omega(t) = \omega_P(t) + \dot{\omega}_P(t)t - \omega_S(t) - \dot{\omega}_S(t)t, \tag{4.43}$$

where $\dot{\omega}$ denotes first-order differentiation of ω with respect to time. As for Eq. (4.39), I specified only the generic term in each block of Eq. (4.42). Note

$$
\begin{array}{c}
\\
\\
\\

that *non-chirped* lasers have time-independent frequencies

$$\omega_P(t) = \omega_P \qquad \text{and} \qquad \omega_S(t) = \omega_S, \tag{4.44}$$

consequently $\dot{\omega}_P(t) = \dot{\omega}_S(t) = 0$, making non-chirped lasers a limiting case of chirped lasers. As long as the time derivative of the laser frequency ($\dot{\omega}_P(t)$ or $\dot{\omega}_S(t)$ above) remains unspecified, so is the type of chirping. Thus Eq. (4.42) is valid for *any* chirped laser fields, in particular non-chirped lasers and linearly chirped lasers. Also Eq. (4.42) is valid for both continuous-wave and pulsed lasers (see below).

I summarized in Sec. 2.3.1.2, p. 21 the **Rotating Wave Approximation** (RWA), which allows one to neglect highly oscillatory terms from the equations for the probability amplitudes. First remember (Sec. 2.1.3, p. 13) that each laser pulse has an electric field

$$\mathscr{E}_P(t) = \mathscr{E}_0^P(t)\cos(\omega_P(t)t) = \frac{\mathscr{E}_0^P(t)}{2}\left(\mathbf{e}^{+\mathbf{i}\,\omega_P(t)t} + \mathbf{e}^{-\mathbf{i}\,\omega_P(t)t}\right) \tag{4.45a}$$

$$\mathscr{E}_S(t) = \mathscr{E}_0^S(t)\cos(\omega_S(t)t) = \frac{\mathscr{E}_0^S(t)}{2}\left(\mathbf{e}^{+\mathbf{i}\,\omega_S(t)t} + \mathbf{e}^{-\mathbf{i}\,\omega_S(t)t}\right) \tag{4.45b}$$

Note that if the field envelope $\mathscr{E}_0^P(t)$ or $\mathscr{E}_0^S(t)$ is made time-independent, the corresponding laser is a continuous wave (chirped, as the time-dependence of the corresponding ω is not necessarily removed) laser. The total electric field $\mathscr{E}(t)$ that appears in all equations so far, is the sum of each laser field. Let's pick an example, and fully expand

$$\begin{aligned}\mathscr{E}(t)\mathbf{e}^{+\mathbf{i}\,\omega_P(t)t} &= \left[\frac{\mathscr{E}_0^P(t)}{2}\left(\mathbf{e}^{+\mathbf{i}\,\omega_P(t)t} + \mathbf{e}^{-\mathbf{i}\,\omega_P(t)t}\right) + \frac{\mathscr{E}_0^S(t)}{2}\left(\mathbf{e}^{+\mathbf{i}\,\omega_S(t)t} + \mathbf{e}^{-\mathbf{i}\,\omega_S(t)t}\right)\right]\mathbf{e}^{+\mathbf{i}\,\omega_P(t)t} \\ &= \frac{\mathscr{E}_0^P(t)}{2}\left(\mathbf{e}^{+2\mathbf{i}\,\omega_P(t)t} + 1\right) + \frac{\mathscr{E}_0^S(t)}{2}\left(\mathbf{e}^{+\mathbf{i}\,(\omega_S(t)+\omega_P(t))t} + \mathbf{e}^{-\mathbf{i}\,(\omega_S(t)-\omega_P(t))t}\right).\end{aligned} \tag{4.46}$$

The idea of the RWA is that all oscillatory terms in Eq. (4.46), when averaged over the many optical cycles that the process lasts, are negligible compared to the slowly varying term $\mathscr{E}_0^P(t)/2$. Thus the RWA consists in applying the following replacement rule in Eq. (4.42):

$$\mathscr{E}(t)\mathbf{e}^{\pm\mathbf{i}\,\omega_P(t)t} \to \frac{\mathscr{E}_0^P(t)}{2} \tag{4.47}$$

$$\mathscr{E}(t)\mathbf{e}^{\pm\mathbf{i}\,\omega_S(t)t} \to \frac{\mathscr{E}_0^S(t)}{2} \tag{4.48}$$

Now that I have eliminated the complex exponential factors from Eq. (4.42), I can specify *how* the lasers are chirped. In this research, the lasers are *linearly* chirped[a], *i.e.* their instantaneous frequency is

$$\omega_P(t) = \omega_0^P + \mathscr{Y}_P t \qquad \omega_S(t) = \omega_0^S + \mathscr{Y}_S t, \tag{4.49}$$

where $\mathscr{Y}_P$ (*resp.*$\mathscr{Y}_S$) is the chirp rate for the pump (*resp.* Stokes) pulse, and ω_0^P (*resp.* ω_0^S) is the initial value of the pump (*resp.* Stokes) pulse frequency. If the lasers were non-chirped, then $\mathscr{Y}_P$ and $\mathscr{Y}_S$ would be zero. The time-independent pieces of the diagonal terms in Eq. (4.42) correspond to laser frequency detunings from corresponding resonance. To emphasize these detunings in the final set of equations—the one I made my goal to obtain in this section—let's first pick a vibrational index v_{ref} of a given rovibrational state in the $A^1\Sigma^+$ state, and define the following detunings

$$\Delta_{v_A}^P = \frac{E_{v_A}^{A1} - E_0}{\hbar} - \omega_0^P, \qquad \Delta_j = \frac{E_j - E_0}{\hbar}, \tag{4.50}$$

$$J = 0,\ 2, \quad \Delta_{v_X,J}^S = \frac{E_{v_{\text{ref}}}^{A1} - E_{v_X}^{XJ}}{\hbar} - \omega_0^S, \qquad \Delta_{v_{\text{ref}}}^P = \frac{E_{v_{\text{ref}}}^{A1} - E_0}{\hbar} - \omega_0^P \tag{4.51}$$

[a] This is the simplest type of chirping. A more complicated chirp can be approximated a linear chirp through a Taylor expansion.

Equation (4.52) on page 101 implements the RWA and the above detunings into Eq. (4.42). This last set of equations is the final piece of this section, and shows that laser detunings and chirp rates couple diagonal terms, while the lasers' amplitude envelope couple vibrational states belonging to different electronic states. It is trivial to recover the time-dependent matrix $\mathsf{H}(t)$ of Eq. (2) in Bergmann *et al*. [16] from the generic expression Eq. (4.52) on p. 101, in particular by setting the chirp rates $\mathcal{Y}_P$ and $\mathcal{Y}_S$ to zero, as the lasers in [16] are non-chirped.

Analysing the TDMMEs ${}^{A1}_{v_A}\mathscr{D}^{X0}_{E_j}$, ${}^{A1}_{v_A}\mathscr{D}^{X0}_{v_X}$, and ${}^{A1}_{v_A}\mathscr{D}^{X2}_{v_X}$ can reduce drastically the number of rovibrational states to involve in the problem. Indeed, too small TDMMEs are detrimental to population transfer, unless the corresponding laser pulse is sufficiently intense to compensate for the TDMME and yield an acceptable Rabi frequency. In chapter 6, I will show such analysis.

Section 4.5 will present the method to solve Eq. (4.52). However, the inclusion of the spin-orbit effect gives a set of equations for probability amplitudes with the same structure as Eq. (4.52), as the next section will show.

4.4 Including spin-orbit

4.4.1 The necessity to solve a coupled-channels problem

Because of the spin-orbit coupling between the $A^1\Sigma^+$ state and the $b^3\Pi$ state, it is no longer valid to decide which rovibrational states to include based on examination of the TDMME between the $X^1\Sigma^+$ state and the $A^1\Sigma^+$ state. What follows exposes the necessary preliminary steps that lead to the relevant quantities to analyse in order to pick the proper vibrational state(s) in the $A^1\Sigma^+ - b^3\Pi$ manifold.

$$
\mathbf{i}\,\frac{\mathrm{d}}{\mathrm{d}t}
\begin{array}{|c|}\hline \vdots \\ c_{E_j}^{X0} \\ \vdots \\ \hline \vdots \\ c_{v_X}^{X0} \\ \vdots \\ \hline \vdots \\ c_{v_X}^{X2} \\ \vdots \\ \hline \vdots \\ c_{v_A}^{A1} \\ \vdots \\ \hline \end{array}
=
\begin{array}{|c|c|c|c|c|}\hline
 & \text{col. } j & v_X,\, J{=}0 & v_X,\, J{=}2 & v_A,\, J{=}1 \\ \hline
1 & \begin{bmatrix} \Delta_1 & & & \\ & \ddots & & \\ & & \Delta_j & \\ & & & \ddots \\ & & & & \Delta_{N_E} \end{bmatrix} & 0 & 0 & \vdots \\
\vdots & & & & c_{E_j}^{X0} \\
j & & & & \vdots \\ \hline
\vdots & & & & \vdots \\
N_E & & & & \\ \hline
0 & & & & \vdots \\
\vdots & & & & c_{v_X}^{X0} \\
v_X & 0 & \begin{matrix} \ddots & \\ \Delta^P_{v_{\mathrm{ref}}} - \Delta^S_{v_X,0} - 2(\mathfrak{P}_P - \mathfrak{P}_S)t & \\ & \ddots \end{matrix} & 0 & \vdots \\
\vdots & & & & \\ \hline
N_{X0}{-}1 & & & & \vdots \\
v_X{=}0 & & & & c_{v_X}^{X2} \\
\vdots & & & & \vdots \\
v_X & 0 & 0 & \begin{matrix} \ddots & \\ \Delta^P_{v_{\mathrm{ref}}} - \Delta^S_{v_X,2} - 2(\mathfrak{P}_P - \mathfrak{P}_S)t & \\ & \ddots \end{matrix} & \vdots \\
\vdots & & & & \\ \hline
N_{X2}{-}1 & & & & \vdots \\
0 & & & & c_{v_A}^{A1} \\
\vdots & & & & \vdots \\
v_A & \mathscr{A}^{A1}_{v_A}\mathscr{D}^{X0}_{E_j}\frac{\sqrt{3}}{3}\frac{\mathscr{E}_0^P(t)}{2\hbar} & \mathscr{A}^{A1}_{v_A}\mathscr{D}^{X0}_{v_X}\frac{\sqrt{3}}{3}\frac{\mathscr{E}_0^S(t)}{2\hbar} & \mathscr{A}^{A1}_{v_A}\mathscr{D}^{X2}_{v_X}2\frac{\sqrt{15}}{15}\frac{\mathscr{E}_0^S(t)}{2\hbar} & \begin{matrix} \ddots & \\ \Delta^P_{v_A} - 2\mathfrak{P}_P\, t & \\ & \ddots \end{matrix} \\
\vdots & & & & \\
N_{A1}{-}1 & & & & \\ \hline
\end{array}
\tag{4.52}
$$

First let's remember the 4×4 matrix of Eq. (4.26)

$$\begin{bmatrix} -\frac{\hbar^2}{2\mu}\frac{\partial^2}{\partial R^2}+V_X(R) & 0 & -\frac{\sqrt{3}}{3}\mathscr{E}(t)\mathscr{D}_{AX}(R) & 0 \\ 0 & -\frac{\hbar^2}{2\mu}\left(\frac{\partial^2}{\partial R^2}-\frac{6}{R^2}\right)+V_X(R) & -2\frac{\sqrt{15}}{15}\mathscr{E}(t)\mathscr{D}_{AX}(R) & 0 \\ -\frac{\sqrt{3}}{3}\mathscr{E}(t)\mathscr{D}_{AX}(R) & -2\frac{\sqrt{15}}{15}\mathscr{E}(t)\mathscr{D}_{AX}(R) & -\frac{\hbar^2}{2\mu}\left(\frac{\partial^2}{\partial R^2}-\frac{4}{R^2}\right)+V_A(R) & -\sqrt{2}\xi(R) \\ 0 & 0 & -\sqrt{2}\xi(R) & -\frac{\hbar^2}{2\mu}\left(\frac{\partial^2}{\partial R^2}-\frac{4}{R^2}\right)+V_b(R)-\eta(R) \end{bmatrix} \tag{4.53}$$

I can split the 4×4 matrix of (4.53) in 4 terms: the nuclear kinetic energy $\mathbf{T}$, the rotational energy $\mathbf{R}$, the electric dipole $\mathbf{D}$, and the electronic and spin-orbit term $\mathbf{H}^{\rm el}$. In the Hund's case (a) basis $\mathcal{A}$ defined by the 4 kets $\{|X^1\Sigma^+,J=0\rangle$, $|X^1\Sigma^+,2\rangle$, $|A^1\Sigma^+,1\rangle$, $|b^3\Pi,1\rangle\}$, these matrices are:

$$\mathbf{T}_{\mathcal{A}}=-\frac{\hbar^2}{2\mu}\begin{bmatrix} \frac{\partial^2}{\partial R^2} & 0 & 0 & 0 \\ 0 & \frac{\partial^2}{\partial R^2} & 0 & 0 \\ 0 & 0 & \frac{\partial^2}{\partial R^2} & 0 \\ 0 & 0 & 0 & \frac{\partial^2}{\partial R^2} \end{bmatrix}_{\mathcal{A}} \qquad \mathbf{R}_{\mathcal{A}}=-\frac{\hbar^2}{2\mu}\begin{bmatrix} 0 & 0 & 0 & 0 \\ 0 & -\frac{6}{R^2} & 0 & 0 \\ 0 & 0 & -\frac{4}{R^2} & 0 \\ 0 & 0 & 0 & -\frac{4}{R^2} \end{bmatrix}_{\mathcal{A}} \tag{4.54a}$$

$$\mathbf{D}_{\mathcal{A}}=\begin{bmatrix} 0 & 0 & \mathscr{D}_{AX}(R)\frac{\sqrt{3}}{3} & 0 \\ 0 & 0 & \mathscr{D}_{AX}(R)2\frac{\sqrt{15}}{15} & 0 \\ \mathscr{D}_{AX}(R)\frac{\sqrt{3}}{3} & \mathscr{D}_{AX}(R)2\frac{\sqrt{15}}{15} & 0 & 0 \\ 0 & 0 & 0 & 0 \end{bmatrix}_{\mathcal{A}} \tag{4.54b}$$

$$\mathbf{H}^{\rm el}_{\mathcal{A}}=\begin{bmatrix} V_X^{BO}(R) & 0 & 0 & 0 \\ 0 & V_X^{BO}(R) & 0 & 0 \\ 0 & 0 & V_A^{BO}(R) & -\sqrt{2}\xi(R) \\ 0 & 0 & -\sqrt{2}\xi(R) & V_b^{BO}(R)-\eta(R) \end{bmatrix}_{\mathcal{A}} \tag{4.54c}$$

Diagonalizing $\mathbf{H}^{\text{el}}$ provides a new hybrid[a] basis $\mathcal{H}$. Expressing the eigenvectors of $\mathbf{H}^{\text{el}}$ in the basis $\mathcal{A}$ gives the passage matrix $\mathbf{U}$ from $\mathcal{H}$ to $\mathcal{A}$.

The eigenvalues of $\mathbf{H}^{\text{el}}$ are

$$V_X^{BO}(R), \qquad \text{(doubly degenerate)} \tag{4.55a}$$

$$V_{1/2}(R) = \frac{1}{2}\left(V_A + V_{b0} - \sqrt{(V_A - V_{b0})^2 + 8\xi^2}\right), \tag{4.55b}$$

$$V_{3/2}(R) = \frac{1}{2}\left(V_A + V_{b0} + \sqrt{(V_A - V_{b0})^2 + 8\xi^2}\right), \tag{4.55c}$$

where all quantities are R-dependent, $V_A = V_A^{BO}$, and $V_{b0} = V_b^{BO}(R) - \eta(R)$ to simplify the notation. With the origin of the energy scale[b] at the asymptote of the $X^1\Sigma^+$ state potential energy curve, the asymptotic value of the $V_{1/2}(R)$ PEC corresponds to the transition energy of the cesium atom from the ground atomic state $6^2S_{1/2}$ to the first excited fine-structure state $6^2P_{1/2}$. Similarly, the asymptotic value of the $V_{3/2}(R)$ PEC corresponds to the transition energy of the cesium atom from the ground atomic state $6^2S_{1/2}$ to the second excited fine-structure state $6^2P_{3/2}$. Thus the asymptotic separation between the two PEC $\lim_{R\to+\infty} V_{3/2}(R) - V_{1/2}(R)$ corresponds to the 6^2P fine-structure splitting of the cesium atom.

The passage matrix $\mathbf{U}$ from $\mathcal{H}$ to $\mathcal{A}$ is

$$\mathbf{U} = \begin{array}{c} \\ \langle X^1\Sigma^+, 0| \\ \langle X^1\Sigma^+, 2| \\ \langle A^1\Sigma^+, 1| \\ \langle b^3\Pi_0, 1| \end{array} \begin{array}{c} \begin{array}{cccc} |X^1\Sigma^+, 0\rangle & |X^1\Sigma^+, 2\rangle & |V_{1/2}, 1\rangle & |V_{3/2}, 1\rangle \end{array} \\ \begin{bmatrix} 1 & 0 & 0 & 0 \\ 0 & 1 & 0 & 0 \\ 0 & 0 & \cos\gamma & -\sin\gamma \\ 0 & 0 & \sin\gamma & \cos\gamma \end{bmatrix}_{\mathcal{H}\to\mathcal{A}} \end{array} \tag{4.56}$$

[a] This basis is *hybrid* because it does not correspond to any pure Hund's case, neither is it diabatic or adiabatic since $\widetilde{\mathcal{F}_n}$ is almost diagonal in $\mathcal{H}$ for some ranges of R and definitely non-diagonal in other ranges.

[b] The zero of energy.

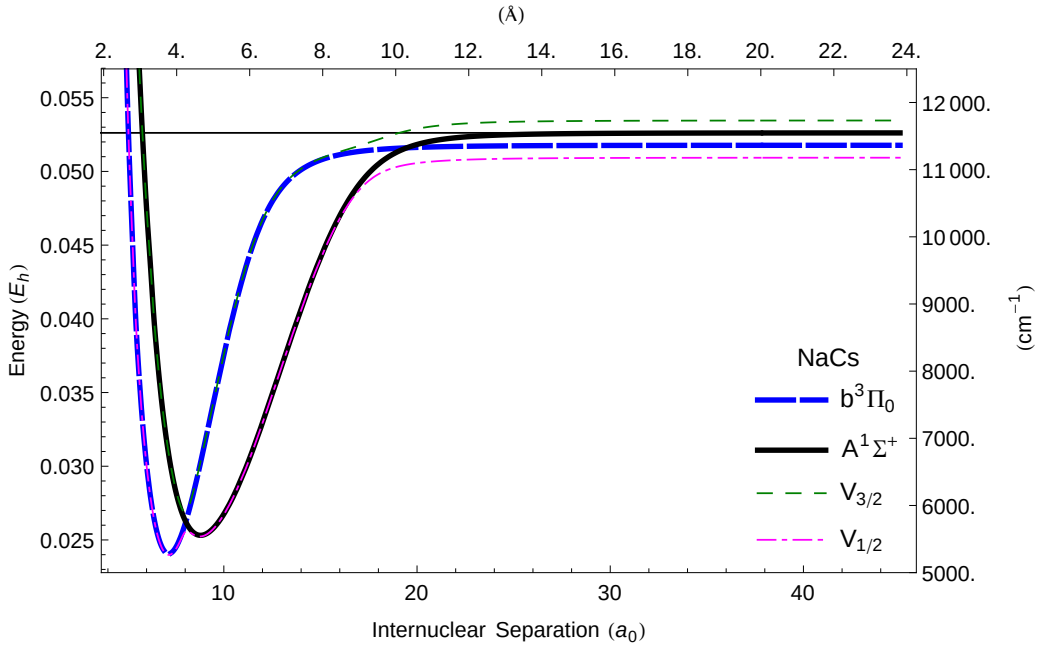

Figure 4.2: NaCs Hund's case (a) potential energy curves (PECs) for the $b^3\Pi$ and $A^1\Sigma^+$ state, coupled by spin-orbit interactions to yield hybrid PECs $V_{1/2}$ and $V_{3/2}$. Note the double-well of the $V_{1/2}$ curve with a local maximum around 4.25 Å, and the smooth step of the $V_{3/2}$ adiabatic curve for internuclear separations around 9.27 Å. The PECs are drawn using potential models constructed at the University of Oklahoma in 2012.

where the mixing angle γ is defined by the trigonometric functions

$$\cos\gamma = \frac{\sqrt{2}\xi(R)}{(2\xi^2(R)+(V_A-V_{1/2})^2)^{1/2}} \qquad \sin\gamma = \frac{(V_A-V_{1/2})}{(2\xi^2(R)+(V_A-V_{1/2})^2)^{1/2}} \tag{4.57}$$

A similar situation and set of definitions appears in Londoño *et al.* [73].

Rotational matrix in the hybrid basis The particular shape of the matrices $\mathbf{U}$ and $\mathbf{R}_\mathcal{A}$ renders the transformation of $\mathbf{R}_\mathcal{A}$ into the hybrid basis $\mathcal{H}$ rather trivial:

$$\mathbf{R}_\mathcal{H} = \mathbf{U}^{-1}\mathbf{R}_\mathcal{A}\mathbf{U} = \mathbf{U}^\dagger\mathbf{R}_\mathcal{A}\mathbf{U} = -\frac{\hbar^2}{2\mu}\begin{bmatrix} 0 & 0 & 0 & 0 \\ 0 & -\frac{6}{R^2} & 0 & 0 \\ 0 & 0 & -\frac{4}{R^2} & 0 \\ 0 & 0 & 0 & -\frac{4}{R^2} \end{bmatrix}_\mathcal{H} = \mathbf{R}_\mathcal{A}. \tag{4.58}$$

The electric dipole matrix in the hybrid basis The transformation of the dipole matrix from basis $\mathcal{A}$ to basis $\mathcal{H}$ gives

$$\mathbf{D}_{\mathcal{H}} = \mathbf{U}^{-1}\mathbf{D}_{\mathcal{A}}\mathbf{U} = \mathbf{U}^{\dagger}\mathbf{D}_{\mathcal{A}}\mathbf{U} \tag{4.59}$$

$$\mathbf{D}_{\mathcal{H}} = \begin{bmatrix} 0 & 0 & -\frac{\sqrt{3}}{3}\mathscr{D}_{AX}\cos\gamma & \frac{\sqrt{3}}{3}\mathscr{D}_{AX}\sin\gamma \\ 0 & 0 & -2\frac{\sqrt{15}}{15}\mathscr{D}_{AX}\cos\gamma & -2\frac{\sqrt{15}}{15}\mathscr{D}_{AX}\sin\gamma \\ -\frac{\sqrt{3}}{3}\mathscr{D}_{AX}\cos\gamma & -2\frac{\sqrt{15}}{15}\mathscr{D}_{AX}\cos\gamma & 0 & 0 \\ \frac{\sqrt{3}}{3}\mathscr{D}_{AX}\sin\gamma & 2\frac{\sqrt{15}}{15}\mathscr{D}_{AX}\sin\gamma & 0 & 0 \end{bmatrix}_{\mathcal{H}}$$

Thus, the matrix above gives the transition dipole moment function from the $X^1\Sigma^+$ state to the $V_{1/2}$ and $V_{3/2}$ states:

$$\mathscr{D}_{X^1\Sigma^+\leftrightarrow V_{1/2}}(R) = \mathscr{D}_{AX}(R)\cos\gamma \quad \text{and} \quad \mathscr{D}_{X^1\Sigma^+\leftrightarrow V_{3/2}}(R) = \mathscr{D}_{AX}(R)\sin\gamma. \tag{4.60}$$

Kinetic energy operator expressed in the hybrid basis Since the transformation $\mathbf{U}$ depends on the internuclear separation R, the kinetic energy matrix $\mathbf{T}$ is no longer diagonal in the hybrid basis $\mathcal{H}$ (as expected, see [34, p. 94]):

$$\mathbf{T}_{\mathcal{H}} = \mathbf{U}^{-1}\mathbf{T}_{\mathcal{A}}\mathbf{U} = \mathbf{U}^{\dagger}\mathbf{T}_{\mathcal{A}}\mathbf{U}$$

$$\mathbf{T}_{\mathcal{H}} = -\frac{\hbar^2}{2\mu}\begin{bmatrix} \frac{\partial^2}{\partial R^2} & 0 & 0 & 0 \\ 0 & \frac{\partial^2}{\partial R^2} & 0 & 0 \\ 0 & 0 & -\left(\frac{\mathrm{d}\gamma}{\mathrm{d}R}\right)^2 + \frac{\partial^2}{\partial R^2} & -\frac{\mathrm{d}^2\gamma}{\mathrm{d}R^2} - 2\frac{\mathrm{d}\gamma}{\mathrm{d}R}\frac{\partial}{\partial R} \\ 0 & 0 & \frac{\mathrm{d}^2\gamma}{\mathrm{d}R^2} + 2\frac{\mathrm{d}\gamma}{\mathrm{d}R}\frac{\partial}{\partial R} & -\left(\frac{\mathrm{d}\gamma}{\mathrm{d}R}\right)^2 + \frac{\partial^2}{\partial R^2} \end{bmatrix}_{\mathcal{H}}. \tag{4.61}$$

The change of basis $\mathcal{A} \rightarrow \mathcal{H}$ did not decouple the electronic states: instead of the $A^1\Sigma^+$ and $b^3\Pi$ states coupled by $\sqrt{2}\xi(R)$, I now have the $V_{1/2}(R)$ and $V_{3/2}(R)$

states coupled by the mixing angle matrix

$$\mathbf{A}_\gamma = -\frac{\hbar^2}{2\mu}\begin{bmatrix} 0 & 0 & 0 & 0 \\ 0 & 0 & 0 & 0 \\ 0 & 0 & -\left(\frac{\mathrm{d}\gamma}{\mathrm{d}R}\right)^2 & -\frac{\mathrm{d}^2\gamma}{\mathrm{d}R^2} - 2\frac{\mathrm{d}\gamma}{\mathrm{d}R}\frac{\partial}{\partial R} \\ 0 & 0 & \frac{\mathrm{d}^2\gamma}{\mathrm{d}R^2} + 2\frac{\mathrm{d}\gamma}{\mathrm{d}R}\frac{\partial}{\partial R} & -\left(\frac{\mathrm{d}\gamma}{\mathrm{d}R}\right)^2 \end{bmatrix}_{\mathcal{H}} . \tag{4.62}$$

Figure 4.3 shows the various derivatives of γ that appear in the above matrix $\mathbf{A}_\gamma$. Appendix D explains how to obtain the derivative of the mixing angle γ without actually computing γ itself. In Appendix E, I check the hermicity of the kinetic energy operator in basis $\mathcal{H}$, as it is not obvious from the expression of $\mathbf{T}_{\mathcal{H}}$ inEq. (4.61).

Once I obtain the mixing angle matrix elements (MAMEs), I can solve the coupled-channels problem using a basis expansion technique. Let's see how in the next section.

4.4.2 The solution to the coupled-channels problem

4.4.2.1 A bit of introduction

Three parts make up the current section. First, I give the mathematical expression of the coupled-channels problem I have to solve. Next, I explain how I can simplify the problem given the R-dependence of the functions $\frac{\mathrm{d}\gamma}{\mathrm{d}R}$, $\left(\frac{\mathrm{d}\gamma}{\mathrm{d}R}\right)^2$, and $\frac{\mathrm{d}^2\gamma}{\mathrm{d}R^2}$, and the behavior of the MAMEs. Last, I recall the basic mathematical properties of the coupled-channels eigenstates.

4.4.2.2 Formulating the coupled-channels problem

The coupled-channels problem to solve involves the hybrid electronic states $|V_{1/2}\rangle$ and $|V_{3/2}\rangle$, and *only* the rotational state $|J = 1, M = 0, \Omega = 0\rangle$. Since there

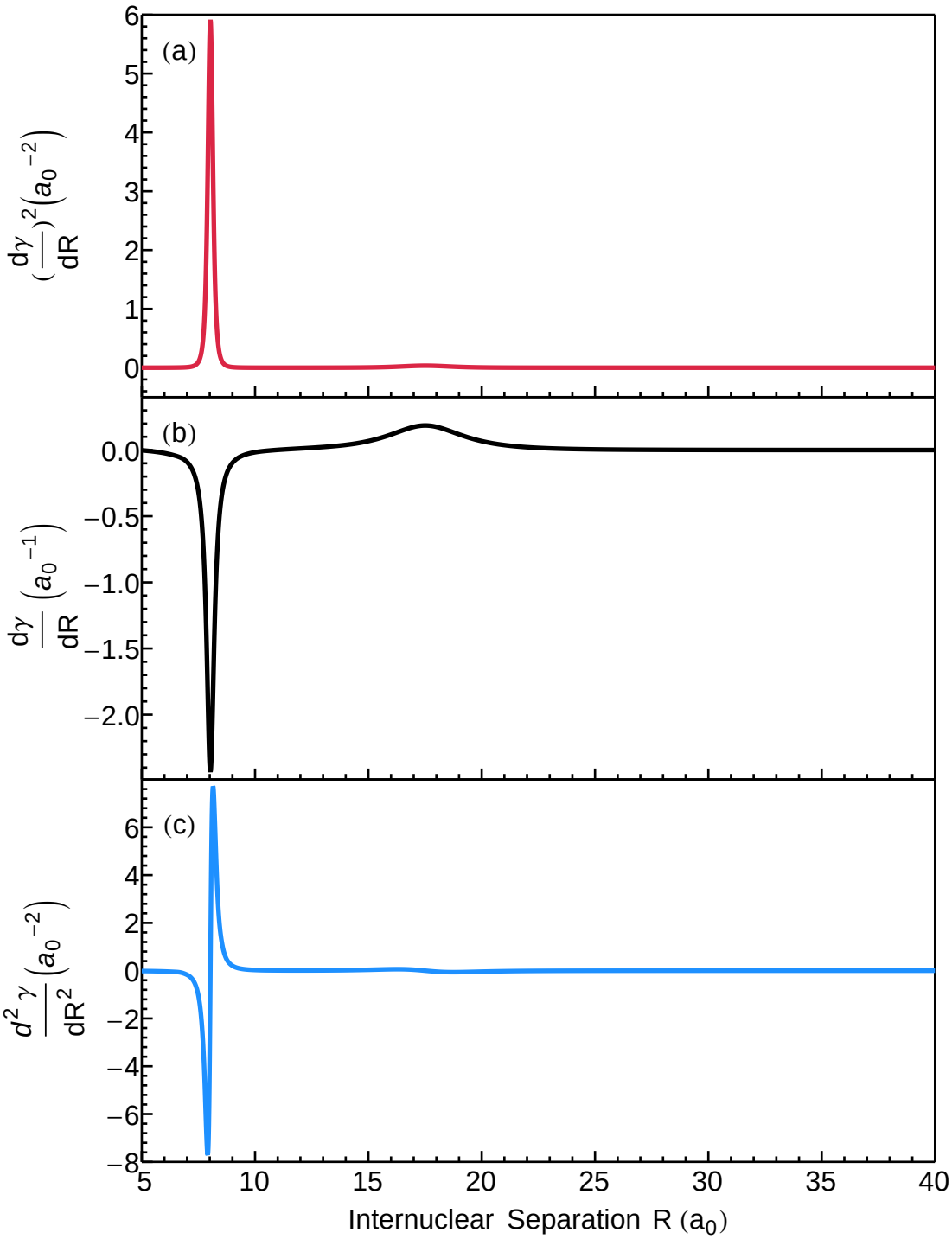

Figure 4.3: (**a**): **Square** of the first derivative of the mixing angle γ with respect to the internuclear separation R. (**b**): First derivative of the mixing angle γ with respect to R. The extrema occur at $R \approx 8.03\,a_0 \approx 4.25$ Å and $R \approx 17.51\,a_0 \approx 9.27$ Å with respective values $(\mathrm{d}\gamma/\mathrm{d}R)_{\min} \approx -2.43\,{a_0}^{-1}$ and $(\mathrm{d}\gamma/\mathrm{d}R)_{\max} \approx 0.18\,{a_0}^{-1}$. (**c**): Second derivative of the mixing angle γ with respect to R. All functions are smooth and continuous at all R.

is only *one* rotational state involved in the solution to this coupled-channels problem, I do not mention J, M, and Ω anymore below. In the sub-basis $\mathsf{h} = \{|V_{1/2}, J=1\rangle, |V_{3/2}, J=1\rangle\}$ of $\mathcal{H}$, the operators in the relevant coupled-channels portion $\widehat{\mathscr{H}_{\text{cc}}}$ of the total hamiltonian,

$$\widehat{\mathscr{H}_{\text{cc}}} = \widehat{\mathscr{T}} + \frac{\widehat{\vec{\mathscr{R}}}^2}{2\mu R^2} + \widehat{\mathscr{V}}^{\text{tot}} + \widehat{\gamma}, \tag{4.63}$$

have matrices easily extracted from the ones obtained in the previous section

$$\mathbf{T}_{\mathsf{h}} = -\frac{\hbar^2}{2\mu}\begin{bmatrix} \frac{\mathrm{d}^2}{\mathrm{d}R^2} & 0 \\ 0 & \frac{\mathrm{d}^2}{\mathrm{d}R^2} \end{bmatrix}_{\mathsf{h}}, \qquad \mathbf{R}_{\mathsf{h}} = -\frac{\hbar^2}{2\mu}\begin{bmatrix} -\frac{4}{R^2} & 0 \\ 0 & -\frac{4}{R^2} \end{bmatrix}_{\mathsf{h}}, \tag{4.64a}$$

$$\mathbf{V}^{\text{tot}}_{\mathsf{h}} = \begin{bmatrix} V_{1/2}(R) & 0 \\ 0 & V_{3/2}(R) \end{bmatrix}_{\mathsf{h}}, \quad \mathbf{A}_{\mathsf{h}} = \frac{\hbar^2}{2\mu}\begin{bmatrix} \left(\frac{\mathrm{d}\gamma}{\mathrm{d}R}\right)^2 & \frac{\mathrm{d}^2\gamma}{\mathrm{d}R^2} + 2\frac{\mathrm{d}\gamma}{\mathrm{d}R}\frac{\partial}{\partial R} \\ -\frac{\mathrm{d}^2\gamma}{\mathrm{d}R^2} - 2\frac{\mathrm{d}\gamma}{\mathrm{d}R}\frac{\partial}{\partial R} & \left(\frac{\mathrm{d}\gamma}{\mathrm{d}R}\right)^2 \end{bmatrix}_{\mathsf{h}}. \tag{4.64b}$$

Notice that the matrix $\mathbf{A}_{\mathsf{h}}$, which corresponds to the lower-right block of $\mathbf{A}_\gamma$ in Eq. (4.62) defines the operator $\widehat{\gamma}$.

I used LEVEL [45] to obtain the $J = 1$ rovibrational eigenenergies and eigenstates of the $V_{1/2}(R)$ and $V_{3/2}(R)$ states, which respectively support 146 and 114 eigenstates.

Let's define the orthonormal basis $\mathcal{B} = \Big\{\{|\chi_v\rangle|V_{1/2}\rangle\}_v, \{|e\rangle|V_{1/2}\rangle\}_e, \{|\Xi_q\rangle|V_{3/2}\rangle\}_q, \{|\text{E}\rangle|V_{1/2}\rangle\}_{\text{E}}\Big\}$, where $v \in [\![0, 145]\!]$ and $q \in [\![0, 113]\!]$, e represents a scattering energy above the asymptote $e_\infty = \lim_{R\to\infty} V_{1/2}(R)$ of $V_{1/2}(R)$, and E is a scattering energy above the asymptote $\text{E}_\infty = \lim_{R\to\infty} V_{3/2}(R)$ of $V_{3/2}(R)$. Figure 4.4 illustrates the meaning of these symbols. The various kets in $\mathcal{B}$ are eigenstates of the

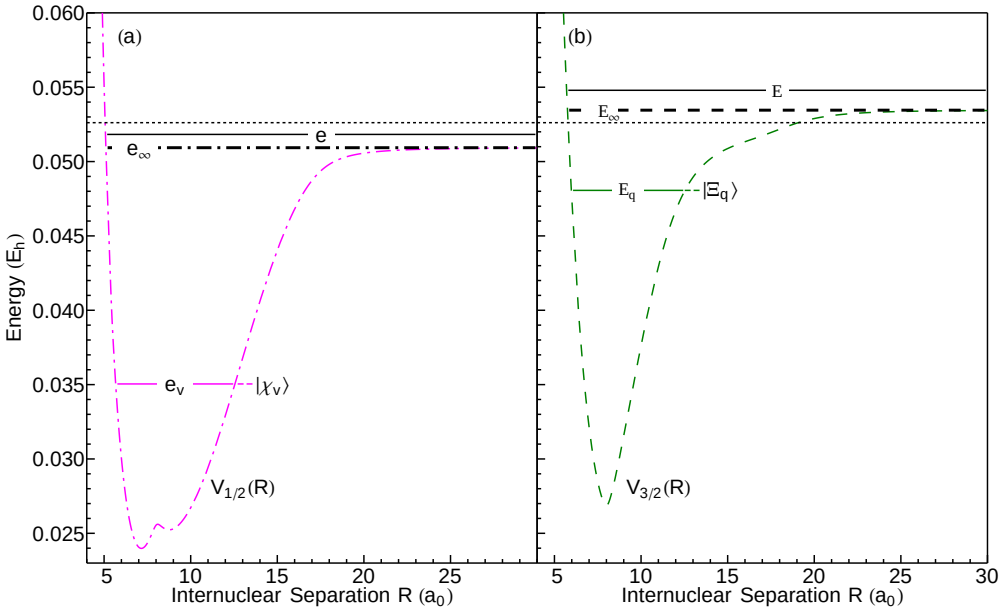

Figure 4.4: (Color online) Definition of notation for bound states, scattering states, and asymptotic energy for the hybrid potentials energy curves (**a**) $V_{1/2}$ and (**b**) $V_{3/2}$. The thin dotted line common to both panels is the asymptote of the $A^1\Sigma^+$ state. Note that e can be greater or smaller than E_∞, but always remains greater than e_∞. As stated at the end of Sec. 4.1.1, the zero of energy is at the asymptote of the $X^1\Sigma^+$ state.

corresponding time-independent, uncoupled hamiltonians:

$$\left(\widehat{\mathscr{T}} + \frac{\widehat{\vec{\mathscr{R}}}^2}{2\mu R^2} + \widehat{\mathscr{V}}^{\mathrm{tot}}\right)|\chi_v\rangle|V_{1/2}\rangle = \left(-\frac{\hbar^2}{2\mu}\frac{\mathrm{d}^2}{\mathrm{d}R^2} + 4\frac{\hbar^2}{2\mu R^2} + V_{1/2}(R)\right)|\chi_v\rangle|V_{1/2}\rangle$$
$$= e_v|\chi_v\rangle|V_{1/2}\rangle \tag{4.65a}$$

$$\left(\widehat{\mathscr{T}} + \frac{\widehat{\vec{\mathscr{R}}}^2}{2\mu R^2} + \widehat{\mathscr{V}}^{\mathrm{tot}}\right)|e\rangle|V_{1/2}\rangle = e|e\rangle|V_{1/2}\rangle \tag{4.65b}$$

$$\left(\widehat{\mathscr{T}} + \frac{\widehat{\vec{\mathscr{R}}}^2}{2\mu R^2} + \widehat{\mathscr{V}}^{\mathrm{tot}}\right)|\Xi_q\rangle|V_{3/2}\rangle = \left(-\frac{\hbar^2}{2\mu}\frac{\mathrm{d}^2}{\mathrm{d}R^2} + 4\frac{\hbar^2}{2\mu R^2} + V_{3/2}(R)\right)|\Xi_q\rangle|V_{3/2}\rangle$$
$$= E_q|\Xi_q\rangle|V_{3/2}\rangle \tag{4.65c}$$

$$\left(\widehat{\mathscr{T}} + \frac{\widehat{\vec{\mathscr{R}}}^2}{2\mu R^2} + \widehat{\mathscr{V}}^{\mathrm{tot}}\right)|\mathrm{E}\rangle|V_{3/2}\rangle = \mathrm{E}|\mathrm{E}\rangle|V_{3/2}\rangle \tag{4.65d}$$

The coupled-channels eigenstate $|\Phi^{cc}_{v_{cc}}\rangle$ with eigenenergy $E^{cc}_{v_{cc}}$ satisfies

$$\widehat{\mathscr{H}_{cc}}\,|\Phi^{cc}_{v_{cc}}\rangle = E^{cc}_{v_{cc}}\,|\Phi^{cc}_{v_{cc}}\rangle \tag{4.66}$$

and may be expanded over the basis $\mathcal{B}$

$$\begin{aligned}|\Phi^{cc}_{v_{cc}}\rangle = \sum_v a_{v,v_{cc}}\,|\chi_v\rangle|V_{1/2}\rangle + \int_{e_\infty}^{\infty} a_{e,v_{cc}}\,|e\rangle|V_{1/2}\rangle\,\mathrm{d}e \\ + \sum_q b_{q,v_{cc}}\,|\Xi_q\rangle|V_{3/2}\rangle + \int_{E_\infty}^{\infty} b_{E,v_{cc}}\,|E\rangle|V_{3/2}\rangle\,\mathrm{d}E.\end{aligned} \tag{4.67}$$

where all expansion coefficients are constants. Plugging equation 4.67 into Eq. (4.66), and using the definitions of Eqs. (4.65) yields the following system of equations for the expansion coefficients of the coupled-channels eigenstate:

$$\begin{aligned}\forall v \in [\![0,145]\!],\quad E^{cc}_{v_{cc}} a_{v,v_{cc}} &= e_v a_{v,v_{cc}} + \sum_{v'} a_{v',v_{cc}} \langle\chi_v|\left\langle V_{1/2}\left|\widehat{\gamma}\right|V_{1/2}\right\rangle|\chi_{v'}\rangle \\ &\quad + \int_{e'_\infty}^{\infty} a_{e',v_{cc}} \langle\chi_v|\left\langle V_{1/2}\left|\widehat{\gamma}\right|V_{1/2}\right\rangle|e'\rangle\,\mathrm{d}e' \\ &\quad + \sum_{q'} b_{q',v_{cc}} \langle\chi_v|\left\langle V_{1/2}\left|\widehat{\gamma}\right|V_{3/2}\right\rangle|\Xi_{q'}\rangle + \int_{E'_\infty}^{\infty} b_{E',v_{cc}} \langle\chi_v|\left\langle V_{1/2}\left|\widehat{\gamma}\right|V_{3/2}\right\rangle|E'\rangle\,\mathrm{d}E',\end{aligned} \tag{4.68a}$$

$$\begin{aligned}\forall q \in [\![0,113]\!],\quad E^{cc}_{v_{cc}} b_{q,v_{cc}} &= E_q b_{q,v_{cc}} + \sum_{q'} b_{q',v_{cc}} \langle\Xi_q|\left\langle V_{3/2}\left|\widehat{\gamma}\right|V_{3/2}\right\rangle|\Xi_{q'}\rangle \\ &\quad + \int_{E'_\infty}^{\infty} b_{E',v_{cc}} \langle\Xi_q|\left\langle V_{3/2}\left|\widehat{\gamma}\right|V_{3/2}\right\rangle|E'\rangle\,\mathrm{d}E' \\ &\quad + \sum_{v'} a_{v',v_{cc}} \langle\Xi_q|\left\langle V_{3/2}\left|\widehat{\gamma}\right|V_{1/2}\right\rangle|\chi_{v'}\rangle + \int_{e'_\infty}^{\infty} a_{e',v_{cc}} \langle\Xi_q|\left\langle V_{3/2}\left|\widehat{\gamma}\right|V_{1/2}\right\rangle|e'\rangle\,\mathrm{d}e',\end{aligned} \tag{4.68b}$$

$$\begin{aligned}\forall e > e_\infty,\quad E^{cc}_{v_{cc}} a_{e,v_{cc}} &= e a_{e,v_{cc}} + \sum_{v'} a_{v',v_{cc}} \langle e|\left\langle V_{1/2}\left|\widehat{\gamma}\right|V_{1/2}\right\rangle|\chi_{v'}\rangle \\ &\quad + \int_{e'_\infty}^{\infty} a_{e',v_{cc}} \langle e|\left\langle V_{1/2}\left|\widehat{\gamma}\right|V_{1/2}\right\rangle|e'\rangle\,\mathrm{d}e' \\ &\quad + \sum_{q'} b_{q',v_{cc}} \langle e|\left\langle V_{1/2}\left|\widehat{\gamma}\right|V_{3/2}\right\rangle|\Xi_{q'}\rangle + \int_{E'_\infty}^{\infty} b_{E',v_{cc}} \langle e|\left\langle V_{1/2}\left|\widehat{\gamma}\right|V_{3/2}\right\rangle|E'\rangle\,\mathrm{d}E',\end{aligned} \tag{4.68c}$$

$$\forall \mathrm{E} > \mathrm{E}_\infty, \quad \mathrm{E}^{\mathrm{cc}}_{\mathrm{v_{cc}}} b_{\mathrm{E},\mathrm{v_{cc}}} = \mathrm{E} b_{\mathrm{E},\mathrm{v_{cc}}} + \sum_{q'} b_{q',\mathrm{v_{cc}}} \langle \mathrm{E} | \left\langle V_{3/2} \left| \widehat{\gamma} \right| V_{3/2} \right\rangle | \Xi_{q'} \rangle$$
$$+ \int_{\mathrm{E}'_\infty}^{\infty} b_{\mathrm{E}',\mathrm{v_{cc}}} \langle \mathrm{E} | \left\langle V_{3/2} \left| \widehat{\gamma} \right| V_{3/2} \right\rangle | \mathrm{E}' \rangle \, \mathrm{d}\mathrm{E}'$$
$$+ \sum_{v'} a_{v',\mathrm{v_{cc}}} \langle \mathrm{E} | \left\langle V_{3/2} \left| \widehat{\gamma} \right| V_{1/2} \right\rangle | \chi_{v'} \rangle + \int_{e'_\infty}^{\infty} a_{e',\mathrm{v_{cc}}} \langle \mathrm{E} | \left\langle V_{3/2} \left| \widehat{\gamma} \right| V_{1/2} \right\rangle | e' \rangle \, \mathrm{d}e'. \quad (4.68\mathrm{d})$$

If all the bound-continuum and continuum-continuum matrix elements of $\widehat{\gamma}$ are ignored, obtaining the expansion coefficients amounts to diagonalize a 260× 260 matrix.

4.4.2.3 Examining the bound-bound matrix elements of $\widehat{\gamma}$

Figures 4.5, 4.6, and 4.7 are plots of the bound-bound matrix elements of $\widehat{\gamma}$. Rather than showing the matrices as arrays of numbers, I chose to represent the matrices as mosaics, where the tile's position corresponds to the row-column position in the matrix, and the tile's color corresponds to the value of the associated number. The legend on the right of each figure provides an *indicator* for the values of the matrix elements. In all figures, each axis corresponds to the value of the relevant vibrational quantum number. I reinforced the notation for the vibrational quantum number from Eq. (4.68) by adding a 1/2 or 3/2 subscript: my intent is to remind the reader to which electronic state does a given vibrational quantum number belongs. A little help with the legend: the closer to white a given tile is, the closer to zero the corresponding number, and so the smaller the coupling due to the operator $\widehat{\gamma}$ between the vibrational states considered. For example, in Fig. 4.5, the matrix elements $\frac{\hbar^2}{2\mu} \langle \chi_{145} | \left\langle V_{1/2} \left| \widehat{\gamma} \right| V_{1/2} \right\rangle | \chi_{v_{1/2}} \rangle = \frac{\hbar^2}{2\mu} \left\langle \chi_{145} \left| \left(\frac{\mathrm{d}\gamma}{\mathrm{d}R} \right)^2 \right| \chi_{v_{1/2}} \right\rangle$ is extremely small for all values of $v_{1/2}$ compared to other couplings: the color of the couplings always stays in the white range of the legend, indicating closeness to zero and the weakness of the $\widehat{\gamma}$-coupling between $|\chi_{145}\rangle$ and any $|\chi_{v_{1/2}}\rangle$. Figures 4.6 and

4.7 display the same behavior for the matrix elements

$$\frac{\hbar^2}{2\mu}\langle \Xi_{q_{3/2}} | \left\langle V_{3/2} \middle| \widehat{\gamma} \middle| V_{3/2} \right\rangle | \Xi_{q'_{3/2}} \rangle = \frac{\hbar^2}{2\mu} \left\langle \Xi_{q_{3/2}} \middle| \left(\frac{\mathrm{d}\gamma}{\mathrm{d}R} \right)^2 \middle| \Xi_{q'_{3/2}} \right\rangle \tag{4.69a}$$

and

$$-\frac{\hbar^2}{2\mu}\langle \Xi_{q_{3/2}} | \left\langle V_{3/2} \middle| \widehat{\gamma} \middle| V_{1/2} \right\rangle | \chi_{v_{1/2}} \rangle = -\frac{\hbar^2}{2\mu} \left\langle \Xi_{q_{3/2}} \middle| \frac{\mathrm{d}^2\gamma}{\mathrm{d}R^2} + 2\frac{\mathrm{d}\gamma}{\mathrm{d}R}\frac{\mathrm{d}}{\mathrm{d}R} \middle| \chi_{v_{1/2}} \right\rangle \tag{4.69b}$$

for very high values of $q_{3/2}$ and $v_{1/2}$. On the contrary, the darker regions in Figs. 4.5, 4.6, and 4.7 correspond to comparatively strong $\widehat{\gamma}$-coupling between the vibrational states. For example, the red (darkest) spot in Fig. 4.5 corresponds to the matrix element $\frac{\hbar^2}{2\mu} \left\langle \chi_6 \middle| \left(\frac{\mathrm{d}\gamma}{\mathrm{d}R} \right)^2 \middle| \chi_6 \right\rangle$.

One very important feature common to these three figures is the trend of the matrix elements. The bottom-left and top-right region of each figure are very light-colored, indicating weak $\widehat{\gamma}$-coupling between the very high-lying vibrational states and the ones deep in the $V_{1/2}$ or $V_{3/2}$ potential well. The higher the vibrational quantum number, the whiter the corresponding row or column, *i.e.* the less will $\widehat{\gamma}$ couple this particular vibrational state to other vibrational states belonging to either the same potential (Figs. 4.5 and 4.6), or the other potential (Fig. 4.7).

Continuum wave functions oscillate with very small amplitude—compared to bound states—until the internuclear separation approaches the value of the right classical turning point of the highest bound state[a]. Given the shape of the coupling functions in Fig. 4.3 (p. 107), the continuum-continuum and bound-continuum matrix elements of $\widehat{\gamma}$ are therefore likely to be negligible.

Consequently, it seems reasonable to neglect all $\widehat{\gamma}$-couplings involving any

[a] What Londoño *et al.* [73] call R_N is somewhat greater than the rightmost classical turning point. The rightmost classical turning point is thus a good estimate for a lower bound on R_N.

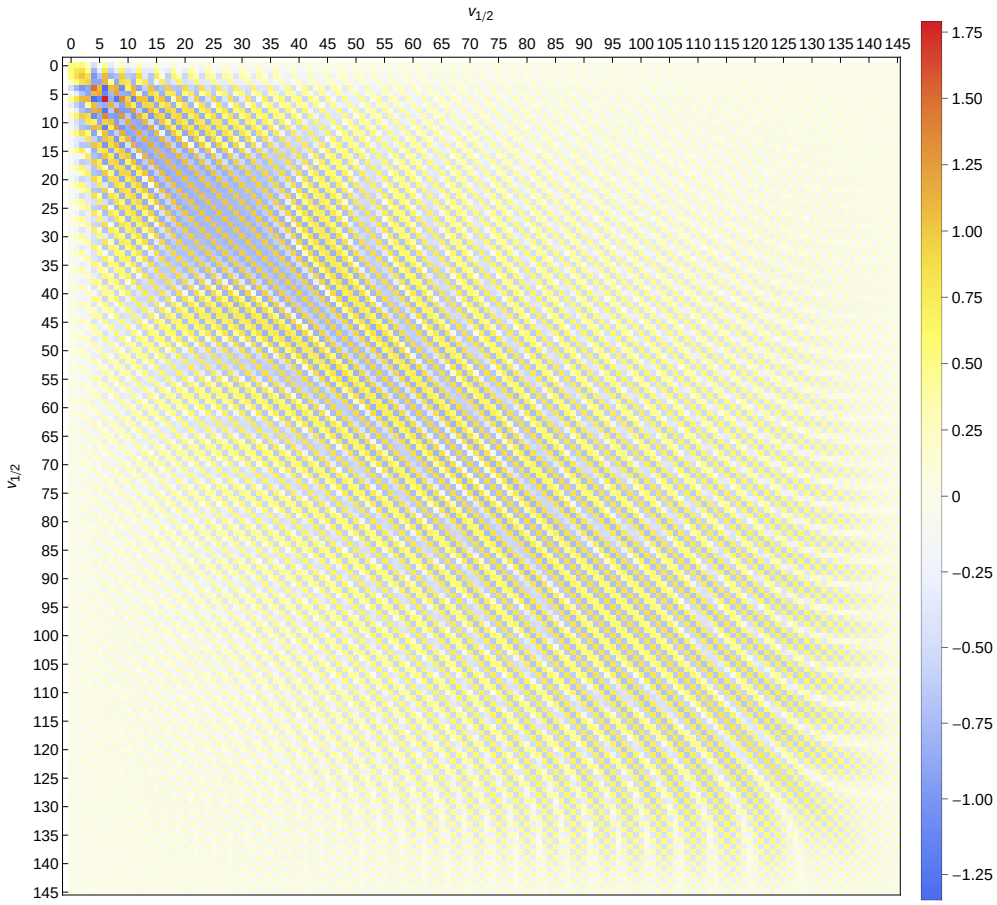

Figure 4.5: (Color online) Diagonal bound-bound matrix elements $\frac{\hbar^2}{2\mu}\langle\chi_{v_{1/2}}|\left\langle V_{1/2}\left|\widehat{\gamma}\right|V_{1/2}\right\rangle|\chi_{v'_{1/2}}\rangle = \frac{\hbar^2}{2\mu}\left\langle\chi_{v_{1/2}}\left|\left(\frac{\mathrm{d}\gamma}{\mathrm{d}R}\right)^2\right|\chi_{v_{1/2}}\right\rangle$. The legend on the right is in atomic units $\times 10^{-5}$.

of the continuum states that appear in Eqs. (4.68); in particular, these couplings play no role in the transfer of population to and from the $X^1\Sigma^+$ state. This approximation reduces the problem of finding the eigenstates of the coupled-channel Time-Independent Schrödinger Equation to the diagonalization of a 260×260 matrix. Indeed the $J = 1, V_{1/2}$ potential holds $145 + 1 = 146$ rovibrational states, and the $J = 1, V_{3/2}$ potential holds $113 + 1 = 114$, thus the total matrix to diagonalize has dimensions 260×260.

Results of that operation are examined below.

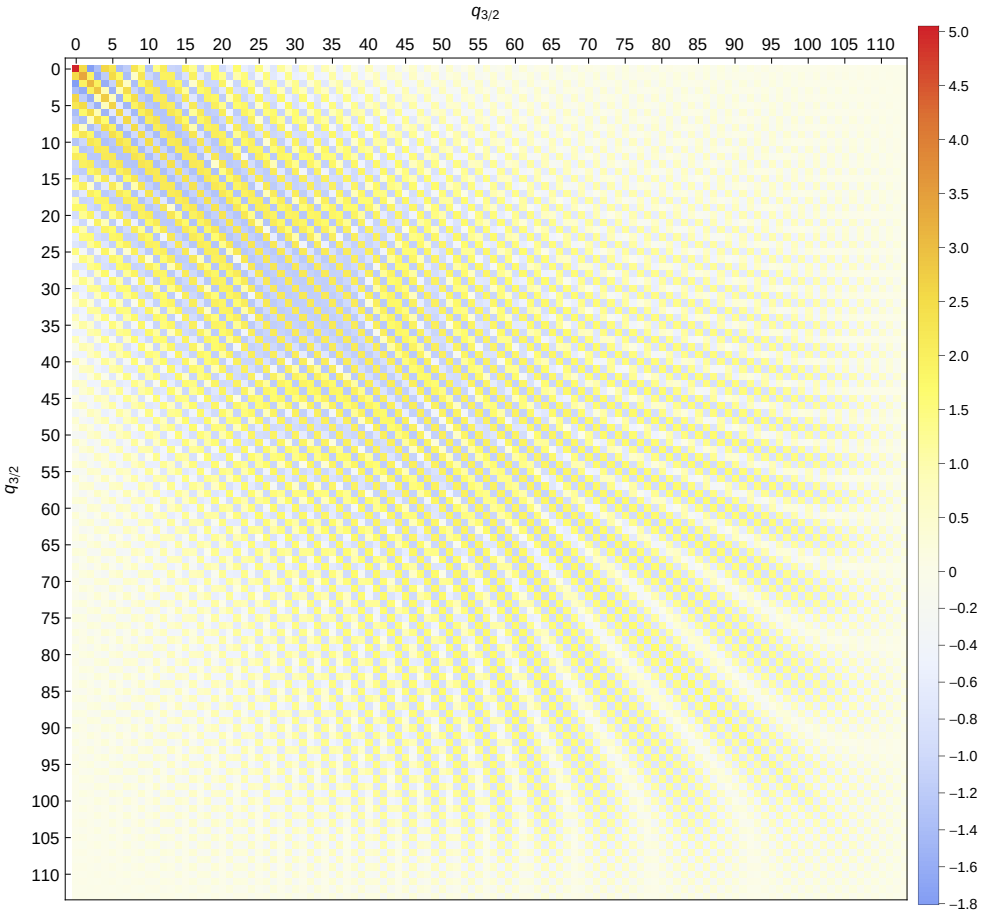

Figure 4.6: (Color online) Diagonal bound-bound matrix elements $\frac{\hbar^2}{2\mu}\langle\Xi_{q_{3/2}}|\left\langle V_{3/2}\middle|\widehat{\gamma}\middle|V_{3/2}\right\rangle|\Xi_{q'_{3/2}}\rangle = \frac{\hbar^2}{2\mu}\left\langle\Xi_{q_{3/2}}\middle|\left(\frac{\mathrm{d}\gamma}{\mathrm{d}R}\right)^2\middle|\Xi_{q'_{3/2}}\right\rangle$. The legend on the right is in atomic units $\times 10^{-5}$.

4.4.2.4 Wave functions for each separated channels

The diagonalization of the real, symmetric 260×260 matrix takes about 0.03s to run in *Mathematica*®, and yields the coefficients $\{\{a_{v,\mathrm{v_{cc}}}\}_v, \{b_{q,\mathrm{v_{cc}}}\}_q\}$ defined for each value of $\mathrm{v_{cc}}$ in Eq. (4.67). One may express the 2 components

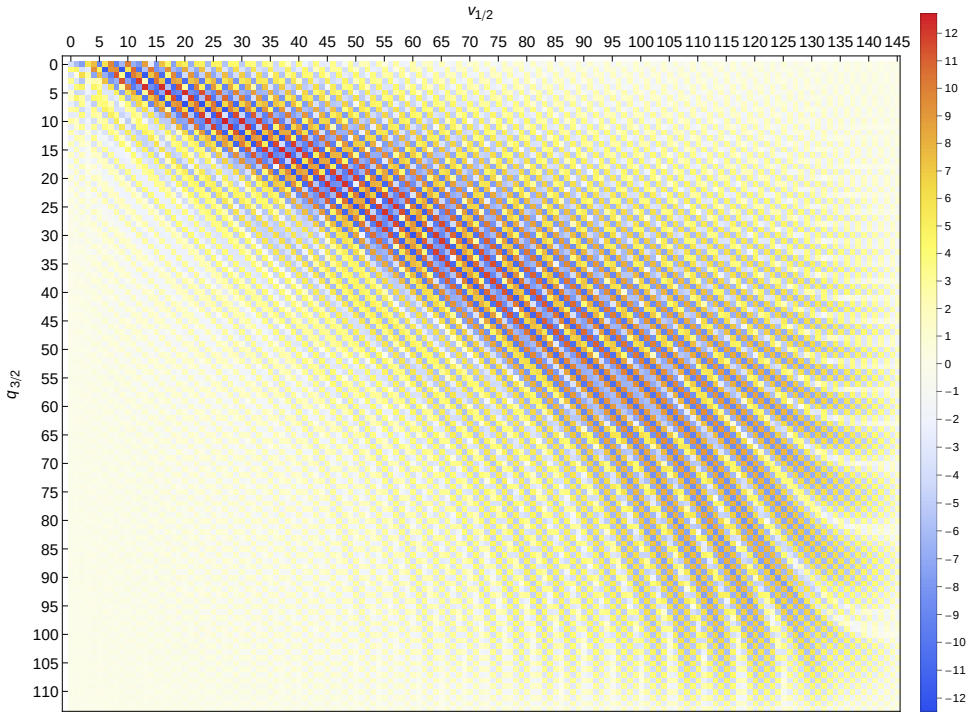

Figure 4.7: (Color online) Off-diagonal bound-bound matrix elements $-\frac{\hbar^2}{2\mu}\langle\Xi_{q_{3/2}}|\left\langle V_{3/2}\middle|\widehat{\gamma}\middle|V_{1/2}\right\rangle|\chi_{v_{1/2}}\rangle = -\frac{\hbar^2}{2\mu}\left\langle\Xi_{q_{3/2}}\middle|\frac{\mathrm{d}^2\gamma}{\mathrm{d}R^2}+2\frac{\mathrm{d}\gamma}{\mathrm{d}R}\frac{\mathrm{d}}{\mathrm{d}R}\middle|\chi_{v_{1/2}}\right\rangle$. The legend on the right is in atomic units $\times 10^{-5}$.

coupled-channel eigenket $|\Phi^{cc}_{v_{cc}}\rangle$ in vector form:

$$\begin{matrix} & |\Phi^{cc}_{v_{cc}}\rangle \\ \langle V_{1/2}| & \\ \langle V_{3/2}| & \end{matrix}\begin{bmatrix} \psi^{[1/2]}_{v_{cc}}(R) \\ \psi^{[3/2]}_{v_{cc}}(R) \end{bmatrix} \quad \text{with} \quad \begin{aligned} \psi^{[1/2]}_{v_{cc}}(R) &= \sum_v a_{v,v_{cc}}\chi_v(R) \\ \psi^{[3/2]}_{v_{cc}}(R) &= \sum_q b_{q,v_{cc}}\Xi_q(R). \end{aligned} \tag{4.70}$$

The ket $|\Phi^{cc}_{v_{cc}}\rangle$ is a solution of the Time-Independent Schrödinger Equation with energy $E^{cc}_{v_{cc}}$ if and only if it satisfies Eq. (4.66), or equivalently if $\psi^{[1/2]}_{v_{cc}}(R)$ and $\psi^{[3/2]}_{v_{cc}}(R)$ satisfy

$$\begin{aligned} &\left[-\frac{\hbar^2}{2\mu}\left(\frac{\mathrm{d}^2}{\mathrm{d}R^2}-\left(\frac{\mathrm{d}\gamma}{\mathrm{d}R}\right)^2\right)+V_{1/2}(R)+4\frac{\hbar^2}{2\mu R^2}\right]\psi^{[1/2]}_{v_{cc}}(R) \\ &\qquad +\frac{\hbar^2}{2\mu}\left[\frac{\mathrm{d}^2\gamma}{\mathrm{d}R^2}+2\frac{\mathrm{d}\gamma}{\mathrm{d}R}\frac{\mathrm{d}}{\mathrm{d}R}\right]\psi^{[3/2]}_{v_{cc}}(R) = E^{cc}_{v_{cc}}\psi^{[1/2]}_{v_{cc}}(R), \end{aligned} \tag{4.71a}$$

and

$$-\frac{\hbar^2}{2\mu}\left[\frac{\mathrm{d}^2\gamma}{\mathrm{d}R^2}+2\frac{\mathrm{d}\gamma}{\mathrm{d}R}\frac{\mathrm{d}}{\mathrm{d}R}\right]\psi_{v_{cc}}^{[1/2]}(R)$$
$$+\left[-\frac{\hbar^2}{2\mu}\left(\frac{\mathrm{d}^2}{\mathrm{d}R^2}-\left(\frac{\mathrm{d}\gamma}{\mathrm{d}R}\right)^2\right)+V_{3/2}(R)+4\frac{\hbar^2}{2\mu R^2}\right]\psi_{v_{cc}}^{[3/2]}(R)=E_{v_{cc}}^{cc}\psi_{v_{cc}}^{[3/2]}(R). \quad (4.71b)$$

In Appendix F, I verify—for certain values of v_{cc}—that the coupled-channels eigenkets $|\Phi_{v_{cc}}^{cc}\rangle$ I obtained are indeed solution of the Time-Independent Schrödinger Equation. I discuss the features of the coupled-channels probability density functions that correspond to the chosen sample of v_{cc}'s in chap. 5.

I should now return to the quest of getting equations for the time-dependent probability amplitudes relevant to my problem.

4.4.3 Probability amplitudes when using spin-orbit coupled channels

The kets and energies $|\Phi_{v_{cc}}^{cc}\rangle$ and $E_{v_{cc}}^{cc}$ are solutions of the Time-Independent Schrödinger Equation Eq. (4.66). However the heart of the problem is to solve the time-*dependent* Eq. (4.26). Let's use the coupled-channels results I obtained in the previous section (4.4.2) to derive a set of equations, similar to Eq. (4.52), that will include the physics of spin-orbit coupling embedded in $|\Phi_{v_{cc}}^{cc}\rangle$ and $E_{v_{cc}}^{cc}$.

After performing the unitary transformation $\mathbf{U}$ of Eq. (4.56), I could use the two single-channel wave packets $\Gamma_1^{[1/2]}(R,t)$ and $\Gamma_1^{[3/2]}(R,t)$, each a linear combination of Γ_1^A and Γ_1^b. Yet I now have the coupled-channels kets $|\Phi_{v_{cc}}^{cc}\rangle$. Thus, a 2-dimensional coupled-channels wave packet

$$|\Gamma^{cc}(t)\rangle=\sum_{v_{cc}=0}^{N_{cc}-1}a_{v_{cc}}^{cc}(t)\,|\Phi_{v_{cc}}^{cc}\rangle, \quad (4.72)$$

with $|\Phi^{cc}_{v_{cc}}\rangle = \psi^{[1/2]}_{v_{cc}}(R)|V_{1/2}\rangle + \psi^{[3/2]}_{v_{cc}}(R)|V_{3/2}\rangle$, is more practical for the derivation. I only need to replace $|A,1,v_A\rangle$ by $|\Phi^{cc}_{v_{cc}}\rangle$ and $\mathscr{D}_{AX}$ by $\widehat{\mathscr{D}}$ in Eqs. (4.32), (4.35), (4.36), and (4.37), thereby obtaining the following equations

$$\forall v_X \in [\![0, N_{X0}-1]\!],$$

$$\mathbf{i}\hbar\frac{\mathrm{d}}{\mathrm{d}t}a^{X0}_{v_X}(t) = E^{X0}_{v_X}a^{X0}_{v_X} - \sum_{v_{cc}=0}^{N_{cc}-1}\frac{\sqrt{3}}{3}\mathscr{E}(t)\left\langle X,0,v_X\left|\widehat{\mathscr{D}}\right|\Phi^{cc}_{v_{cc}}\right\rangle a^{cc}_{v_{cc}}(t); \tag{4.73a}$$

$$\forall j \in [\![1, N_E]\!],$$

$$\mathbf{i}\hbar\frac{\mathrm{d}}{\mathrm{d}t}\alpha^{X0}_{E_j}(t) = E^{X0}_{j}\alpha^{X0}_{E_j} - \sum_{v_{cc}=0}^{N_{cc}-1}\frac{\sqrt{3}}{3}\mathscr{E}(t)\sqrt{\Delta E_j}\left\langle \chi^{X0}_{E_j}\left|\widehat{\mathscr{D}}\right|\Phi^{cc}_{v_{cc}}\right\rangle a^{cc}_{v_{cc}}(t); \tag{4.73b}$$

$$\forall v_X \in [\![0, N_{X2}-1]\!],$$

$$\mathbf{i}\hbar\frac{\mathrm{d}}{\mathrm{d}t}a^{X2}_{v_X}(t) = E^{X2}_{v_X}a^{X2}_{v_X} - \sum_{v_{cc}=0}^{N_{cc}-1}2\frac{\sqrt{15}}{15}\mathscr{E}(t)\left\langle X,2,v_X\left|\widehat{\mathscr{D}}\right|\Phi^{cc}_{v_{cc}}\right\rangle a^{cc}_{v_{cc}}(t); \tag{4.73c}$$

and finally for the coupled-channels probability amplitudes

$$\begin{aligned}\forall \mathrm{v}_{cc} \in [\![0, N_{cc}-1]\!],\\ \mathbf{i}\hbar\frac{\mathrm{d}}{\mathrm{d}t}a^{cc}_{v_{cc}}(t) = \mathrm{E}^{cc}_{v_{cc}}a^{cc}_{v_{cc}} &- \sum_{v_X=0}^{N_{X2}-1}2\frac{\sqrt{15}}{15}\mathscr{E}(t)\left\langle \Phi^{cc}_{v_{cc}}\left|\widehat{\mathscr{D}}\right|X,2,v_X\right\rangle a^{X2}_{v_X}(t)\\ &- \sum_{v_X=0}^{N_{X0}-1}\frac{\sqrt{3}}{3}\mathscr{E}(t)\left\langle \Phi^{cc}_{v_{cc}}\left|\widehat{\mathscr{D}}\right|X,0,v_X\right\rangle a^{X0}_{v_X}(t)\\ &- \sum_{j=1}^{N_E}\frac{\sqrt{3}}{3}\mathscr{E}(t)\left\langle \Phi^{cc}_{v_{cc}}\left|\widehat{\mathscr{D}}\right|\chi^{X0}_{E_j}\right\rangle\sqrt{\Delta E_j}\alpha^{X0}_{E_j}(t).\end{aligned} \tag{4.73d}$$

Naturally the question arises:"What are the $\widehat{\mathscr{D}}$ matrix elements ?" Let's consider for example $\left\langle X,0,v_X\left|\widehat{\mathscr{D}}\right|\Phi^{cc}_{v_{cc}}\right\rangle$, and remember that $|\Phi^{cc}_{v_{cc}}\rangle$ has 2 components, one over $|V_{1/2}\rangle$ and another over $|V_{3/2}\rangle$, as recalled below Eq. (4.72).

Since $\widehat{\mathscr{D}}$ is linear

$$\left\langle X,0,v_X \left| \widehat{\mathscr{D}} \right| \Phi^{\mathrm{cc}}_{\mathrm{v_{cc}}} \right\rangle = \left\langle X,0,v_X \left| \widehat{\mathscr{D}} \right| V_{1/2} \right\rangle |\psi^{[1/2]}_{\mathrm{v_{cc}}}\rangle + \left\langle X,0,v_X \left| \widehat{\mathscr{D}} \right| V_{3/2} \right\rangle |\psi^{[3/2]}_{\mathrm{v_{cc}}}\rangle \tag{4.74}$$

The expression of $\widehat{\mathscr{D}}$ in the hybrid basis $\mathcal{H}$ gives the matrix elements of $\widehat{\mathscr{D}}$ between the relevant electronic states, thus

$$\left\langle X,0,v_X \left| \widehat{\mathscr{D}} \right| \Phi^{\mathrm{cc}}_{\mathrm{v_{cc}}} \right\rangle = \frac{\sqrt{3}}{3}\left(\left\langle X,0,v_X \left| -\mathscr{D}_{AX}\cos\gamma \right| \psi^{[1/2]}_{\mathrm{v_{cc}}} \right\rangle + \left\langle X,0,v_X \left| \mathscr{D}_{AX}\sin\gamma \right| \psi^{[1/2]}_{\mathrm{v_{cc}}} \right\rangle\right). \tag{4.75a}$$

Likewise,

$$\left\langle X,2,v_X \left| \widehat{\mathscr{D}} \right| \Phi^{\mathrm{cc}}_{\mathrm{v_{cc}}} \right\rangle = 2\frac{\sqrt{15}}{15}\left(\left\langle X,2,v_X \left| -\mathscr{D}_{AX}\cos\gamma \right| \psi^{[1/2]}_{\mathrm{v_{cc}}} \right\rangle + \left\langle X,2,v_X \left| \mathscr{D}_{AX}\sin\gamma \right| \psi^{[1/2]}_{\mathrm{v_{cc}}} \right\rangle\right) \tag{4.75b}$$

and

$$\left\langle \chi^{X0}_{E_j} \left| \widehat{\mathscr{D}} \right| \Phi^{\mathrm{cc}}_{\mathrm{v_{cc}}} \right\rangle = \frac{\sqrt{3}}{3}\left(\left\langle \chi^{X0}_{E_j} \left| -\mathscr{D}_{AX}\cos\gamma \right| \psi^{[1/2]}_{\mathrm{v_{cc}}} \right\rangle + \left\langle \chi^{X0}_{E_j} \left| \mathscr{D}_{AX}\sin\gamma \right| \psi^{[1/2]}_{\mathrm{v_{cc}}} \right\rangle\right). \tag{4.75c}$$

Equations (4.75) clearly show what TDMMEs are required, and how to combine them to obtain quantities that are physically relevant to the dynamics.

Finally, I may define shorthands similar to those of Eqs. (4.38)

$$
{}^{cc}_{\mathrm{v_{cc}}}\mathscr{D}^{X0}_{v_X} = \left\langle \Phi^{\mathrm{cc}}_{\mathrm{v_{cc}}} \middle| \widehat{\mathscr{D}} \middle| X,0,v_X \right\rangle = \left\langle X,0,v_X \middle| \widehat{\mathscr{D}} \middle| \Phi^{\mathrm{cc}}_{\mathrm{v_{cc}}} \right\rangle, \tag{4.76a}
$$

$$
{}^{cc}_{\mathrm{v_{cc}}}\mathscr{D}^{X2}_{v_X} = \left\langle \Phi^{\mathrm{cc}}_{\mathrm{v_{cc}}} \middle| \widehat{\mathscr{D}} \middle| X,2,v_X \right\rangle = \left\langle X,2,v_X \middle| \widehat{\mathscr{D}} \middle| \Phi^{\mathrm{cc}}_{\mathrm{v_{cc}}} \right\rangle, \tag{4.76b}
$$

$$
{}^{cc}_{\mathrm{v_{cc}}}\mathscr{D}^{X0}_{E_j} = \left\langle \Phi^{\mathrm{cc}}_{\mathrm{v_{cc}}} \middle| \widehat{\mathscr{D}} \middle| \chi^{X0}_{E_j} \right\rangle \sqrt{\Delta E_j} = \left\langle \chi^{X0}_{E_j} \middle| \widehat{\mathscr{D}} \middle| \Phi^{\mathrm{cc}}_{\mathrm{v_{cc}}} \right\rangle \sqrt{\Delta E_j}. \tag{4.76c}
$$

I can apply the same transformations from Sec. 4.3 that yielded Eq. (4.52) to Eqs. (4.73), obtaining Eq. (4.79) on page 120. I should remind the reader that

$$
\hbar\Delta^{P}_{\mathrm{v_{cc}}} = \mathrm{E}^{\mathrm{cc}}_{\mathrm{v_{cc}}} - E_0 - \hbar\omega^{P}_{0}, \qquad \hbar\Delta_j = E_j - E_0, \tag{4.77}
$$

$$
J = 0,\ 2, \quad \hbar\Delta^{S}_{v_X,J} = \mathrm{E}^{\mathrm{cc}}_{v_{\mathrm{ref}}} - E^{XJ}_{v_X} - \hbar\omega^{S}_{0}, \qquad \hbar\Delta^{P}_{v_{\mathrm{ref}}} = \mathrm{E}^{\mathrm{cc}}_{v_{\mathrm{ref}}} - E_0 - \hbar\omega^{P}_{0}. \tag{4.78}
$$

The physical content of Eq. (4.79) and Eq. (4.52) is almost the same. Both equations are first order differential equations for the time-dependent probability amplitudes c's, both are written for linearly-polarized, chirped laser pulses[a]. However I obtained Eq. (4.52) by neglecting spin-orbit coupling between the $\mathrm{A}^1\Sigma^+$ and the $\mathrm{b}^3\Pi$ states, while spin-orbit coupling is embedded in the transition dipole moment matrix elements ${}^{cc}_{\mathrm{v_{cc}}}\mathscr{D}^{\alpha J}_{v_\alpha}$ when writing Eq. (4.79). Because both sets of equations have the same structure, I can solve them using the same algorithm.

[a] The limiting cases described in Secs. 4.2.1 and 4.3 for the lasers still apply.

$$
\begin{array}{c}
\\
\\
\\

4.5 Numerical solution to the problem

4.5.1 Method used

The results of Sec. 4.3 and Sec. 4.4 show that I need to solve a set of first-order, coupled, differential equations subject to the respective initial conditions Eq. (4.5) and Eq. (4.12), where the only variable is time, t. The Runge-Kutta 4 (RK4) method, an iterative procedure based on Taylor expansions [74], is well-suited to solve such systems of differential equations. In particular, the RK4 method does not require a fixed step size during the propagation, thereby easily accommodating solutions that could be rapidly oscillating.

Before presenting the test cases for the *Mathematica*® implementation of RK4, let me explain how I obtained the various matrix elements necessary to my calculation.

4.5.2 Necessary matrix elements

The matrix elements we encountered in Sec. 4.3 and Sec. 4.4 have the form

$$\int_0^{+\infty} f_1(R) f_2(R) f_3(R)\,\mathrm{d}R = \int_0^{+\infty} F(R)\,\mathrm{d}R. \tag{4.80}$$

At least one of the three integrands above, *e.g.* $f_1(R)$, represents a bound state of an electronic state. Therefore $f_1(R)$ decays exponentially to zero in the classically forbidden region of the potential energy curve. Thus I can restrict the integration domain in Eq. (4.80) from $[0,\infty)$ to a finite range $[a,b]$. I can now approximate the integral using a composite version of Simpson's Rule [74, p. 130].

Consider an even number N of subintervals $[R_i, R_{i+1}]$ that divide $[a,b]$ with

$R_i = a + i(b-a)/N = a + ih$. The composite version of Simpson's Rule states that

$$\int_a^b F(R)\,\mathrm{d}R \approx \frac{h}{3}\left(F(a) + \sum_{i=1}^{N/2-1} F(R_{2i}) + \sum_{i=1}^{N/2} F(R_{2i-1}) + F(b)\right). \tag{4.81}$$

The following section presents how I tested the *Mathematica*® notebooks I wrote to use the Runge-Kutta 4 method and the composite Simpson's Rule.

4.5.3 Test cases

4.5.3.1 Matrix Elements

The simplest operator to consider for my implementation of the composite Simpson's Rule is $f_2(R) = 1$. When $f_1(R) = f_3(R) = f(R)$, the integral in Eq. (4.80) is simply the norm of $f(R)$.

For the $A^1\Sigma^+$ state highest-lying wave functions—calculated with LEVEL [45]—Table 4.1 shows their norm obtained with the composite Simpson's Rule of Eq. (4.81). In the table, the percent relative error between the calculated norm and 1 never exceeds 5×10^{-4}%. The highest percent relative error—1.1×10^{-4}%—occurs for $v_A = 106$. The test cases thus validates my implementation of the composite Simpson's Rule when determining matrix elements.

4.5.3.2 Runge Kutta

In order to solve Eq. (4.52) and Eq. (4.79), I wrote *Mathematica*® notebooks that load all the necessary information (transition dipole moment matrix elements, eigenvalues for the relevant electronic states, laser parameters,...) for the problem, and applies the Runge-Kutta 4 method [74]. To test that the implementation of RK4 included in *Mathematica*® can actually solve the equations of my problem, I need test cases. I am lucky that there exist analytic

v_A	$E_{v_A}(E_h)$	$E_{v_A}(\mathrm{cm}^{-1})$	$\lvert\langle A,1,v_A \rvert A,1,v_A\rangle\rvert^2$
130	0.0522816445	11474.49465	0.9999995209
131	0.05233550722	11486.31615	0.9999995381
132	0.05238371461	11496.89645	0.9999996512
133	0.05242635143	11506.25415	0.9999996525
134	0.05246357487	11514.42375	0.99999973
135	0.05249559178	11521.45065	0.9999997441
136	0.05252268603	11527.39715	0.999999793
137	0.05254519204	11532.33665	0.9999997988
138	0.05256351307	11536.35765	0.9999998439
139	0.05257809699	11539.55845	0.9999999084
140	0.0525894172	11542.04295	0.9999999518
141	0.05259798539	11543.92345	0.9999999272
142	0.05260427222	11545.30325	0.9999999832
143	0.05260865997	11546.26625	0.9999999498
144	0.05261136461	11546.85985	1.000000014
145	0.05261293518	11547.20455	0.9999999673
146	0.05261369199	11547.37065	0.9999999574

Table 4.1: Norm of the highest lying rovibrational wave functions of the $A^1\Sigma^+$ state of NaCs. The norm is calculated using the composite Simpson's Rule. The wave functions were determined using LEVEL [45]. The rovibrational energies are measured from the asymptote of the $X^1\Sigma^+$ state (see Fig. 2.12, p. 40).

solutions to the 2-state problem, both with continuous and pulsed laser (see Sec. 2.3.1), and to the 3-state problem with continuous wave lasers [30, p. 787]. Finally Eq. (4.52) and Eq. (4.79) can easily be reduced to the 2 or 3-state problem.

A test case should be as simple as possible but not simpler, and as close to the actual problem to solve as possible. Let's consider only the reduction of Eq. (4.52) into the 2-state problem, and later into the 3-state problem. Thus the spin-orbit coupling cannot be the source of any discrepancy between the numerical solutions obtained with RK4, and the analytic solutions. Another overall simplification consists in using un-chirped lasers, *i.e.* I set $\mathcal{Y}_P = \mathcal{Y}_S = 0$ in my test cases.

I explained in chap. 3 that I will consider only *one* stationary scattering state. Thus, in Eq. (4.52), $N_E = 1$. I choose the reference energy E_0 equal to the scattering energy of the initial state, so that Δ_1=0. By setting the amplitude of the Stokes pulse, $\mathscr{E}_0^S(t)$ to 0, I restrict the problem to the excitation of population from $|\chi_E^{X0}\rangle$ to the vibrational states of the $A^1\Sigma^+$electronic state. Finally, by setting the pump pulse frequency ω_P in resonance with a given transition, *e.g.* $|\chi_E^{X0}\rangle \rightarrow |A, 1, v_A = 144\rangle$, all other vibrational states in $A^1\Sigma^+$ should not be significantly populated: effectively, Eq. (4.52) reduces to

$$\mathbf{i}\frac{\mathrm{d}}{\mathrm{d}t}\begin{bmatrix} c_E^{X0} \\ c_{144}^{A1} \end{bmatrix} = \begin{bmatrix} 0 & {}^{A1}_{144}\mathscr{D}_E^{X0}\frac{\sqrt{3}}{3}\frac{\mathscr{E}_0^P(t)}{2\hbar} \\ {}^{A1}_{144}\mathscr{D}_E^{X0}\frac{\sqrt{3}}{3}\frac{\mathscr{E}_0^P(t)}{2\hbar} & \Delta_{v_A}^P - 2\mathcal{Y}_P t \end{bmatrix}\begin{bmatrix} c_E^{X0} \\ c_{144}^{A1} \end{bmatrix}, \tag{4.82}$$

To obtain a three state problem, it suffices to set $\mathscr{E}_0^S(t) \neq 0$ and to tune the Stokes laser to a fixed frequency ω_S resonant with a relevant relaxation transition, in the current case the transition $|A, 1, v_A = 144\rangle \rightarrow |X, 0, v_X = 32\rangle$. In this situation, Eq. (4.52) reduces to

$$\mathbf{i}\frac{\mathrm{d}}{\mathrm{d}t}\begin{bmatrix} c_E^{X0} \\ c_{32}^{X0} \\ c_{144}^{A1} \end{bmatrix} = \begin{bmatrix} 0 & 0 & {}^{A1}_{144}\mathscr{D}_E^{X0}\frac{\sqrt{3}}{3}\frac{\mathscr{E}_0^P(t)}{2\hbar} \\ 0 & \Delta_{144}^P - \Delta_{32}^S - 2(\mathcal{Y}_P - \mathcal{Y}_S)t & {}^{A1}_{144}\mathscr{D}_{32}^{X0}\frac{\sqrt{3}}{3}\frac{\mathscr{E}_0^S(t)}{2\hbar} \\ {}^{A1}_{144}\mathscr{D}_E^{X0}\frac{\sqrt{3}}{3}\frac{\mathscr{E}_0^P(t)}{2\hbar} & {}^{A1}_{144}\mathscr{D}_{32}^{X0}\frac{\sqrt{3}}{3}\frac{\mathscr{E}_0^S(t)}{2\hbar} & \Delta_{144}^P - 2\mathcal{Y}_P t \end{bmatrix}\begin{bmatrix} c_E^{X0} \\ c_{32}^{X0} \\ c_{144}^{A1} \end{bmatrix} \tag{4.83}$$

Figure 4.8 compares the analytic solution of Eq. (4.82) for $\Delta^P_{144} = 0$ to the corresponding numerical solution I obtained with my *Mathematica*® notebook. The top panel shows the—constant—intensity of the continuous wave pump laser. The Stokes laser is effectively off, with intensity equal to zero. The middle panel represents the populations in the states $|\chi^{X0}_E\rangle$ and $|A, 1, v_A = 144\rangle$. Notice that the Stokes laser being off, no population gets transferred into the states $|X, J, 32\rangle, J = 0, 2$. Last, the bottom panel represents the absolute error between the analytic and the numerical solution. The absolute error remains below[a] 10^{-15}, *i.e.* *Mathematica*® default machine precision. Therefore, the numerical and analytic solutions are in agreement: the code passes the first test case.

Figure 4.9 shows the analytic and numerical solutions of Eq. (4.83) for $\Delta^P_{144} = \Delta^S_{32} = 0$. The absolute difference between the two types of solutions for all three populations calculated, always remain below 10^{-6}. This amount of error remains acceptable for the populations, and I consider this test case satisfactory.

To end this series of test cases, Fig. 4.10 compares the analytic and numerical solution of Eq. (4.82) for a Gaussian π-pulse at zero detuning. As in the case of Fig. 4.8, the absolute error is still on the order of *Mathematica*® machine precision. This test case is also satisfactory.

In this chapter I derived the key equations I need to solve my problem, Eqs. (4.52) and (4.79). Then I validated with test cases my implementation or use of the mathematical methods necessary to actually solve the problem. The next chapter will present the results of my calculations.

[a] Populations and absolute errors on dimensions are dimensionless

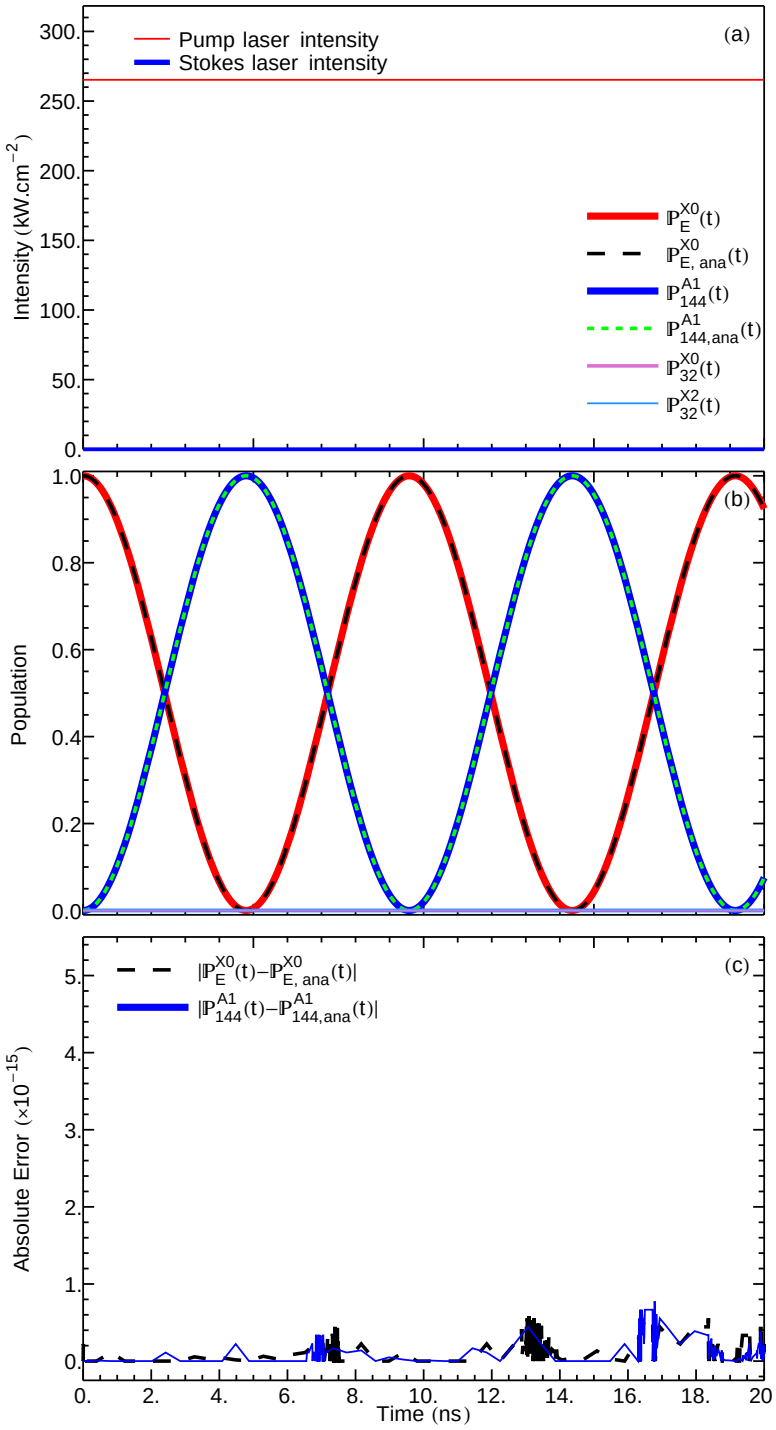

Figure 4.8: (Color online) Test case: 2-state problem with continuous wave laser. **Top panel (a):** Laser intensities. **Middle panel (b):** Populations, the legend appears on panel (a) to avoid clutter. The subscripts "ana" abbreviates "analytic". **Bottom panel (c):** Absolute error between the numerical and analytic solutions. The error is on the order of *Mathematica*® machine precision. The graphical agreement from panel (b) is reinforced by the quantitative agreement of panel (c).

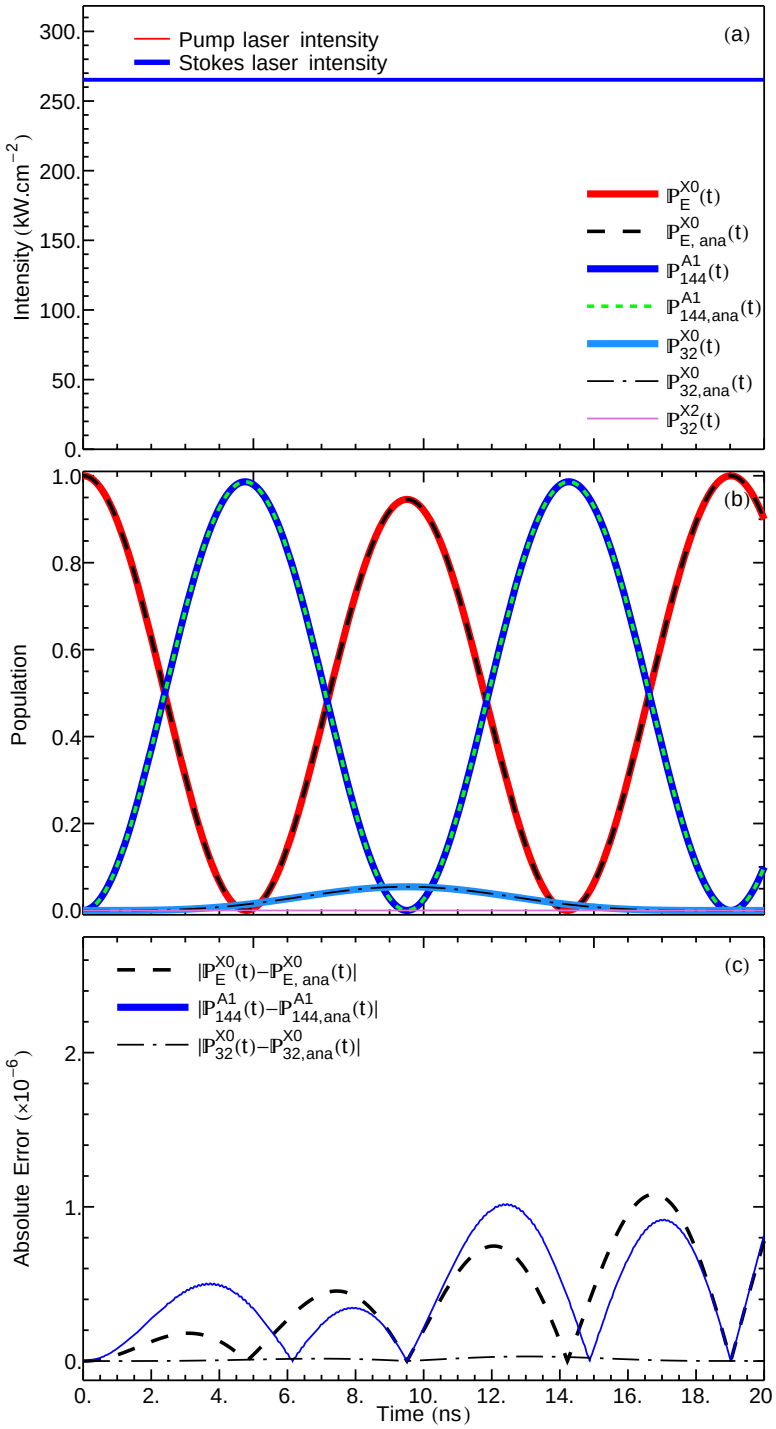

Figure 4.9: (Color online) Test case: 3-state problem with continuous wave laser. **Top panel (a):** Laser intensities. The lasers have equal intensities, hence the 2 lines are superimposed. **Middle panel (b):** Populations (see also Fig. 4.8). **Bottom panel (c):** Absolute error between the numerical and analytic solutions.

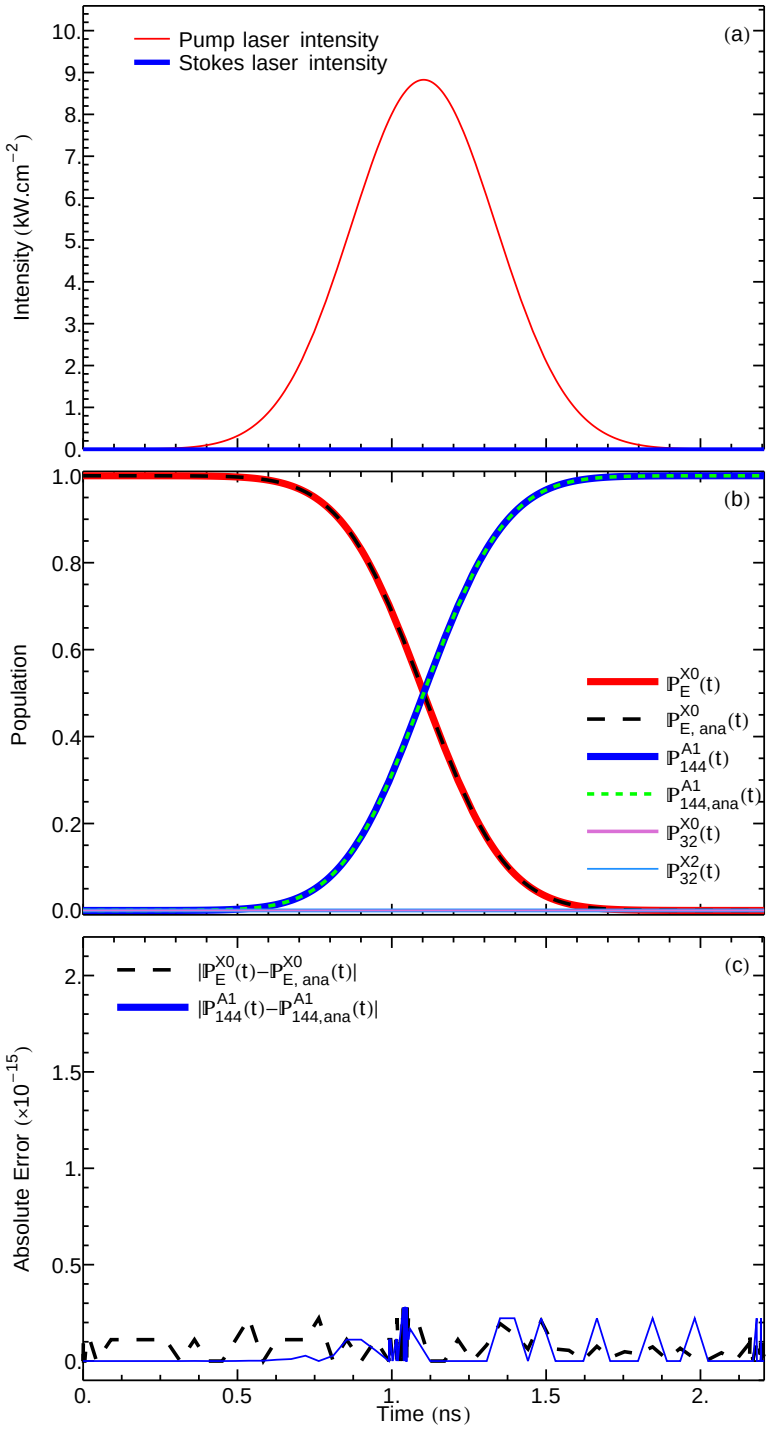

Figure 4.10: (Color online) Test case: 2-state problem with π-pulse laser. **Top panel (a):** Laser intensities. Only the pump laser is on in the 2-state problem. **Middle panel (b):** Populations (see also Fig. 4.8). **Bottom panel (c):** Absolute error between the numerical and analytic solutions. The error is on the order of *Mathematica*® machine precision.

Chapter 5

Results 1: spin-orbit coupled probability density functions

This chapter combines the spin-orbit wave-functions discussed in App. F to form the corresponding probability density functions (PDFs), and discusses their features, which are strikingly different from usual single-channel PDFs.

Figures **5.1** to **5.9** (pp. 133–141) plot the coupled-channel probability density functions (PDFs), on top of the potential energy curves, for the same values of the coupled-channel vibrational index v_{cc} as in Figs. **F.1** to **F.9**. The coupled-channels wave function *are unit-normalized* as they represent bound states, however the amplitude of the PDFs is not to scale in any of the figures. The amplitude was adjusted in each figure to display as much of the important features as possible, and these graphs should not be used to gain any quantitative information about the PDFs. The base line of the PDF matches the value of the corresponding coupled-channels vibrational energy. The top part of each figure represents the square modulus of the expansion coefficients $a_{v_{1/2},v_{cc}}$ and $b_{q_{3/2},v_{cc}}$, defined by Eq. (4.67), and such that[a]:

$$|\Phi^{cc}_{v_{cc}}\rangle = \sum_{v} a_{v,v_{cc}} |\chi_v\rangle |V_{1/2}\rangle + \sum_{q} b_{q,v_{cc}} |\Xi_q\rangle |V_{3/2}\rangle .$$

The quantity $|a_{v_{1/2},v_{cc}}|^2$ is the probability for the system in the coupled-channel state $|\Phi^{cc}_{v_{cc}}\rangle$ to be found in the single-channel state $|\chi_{v_{1/2}}\rangle$, while $|b_{q_{3/2},v_{cc}}|^2$ is the probability for the system in the coupled-channel state $|\Phi^{cc}_{v_{cc}}\rangle$ to be found in the

[a] I justified in Sec. 4.4.2.3 p. 111 how to neglect the part of the expansion that runs over the continuum.

single-channel state $|\Xi_{q_{3/2}}\rangle$. The probability density functions are calculated as

$$|\Phi^{cc}_{v_{cc}}|^2 = \left|\psi^{[1/2]}_{v_{cc}}\right|^2 + \left|\psi^{[3/2]}_{v_{cc}}\right|^2 \tag{5.1}$$

from Eq. (4.70).

For $v_{cc} = 0$, figure 5.1 shows that the PDF has the expected behavior of a ground state vibrational wave function: a single, sharp peak above the minimum of the potential. Likewise for $v_{cc} = 3$, figure 5.2 displays the same feature: the $v_{cc} = 3$ vibrational energy is barely above the minimum of the $A^1\Sigma^+$ state, and not yet above the potential energy crossing, thus the effect of spin-orbit coupling on this state is very small, and the bottom of the well of the $A^1\Sigma^+$ state dominates the behavior of $|\Phi^{cc}_{v_{cc}=3}\rangle$. However, a bit of the probability density tunnels through the local maximum at the bottom of the $V_{1/2}$ potential energy curve.

In figure 5.3, the $v_{cc} = 6$ vibrational energy grazes the local maximum at the bottom of $V_{1/2}(R)$. Imagine that at this energy, the $b^3\Pi_0$ and the $A^1\Sigma^+$ states each have a vibrational state. The rightmost lobe of the wave function belonging to $b^3\Pi_0$ would combine through the spin-orbit interaction with the leftmost lobe of the PDF belonging to $A^1\Sigma^+$, thereby producing the sharp peak in the middle of the coupled-channels state $|\Phi^{cc}_{v_{cc}=6}\rangle$. In terms of the hybrid potentials, the top panels of Fig. 5.3 show that $\chi_{v=6}(R)$ dominates the components of $|\Phi^{cc}_{v_{cc}=6}\rangle$. Looking at panel (a) in Fig. F.3, the connection between $\psi^{[1/2]}_{v_{cc}=6}$ and $\chi_{v=6}(R)$ appears clearly.

At $v_{cc} = 75$ (see Figs. F.4 and 5.4), the function $\psi^{[1/2]}_{v_{cc}=75}(R)$ belongs to the [1/2] channel and the single-channel wave function that contributes the most to $\psi^{[1/2]}_{v_{cc}=75}(R)$ is $|\chi_{v_{1/2}=55}\rangle$. Since $|\chi_{v_{1/2}=55}\rangle$ lives on the $V_{1/2}$ PEC (pink dot-dashed curve in Fig. 5.4), it exists in the relevant classically allowed region. Likewise,

the function $\psi^{[3/2]}_{v_{cc}=75}(R)$ belongs to the [3/2] channel and the single-channel wave function that contributes the most to $\psi^{[3/2]}_{v_{cc}=75}(R)$ is $|\Xi_{q_{3/2}=19}\rangle$, which only exists in the classically allowed region of the $V_{3/2}$ PEC, *i.e.* within the long-dashed, dark green curve of Fig. 5.4. As the two classically allowed region do not have the same spatial extension, that difference shows more strikingly in Fig. F.4. The $v_{cc} = 75$ probability density function also clearly displays a peak above each of the classical turning points at $R \approx 5.58\,a_0, 6.61\,a_0, 9.83\,a_0$, and $12.96\,a_0$. Similar features can also be seen in figures 1 & 4 published by Londoño *et al.* [73].

One must examine the cases $v_{cc} = 165$ & 166 together. First notice that the dominant single-channel contributors are $|\chi_{v_{1/2}=111}\rangle$ and $|\Xi_{q_{3/2}=54}\rangle$ in *both* cases. However, $|\Xi_{q_{3/2}=54}\rangle$ significantly prevails in $|\Phi^{cc}_{v_{cc}=165}\rangle$. Indeed for $v_{cc} = 165$, the PDF essentially equals zero around $R \approx 12.3\,a_0$, *i.e.* the right classical turning point of the $V_{3/2}$ channel. Since $|\Xi_{q_{3/2}=54}\rangle$ carries most of the probability, there is no probability left to find the system in state $|\Phi^{cc}_{v_{cc}=165}\rangle$ in the classically forbidden region of $V_{3/2}$ beyond $R \approx 12.3\,a_0$. On the contrary, $|\chi_{v_{1/2}=111}\rangle$ prevails in $|\Phi^{cc}_{v_{cc}=166}\rangle$ and becomes the main probability carrier. Thus $|\Phi^{cc}_{v_{cc}=166}\rangle$ *does* extend in the classically forbidden region of $V_{3/2}$. Notice also how the dominance of $|\chi_{v_{1/2}=111}\rangle$ absorbs the lobe of $|\Xi_{q_{3/2}=54}\rangle$ near $R = 12.3\,a_0$, in contrast to the persistence of the equivalent lobe for $|\Phi^{cc}_{v_{cc}=75}\rangle$. Interferences similar to those that appear for $v_{cc} = 165$ & 166 on the left of the potential avoided crossing exist on the right of said crossing for $v_{cc} = 194$ & 195, which I discuss next.

The PDF of $v_{cc} = 195$ shows destructive interferences to the right of the potential avoided crossing. Constructive interferences occur immediately after. While the internuclear separation increases, the succession of destructive and constructive interferences is blurred. As $|\Xi_{q_{3/2}=66}\rangle$ reaches its right classical

turning point on $V_{3/2}$, it interferes less and less with $|\chi_{v_{1/2}=128}\rangle$ (see the difference in oscillations in Fig. F.8), creating the jagged peaks between $R = 12\,a_0$ and $R = 14.5\,a_0$. Then as $|\Xi_{q_{3/2}=66}\rangle$ decreases to 0 in the classically forbidden region of $V_{3/2}$, it no longer interferes with $|\chi_{v_{1/2}=128}\rangle$, yielding a smooth PDF. The state $v_{cc} = 194$ has the same dominant single-channel contributors as $v_{cc} = 195$, however the contributions are swapped: $|\Xi_{q_{3/2}=66}\rangle$ now dominates the coupled PDF for $|\Phi^{cc}_{v_{cc}=194}\rangle$. Consequently the interference effect of $|\chi_{v_{1/2}=128}\rangle$ is not as strong as for $v_{cc} = 195$. In particular, the destructive interferences do not appear. The constructive interference effect near $R = 9\,a_0$ has a greater amplitude, and the residual interference that cause the jagged peaks of $v_{cc} = 195$ are virtually nonexistent for $v_{cc} = 194$. The structure of the $v_{cc} = 194$ & 195 PDFs for NaCs is more pronounced than for the RbCs PDFs reported in in [73]. In this reference, only one constructive or destructive interference particularly stands out (see Fig. 4 therein).

The last probability density figure (5.9) for $v_{cc} = 235$ is quite different from the $v_{cc} = 195$ case, in particular the intermediate peak disappeared. Notice that $|\Phi^{cc}_{235}\rangle$ has no probability for small R values between the inner walls of the potentials. Also, above the potential avoided crossing, spin-orbit coupling causes a slight bump *up from* the base line on the PDF, rather than a dip *down to* the base line. Furthermore, for $R > 9\,a_0$, the locus of the top of the arches of $|\Phi^{cc}_{235}\rangle$ does not increase monotonically, the coupling between the channels causes a slight change in the slope of this locus around $R = 15\,a_0$. This behavior is more pronounced for coupled-channel states with vibrational energy *above* the asymptote of $V_{1/2}$.

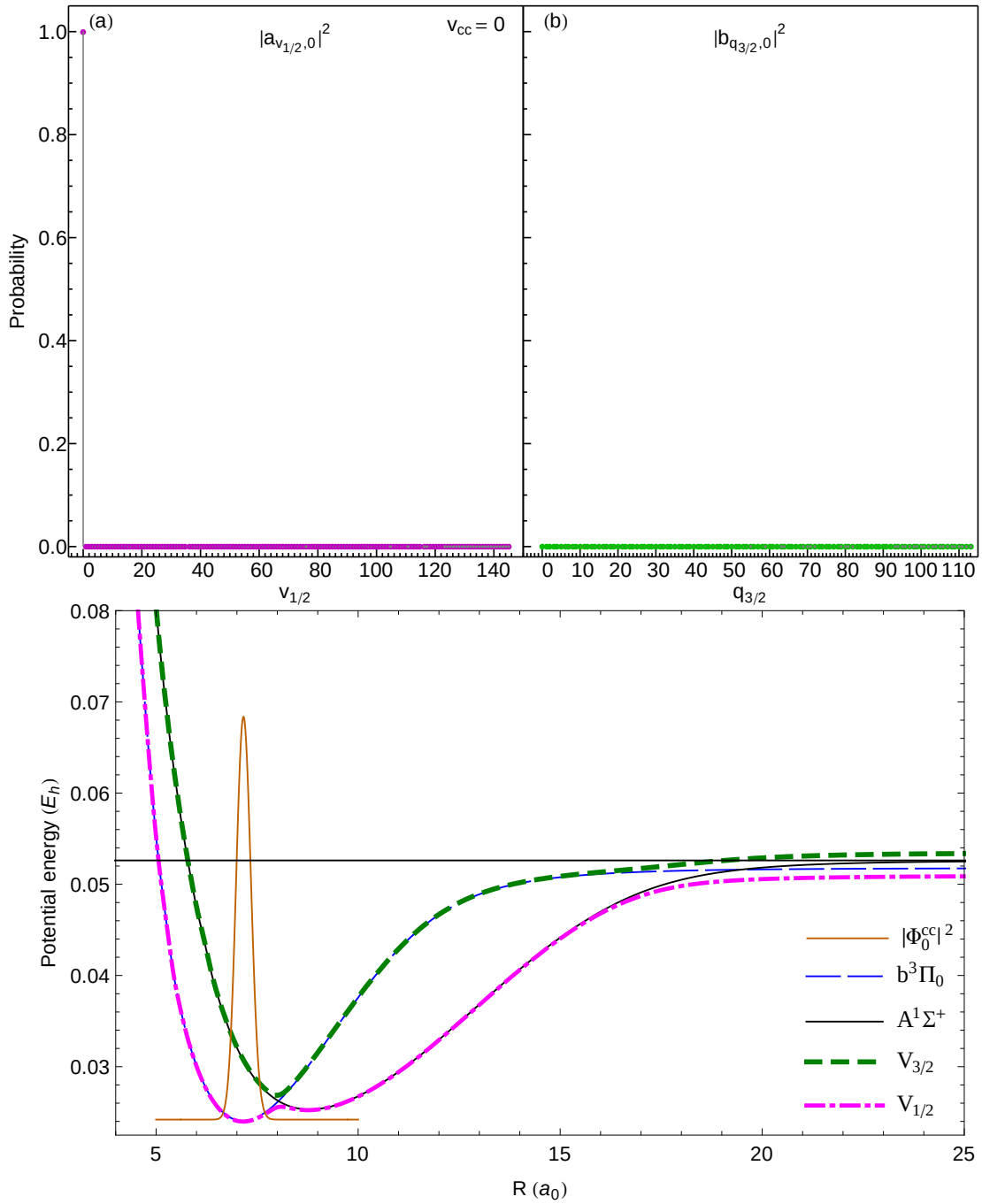

Figure 5.1: (Color online) **Bottom**—Coupled-channel probability density function for $v_{cc} = 0$. Potential energy curves are in the background. The base line for the probability density function matches the corresponding rovibrational energy. As the ground coupled-channel state, with rovibrational energy barely above the lowest of all potentials minima, the probability density function has the expected characteristic single peak centered in the middle of the well. **Top**—Probability for the system in the coupled-channel state $|\Phi^{cc}_{v_{cc}=0}\rangle$ to be found (panel (**a**)) in the state $|\chi_{v_{1/2}}\rangle$ or (panel (**b**)) the state $|\Xi_{q_{3/2}}\rangle$. The dominant contribution comes from $|\chi_{v_{1/2}=0}\rangle$, since $|\Phi^{cc}_{v_{cc}=0}\rangle$ lies at the very bottom of the $V_{1/2}$ potential energy curve.

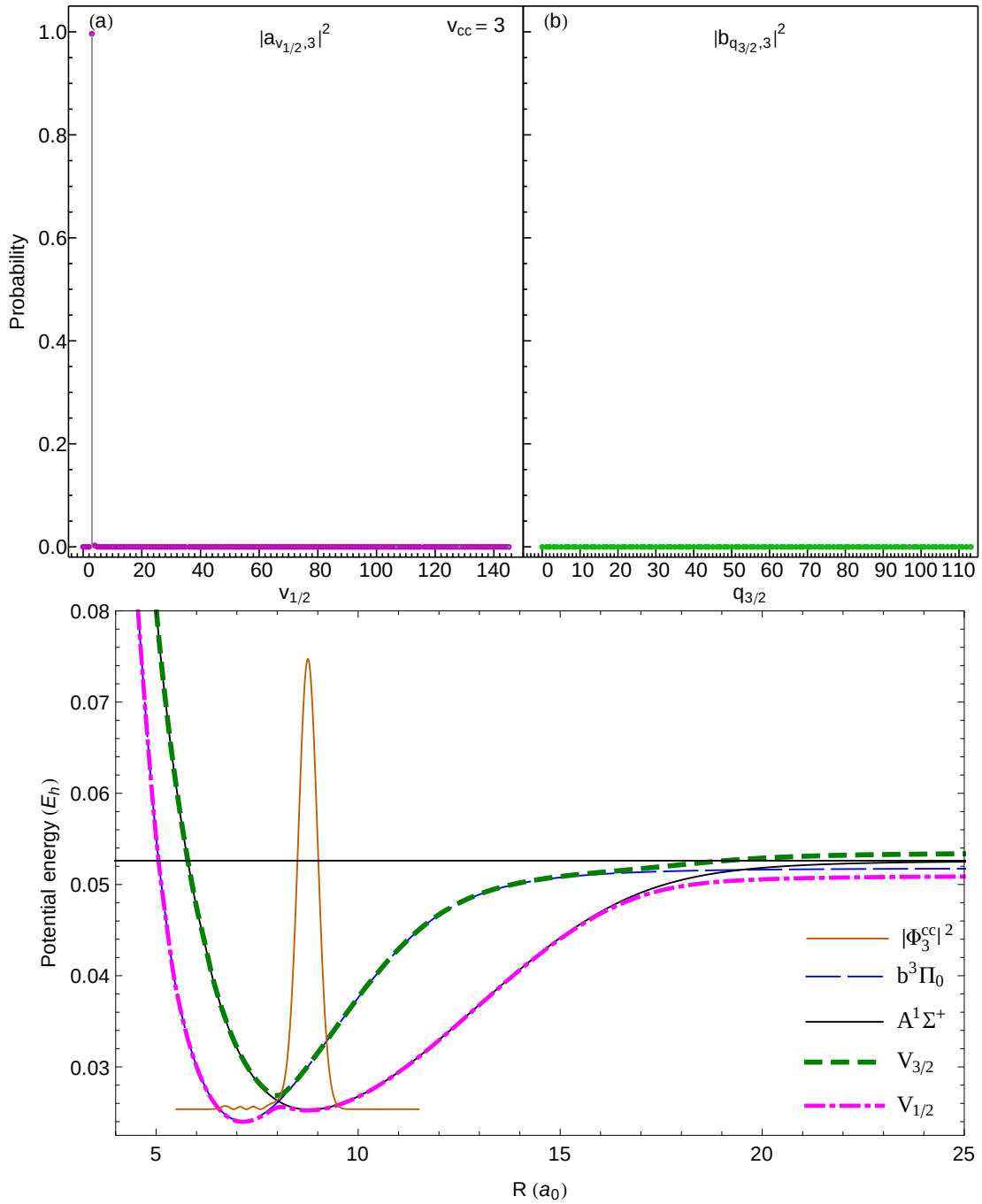

Figure 5.2: (Color online) **Bottom**— Coupled-channel probability density function for $v_{cc} = 3$. This state has a rovibrational energy barely above the second minimum of the lowest potential, again the probability density function has the expected characteristic single peak centered in the middle of this well. **Top**—The dominant contribution comes from $|\chi_{v_{1/2}=3}\rangle$, since $|\Phi^{cc}_{v_{cc}=3}\rangle$ lies at the bottom of the second well of the $V_{1/2}$ potential energy curve. See Fig. 5.1 p. 133 for additional information.

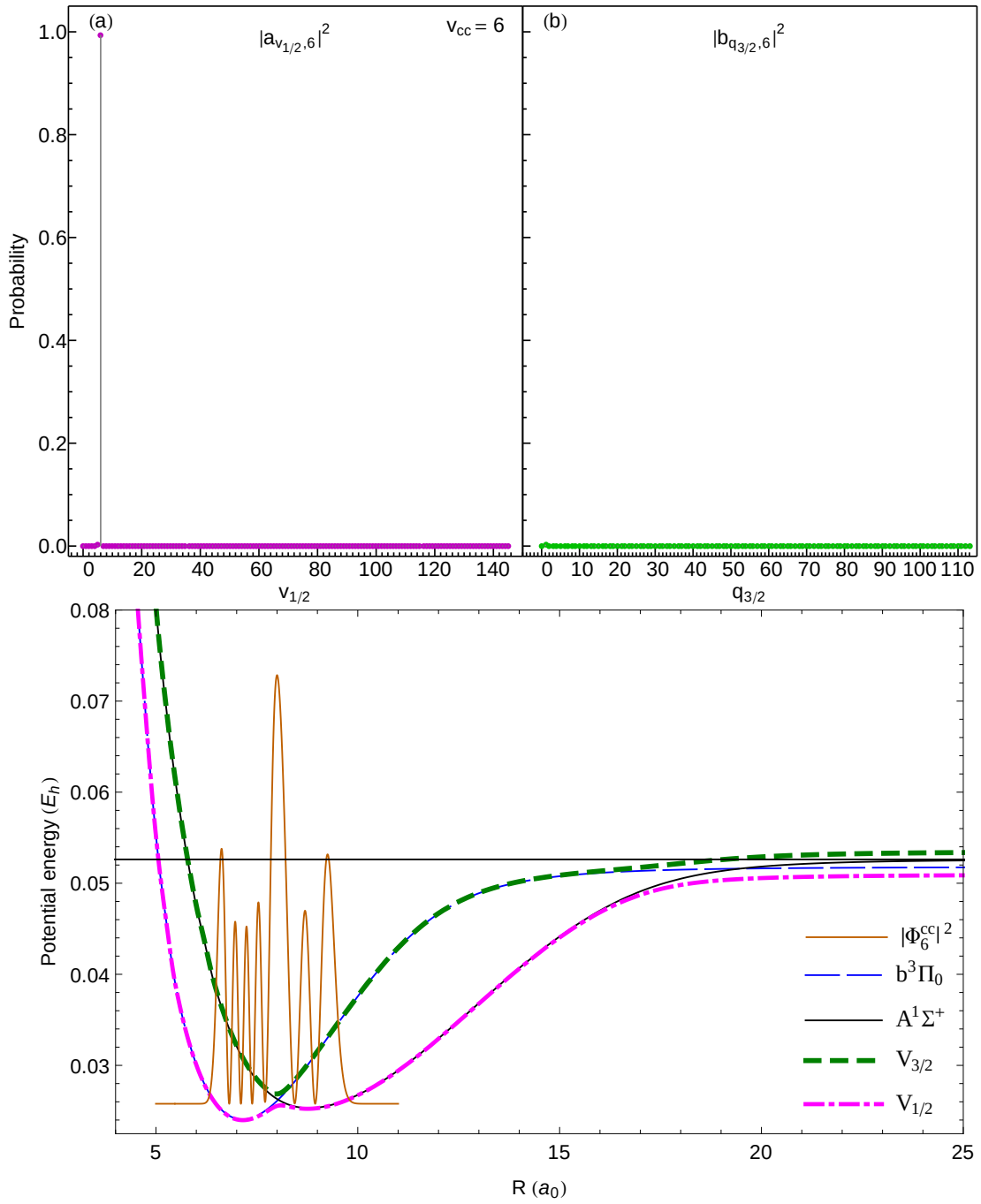

Figure 5.3: (Color online) **Bottom**—Coupled-channel probability density function for $v_{cc} = 6$. The rovibrational energy is barely grazing the local maximum of the potential, producing the pronounced peak above the local maximum. **Top**—The dominant contribution comes from $|\chi_{v_{1/2}=6}\rangle$: the energy does not yet go into the classically region of the $V_{3/2}$, hence the lack of contribution from any of the $|\Xi_{v_{3/2}}\rangle$. See Fig. 5.1 p. 133 for additional information.

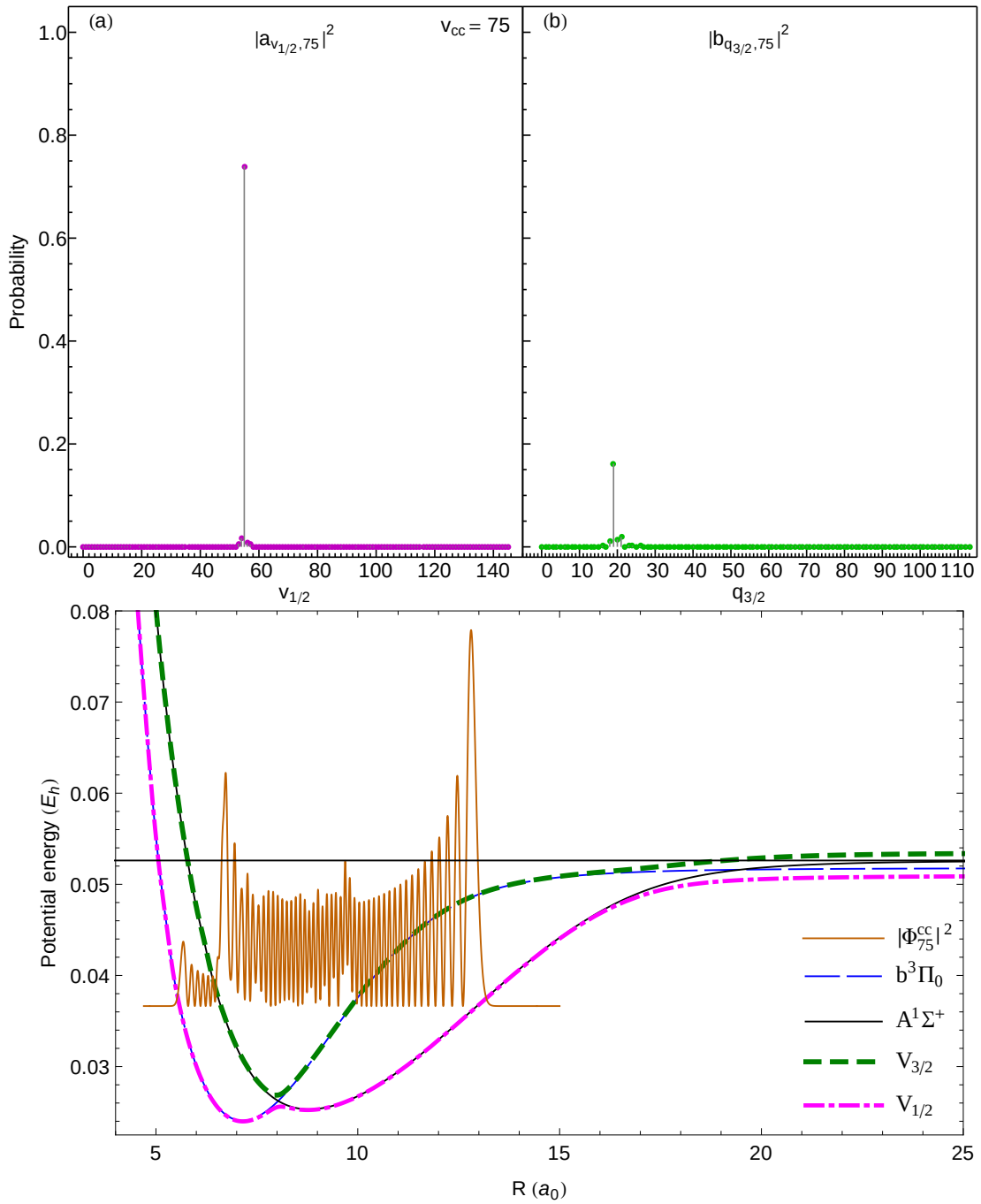

Figure 5.4: (Color online) **Bottom**—Coupled-channel probability density function for $v_{cc} = 75$. The probability density function resembles that of the single-channel $V_{1/2}$ potential. However, the spin-orbit interaction causes the disturbance in the oscillations around $7\,a_0$ near the inner wall of the $V_{3/2}$ potential. **Top**—The state $|\chi_{v_{1/2}=55}\rangle$ dominates the contributions from $V_{1/2}$, while the state $|\Xi_{v_{3/2}=19}\rangle$ is the dominant contribution from $V_{3/2}$. The small components of the states $|\chi_{v_{1/2}=54,56}\rangle$ and $|\Xi_{v_{3/2}=18,20,21}\rangle$ contribute to the disturbances in the region between $7\,a_0$ and $9.5\,a_0$. See Fig. 5.1 p. 133 for additional information.

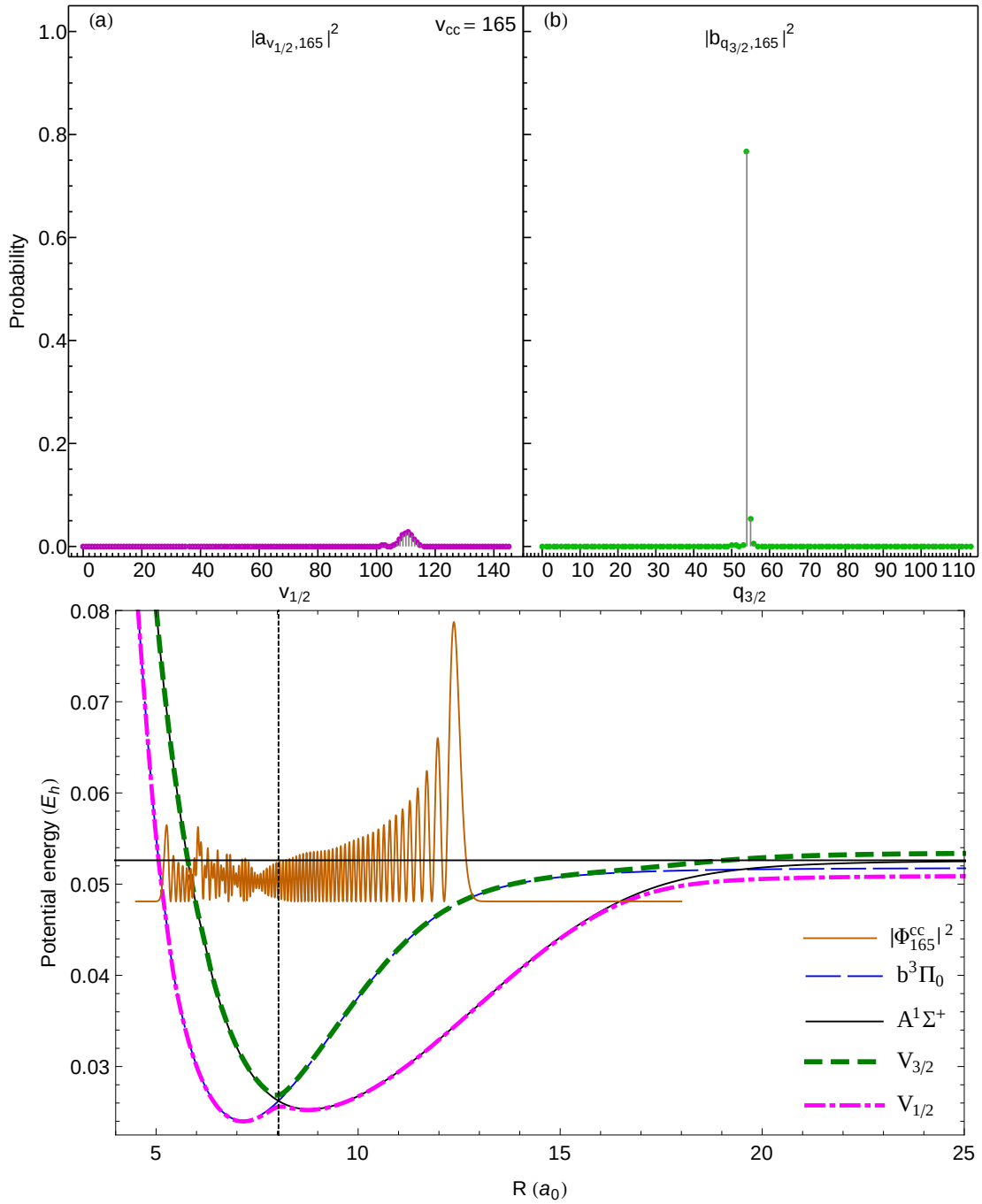

Figure 5.5: (Color online) **Bottom**—Coupled-channel probability density function for v_{cc} = 165. **Top**—The state $|\Phi^{cc}_{v_{cc}=165}\rangle$ is mostly dominated by $|\Xi_{q_{3/2}=54}\rangle$. The contribution of the $|\chi_{v_{1/2}}\rangle$ states near $v_{1/2} = 111$ yields the part of the probability density function below $6\,a_0$. This contribution is responsible for the interferences between $6\,a_0$ and $7.5\,a_0$. The probability density is drawn with the same scaling factor as v_{cc} = 166 in Fig. 5.6. Vertical dashes: position of the potential avoided crossing. See Fig. 5.1 p. 133 for additional information.

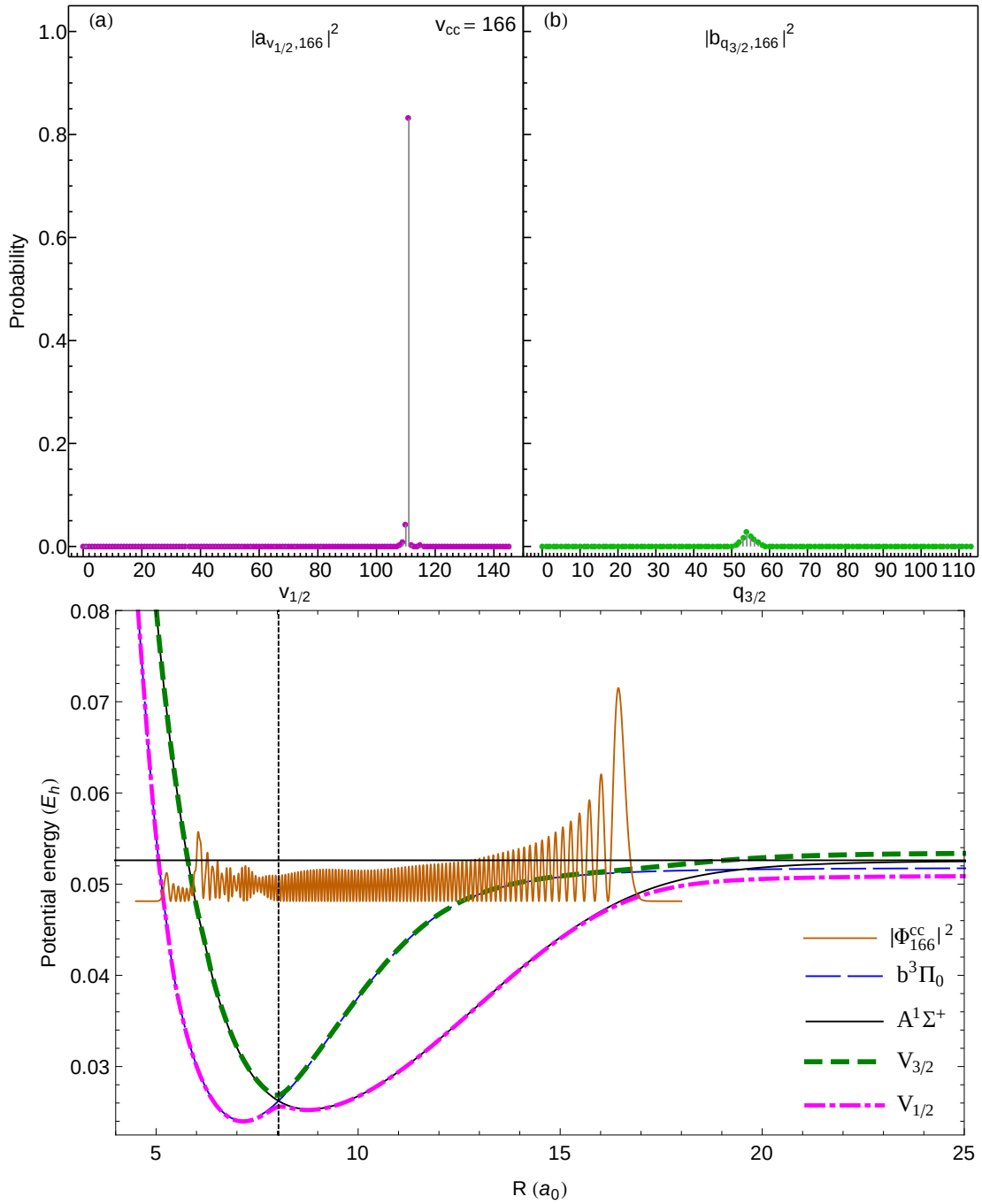

Figure 5.6: (Color online) **Bottom**—Coupled-channel probability density function for $v_{cc} = 166$. **Top**—The state $|\Phi^{cc}_{v_{cc}=166}\rangle$ is mostly dominated by $|\chi_{v_{1/2}=111}\rangle$. The contribution of the $|\chi_{v_{1/2}=111}\rangle$ states yields the part of the probability density function below $6\,a_0$. The small contributions from the states near $|\Xi_{q_{3/2}=54}\rangle$ are responsible for the interferences between $6\,a_0$ and $7.5\,a_0$. The probability density is drawn with the same scaling factor as $v_{cc} = 165$ in Fig. 5.5. Vertical dashes: position of the potential avoided crossing. See Fig. 5.1 p. 133 for additional information.

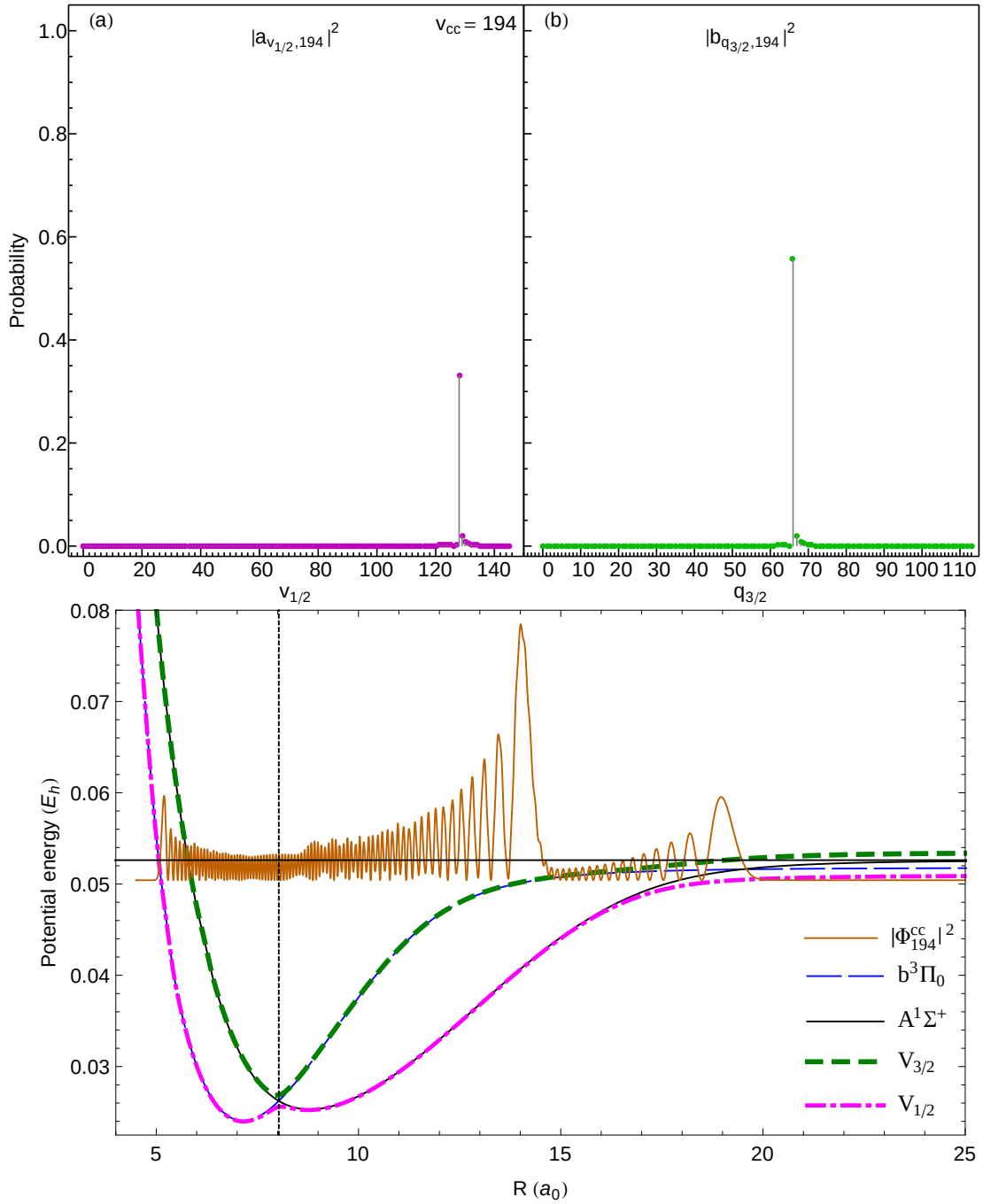

Figure 5.7: (Color online) **Bottom**—Coupled-channel probability density function for v_{cc} = 194. This probability density function shows features similar to those reported by Londoño *et al.* [73]; 4 local maxima located above the corresponding classical turning points, although the maximum above the inner $V_{3/2}$ classical turning point is barely visible, and a irregular envelope of the probability density function. Vertical dashes: position of the potential avoided crossing. **Top**—The main contributions are from $|\chi_{v_{1/2}=128}\rangle$ and $|\Xi_{q_{3/2}=66}\rangle$. The probability density is drawn with the same scaling factor as v_{cc} = 195 in Fig. 5.8. See Fig. 5.1 p. 133 for additional information.

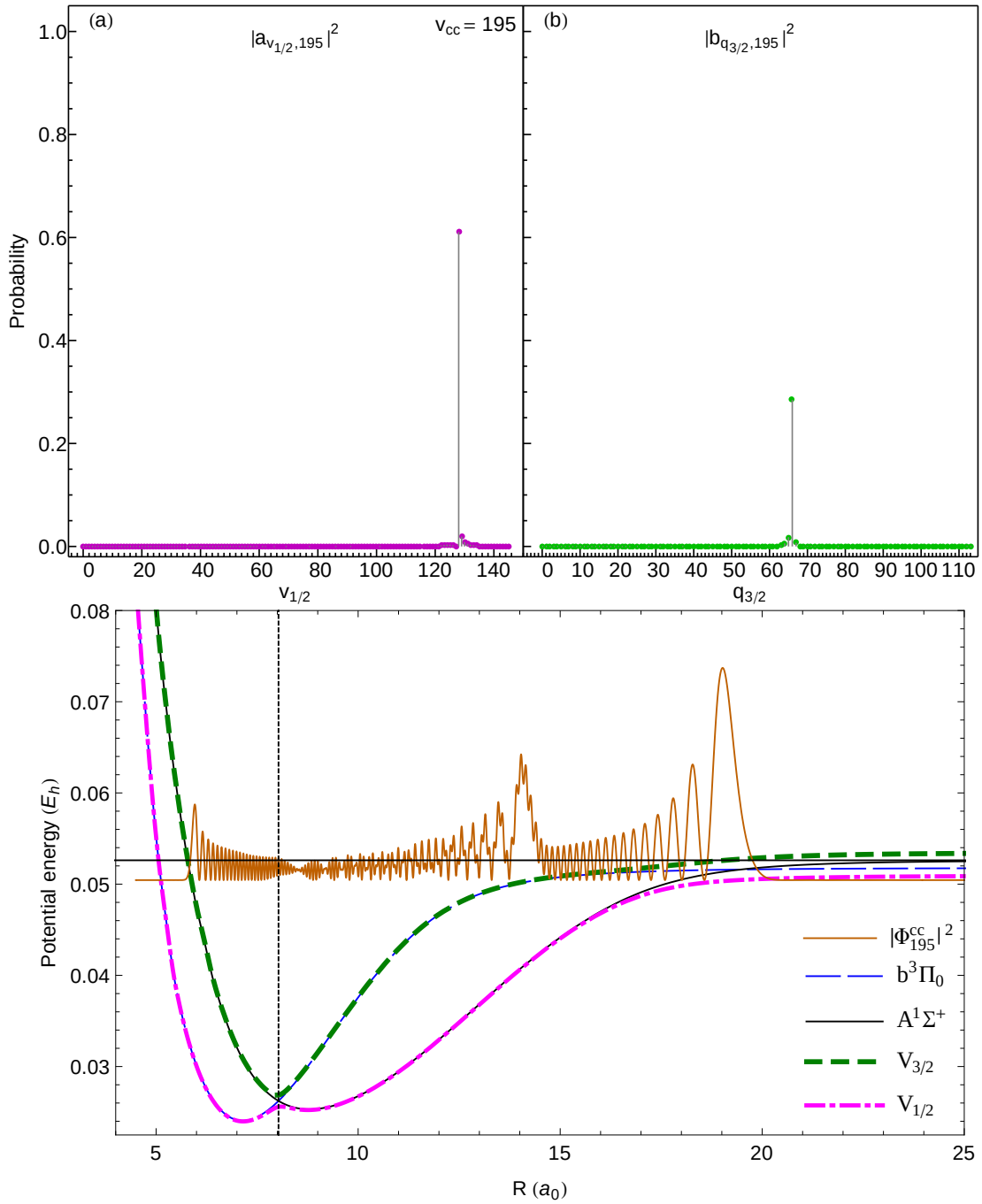

Figure 5.8: (Color online) **Bottom**—Coupled-channel probability density function for v_{cc} = 195. This probability density function exhibits spin-orbit coupling consequences through the compression above the potential avoided crossing, and the jagged intermediate peak. Vertical dashes: position of the potential avoided crossing. **Top**—The main contributions are from $|\chi_{v_{1/2}=128}\rangle$ and $|\Xi_{q_{3/2}=66}\rangle$. The probability density is drawn with the same scaling factor as v_{cc} = 194 in Fig. 5.7. See Fig. 5.1 p. 133 for additional information.

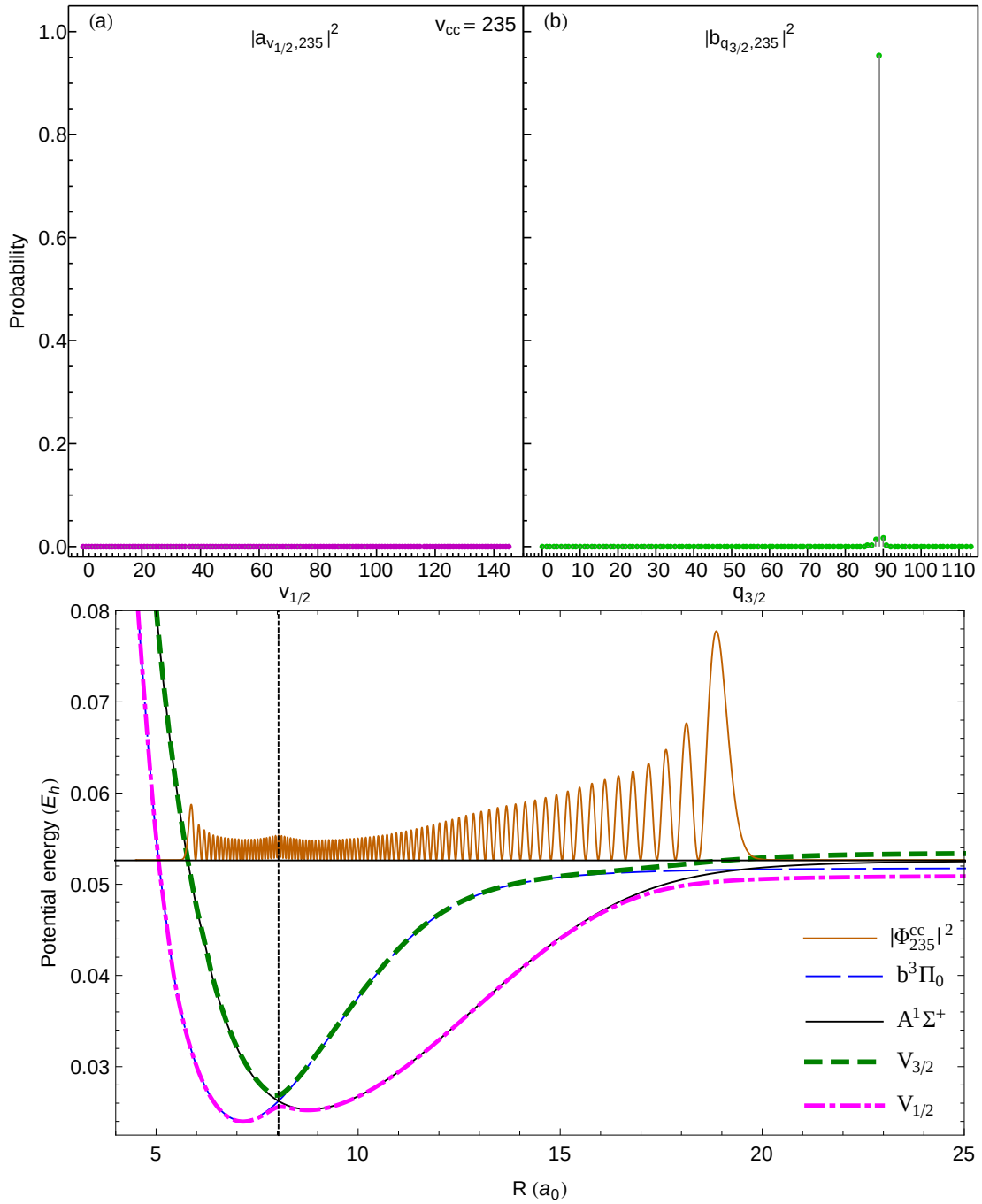

Figure 5.9: (Color online) **Bottom**—Coupled-channel probability density function for $v_{cc} = 235$. The probability density function appears to belong only to $V_{3/2}$. The spin-orbit coupling bulges the probability above the potential avoided crossing. For high-lying states, spin-orbit coupling replaces the local maximum in the probability density function above the right classical turning point for $V_{3/2}$ with a slightly non monotonic increase of the locus of the top of the arches: the tops form a less steep slope from $13\,a_0$ to $\approx 17\,a_0$. **Top**—The main contribution is from $|\Xi_{q_{3/2}=89}\rangle$. Since $E^{cc}_{v_{cc}=235} > e_\infty$, there are no contributions from the $|\chi_{v_{1/2}}\rangle$ states. Vertical dashes: position of the potential avoided crossing. See Fig. 5.1 p. 133 for additional information.

Chapter 6

Results 2: Transfer of populations

This chapter has two parts. First, Sec. 6.1 discusses the free-bound and bound-bound electric transition dipole moment matrix elements defined in Chap. 4. There, I explain which intermediate state I chose and why. In Sec. 6.2, I present estimated formation rates for the photoassociation of NaCs into states below the Na(3S)+Cs(6^2P) asymptote, and find these rates similar to those obtained experimentally for other alkali diatomic molecules.

Second, Sec. 6.4 presents the solution to Eq. (4.52) and Eq. (4.79), in the various laser configurations I studied. In particular for chirped laser, I emphasize the importance of the initial laser detunings and how chirping stabilizes the population transfer when the pulse delay changes.

6.1 Transition Dipole Moment Matrix Elements

Two sets of transition dipole moment matrix elements (TDMME) are relevant to this research: (a) the free-bound TDMME (fbTDMME) that represent the coupling strength between the continuum states and the bound states of the excited electronic state, and (b) the bound-bound (bbTDMME) that represent the coupling between the bound states of the excited state and the bound state of the ground electronic states. Both sets were defined in Chap. 4.

I explained in Chap. 3 the choice of the initial state; let's explain my choice of the final state. Keep in mind the goal of this project, exposed in Chap. 1: to create molecules in a low lying level of the $X^1\Sigma^+$ state, with a permanent electric dipole moment as high as possible. Ideally, one would aim for the

$|X, J_X = 0, v_X = 0\rangle$ bound state, however the bbTDMME between this state and the high-lying states of the excited electronic state are detrimental to a transition by stimulated emission. Yet, Aymar and Dulieu [19] showed (see their Fig. 4) that for NaCs the permanent electric dipole moment is fairly constant when the vibrational quantum number v_X increases: the permanent electric dipole moment stays close to −4.5 Debye for all $v_X \leq 40$.

I should choose a state in $X^1\Sigma^+$ not so low in the well that it would be inaccessible by stimulated emission from the first excited electronic asymptote, and yet no so high that its permanent electric dipole moment would be too different from the average value −4.5 Debye. The state $|X, J_X = 0, v_X = 32\rangle$ meets those criteria.

Figure 6.1 p. 144 (top panel) shows the free-bound TDMMEs defined in Eq. (4.38) between the continuum stationary scattering state chosen in Sec. 3.1 and the bound vibrational states of the $A^1\Sigma^+$ state. As expected from the Franck-Condon principle [24, Chap. 11], the fbTDMMEs are close to 0 for bound-states that lie low in the well, but are much greater for bound states of $A^1\Sigma^+$ near dissociation. Experimentalists [22, 75] rely on the magnitude of these bfTDMMEs to perform photoassociation spectroscopy. The bottom panel of Fig. 6.1 displays the bound-bound TDMMEs from any $|A, J_A = 1, v_A\rangle$ of the $A^1\Sigma^+$ electronic state into the state $|X, 0, 32\rangle$. The rovibrational states $|X, 0, 32\rangle$ and $|X, 2, 32\rangle$ are so close in energy that their wave function are almost identical, yielding no significant difference between the bbTDMMEs from $A^1\Sigma^+$ into $|X, 0, v_X = 32\rangle$ or $|X, 2, 32\rangle$. Once more, as expected from the Franck-Condon principle, the higher v_A, the lower the amplitude of the oscillations of the bbTDMME. With the help of Fig. 6.1, one can choose a range of intermediate states $|A, J_A = 1, v_A\rangle$ that (i) are not to close to the dissociation asymptote of the $A^1\Sigma^+$

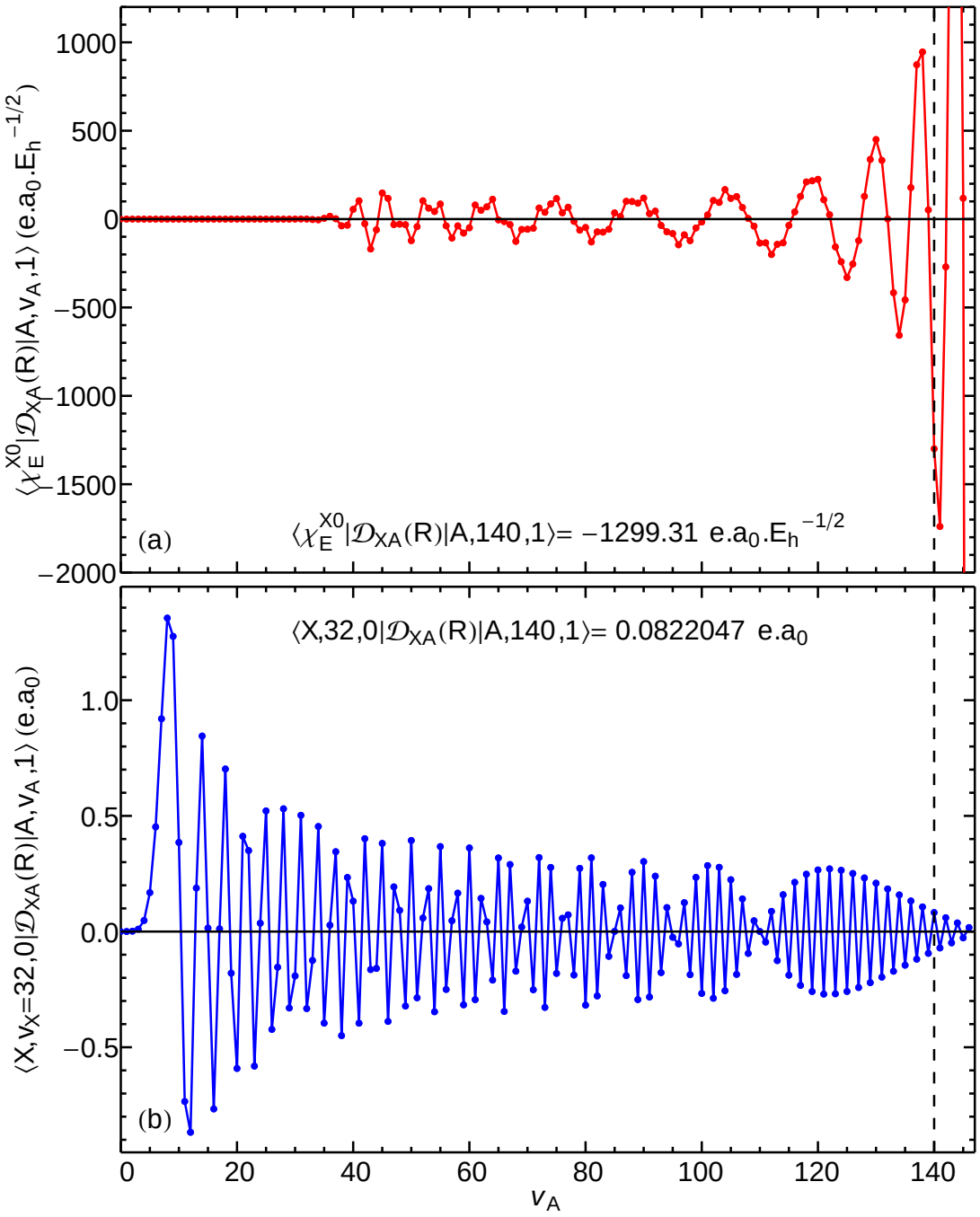

Figure 6.1: (Color online) **Top**—Free-bound transition dipole moment matrix elements between the stationary scattering state with energy $E = 0.317 \times 10^{-9}\, E_h$, and the vibrational states of the $A^1\Sigma^+$electronic state. **Bottom**—Bound-bound transition dipole moment matrix elements between the vibrational state $|X, J_X = 0, v_X = 32\rangle$ of $X^1\Sigma^+$, and the vibrational states of the $A^1\Sigma^+$electronic state. The vertical dashed line marks the intermediate state chosen, $v_A = 140$.

state, to prevent the pump laser pulse from exciting the scattering atoms into the continuum above $A^1\Sigma^+$, (ii) that are not so far from the same asymptote that the fbTDMME is too small (iii) and finally that have a reasonable bbTDMME with $|X, J_X = 0, v_X = 32\rangle$. With these criteria, I chose $|A, J_A = 1, v_A = 140\rangle$, marked by the vertical dashed line on Fig. 6.1 as the stepping stone in my process to transfer population from the continuum to $|X, J_X = 0, v_X = 32\rangle$. The pump laser will be tuned close to the $|\chi_E^{X0}\rangle \rightarrow |A, J_A = 1, v_A = 140\rangle$ transition energy, and the Stokes pulse close to the $|A, J_A = 1, v_A = 140\rangle \rightarrow |X, J_X = 0, v_X = 32\rangle$ transition energy.

Figure 6.2 shows the free-bound and bound-bound transition dipole moment matrix elements calculated when accounting for spin-orbit coupling effect, as explained in Eq. (4.75), p. 118. The free-bound TDMMEs (top panel) increase drastically when the coupled-channel bound state energy nears either the Na(3S)+Cs($6^2P_{1/2}$) asymptote ($v_{cc} \rightarrow 215$) or the Na(3S)+Cs($6^2P_{3/2}$) asymptote ($216 \leq v_{cc} \leq 259$). For states near a dissociation asymptote, much of the probability density accumulates around the rightmost classical turning point: thus the overlap with continuum states of the $X^1\Sigma^+$ state have higher values, making the fbTDMME greater than between the same continuum states and coupled-channel bound states that lie lower in energy. The probability density function for the states $210 \leq v_{cc} \leq 215$, very near the Na(3S)+Cs($6^2P_{1/2}$) asymptote, are significant only at large R values. Thus, the TDMME between these states and the continuum states of $X^1\Sigma^+$ state are comparatively large. Conversely, the bbTDMME are very small for these values of v_{cc}. This explains the features just below $v_{cc} = 215$ in Fig. .6.2. The probability density functions for the states immediately above the Na(3S)+Cs($6^2P_{1/2}$) asymptote receive a nearly exclusive contribution from the $V_{3/2}$ channel, which matches the $b^3\Pi_0$ state in

this range of energy. The probability density function accumulates at the right classical turning point with $V_{3/2}$. Consequently, the overlap with the continuum states of the $X^1\Sigma^+$ state and the corresponding fbTDMME are very small (see Fig. 6.2), illustrating the $\Delta S = 0$ that forbids transitions between the singlet and the triplet.

For the purpose of my study, I chose as an intermediate state the coupled-channel bound state $|\Phi^{cc}_{v_{cc}=254}\rangle$. This state has TDMMEs that meet the same criteria as those outlined when choosing a bound state for the $A^1\Sigma^+$ state.

6.2 Photoassociation rates for NaCs

6.2.1 Validation of photoassociation rates obtained

For a given temperature and intensity of a continuous wave laser, the photoassociation rate K_{PA} is an experimental measure of the fbTDMMEs. The rate K_{PA} from the continuum at temperature T of the ground electronic state into a bound state $|Y, v_Y, J = 1\rangle$ of electronic state Y with rotational quantum number $J = 1$ is related to the fbTDMME through [76, Eq. (1)]

$$K_{PA}(v) = 3\left(\frac{3\lambda_{th}^2}{2\pi}\right)^{\frac{3}{2}} \frac{h}{2} \left| \left\langle Y, v_Y, J = 1 \,|\mathscr{D}_{YX}|\, \chi^{X0}_{E=k_BT/2} \right\rangle \right|^2, \tag{6.1}$$

where λ_{th} is the thermal de Broglie wavelength $\lambda_{th}^2 = \frac{h}{3\mu k_B T}$. More details on the theory of photoassociation appear in [69, 77, 78].

The photoassociation rate is calculated from a continuum state into a single bound state of an excited electronic potential. Among the quantities that enter the calculation of the photoassociation rate is the fbTDMME between that continuum state and the bound state one photoassociates to [77, 78]. There-

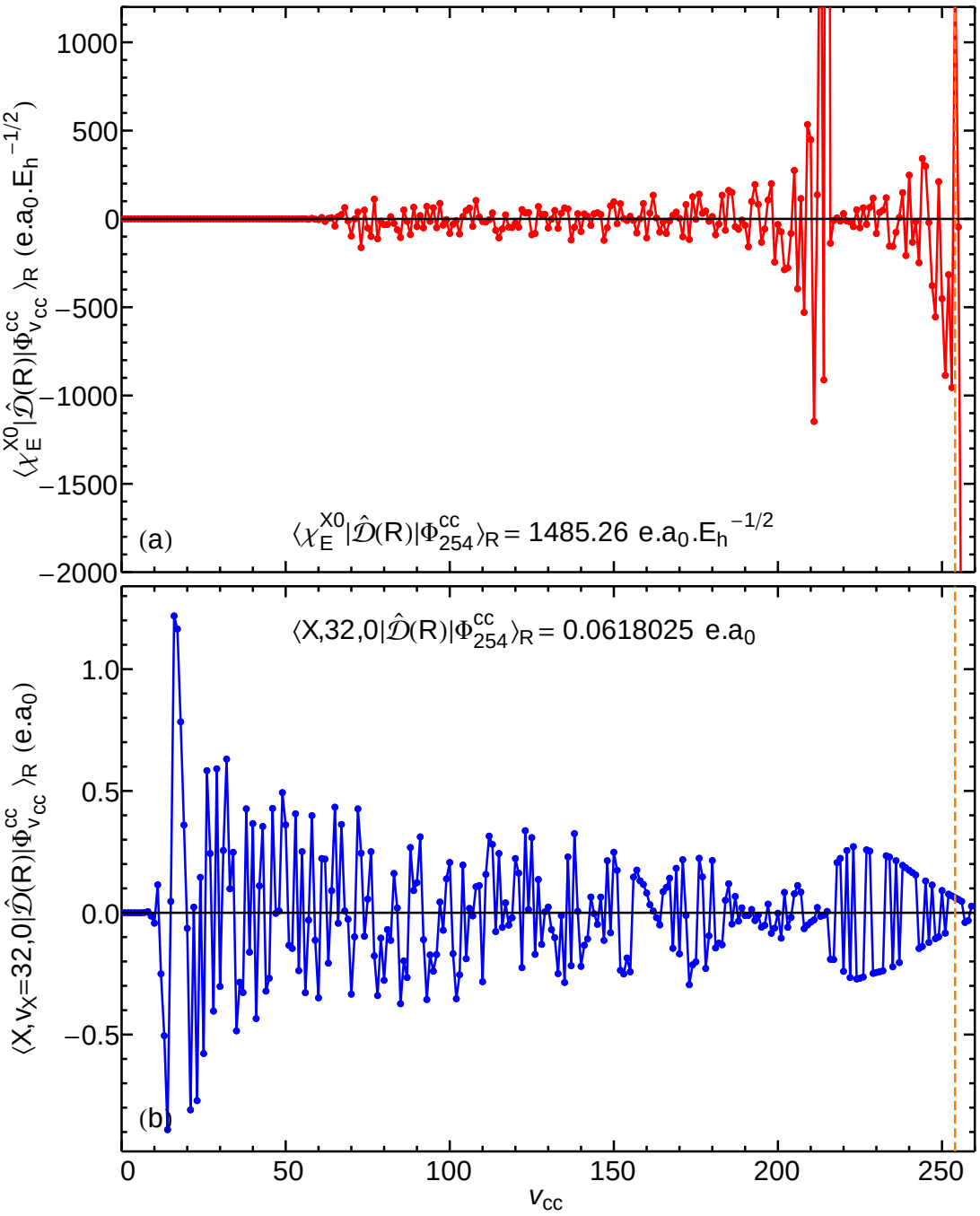

Figure 6.2: (Color online) **Top**—Free-bound transition dipole moment matrix elements between the stationary scattering state with energy $E = 0.317 \times 10^{-9}\, E_h$, and the coupled-channel vibrational states of the $A^1\Sigma^+ \sim b^3\Pi_0$ manifold, equivalent to the coupled-channels $V_{1/2} \sim V_{3/2}$. **Bottom**—Bound-bound transition dipole moment matrix elements between the vibrational state $|X, J_X = 0, v_X = 32\rangle$ of $X^1\Sigma^+$, and the coupled-channel vibrational states of the $A^1\Sigma^+ \sim b^3\Pi_0$ manifold. The vertical dashed line marks the intermediate state chosen, $v_{cc} = 254$.

fore one can only calculate K_{PA}'s towards the bound states of the potential one is interested to probe, and essentially K_{PA} is another way of representing the fbTDMMEs, while including at the same time more experimental details. Ultimately, one can not calculate more K_{PA} than there are bound states in a given potential.

In this section, I use Eq. (6.1) to validate my calculation of the fbTDMMEs by comparing with the experimental results obtained in [22] for NaCs. Moreover by using similar laser intensities and sample temperature, I can also compare my results for NaCs to those published in [18] for RbCs and in [79] for LiCs.

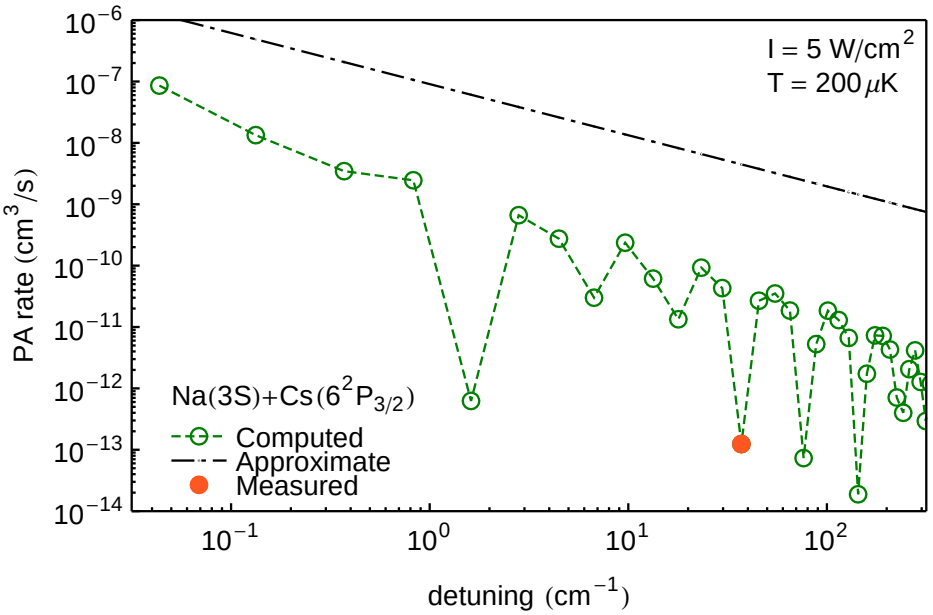

Figure 6.3: (Color online) Photoassociation rate for NaCs at $T = 200\mu K$ using a continuous wave laser with intensity $I = 5\text{W/cm}^2$ vs. detuning. Detunings are measured below the Na(3S)+Cs(6$^2P_{3/2}$) asymptote. The filled green circle corresponds to the detuning closest to the experimental condition of [22].

Figures 6.3 & 6.4 show the photoassociation rates for NaCs from the continuum of the $X^1\Sigma^+$ state state into all of the bound states of the spin-orbit coupled $A^1\Sigma^+ - b^3\Pi_0$ manifold (down to a reasonable value of the detuning, photoassociation into states that lay low in the potential well is irrelevant). The colors are

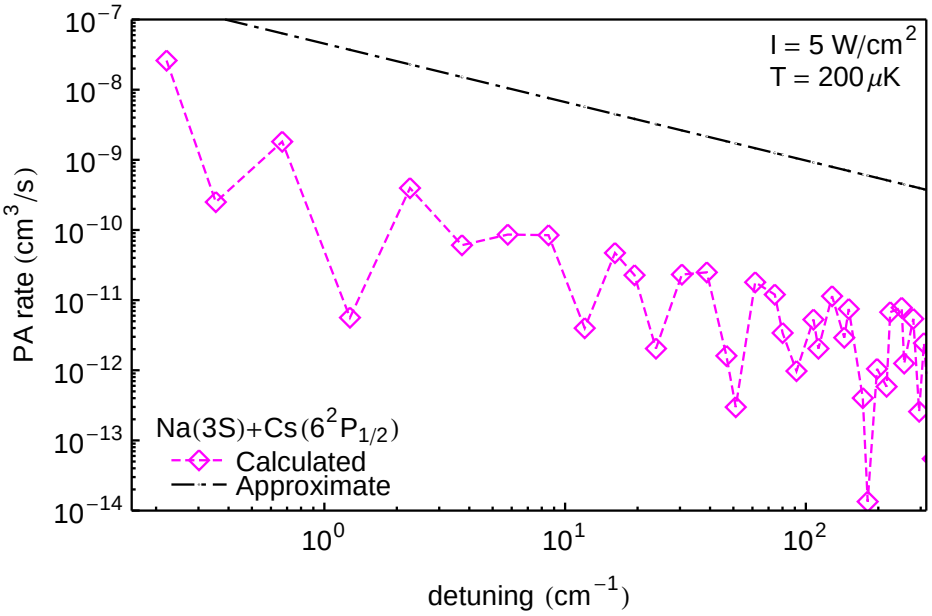

Figure 6.4: (Color online) Photoassociation rate for NaCs at $T = 200\mu K$ using a continuous wave laser with intensity $I = 5\text{W/cm}^2$ vs. detuning. Detunings are measured below the Na($3S$)+Cs($6^2P_{1/2}$) asymptote.

chosen to correspond to the relevant potential asymptotes, in order to remain consistent with the graphs in Chaps. 4 & 5, and in particular Fig. 4.4, p. 109: photoassociation rates for detunings measured below the asymptote of the $V_{3/2}$ potential are in green, photoassociation rates for detunings measured below the asymptote of the $V_{1/2}$ asymptote are in magenta. Each figure is labeled with the dissociation limit from which the detunings are measured. Both figures are obtained at a photoassociation laser intensity of $I = 5\text{W/cm}^2$, as in [22]. In each figure, the jagged dashed line connects the successive symbols to prevent the eye from perceiving the data as a scatter plot. The dashed dotted line in the upper right portion of each graph is an estimate to the photoassociation rate obtained from an estimate of the fbTDMME based on the approximation formulae found in [73, 80] and based on the long-range dispersion coefficients that govern the potential at large value of the internuclear separation. Notice that the approximation constitutes an upper limit to the actual calculation, and

that the actual results never exceed the approximate prediction. In particular the filled data point in Fig. 6.3 reproduces within experimental uncertainty the photoassociation rate reported in [22].

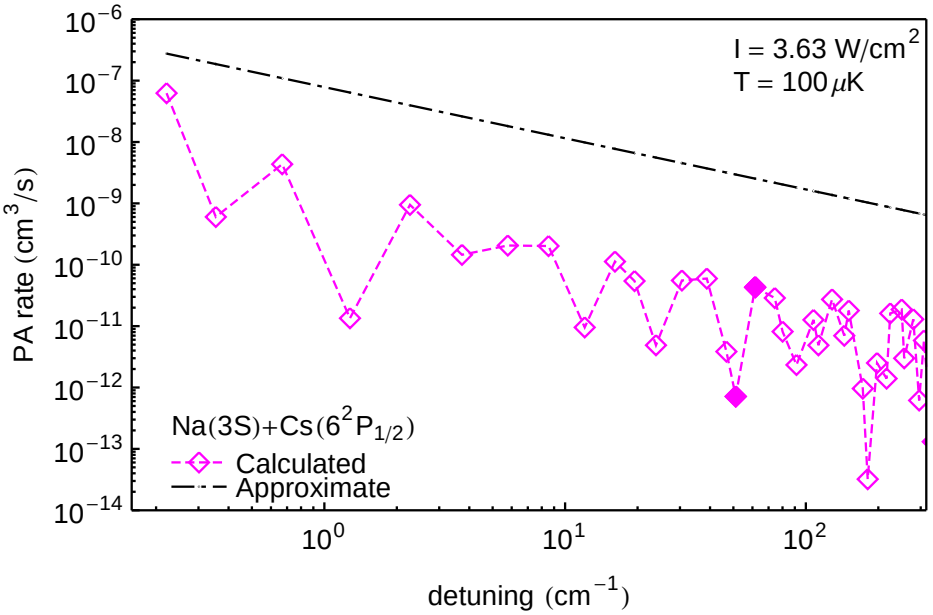

Figure 6.5: (Color online) Photoassociation rate for NaCs at $T = 100\mu K$ using a continuous wave laser with intensity $I = 3.63\text{W/cm}^2$ vs. detuning. Detunings are measured below the Na($3S$)+Cs($6^2P_{1/2}$) asymptote. The filled magenta diamonds corresponds to the detuning closest to the experimental condition of [18].

In Figure 6.5, I used the experimental conditions from [18]. The two filled diamonds correspond to detunings for NaCs closest to the detunings for RbCs used in [18]. In fact, I was able to find a detuning and intensity that yielded the same photoassociation rate at $T = 100\,\mu K$ for NaCs than for RbCs. Note that for NaCs at $51\,\text{cm}^{-1}$ below Na($3S$)+Cs($6^2P_{1/2}$), K_{PA} is a minimum. Actually I set the intensity of the photoassociation laser so that the minimum K_{PA} at this detuning is equal between the two molecules. If I want K_{PA} at a detuning of $61\,\text{cm}^{-1}$below Na($3S$)+Cs($6^2P_{1/2}$) (the closest maximum) to match the published photoassociation rate of [18], I need a lower photoassociation intensity[a].

[a]Photoassociation rates vary linearly with the photoassociation intensity.

It is worth remembering that Kerman *et al.* [18] do not state the actual intensity they use to obtain the K_{PA}'s they report; they only give the maximum photoassociation intensity that their set up allows (4kW/cm^2).

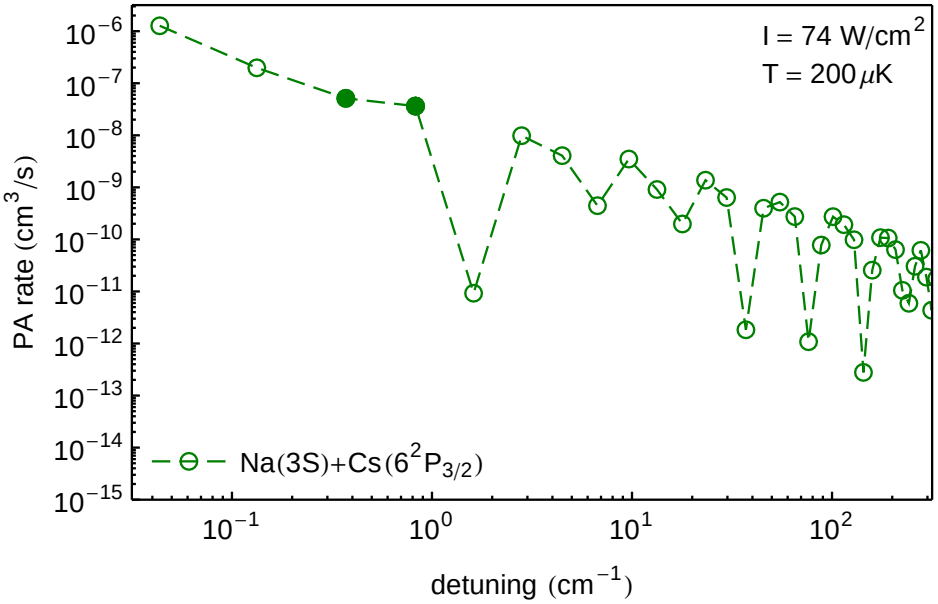

Figure 6.6: (Color online) Photoassociation rate for NaCs at $T = 200\mu K$ using a continuous wave laser with intensity $I = 74\text{W/cm}^2$ vs. detuning. Detunings are measured below the Na($3S$)+Cs($6^2P_{3/2}$) asymptote. The filled green circles corresponds to the detuning closest to the experimental condition of [79].

In Figures 6.6 and 6.7, Dutta *et al.* [79] report a detuning of 15.08 GHz $\approx$ $0.50\,\text{cm}^{-1}$ below the Li($2S$)+Rb($5^2P_{3/2}$) asymptote. In NaCs there are two bound states below the Na($3S$)+Cs($6^2P_{3/2}$) asymptote, one with detuning $0.371\,\text{cm}^{-1}$, the other with a detuning of $0.827\,\text{cm}^{-1}$; these data points are marked with filled symbols in Figs. 6.6 and 6.7. Although Dutta *et al.* [79] are quite specific about the intensity of their photoassociation laser, they only provide the separate temperatures of their Li MOT[a] ($1000\mu K$) and their Rb MOT ($200\mu K$, similar than the NaCs temperature in the experiments reported by the group of Prof. Bigelow at the University of Rochester). So, I obtained PA rates for NaCs at both temperatures: as the temperature of the mixture is bound by

[a] Magneto-Optical Trap

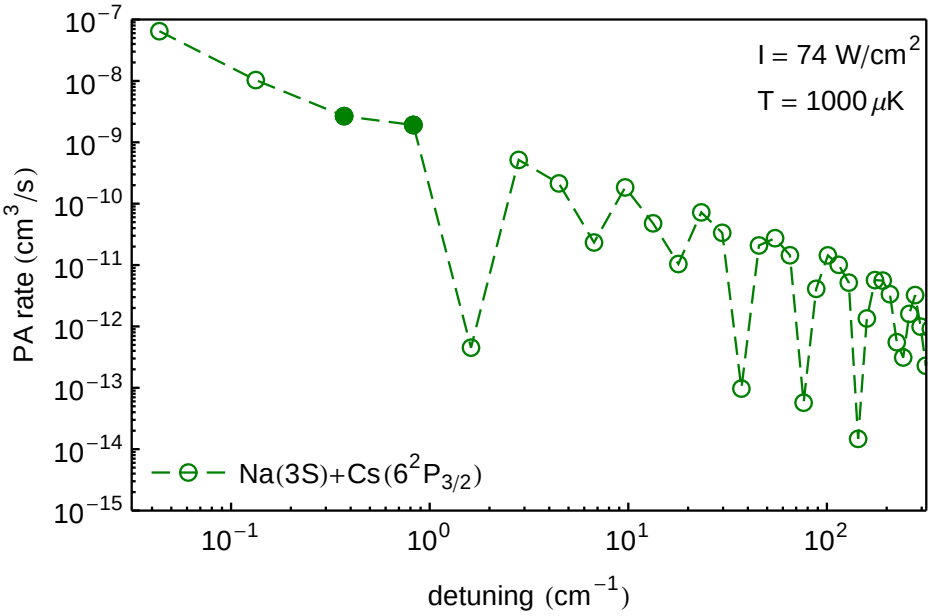

Figure 6.7: (Color online) Photoassociation rate for NaCs at $T = 1000\mu K$ using a continuous wave laser with intensity $I = 74\text{W/cm}^2$ vs. detuning. Detunings are measured below the Na($3S$)+Cs($6^2P_{3/2}$) asymptote. The filled green circles corresponds to the detuning closest to the experimental condition of [79].

the temperature of the individual species, and photoassociation rates decrease smoothly when the temperature increases, the NaCs photoassociation rate at the—unreported—temperature of the LiRb mixture is within these bounds. At both temperatures, the photoassociation rate for NaCs is larger than for LiRb. Note that I could always lower the photoassociation laser intensity to obtain the same rate for the two molecules. The photoassociation rate at these detunings is larger for NaCs because the scattering wave function is almost in phase with the excited state coupled-channel wave function: the oscillations of both wave function are thus constructive thereby enhancing the value of the bound-free transition dipole moment. A similar phenomenon might occur for LiRb but due to the nature of the potentials, the amplitude of the constructively-interfering lobes is smaller, yielding an overall smaller bfTDMME.

6.2.2 Evaluation of spin-orbit coupling effects

Given a photoassociation intensity and a temperature of the alkali mixture, how does the photoassociation rate vary when the photoassociation laser is detuned from a given asymptote? For NaCs, one sees from Figs. 6.3 and 6.4 that the photoassociation rate changes more smoothly at small detuning ($\Delta_v < 1\,\mathrm{cm}^{-1}$) below the Na($3S$)+Cs($6^2P_{3/2}$) asymptote than below Na($3S$)+Cs($6^2P_{1/2}$). However for $4\,\mathrm{cm}^{-1} < \Delta_v < 9\,\mathrm{cm}^{-1}$, the photoassociation rate is more stable for states below the Na($3S$)+Cs($6^2P_{1/2}$) asymptote.

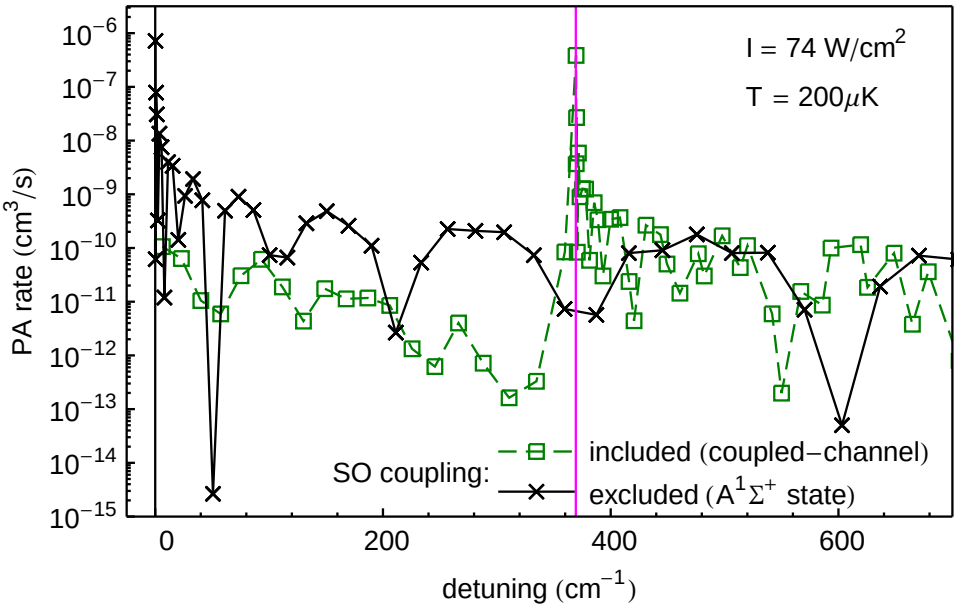

Figure 6.8: (Color online) Difference between including and neglecting spin-orbit coupling when determining photoassociation rates for NaCs at $T = 200\mu K$ using a continuous wave laser with intensity $I = 74\mathrm{W/cm}^2$ vs. detuning. Detunings are measured below the Na($3S$)+Cs(6^2P) asymptote, the dissociation asymptote of the $A^1\Sigma^+$electronic state, marked by the black vertical line at zero detuning. The vertical magenta line near $370\,\mathrm{cm}^{-1}$, in the middle of the plot, marks the Na($3S$)+Cs($6^2P_{1/2}$) asymptote.

From a theoretical point of view, one would first try to predict photoassociation rates using Hund's case (a) potential energy curves, notorious for *not* including spin-orbit effects. In such model, photoassociation occurs into vibrational states belonging to the $A^1\Sigma^+$electronic state. However in Nature, spin-

orbit coupling can not be turned off. Realistic photoassociation thus aims for the spin-orbit coupled-channel bound state $|\Phi^{cc}_{v_{cc}}\rangle$. Figure 6.8 compares the rates for photoassociation into the high-lying bound states of $A^1\Sigma^+$ to the rates for photoassociation into the spin-orbit coupled-channel bound states $|\Phi^{cc}_{v_{cc}}\rangle$ that actually exist below the asymptote of the (purely theoretical) $A^1\Sigma^+$ state. Between the Na(3S)+Cs(6^2P) asymptote of the $A^1\Sigma^+$electronic state and the Na(3S)+Cs(6$^2P_{1/2}$) asymptote[a], the—realistic—photoassociation rates that account for spin-orbit coupling are lower than those predicted using only the $A^1\Sigma^+$ state. When the detuning is such that the laser becomes resonant with the coupled-channel bound states just below the Na(3S)+Cs(6$^2P_{1/2}$) asymptote, then the photoassociation rates that include spin-orbit coupling are much higher than those determined using only the $A^1\Sigma^+$ state. Along with showing the difference in photoassociation rates between the two formalisms (with & without spin-orbit coupling), Figure 6.8 also shows that in Nature there are less vibrational states below the asymptote of the $A^1\Sigma^+$ state than what a pure Hund's case (a) formalism predicts, and that the density of vibrational states is quite different.

6.3 A break and a breather

The part of this chapter covering the obtention of key quantities for the final calculation, is over. Before actually looking at the solutions to Eq. (4.52) and Eq. (4.79), I must explain the order of the sections that follow.

I divided the study into 16 different scenarios, each identified by a four letters code[b] $\ell_1\ell_2\ell_3\ell_4$ (see below and Tbl. 6.1). The underlying principle in the

[a] Of the state I've called $V_{1/2}$ of Fig. 4.4

[b] None of the symbols $\ell_1,\ell_2,\ell_3,\ell_4$ have any physical meaning. They are just placeholders used solely in this section.

sequence of cases is to proceed from as-simple-as-possible-but-no-simpler situations to more intricate ones. During such journey, I can relate the teachings from a previous case to the one under scrutiny at a given moment. The topics of Sec. 2.3.1 and 2.3.2 will now become handy.

The simplest situation is to set up the lasers so that the system behaves as a 3 (or even sometimes as 2) states problem. The near dissociation (ND) vibrational states involved are close to each other in energy. In order to favor only one of these ND states out of the many that exist below the dissociation asymptote, I ran the first block of calculations using laser pulses with a **narrow** spectral **b**andwidth of 0.5 GHz. The corresponding temporal Full Width at Half Maximum (FWHM) is then 882 ps. I identify this block with $\ell_1 = \mathrm{b}$. The second principal block of calculation uses laser with a broader spectral bandwidth of 10 GHz, thereby exciting the vibrational states that the previous laser were trying to leave alone. Broader laser pulses are faster: the pulses now have a temporal FWHM of 62 ps. Although 10 GHz is below the energy separation between the ND vibrational states near the chosen ones, such spectral bandwidth is sufficient for the neighboring states to affect the dynamics of the process. For calculations ran at this—comparatively—**large** spectral **B**andwidth, $\ell_1 = B$.

Within a spectral bandwidth, I applied the same philosophy as when choosing test cases. I first examined processes where I **N**eglected the effects of spin-orbit coupling (cases with $\ell_2 = N$), and subsequently looked at situations where I included **S**O effects (cases with $\ell_2 = S$). The 4 combinations I just outlined span the four columns of Tbl. **6.1**

I now split each column into 2 rows: the first row is for lasers in the **I**ntuitive sequence ($\ell_3 = I$), the second row is for lasers in the **C**ounter-intuitive sequence ($\ell_3 = C$).

		0.5 GHz (b)		10 GHz (B)	
		No (N) SO	with SO (S)	No (N) SO	with SO (S)
Intuitive (I)	unchirped (u)	bNIu (1)	bSIu (5)	BNIu (9)	BSIu (13)
	chirped (c)	bNIc (2)	bSIc (6)	BNIc (10)	BSIc (14)
Counterintuitive (C)	unchirped (u)	bNCu (3)	bSCu (7)	BNCu (11)	BSCu (15)
	chirped (c)	bNCc (4)	bSCc (8)	BNCc (12)	BSCc (16)

Table 6.1: Four letters codes that uniquely identify the 16 situations examined in this chapter.

Finally each row is separated into two shelves: the top one is for **u**nchirped lasers ($\ell_4 = u$) while the bottom shelf is for **c**hirped lasers ($\ell_4 = c$). I summarize in Tbl. 6.1 all 16 codes for quick identification, and I also indicate the order of presentation in this manuscript.

We are now ready to dive into the analysis and discussion of the solutions to Eq. (4.52) and Eq. (4.79).

6.4 Populations as functions of time

The idea here is to fiddle with the various parameters of the laser available and attempt to achieve three goals:

1. transfer a significant ($\geq 90\%$) portion of the population from the continuum into the final state $|X, 0, 32\rangle$

2. avoid population to linger in the intermediate state(s) $|A, 1, v_A\rangle$ or $|\Phi^{cc}_{v_{cc}}\rangle$ to prevent loss of population by spontaneous emission

3. complete the population transfer within at most a few nanoseconds.

Note that choosing a spectral bandwidth uniquely determines the temporal bandwidth and the maximum chirp rate that a filter can impart onto a laser. In planning for the later use of adiabatic transfer, I follow the recommendation of [16, 30, 81]: I always choose pump and Stokes chirp rates equal to each others, lasers with identical temporal bandwidth, and intensities such that the peak Rabi frequencies are equal.

To warm up, let's begin with case 1-bNIu.

6.4.1 Case 1—bNIu: intuitive sequence of unchirped lasers with narrow spectral bandwidth, without SO coupling

To generate Figure 6.9 p. 158, the laser intensities are set so the corresponding Rabi frequencies are π-pulses. In the intuitive sequence (pump before Stokes pulse), the action of each laser can be viewed independently, and the system undergoes 2-state π-pulse transfer within each set of relevant states. The laser intensities are also optimized to minimize oscillations of population during the action of a given pulse.

By separating the lasers as shown, the population is transferred sequentially from one state to the other. The transfer yields 99.5% of population in $|X, 0, 32\rangle$. For each transfer, the optimal detuning of the laser is 0 (see Sec. 2.3.1). What about the intermediate population in $|A, 1, 140\rangle$? The typical lifetimes of vibrational states $|A, v_A > 100\rangle$ are greater than 40 ns [10]. Therefore, no population should be lost from the intermediate state by spontaneous emission. Let's now

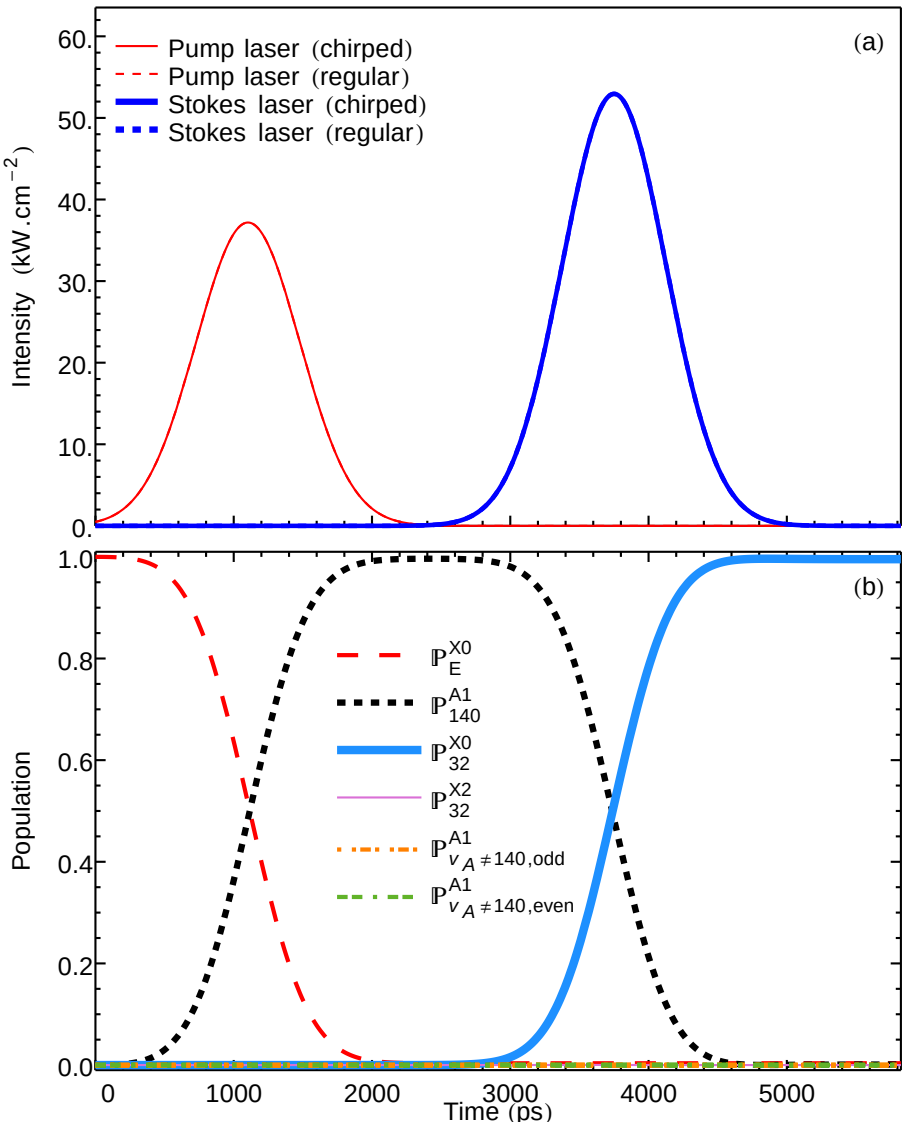

Figure 6.9: (Color online) Population transfer as a function of time, case 1—bNIu. Narrow spectral bandwidth of 0.5 GHz, no spin-orbit effects accounted for, unchirped lasers in intuitive sequence. The laser intensities are chosen to obtain the simplest π-pulse as possible.

study the influence of chirping the lasers.

6.4.2 Case 2—bNIc: intuitive sequence of chirped lasers with narrow spectral bandwidth, without SO coupling

6.4.2.1 Importance of detunings in chirped processes

In this scenario, at first, I run the program using the maximum chirp rate possible. Then, no population was transferred in any state at all. Why?

With chirped lasers, the central frequency of the laser changes with time, and thus the instant when resonance occurs is important. To find the ideal detuning in the intuitive sequence, consider the following. Transfer from the initial state to the intermediate state is most likely when the magnitude[a] of the coupling term in the hamiltonian is maximal, and the diagonal term for the intermediate state is equal to that maximum. Indeed this corresponds to the wave of the system being resonant with the laser wave: as sailors waiting for the tide to exit the harbour, the particles of the system only change state when the laser is maximal. For the hamiltonian of Eq. (4.52), this amounts to

$$\left|\Omega_P^0\right| = \left|2(\Delta^P_{v_A=140} - 2\gamma_P t_P)\right| \tag{6.2}$$

where $\Omega_P^0 = {}_{v_A=140}^{A1}\mathscr{D}_E^{X0}\frac{\sqrt{3}}{3}\frac{\mathscr{E}_0^P(t_P)}{\hbar}$, and thus the optimal detunings are

$$\Delta^P_{v_A=140} = 2\gamma_P t_P \pm \frac{\Omega_P^0}{2}. \tag{6.3}$$

This expression, which features the Rabi frequency that couples the initial and the intermediate state, can easily be adapted for any other vibrational state

[a] The laser envelope, being a Gaussian, is always positive, but the transition dipole moment prefactor may be negative, hence the necessity to specify magnitude.

used as an intermediate. The central frequency of the laser is (Eq. (4.49))

$$\omega_P(t) = \omega_{0,P} - \Delta^P_{v_A=140} + \gamma_P t \tag{6.4}$$

and the laser is on resonance at a time $t_{P,\text{res}}$ such that $\omega_P(t_{P,\text{res}}) = \omega_{0,P}$. Consequently,

$$t_{P,\text{res}} = 2t_P \pm \frac{\Omega^0_P}{2\gamma_P}. \tag{6.5}$$

If the term $2t_P$ in the above equation is the dominant term, then the ideal detuning corresponds to the chirped laser pulse being resonant with its central frequency at twice the peaking time. I call this generalization of the intuitive resonance condition (resonance at the peak of the pulse), the *Generalized Resonance Hypothesis (GRHYP)*. The GRHYP will help later to home in on the ideal detuning value.

What about the detuning of the Stokes pulse? Keeping the pictures of waves in mind, the wave of the system awaits the tide—*i.e.* the peak—of the Stokes pulse to be transferred from the intermediate state to the final state. The relaxation will be most efficient if the intermediate and the final state are in phase, that is if the diagonal term of the hamiltonian for the intermediate state and for the final state are equal to each other when the Stokes laser peaks. Mathematically,

$$2\left(\Delta^P_{v_A=140} - 2\gamma_P t_S\right) = 2\left(\Delta^P_{v_A=140} - \Delta^S_{v_X=32} - 2(\gamma_P - \gamma_S)t_S\right) \tag{6.6a}$$

$$\Leftrightarrow \Delta^S_{v_X=32} = 2\gamma t_S, \tag{6.6b}$$

since here *the chirp rates are equal* $\gamma_P = \gamma_S = \gamma$. The Stokes pulse is resonant at a

time $t_{S,\mathrm{res}}$ such that

$$\omega_S(t) = \omega_{0,S} - \Delta^S_{v_X=32} + \mathcal{Y}_S t_{S,\mathrm{res}} = \omega_{0,S} \tag{6.7a}$$

$$\Leftrightarrow t_{S,\mathrm{res}} = \frac{\Delta^S_{v_X=32}}{\mathcal{Y}_S} = 2t_S \tag{6.7b}$$

Thus the ideal detuning of the Stokes pulse in the intuitive sequence is such that the Stokes pulse appears resonant with its transition frequency at twice its peaking time. This is a corollary of the GRHYP.

Figure 6.10 shows the final population in the final state $|X, 0, 32\rangle$ as a function of both detunings. The top panel shows the numerical search for optimal values of the detunings. A strong dependence of the process efficiency on the detuning of the Stokes pulse is clearly visible. For a given value of the Stokes pulse detuning Δ_S, the final population in the final state is almost insensitive to the detuning of the pump pulse. The bottom panel in Fig. 6.10 represents three slices of the top panel, taken at three different values of the pump pulse detuning Δ_P. Two values of Δ_P correspond to the prediction of the GHRYP. The optimal value happens to be the mid-value between the GHRYP predictions. When Δ_P is outside the range of values predicted by the GRHYP, the final population in the final step drops by a few tenths of a percent. The three curves in the bottom panel delimit the slight bump on the surface plotted in the top panel. These graphs indicate that the GRHYP *correctly delimits a region of optimal detunings*. In the present case the optimal detunings correspond to $\Delta^P_{v_A=140} = 2\mathcal{Y} t_P$ and $\Delta^S_{v_X=32} = 2\mathcal{Y} t_S$.

Figure 6.11 shows the populations when using the maximum chirp rate possible. The detunings were optimized using the GRHYP presented above. Notice that chirping the lasers decreased the efficiency of each step: for each

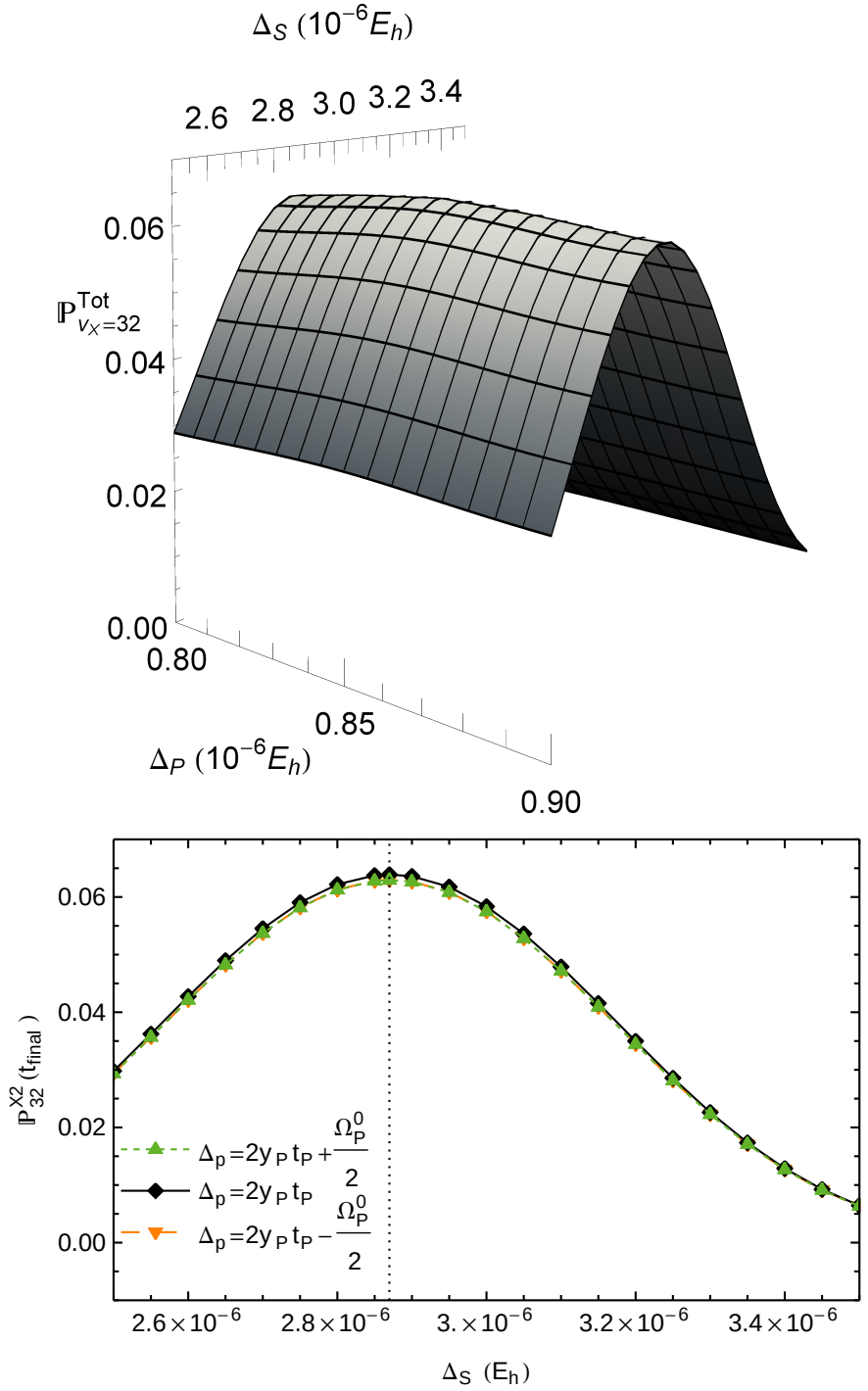

Figure 6.10: (Color online) Sensitivity of the final population in the final state $|X,0,32\rangle$ to the laser detunings for chirped pulses in the intuitive sequence for narrow bandwidth, without spin-orbit coupling (case 2—bNIc). **Top panel:** numerical search in the region predicted by the GRHYP (see text). Notice the slight bump at the top of the ridge. **Bottom panel:** Dependence of the final population in the final state on the detuning of the Stokes pulse, for three values of the pump detuning: two are predicted by the GRHYP, the third is the middle value between those.

transfer, only 25% of the population from one state goes to the next, yielding a final population in the final state of 6.25%.

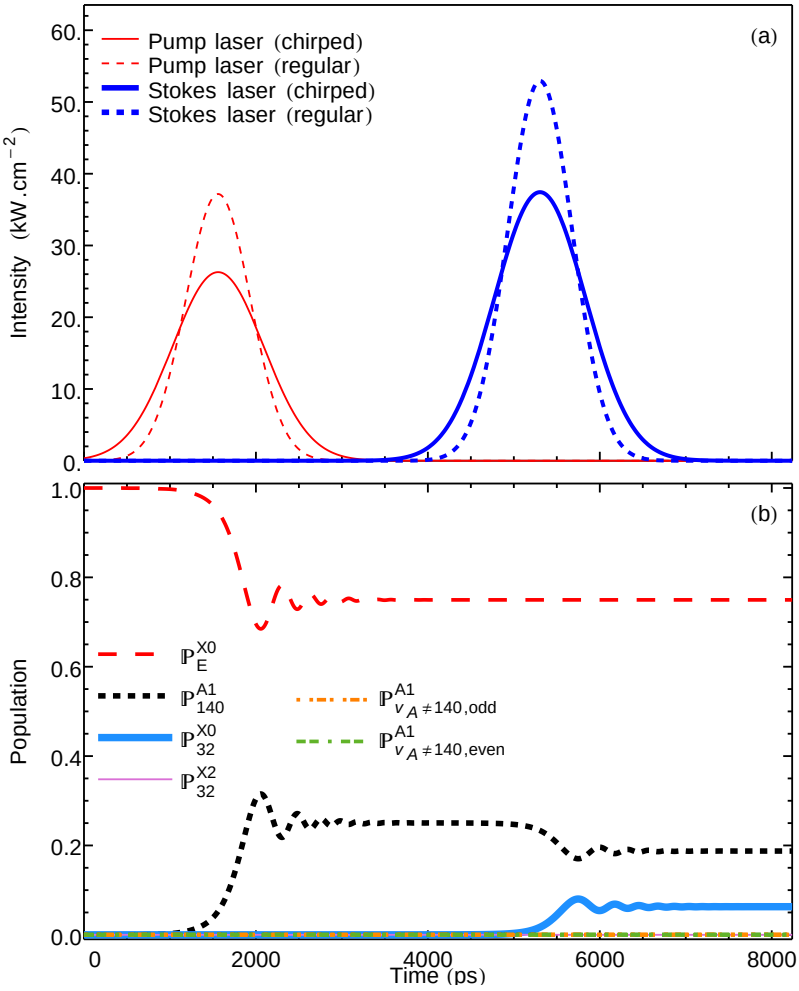

Figure 6.11: (Color online) Population transfer as a function of time, case 2—bNIc. Lasers are chirped: the pulses are temporally stretched and the peak intensity decreases. The laser intensities are chosen to obtain the simplest π-pulse as possible. The detunings are optimized to yield the highest population in the intermediate state, and then in the final state, as the pulses act in the intuitive sequence.

6.4.2.2 Dependence of the transfer on intensity

Once the lasers are chirped, the sensitivity of the population transfer on the intensity of the lasers is quite different from Fig. 2.8. To study such dependence, I turn off the Stokes laser, and examine the final population in the

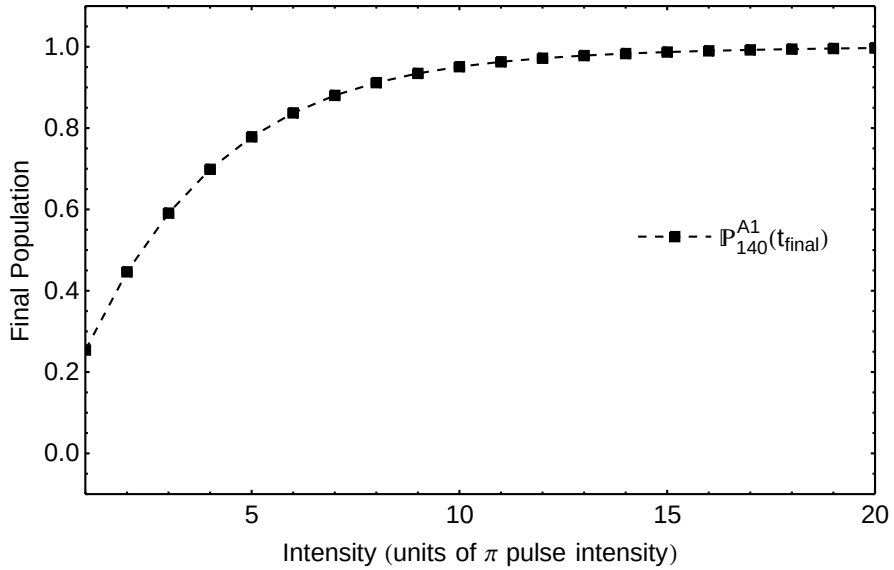

Figure 6.12: (Color online) Dependence of population transfer for chirped pulses on the intensity for case 2—bNIc.

intermediate state as a function of the intensity (Fig. 6.12). The population exceeds 98% for an intensity equal to 16 times the minimum π-pulse intensity: this is the intensity I choose for later runs. I also increased the intensities to maximize the population in the final state. Figure 6.13 shows the population transfer for these increased intensities. Since the population stays in the intermediate state for about 2ns, let's examine the sensitivity of the transfer to the time delay between the pulses.

6.4.2.3 Sensitivity on pulse delay

With all other parameters kept constant, I plot in Fig. 6.14 p. 166 the populations *at the end of the process* as a function of the time delay between the pulses. The horizontal axis is labeled in units of the temporal FWHM of the laser pulses *before* they are chirped. Chirping the lasers makes the process insensitive to the delay between the pulses, although one may increase the final population in the final state from 98.5% to 99% by setting the delay to $\approx 0.45\Delta\tau$. Effectively one may consider that the overall duration of the process

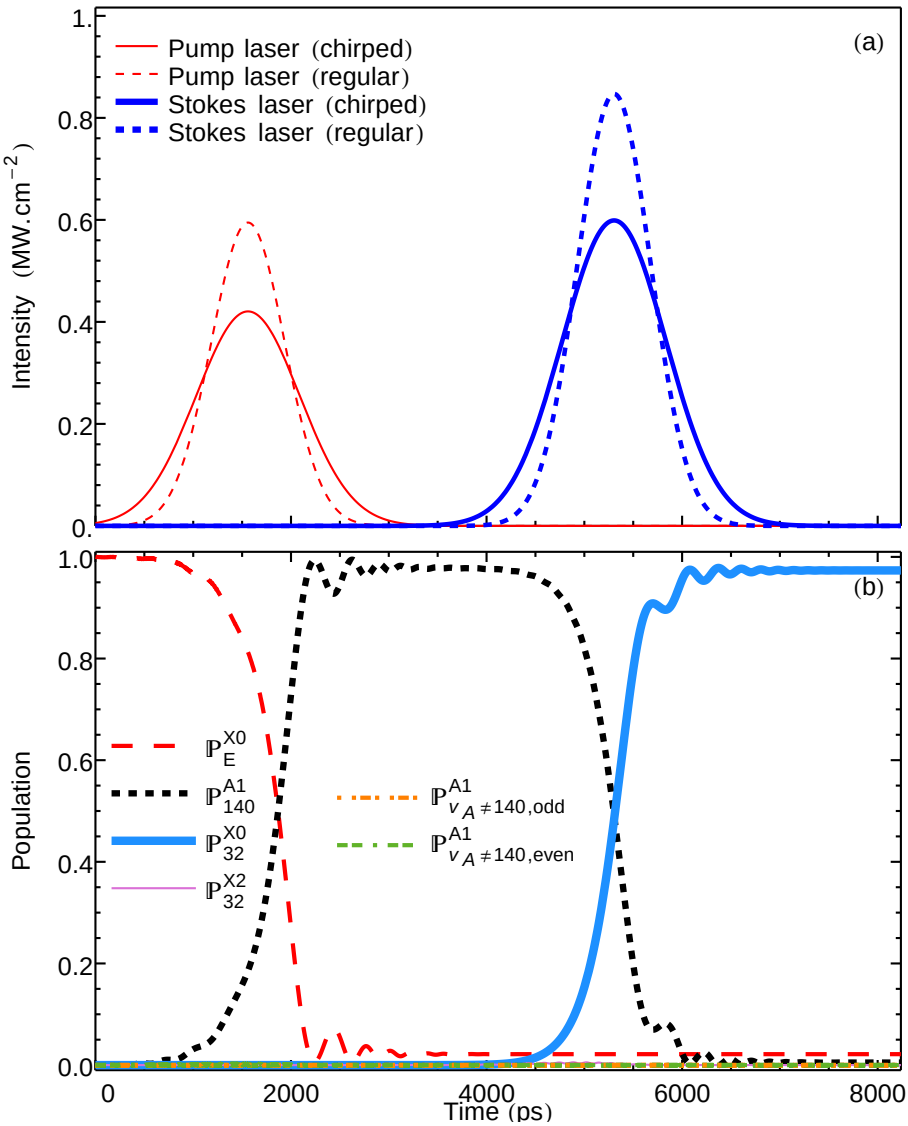

Figure 6.13: (Color online) Population transfer as a function of time, case 2—bNIc. Lasers are chirped: the pulses are temporally stretched and the peak intensity decreases. The laser intensities are chosen to obtain the simplest π-pulse as possible. The detunings are optimized to yield the highest population in the intermediate state, and then in the final state, as the pulses act in the intuitive sequence.

is equal to[a] $2\Delta\tau + \eta$, and thus Fig. 6.14 shows that the minimal duration for the process is $\approx 2.45\Delta\tau$.

Being insensitive to the pulse delay, the process will be overall faster when the delay is shortest. Setting the delay between the pulses to $\approx 0.45\Delta\tau$ yields

[a] Remember that $\Delta\tau$ is the FWHM of the pulse, and η the time delay between the pulses.

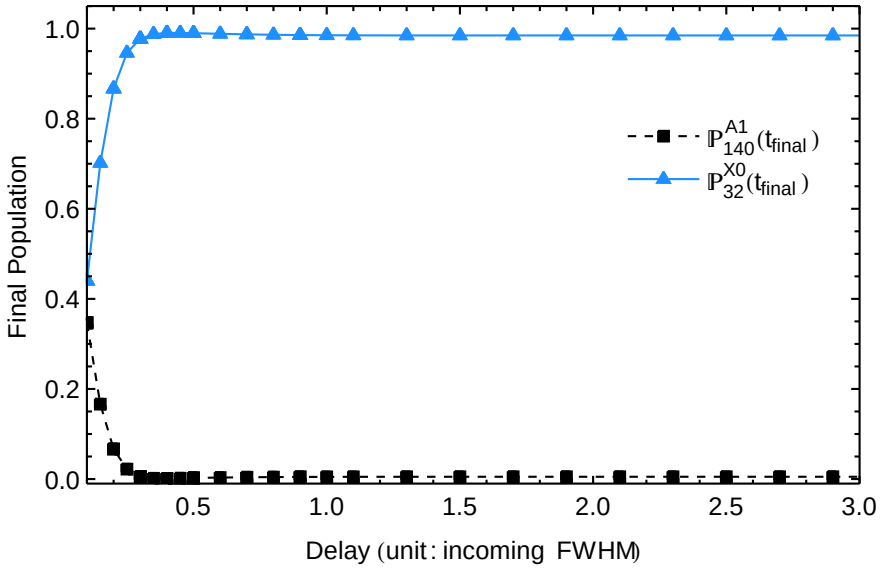

Figure 6.14: (Color online) Insensitivity of the population at the end of the process to the delay between the pulses for *chirped* lasers, case 2—bNIc. The almost flat blue line of triangles rises from 98.5% to 99% at $\approx 0.45\Delta\tau$.

Fig. 6.15 p. 167. The overall duration is divided by 2 from Fig. 6.13, and the intermediate state is not much populated. This figure shares many similarities with Fig. 2.11, let's examine why.

6.4.2.4 Adiabatic passage in practice

This is our first encounter with adiabatic transfer in a real situation. Compare the population in Fig. 6.15—the solution carrier—to the adiabatic carrier in the top panel of Fig. 6.16. At early times the solution matches almost perfectly the adiabatic carrier. Around $t \approx 1000\,\text{ps}$ the component of the adiabatic carrier over the initial state (red long dashes) starts to lose strength to the benefit of the intermediate state. In what follows, I call the *adiabatic companion* the eigenstate of the time-dependent hamiltonian that interacts the most with the adiabatic carrier, as measured by the adiabatic condition Eq. (2.11). Here, the adiabatic ratio (middle panel) indicates a redistribution of population between the adiabatic carrier and its companion. Very small oscillations in the solution

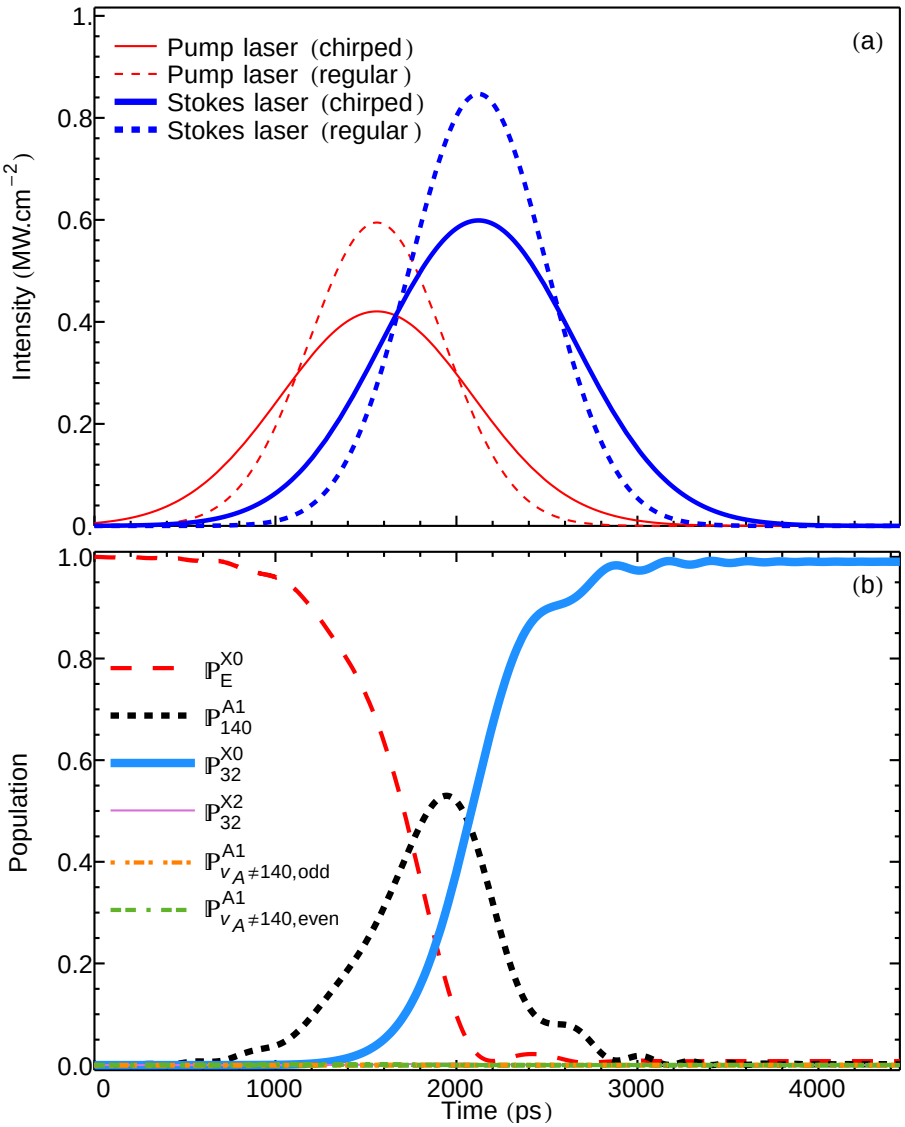

Figure 6.15: (Color online) Population transfer as a function of time for optimal time delay in case 2—bNIc. The process lasts twice less time than in Fig. 6.13. The population in the intermediate state stays above 20% for less than 1ns. The population in the final state at the end of the process is 99%.

carrier (Fig. 6.15, bottom panel) at $t \approx 1000\,\text{ps}$ reflect this exchange, which also happens towards the end of the process ($t \approx 3000\,\text{ps}$), just before $\mathbb{P}_{32}^{X0}$ reaches a plateau.

What did we learn from case 2—bNIc?

- detunings are crucial to chirped-lasers sequences, and the GRHYP pro-

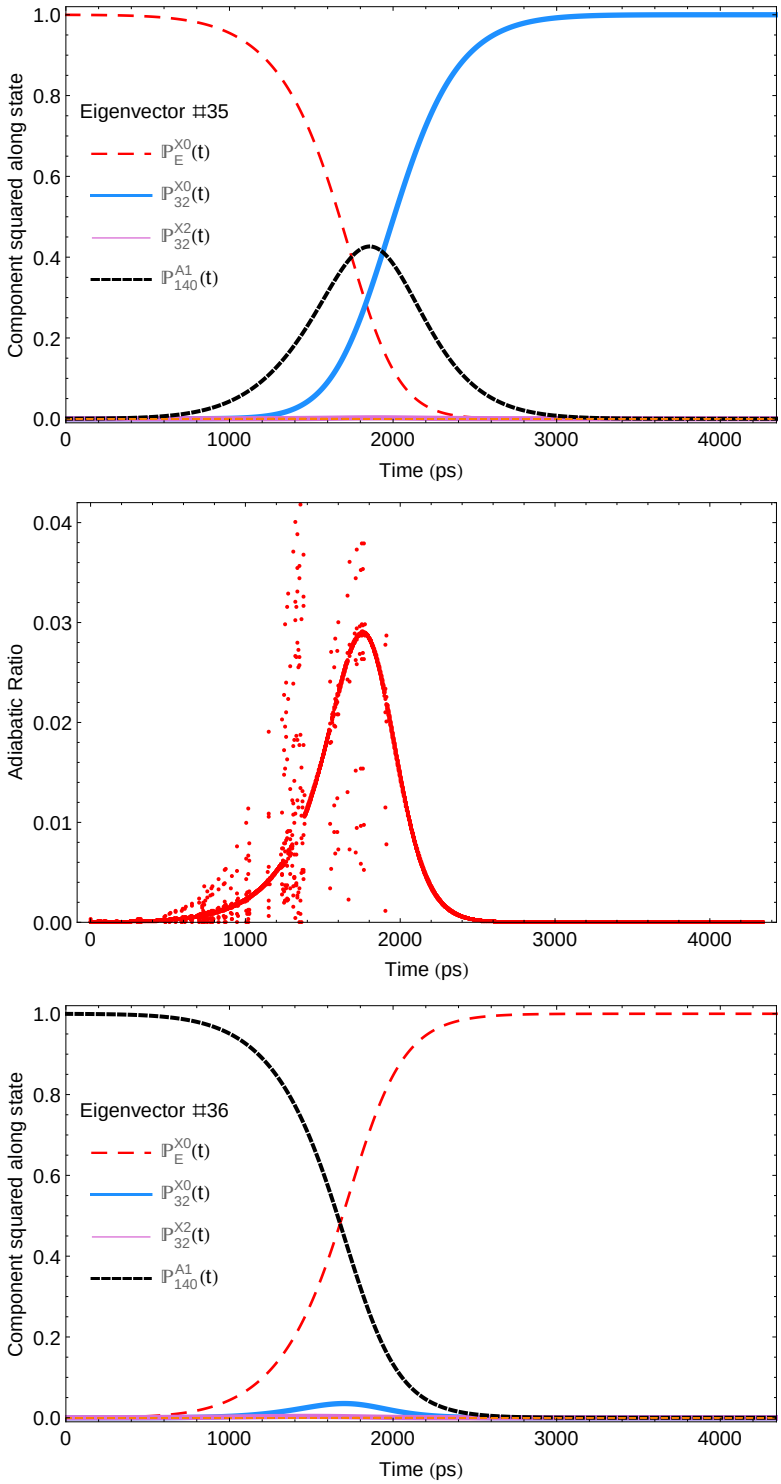

Figure 6.16: (Color online) Adiabatic eigenstates and local adiabatic conditions for case 2—bNIc at optimal detuning, pulse delay, and intensity. **Top panel:** main adiabatic carrier (see text). **Middle panel:** adiabatic condition Eq. (2.11) as a function of time between the adiabatic carrier (top panel), and the companion in the bottom panel. **Bottom panel:** adiabatic companion, interacting with the main carrier of the top panel, and preventing the population transfer

vides an expression to delimit a range of values for optimal detunings

- when chirping the lasers, the sequence of π-pulses becomes insensitive to pulse delay, which can then be reduced to minimize the duration of the overall population transfer
- for the minimal pulse delay, the process becomes adiabatic without resorting to the counterintuitive sequence.

After this first taste of adiabatic passage, let's consider STIRAP.

6.4.3 Case 3—bNCu: STIRAP with narrow spectral bandwidth, without SO coupling

The counterintuitive sequence is an essential requirement of STIRAP (see Sec. 2.3.2). In the present case, the lasers are unchirped: I set the detunings to 0, which is the optimal value for STIRAP [16, 30, 32, 81]. Achieving population transfer in the counterintuitive sequence requires a minimal pulse intensity (Eq. (15) in [16], Eq. (58) in[81]) to reach adiabaticity. Figure 6.17 shows that the minimal required intensity is $10 \times I_{\pi,0}$, where $I_{\pi,0}$ is the minimal π-pulse intensity. Passed that value, the process is rather insensitive to changes in the intensity.

The higher the intensity, the more stable is STIRAP with respect to the delay between the pulses as shown in Fig. 6.18. Regardless of the intensity, the optimal delay is always given by $\eta_{\mathrm{STIRAP}} = -\frac{1}{\sqrt{2\ln 2}}\Delta\tau$, where $\Delta\tau$ is the FWHM of the intensity pulse, as derived in App. C.

To close this case, although this process yields a high final population in $|X, 0, 32\rangle$, the adiabatic condition is not satisfied at all times, as shown by the

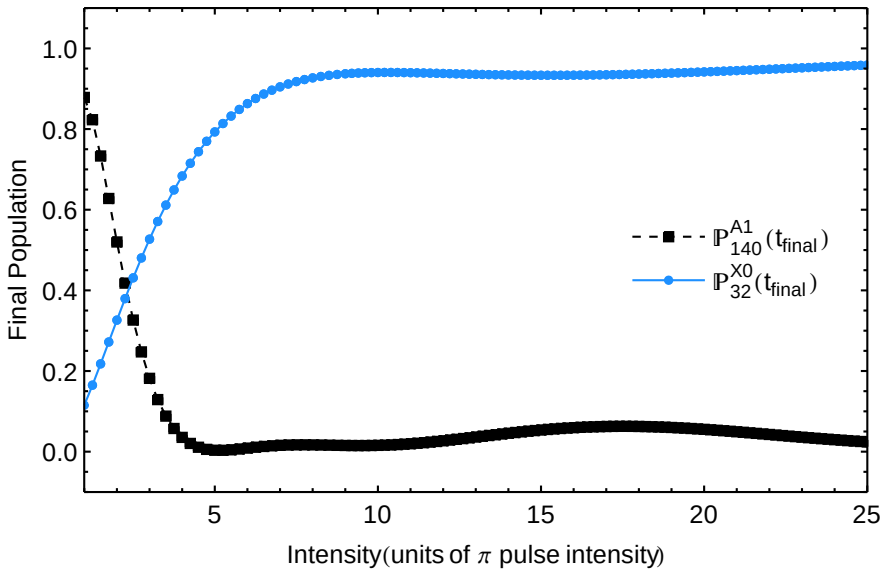

Figure 6.17: (Color online) Final population as a function of pulse intensities for unchirped lasers in the counterintuitive sequence (case 3—bNCu). The unit for the horizontal axis is the minimal π-pulse intensity $I_{\pi,0}$. When the intensity of the laser exceeds $10I_{\pi,0}$, the final population is relatively insensitive to the changes in the intensity.

difference between the adiabatic carrier and the solution carrier in Fig. 6.19. At the end of the process, 5.4% of population remains in the intermediate state

6.4.4 Case 4—bNCc: chirped STIRAP with narrow spectral bandwidth, without SO coupling

This is the final case that deals with a narrow bandwidth and no spin-orbit coupled channels. The laser detunings are crucial to the efficiency of the process, so let's apply the principles of the GRHYP from Sec. 6.4.2.1 to the present situation, since the lasers are chirped. The lasers are in a counterintuitive sequence: the Stokes pulse interacts with the sample first, and the pump pulse

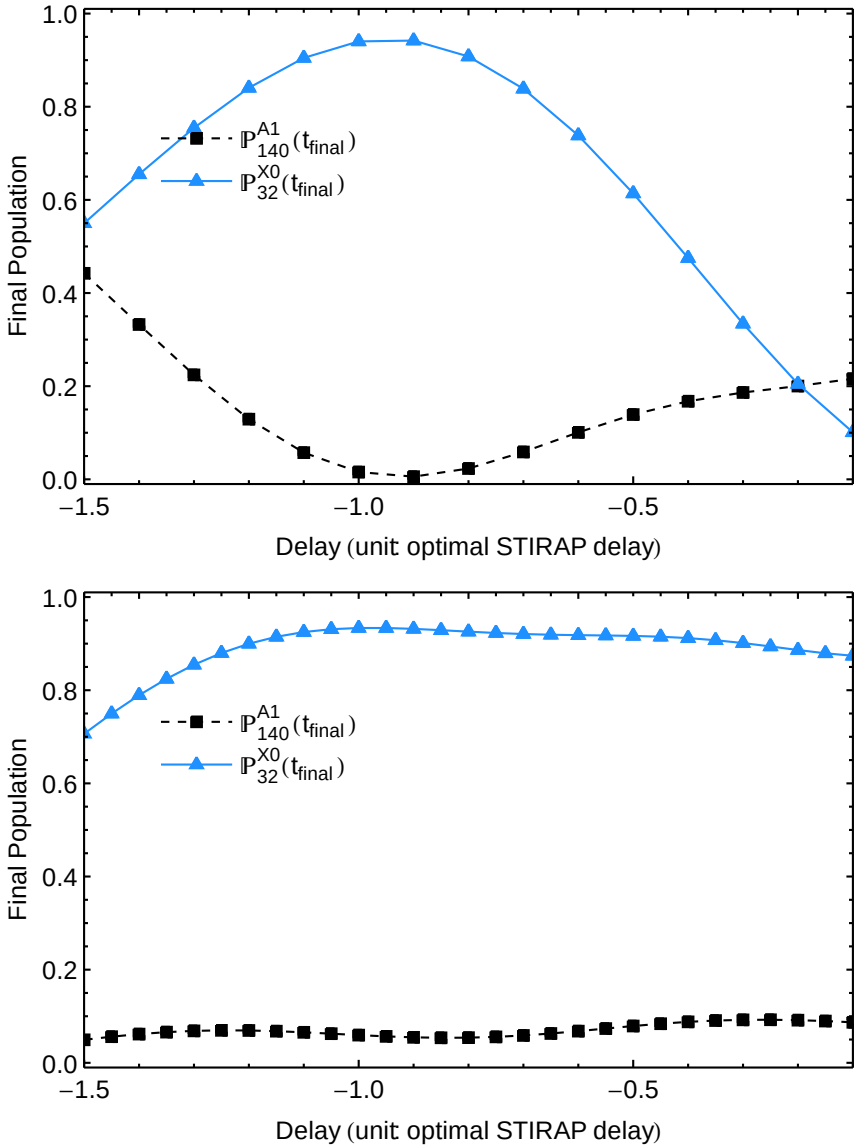

Figure 6.18: (Color online) Final population as a function of pulse delay for unchirped lasers in the counterintuitive sequence (case 3—bNCu) for 2 values of the intensity. **Top panel:** Intensity of $10I_{\pi,0}$. **Bottom panel:** Intensity of $16I_{\pi,0}$. The horizontal axis is scaled to the STIRAP optimal pulse delay $\eta_{\text{STIRAP}} = -\frac{1}{\sqrt{2\ln 2}}\Delta\tau$, where $\Delta\tau$ is the FWHM of the intensity pulse. The sensitivity of the process to the pulse delay decreases when the intensity increases, and η_{STIRAP} optimizes the transfer in both situations.

interacts last. Therefore, in applying the GRHYP, let's solve for $\Delta^P_{v_A=140}$ in

$$\left|\Omega^0_S\right| = 2\left|\Delta^P_{v_A=140} - 2\mathcal{Y}_P t_S\right| \tag{6.8a}$$

$$\Leftrightarrow \Delta^P_{v_A=140} = 2\mathcal{Y}_P t_S \pm \frac{\Omega^0_S}{2} \tag{6.8b}$$

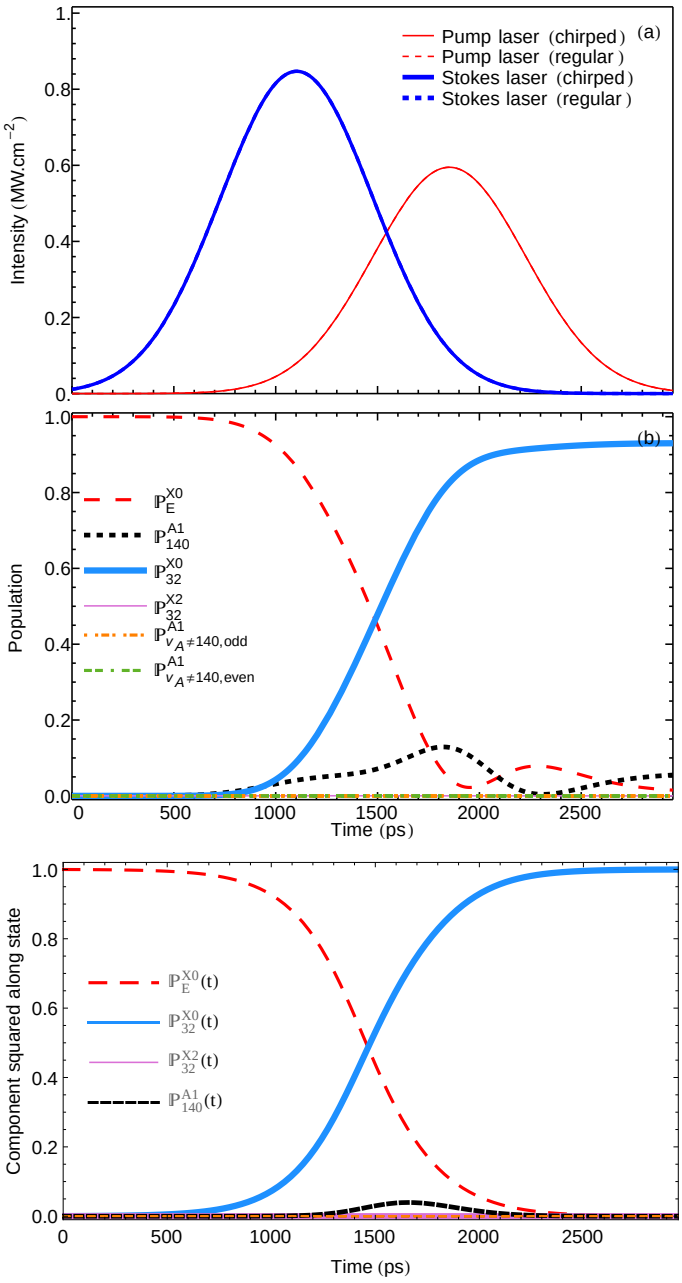

Figure 6.19: (Color online) **Panel (a):** Laser pulses. **Panel (b):**Population as a function of time in STIRAP (case 3—bNCu) for an intensity of $16I_{\pi,0}$ at optimal pulse delay. **Bottom panel:** Adiabatic state followed by the solution carrier for most of the transfer.

where $\left|\Omega_S^0\right| = \left|{}_{v_A=140}^{A1}\mathscr{D}_{v_X=32}^{X0}\frac{\sqrt{3}}{3}\frac{\mathscr{E}_0^S(t_S)}{\hbar}\right|$. With the corollary of the GRHYP, we can deduce the detuning of the Stokes laser: the phase of the final state must equal the phase of the intermediate state when the last pulse—*i.e.* the pump pulse—

interacts with the system. Mathematically

$$\Delta^P_{v_A=140} - 2\mathcal{Y}_P t_P = \Delta^P_{v_A=140} - \Delta^S_{v_X=32} - 2(\mathcal{Y}_P - \mathcal{Y}_S)t_P \tag{6.9a}$$

$$\Leftrightarrow \Delta^S_{v_X=32} = 2\mathcal{Y} t_P, \tag{6.9b}$$

since $\mathcal{Y}_P = \mathcal{Y}_S = \mathcal{Y}$. With such detunings, the *pump* pulse is resonant at the time

$$t^{\mathrm{CI}}_{P,\mathrm{res}} = 2t_S \pm \frac{\Omega^0_S}{2\mathcal{Y}_P}. \tag{6.10}$$

If the term $2t_S$ is dominant in this expression, then the ideal pump detuning corresponds to the chirped pump laser pulse being resonant with its central frequency at twice the peaking time *of the Stokes laser*. The ideal detuning for the Stokes pulse, in the counterintuitive sequence, makes the Stokes pulse resonant with its central frequency at twice the peaking time *of the pump laser*.

Let's look at the dependence of the final populations on the pulse delay in Fig. 6.20. The final population reaches 98.6% for a time delay equal to $0.46\eta_{\mathrm{STIRAP}} \approx 0.39\Delta\tau$. Thus by putting the laser in the counterintuitive sequence, the process has now an overall duration of $2.39\Delta\tau$, only faster 2% faster than the intuitive sequence with chirped lasers. The counterintuitive sequence efficiency decreases rather slowly: at $0.8\eta_{\mathrm{STIRAP}}$, the process still yields 88% in the final state.

To end this section, Fig. 6.21 shows the populations as a function of time for the optimal parameters discussed. The transfer nearly follows the adiabatic carrier shown in the bottom panel of the figure. The difference between the adiabatic carrier and the solution carrier has the same explanations as in Sec. 6.4.2. In the present situation though, the effects of the adiabatic condition breakdown are more striking after the crossing between $\mathbb{P}^{\mathrm{X0}}_{\mathrm{E}}(t)$ and $\mathbb{P}^{\mathrm{X0}}_{32}(t)$.

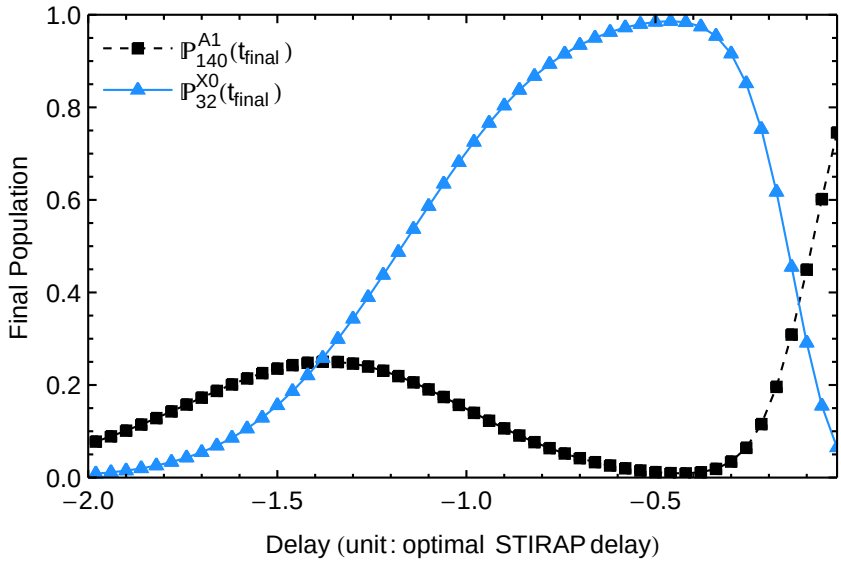

Figure 6.20: (Color online) Dependence of final populations on pulse delay for the counterintuitive sequence with chirped pulses (case 4—bNCc). The population in the $|X, 0, 32\rangle$ reaches 99.1% for a pulse delay of $0.25 \times \eta_{\text{STIRAP}}$

Notice that *chirping the lasers leaves no remaining population in the intermediate state compared to unchirped STIRAP (Fig. 6.19)*.

6.4.5 Case 5—bSIu: intuitive sequence of unchirped lasers with narrow spectral bandwidth, inclusive of SO coupling

I ran this scenario with the same philosophy as for case 1-bNIu : two well-separated π-pulses that succeed in transferring population into the final state. I set the time delay between the lasers to 3 temporal FWHM, and each laser has the appropriate minimal π-pulse intensity. The difference in the relevant transition dipole moment matrix elements (TDMMEs) yields different π-pulse laser intensities between the present case and case 1-bNIu (Sec. 6.4.1). The relevant TDMMEs for all cases in the first column of Tbl. 6.1, along with the

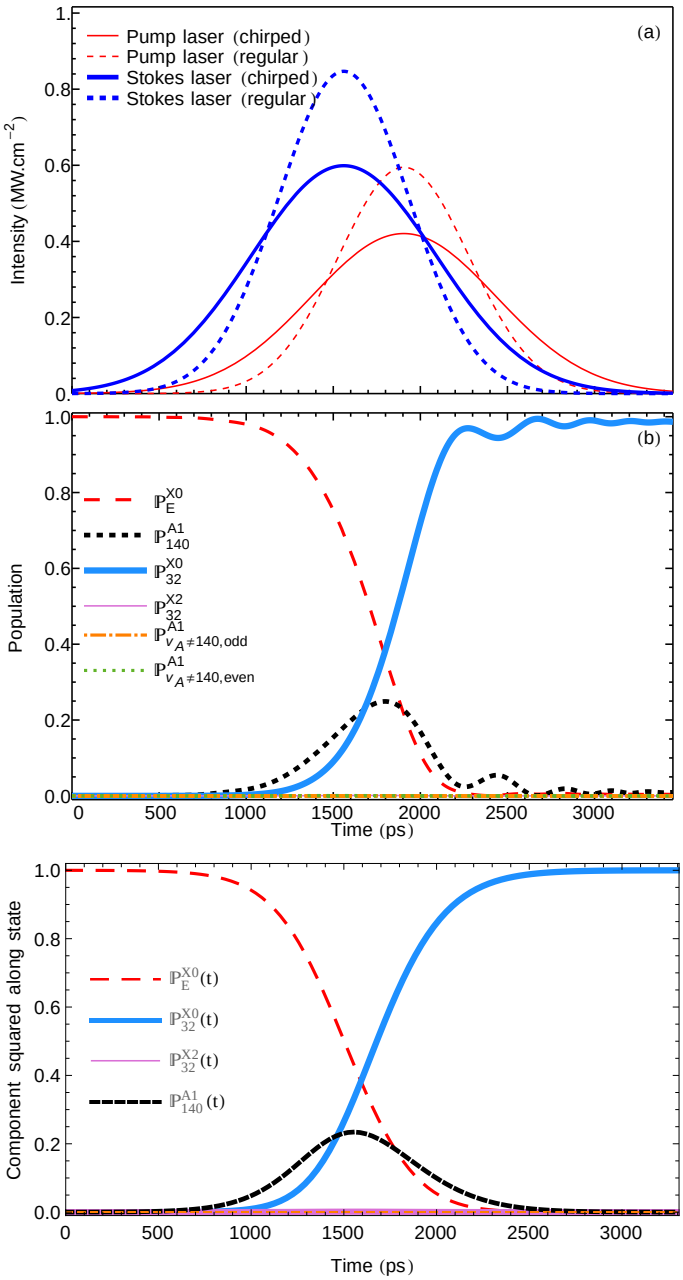

Figure 6.21: (Color online) **Top panel:** Population as a function of time in chirped STIRAP (case 4—bNCc) for an intensity of $16I_{\pi,0}$ at optimal pulse delay. **Bottom panel:** Adiabatic state followed by the solution carrier for most of the transfer.

corresponding minimal π-pulse intensities are

$$\mathscr{D}_{E}^{A1,X0}_{140} = -1299.31\,\mathrm{e}\,a_0\,E_h^{-1/2} \quad \Rightarrow \quad I_{\pi,P} = 37.1706\,\mathrm{kW/cm^2}$$

$$\mathscr{D}_{32}^{A1,X0}_{140} = 0.0822047\,\mathrm{e}\,a_0 \quad \Rightarrow \quad I_{\pi,S} = 52.9330\,\mathrm{kW/cm^2}$$

while for all cases in the second column of Tbl. 6.1,

$$
\begin{aligned}
{}^{cc1}_{254}\mathscr{D}^{X0}_{E} &= -1485.26\,\mathrm{e}\,a_0\,E_h^{-1/2} \qquad \Rightarrow \qquad I_{\pi,P} = 28.4512\,\mathrm{kW/cm^2} \\
{}^{cc1}_{254}\mathscr{D}^{X0}_{32} &= 0.0618025\,\mathrm{e}\,a_0 \qquad \Rightarrow \qquad I_{\pi,S} = 93.6671\,\mathrm{kW/cm^2}
\end{aligned}
$$

Figure Fig. 6.22 shows the result of the calculation. The main change introduced by the spin-orbit coupling effects is the ratio of intensities.

6.4.6 Case 6—bSIc: intuitive sequence of chirped lasers with narrow spectral bandwidth, inclusive of SO coupling

As for case 2-bNIc, where I excluded spin-orbit coupling, the initial detunings of the lasers prove quite important to the efficiency of the transfer. Figure 6.23 shows the numerical search for optimal detunings near the prediction from the GRHYP in the present case. Notice that the surface displays the same features as in Fig. 6.15, in particular the slight bump at the top of the ridge. The bottom panel of Fig. 6.23 shows the strong dependence of the final populations on the Stokes detuning, for the three values of the pump detuning indicated in the figure. Numerically the ideal detunings are almost identical between case 2-bNIc and case 6-bSIc: since the transition dipole moments are very similar, the peak Rabi amplitudes are also almost identical (see previous section). Also the peaking times of the lasers, t_P and t_S, are the same in cases 2-bNIc and 6-bSIc, hence the closeness of the detunings between the two cases.

I ran the calculation with the same parameters as for case 5—bSIu, and encountered the same phenomenon of efficiency reduction at minimal intensity due to chirping as described in Sec. 6.4.2 for case 2—bNIc. However, in the

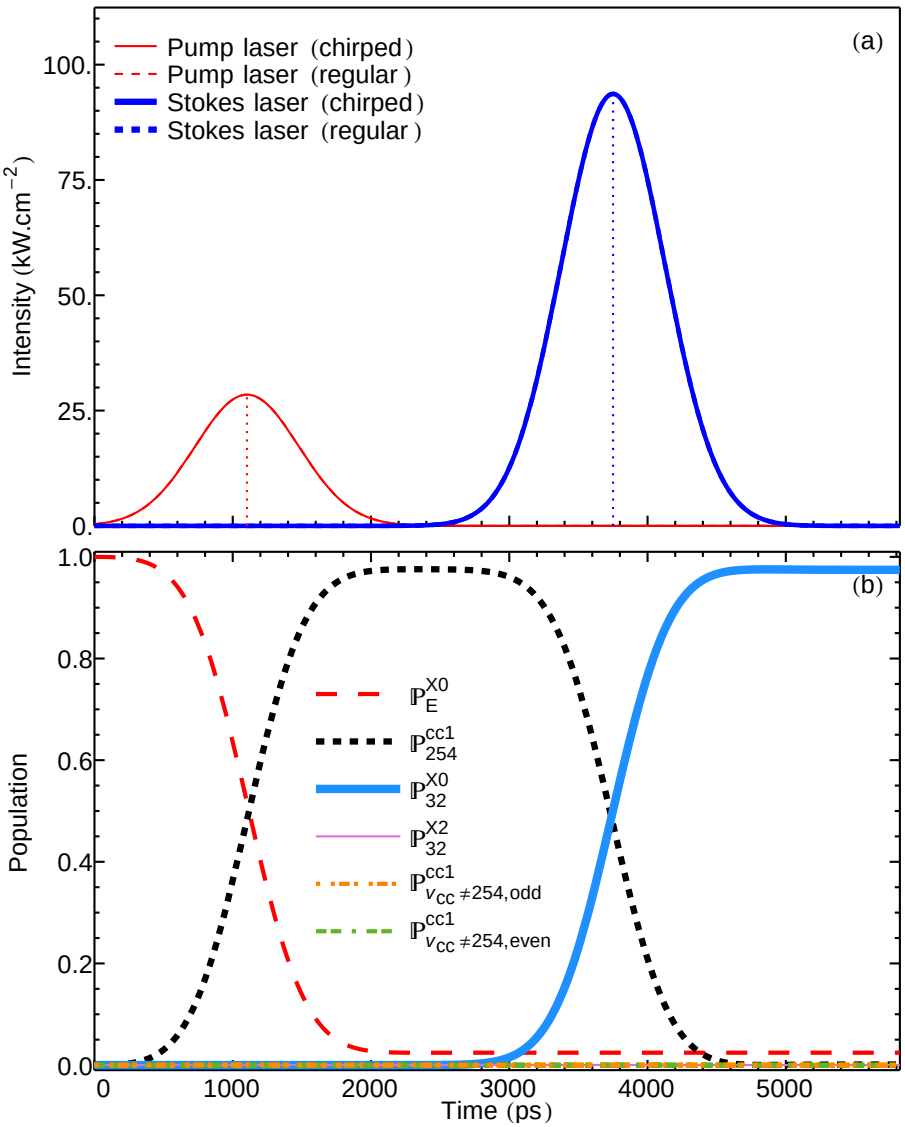

Figure 6.22: (Color online) Population transfer as a function of time, case 5—bSIu. Narrow spectral bandwidth of 0.5 GHz, spin-orbit effects accounted for, unchirped lasers in intuitive sequence. The laser intensities are chosen to obtain the simplest π-pulse as possible.

present case, chirping reduced the efficiency of each single step from $\approx 100\%$ to $\approx 20\%$, requiring a greater increase in the intensity to recover a transfer efficiency greater than 98%. Therefore I readjusted the intensities and went on to study the dependence of the process on time delay. As for case 2—bNIc, the minimal pulse delay was $\approx 0.85\Delta\tau$. Figure 6.24 shows the population transfer for these optimized parameters. Again with the optimized parameters and

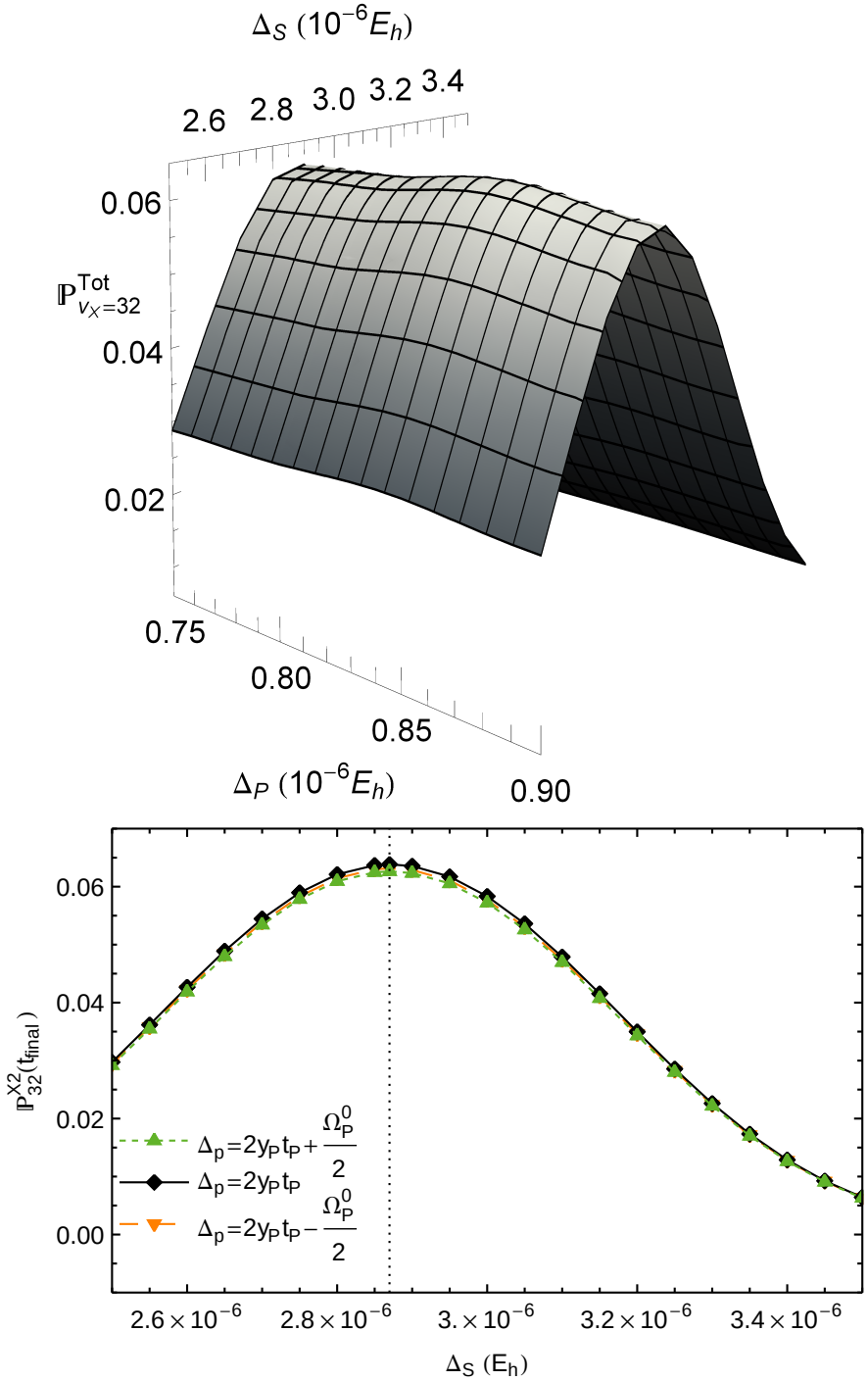

Figure 6.23: (Color online) Sensitivity of the final population in the final state $|X,0,32\rangle$ to the laser detunings for chirped pulses in the intuitive sequence for narrow bandwidth, inclusive of spin-orbit coupling (case 6—bSIc). **Top panel:** numerical search in the region predicted by the GRHYP (see text). Notice the slight bump at the top of the ridge. **Bottom panel:** Dependence of the final population in the final state on the detuning of the Stokes pulse, for three values of the pump detuning: two are predicted by the GRHYP, the third is the middle value between those.

pulse overlap, the transfer is nearly adiabatic: the adiabatic carrier and the solution carrier are almost identical, even though the adiabatic ratio of Eq. (2.11) is on the order of 0.5% at all times.

Here, including pin-orbit coupling not only changes the ratio of intensities as in the previous case, but the population in the intermediate state varies less smoothly than for case 2—bNIc.

6.4.7 Case 7—bSCu: Counterintuitive sequence of unchirped lasers with narrow spectral bandwidth, inclusive of SO coupling

Here, I found numerically a set of parameters which maximizes to 94.2% the populations transferred into the final state. However, 5.4% of population gets trapped into $|\Phi^{cc}_{v_{cc}=254}\rangle$. The population transfer is also not adiabatic, as evidenced by the difference between the adiabatic carrier and the solution carrier shown in Fig. 6.25. From the lack of adiabaticity, I conclude that conventional STIRAP is not possible in this situation: the spin-orbit coupled states do not create a favorable adiabatic basis in the counterintuitive sequence, even though a working adiabatic basis was found for the intuitive sequence.

6.4.8 Case 8—bSCc: Counterintuitive sequence of chirped lasers with narrow spectral bandwidth, inclusive of SO coupling

In the counterintuitive sequence when including spin-orbit effects, chirping the lasers restores the stability of adiabatic passage that we saw in the $A^1\Sigma^+$ state-only case for regular STIRAP (case 3—bNCu). The optimal delay between

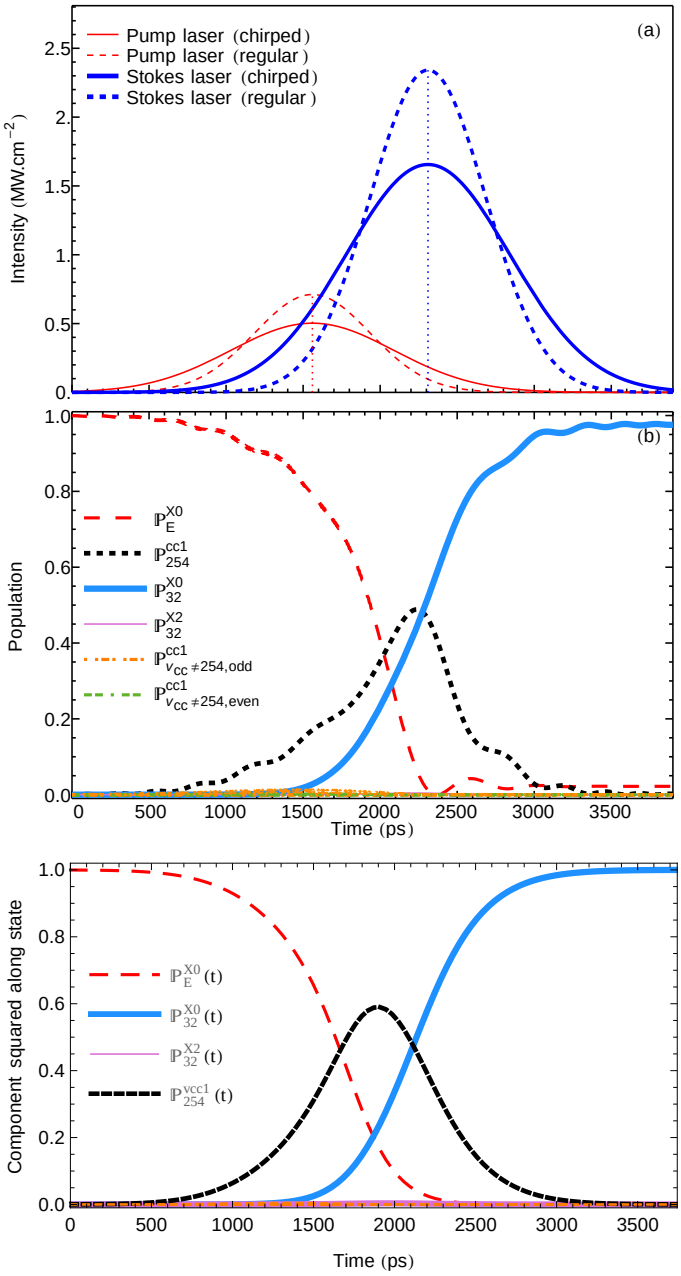

Figure 6.24: (Color online) **Panel (a):** Laser pulses. **Panel (b):**Populations as a function of time in chirped intuitive sequence (case 6—bSIc) for an intensity of $25I_{\pi,0}$ at optimal pulse delay $\eta = 0.85\Delta\tau$. The necessity for higher intensities is a consequence of the inclusion of spin-orbit coupling effects. **Bottom panel:** Adiabatic state followed by the solution carrier for most of the transfer.

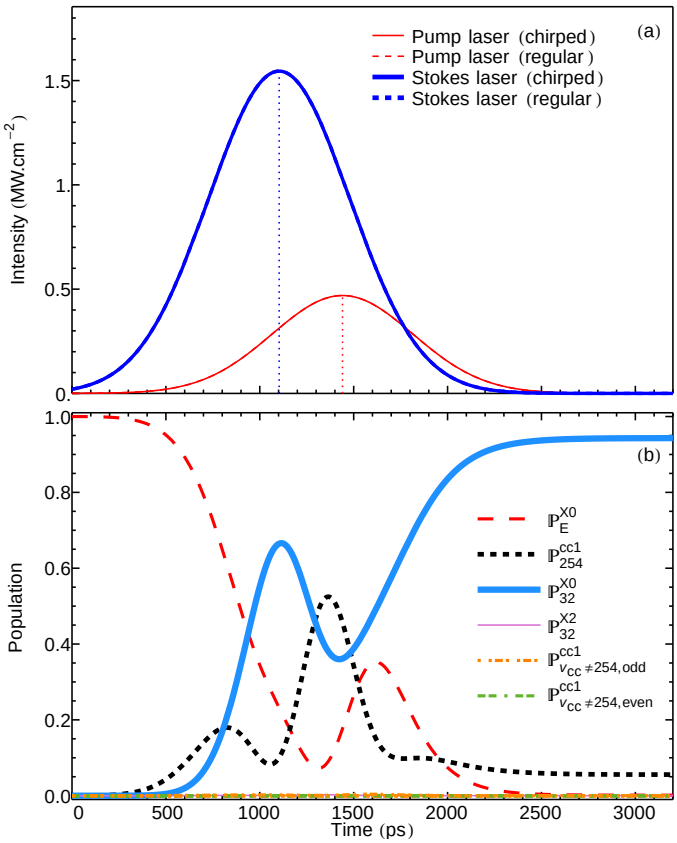

Figure 6.25: (Color online) **Top & middle panel:** Populations as a function of time in unchirped counterintuitive sequence (case 7—bSCu) for an intensity of $16.5I_{\pi,0}$ at optimal pulse delay $\eta = -0.38\Delta\tau$. The higher necessary intensities are a consequence of the inclusion of spin-orbit coupling effects.

the pulses is $0.5\Delta\tau$, the process is thus slightly faster than in case 6—bSIc. Figure 6.26 shows the population transfer for the optimal parameters. Figure

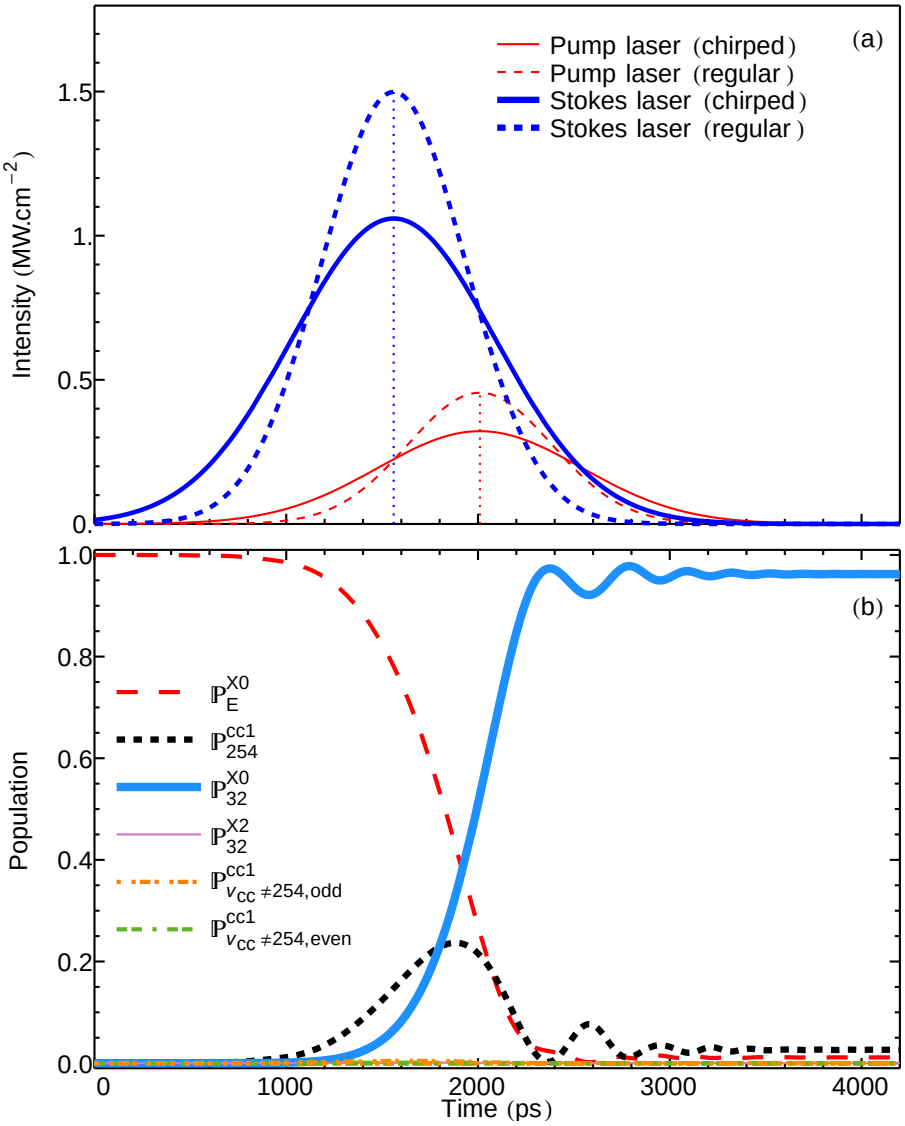

Figure 6.26: (Color online) Optimized population transfer for chirped counterintuitive sequence of lasers with narrow spectral bandwidth, accounting for spin-orbit effects, case 8—bSCc. The final population in the $X^1\Sigma^+$ state reaches 96.2%.

6.27 shows the adiabatic carrier involved, the adiabatic condition as a function of time, and the adiabatic companion. Notice how the small adiabatic transfer actually makes the intermediate population in the solution carrier *smaller* than in the adiabatic carrier. The passage is better in that regard than if the solution

was perfectly matching the adiabatic carrier.

6.4.9 Checkpoint

What have we learned so far? By chirping the lasers, one can achieve adiabatic passage in either laser sequence. The cost is an increase of the intensity, with the benefit of more stability in the procedure, and even making the procedure faster. We've also noted the importance of detunings when chirping the lasers, and derived expressions that lead to the optimal detunings for sequences with lasers of equal chirp rates. When studying STIRAP on spin-orbit coupled channel states, chirping the lasers helped to optimize the process.

To keep making the process faster, a solution is to use lasers with smaller temporal bandwidths. The tradeoff is broader spectral bandwidths. How do the vibrational states close in energy to the chosen intermediate state affect the dynamics of the process? Such cases are described by the two rightmost columns of Tbl. 6.1. Let's embark into those studies.

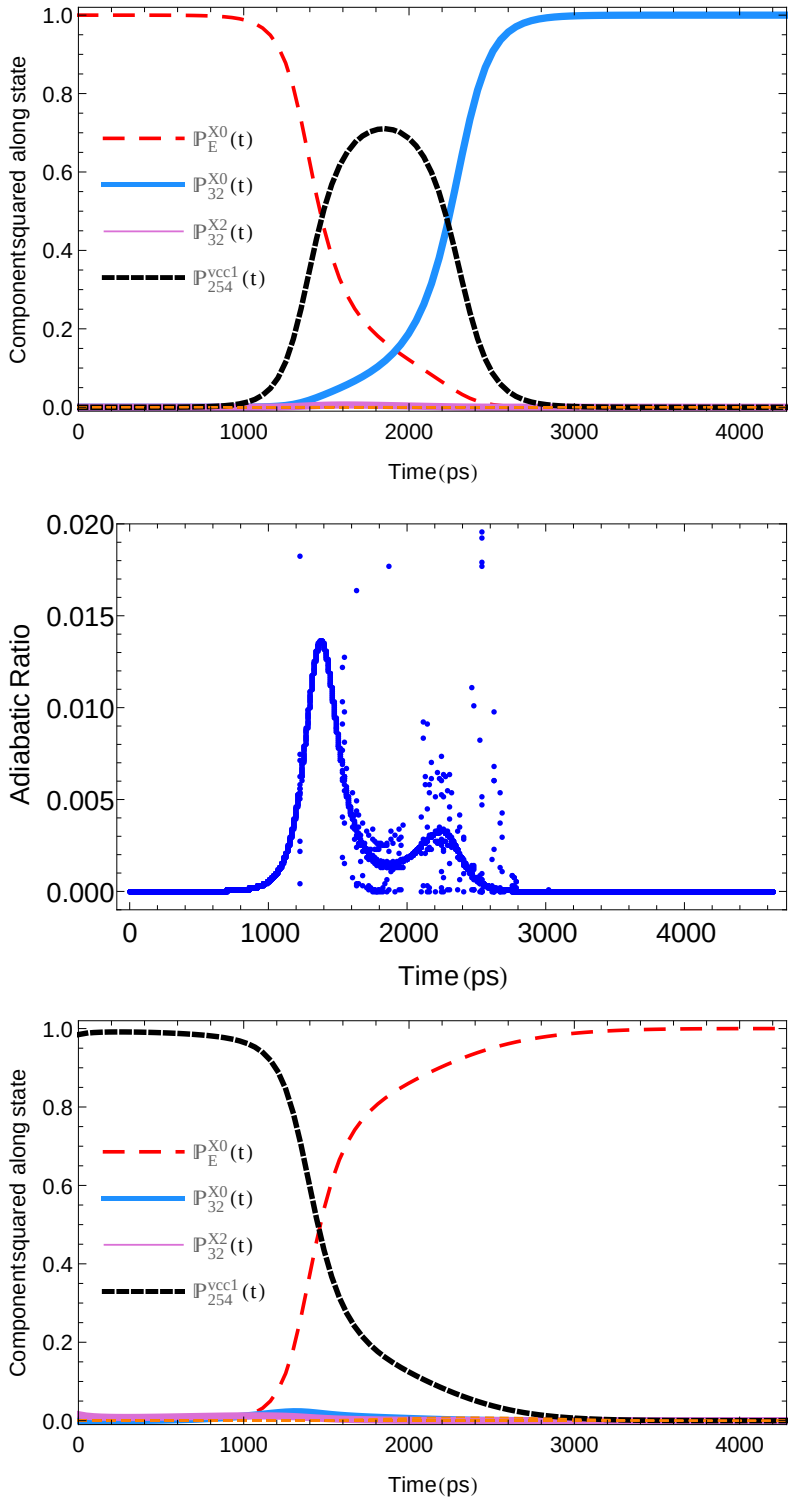

Figure 6.27: (Color online) Adiabatic carrier (top panel), adiabatic condition (middle panel), and adiabatic companion (bottom) for chirped counterintuitive sequence of lasers with narrow spectral bandwidth, accounting for spin-orbit effects, case 8—bSCc. The adiabatic carrier has a stronger component over the intermediate state than the actual solution of the problem.

6.4.10 Case 9—BNIu: Intuitive sequence of unchirped lasers with broad spectral bandwidth, without SO coupling

Since they are not chirped, the pump and Stokes lasers are *a priori* resonant with their respective transitions. Yet, they are detuned from all the *other* transitions possible. As the spectral bandwidth is now 10 GHz, we should expect the vibrational states close in energy to our chosen stepping stone $|A, 1, 140\rangle$ to take part in the process. In this study, I use the same lasers as in case 1—bNIu, except that I broaden the spectral bandwidth to 10 GHz. Figure 6.28 shows the corresponding population transfer. With these broader lasers still in the intuitive sequence, the pump π-pulse fails to achieve a full photoassociation step. The state $|A, 1, 146\rangle$ has such a strong transition dipole moment matrix element with the $X^1\Sigma^+$ scattering state, that even though the pump laser is far detuned from the transition $|\chi_E^{X0}\rangle \rightarrow |A, 1, 146\rangle$, some population transits briefly into $|A, 1, 146\rangle$ (dotted line oscillating around $t = 50$ ps in Fig. 6.28), and prevents $|A, 1, 140\rangle$ from being fully populated by the pump pulse. Consequently, the Stokes pulse can only transfer into $|X, 0, 32\rangle$ at most the population remaining in $|A, 1, 140\rangle$ at the end of the pump pulse. The vibrational states close in energy to $|A, 1, 140\rangle$ are not the only ones to affect the overall transfer: we discussed in chap. 4 how the electric dipole selection rule allows transitions in to $X^1\Sigma^+$, $J_X = 2$. Here the Stokes pulse transfers population preferably to the state with which it resonates, *i.e.* $|X, 0, 32\rangle$. However, 2.2% of the total population ends up in $|X, 2, 32\rangle$.

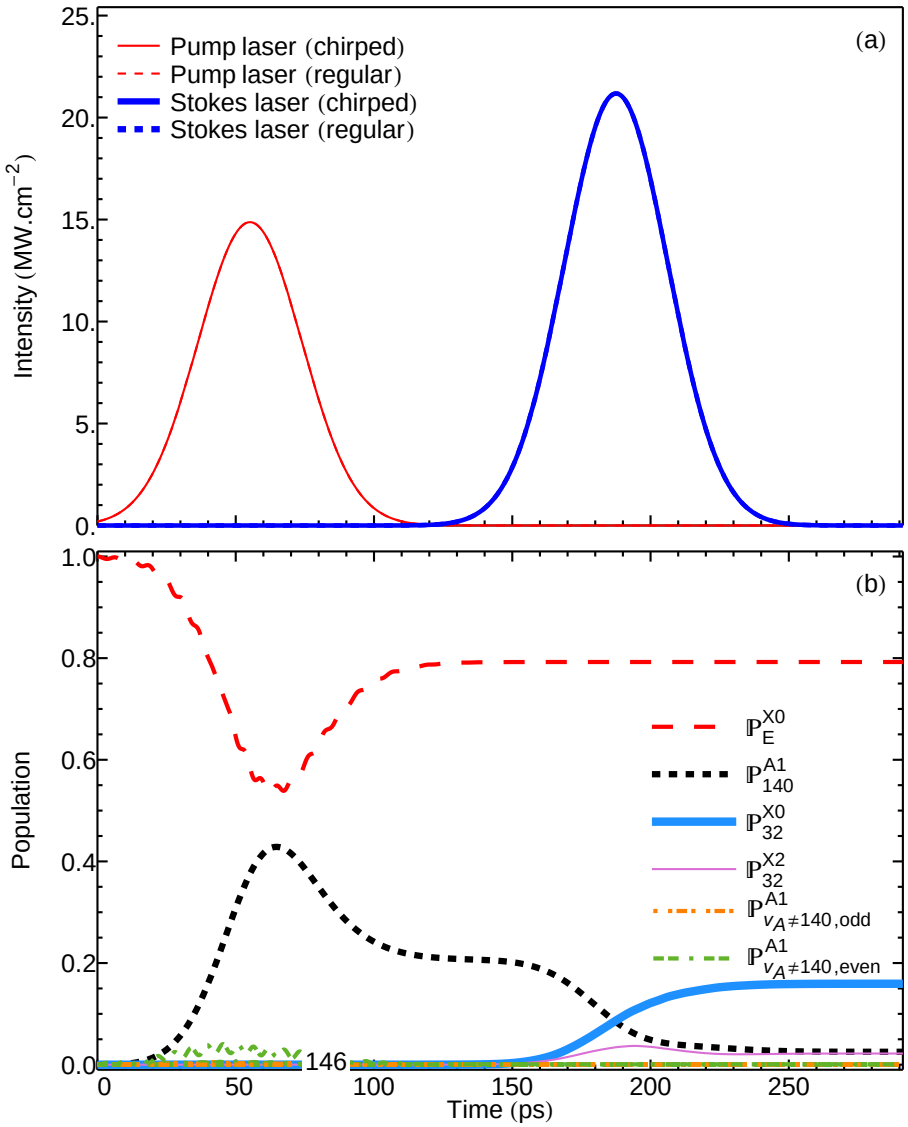

Figure 6.28: (Color online) Population transfer for intuitive sequence of unchirped lasers with broad spectral bandwidth (10 GHz), exclusive of spin-orbit coupling, case 9—BNIu. The strong free-bound transition dipole moment matrix element between the continuum and $|A,1,146\rangle$ prevents the π-pulse from fully achieving photoassociation into $|A,1,141\rangle$. At the end of the process, 15.9% of the population is in $|X,0,32\rangle$, 2.2% in $|X,2,32\rangle$, 2.5% in $|A,1,140\rangle$, and the rest stayed in the continuum state. The $|A,1,146\rangle$ only collected 0.07% of the total population while disturbing the overall process.

With more vibrational states involved in the transfer, particularly in the pump step, the study of the influence of the detuning of the pump laser on the population transfer is now important. In Fig. 6.29, there exists a non-zero value of the detuning of the pump laser that drastically enhances the population in the final state.We will see in case 13—BSIu that the same phenomenon occurs.

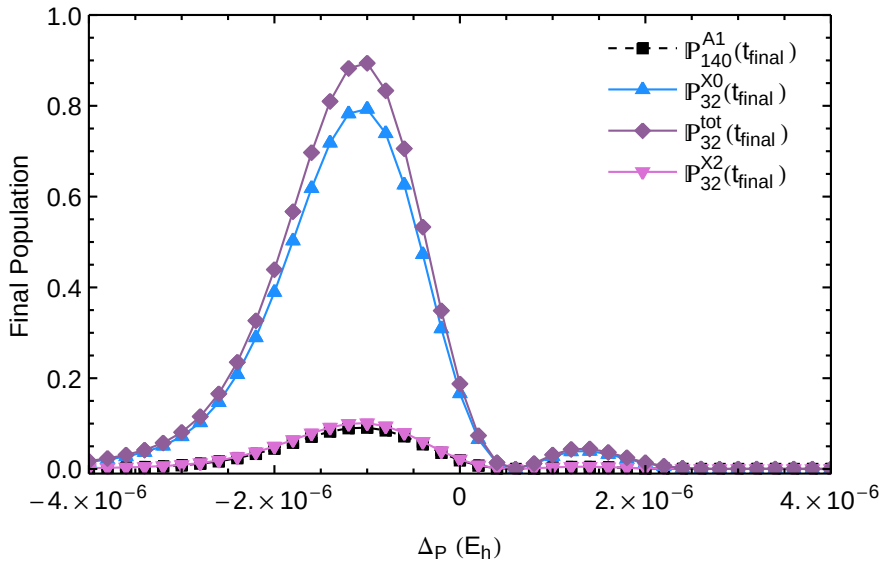

Figure 6.29: (Color online) Dependence of final population on the detuning of the pump pulse for case 9—BNIu. The final population in the final state is greatly enhanced for a detuning of $\Delta_P = -10^{-6}\,E_h$.

Let's use this newly found detuning and examine the dependence of the population transfer on the intensity in Fig. 6.30. Both intensities are always chosen such that the peak Rabi frequencies of each lasers are equal, as suggested for STIRAP. The pattern in Fig. 6.30 is typical of general π-pulses, as explained briefly at the end of Sec. 2.3.1: whenever the intensity of the laser does not make the integral over time of the corresponding Rabi frequency an odd multiple of π, the population is not maximized. Here, the maxima do not reach 100%, and the oscillations are dampened as the intensity increases because of the presence of the neighboring states: increasing the intensity also increases the coupling to these other states, which receive more population,

that in turn does not go into the desired intermediate and final states.

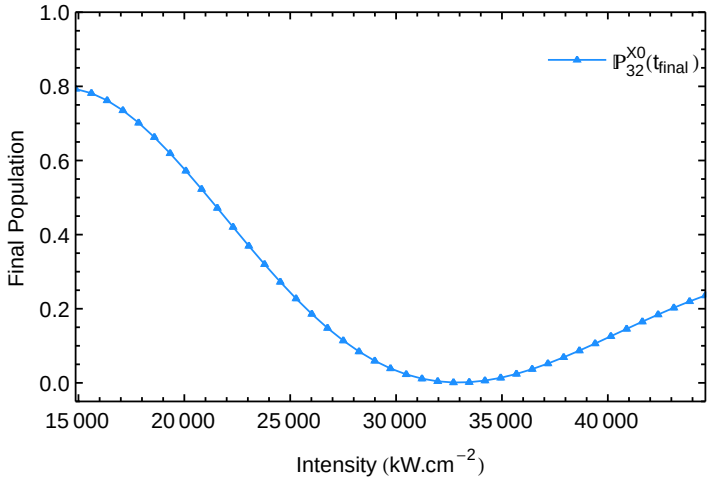

Figure 6.30: (Color online) Dependence of final population on the intensity of the pump pulse for case 9—BNIu. The final population in the final state is maximal for the minimal π-pulse intensity.

For the optimal detuning and intensity above, the process is fairly insensitive to the delay between the pulses, as shown in Fig. 6.31.

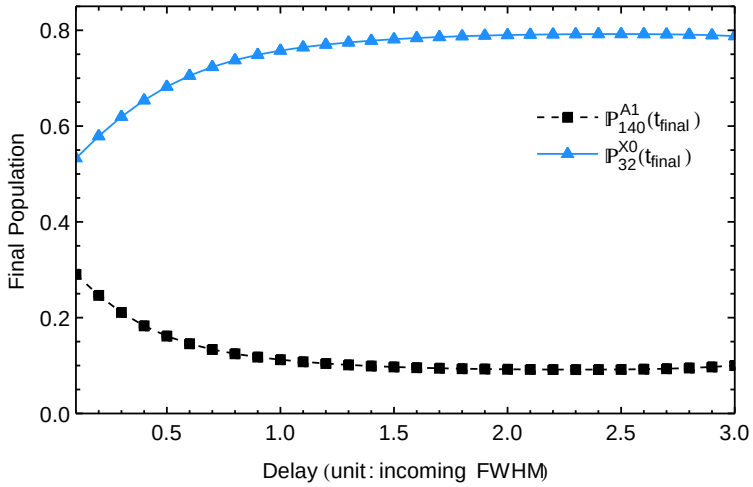

Figure 6.31: (Color online) Dependence of final population on the pulse delay for case 9—BNIu. The final population is comparatively high when the pulse delay is at least 1.5 FWHM of the laser.

Finally, Fig. 6.32 shows the population transfer for the optimal parameters discussed above. The state $|X,0,32\rangle$ receives 78.1% of the total population, 10.2% go into the $|X,2,32\rangle$ state, 9.7% of the population is trapped in $|A,1,140\rangle$,

and 1.8% remains in the continuum state. The neighbors of $|A,1,140\rangle$ in energy share the remaining 0.2% of population.

6.4.11 Case 10—BNIc: Intuitive sequence of chirped lasers with broad spectral bandwidth, without SO coupling

The first simulation assumes all parameters to be the same as in the previous case 9—BNIu. In particular the detunings are zero, despite our knowledge of the GRHYP. Figure 6.33 shows the population transfer in this case. First, no population gets transferred into *any* of the vibrational states of $X^1\Sigma^+$. As the pulse is positively chirped, the central frequency of the pump laser increases with time, and the states *above* $|A,1,140\rangle$ in energy get successively populated. Note that the first state to enter into resonance with the laser is $|A,1,141\rangle$. However the state $|A,1,146\rangle$, with the highest free-bound transition dipole moment, gets populated first as a closer look at early times in Fig. 6.33 shows. The state $|A,1,141\rangle$ then picks up population. The state $|A,1,144\rangle$, which has the second highest fbTDMME in magnitude, is third to enter the scene, immediately followed by $|A,1,143\rangle$. The states $|A,1,142\rangle$ and $|A,1,145\rangle$ remain oblivious to the process, as they have the smallest free-bound transition dipole moment matrix elements, see Tbl. 6.2 p. 192. Apart from $|A,1,141\rangle$, the neighboring states are populated in the same order as their transition dipole moment. Chirping the laser gives priority to $|A,1,141\rangle$ over $|A,1,v_A\rangle, v_A = 143,144$, but is not sufficient for $|A,1,141\rangle$ to precede $|A,1,146\rangle$ in receiving population, due to the strong value of the fbTDMME of $|A,1,146\rangle$. Notice the similarity of this graph with Fig. 5 in [82].

Let's change the detunings using the GRHYP (Fig. 6.34) and see how the process is modified. The state $|A,1,146\rangle$ still collects, however briefly, some

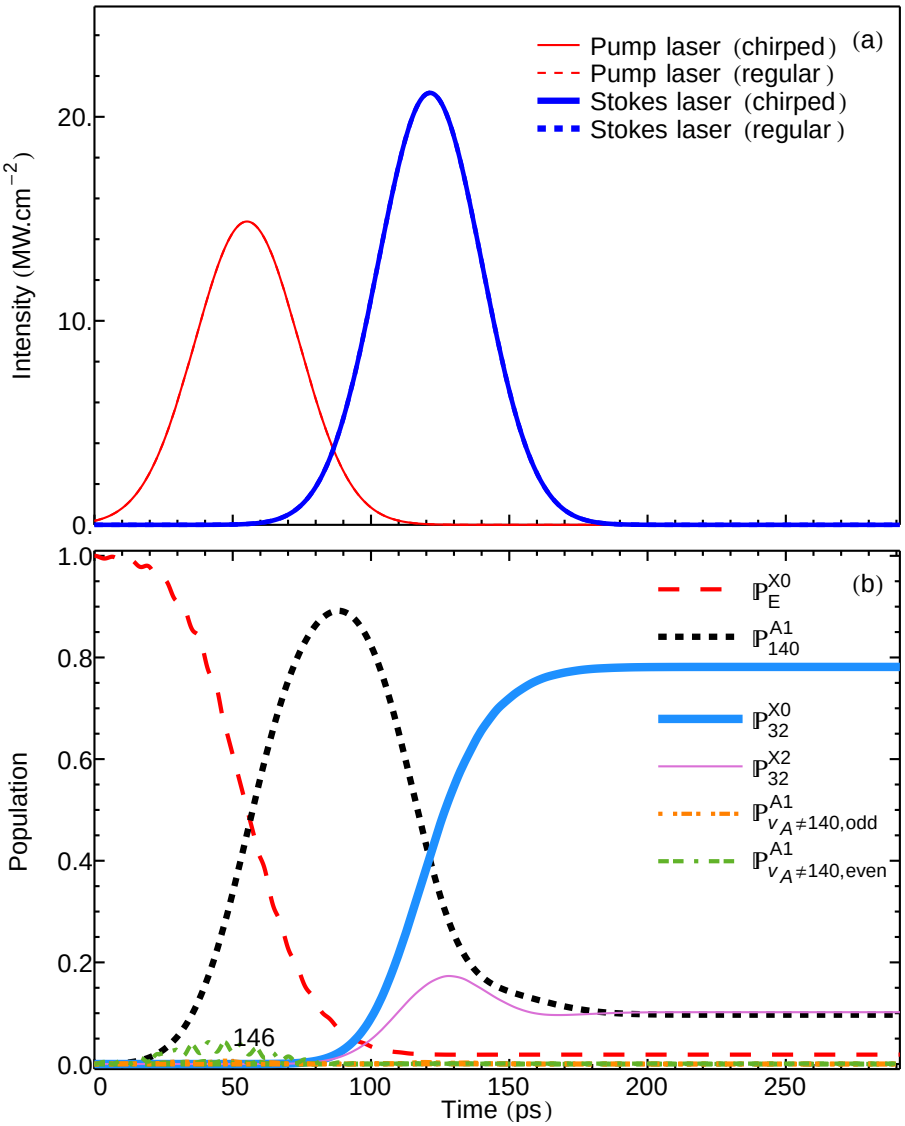

Figure 6.32: (Color online) Population transfer for intuitive sequence of unchirped lasers with broad spectral bandwidth (10GHz), exclusive of spin-orbit coupling, case 9—BNIu with optimized parameters.

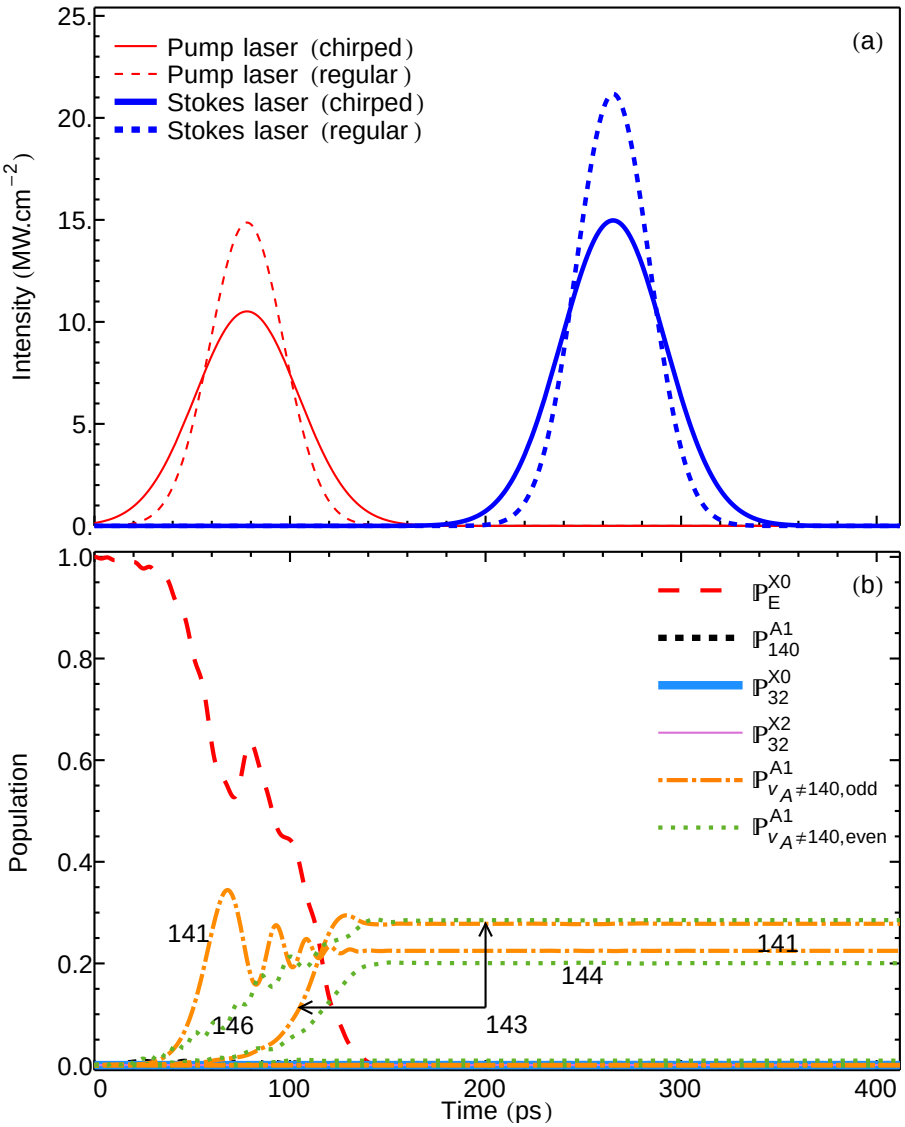

Figure 6.33: (Color online) Population transfer for intuitive sequence of chirped lasers with broad spectral bandwidth (10 GHz), exclusive of spin-orbit coupling, case 10—BNIc. With the detunings set at zero, the intermediate state of interest is never populated, and thus *no* population is transferred to the final state.

transient population. This time, the intermediate state $|A,1,140\rangle$ *is* populated. Again as time passes, the pump laser approaches resonance with $|A,1,141\rangle$, which then receives some population. The detunings are chosen so that when the Stokes peaks, population is stimulated down to $|X,0,32\rangle$ and $|X,2,32\rangle$. Notice that any laser is indifferent to the direction of the transfer: here the Stokes

v_A	$^{A1}_{v_A=140}\mathscr{D}^{X0}_E(\mathrm{e}\,a_0\,E_h^{-1/2})$
146	−12717.5
145	117.779
144	4188.26
143	2628.12
142	−270.391
141	−1739.22
140	−1299.31

Table 6.2: Free-bound transition dipole moment matrix elements for the 7 vibrational states immediately below the configuration average asymptote Na($3S$)+Cs($6P$).

pulse re-excites some population into $|A,1,141\rangle$. Indeed with the passing of time, the central frequency of the Stokes also increases with time, and eventually the Stokes pulse is sufficiently near the transition $|A,1,141\rangle \rightarrow |X,0,32\rangle$ to trigger re-excitation into $|A,1,141\rangle$.

The population transfer is *very* sensitive to the pulse delay (Fig. 6.35). The oscillations in the final population in $|X,0,32\rangle$ as the time delay changes are not in phase with the oscillations in the final population in $|X,2,32\rangle$. Thus although it is possible to maximize the total population in $X^1\Sigma^+$, one cannot minimize the population in $|X,2,32\rangle$ and *simultaneously* maximize the population in $|X,0,32\rangle$. Finally a numerical search showed that for an intensity of 5 times the minimal π-pulse intensity, the total population in the $X^1\Sigma^+$ state reaches 44%, with 30% in $|X,2,32\rangle$ and 14% in $|X,0,32\rangle$. Such intensity corresponds to $\approx 52\,\mathrm{MW/cm^2}$ for the pump pulse, and $\approx 75\,\mathrm{MW/cm^2}$ for the Stokes pulse. With intensities so high, the process would be unrealistic.

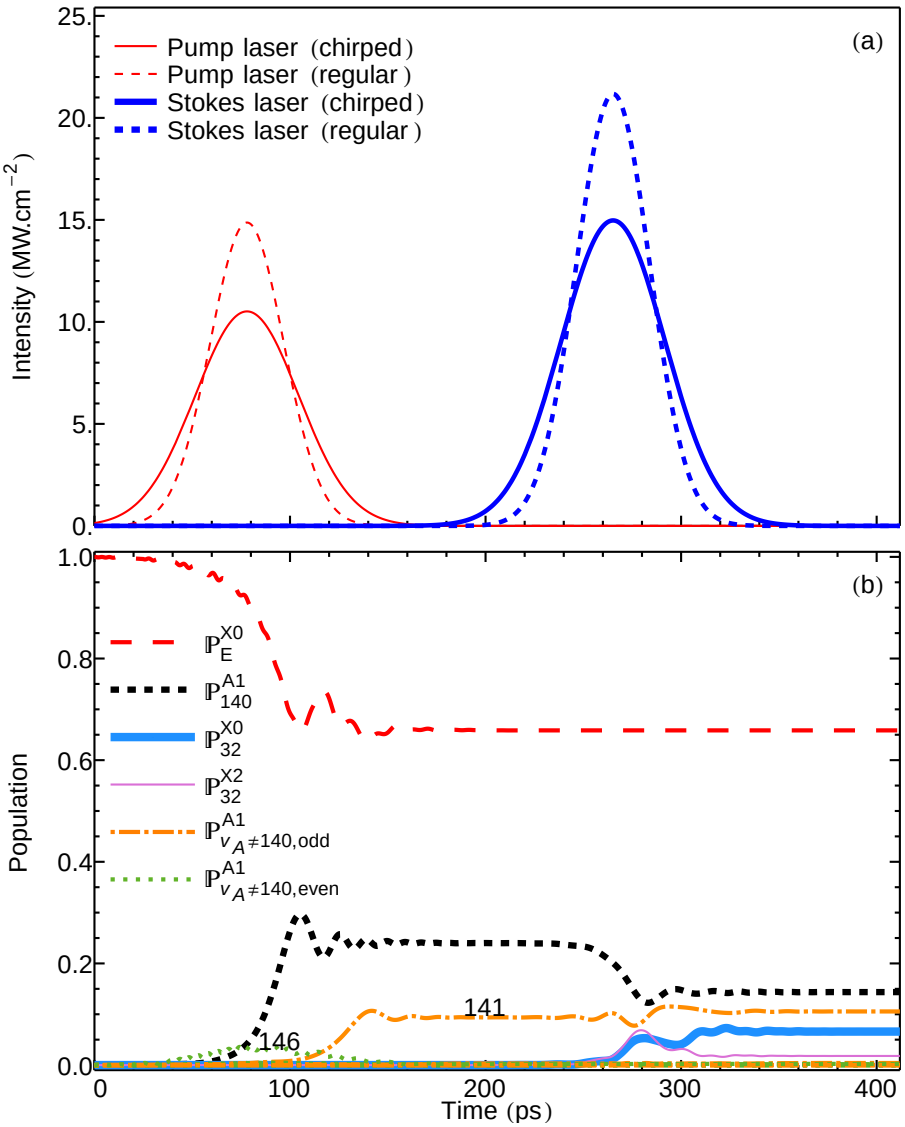

Figure 6.34: (Color online) Population transfer for intuitive sequence of chirped lasers with broad spectral bandwidth (10 GHz), exclusive of spin-orbit coupling, case 10—BNIc. Optimal detunings change the final distribution of populations among the vibrational states available.

6.4.12 Case 11—BNCu: counter-intuitive sequence of unchirped lasers with broad spectral bandwidth, exclusive of SO coupling

Appendix G details the numerical search for the optimal parameters (detunings, intensities, and pulse delay) for this case. Figure 6.36 p. 195 shows

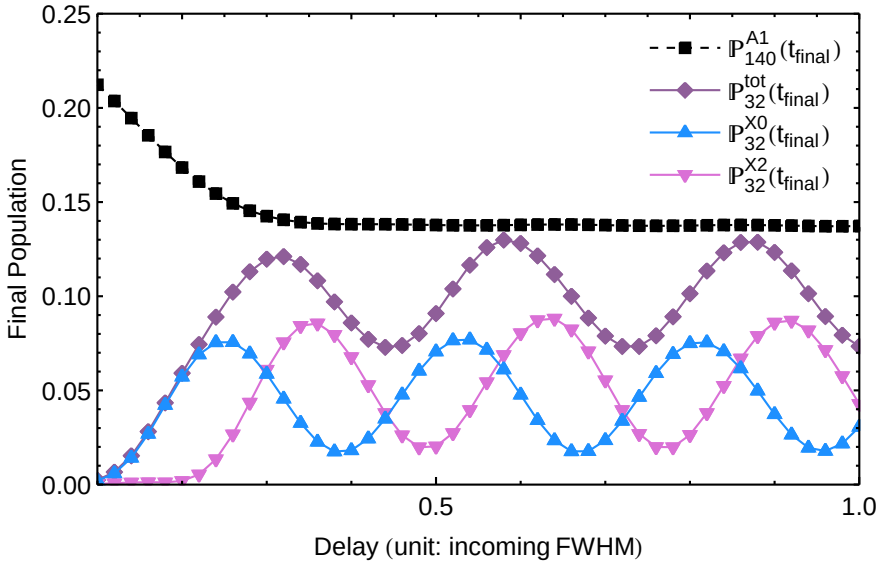

Figure 6.35: (Color online) Variation of final populations in vibrational states of interest as a function of pulse delay for case 10—BNIc. This process is highly unstable compared to the ones studied so far.

the population transfer with the optimized parameters. Similarly to case 9—BNIu, the broader spectral bandwidth of the laser increases the influence of the intermediate vibrational states with the strongest fbTDMME, $|A, v_A = 146, 1\rangle$. Thus in the counter-intuitive sequence, the influence of $|A, v_A = 146, 1\rangle$ prevents the realization of an adiabatic state favorable to a full population transfer into $|X, v_X = 32, 0\rangle$. When both laser pulses are over, only 20.7% of the population ends up in $|X, v_X = 32, 0\rangle$ (1.9% in $|X, v_X = 32, 2\rangle$), 2.6% of the population remains in $|A, v_A = 140, 1\rangle$, and 74.7% of the population stays in the continuum. Therefore making the process faster by decreasing the temporal bandwidth of the laser, correspondingly increasing the spectral bandwidth, prevents successful STIRAP. For unchirped lasers, the counter-intuitive sequence transfers less population into the desired final state than the intuitive sequence.

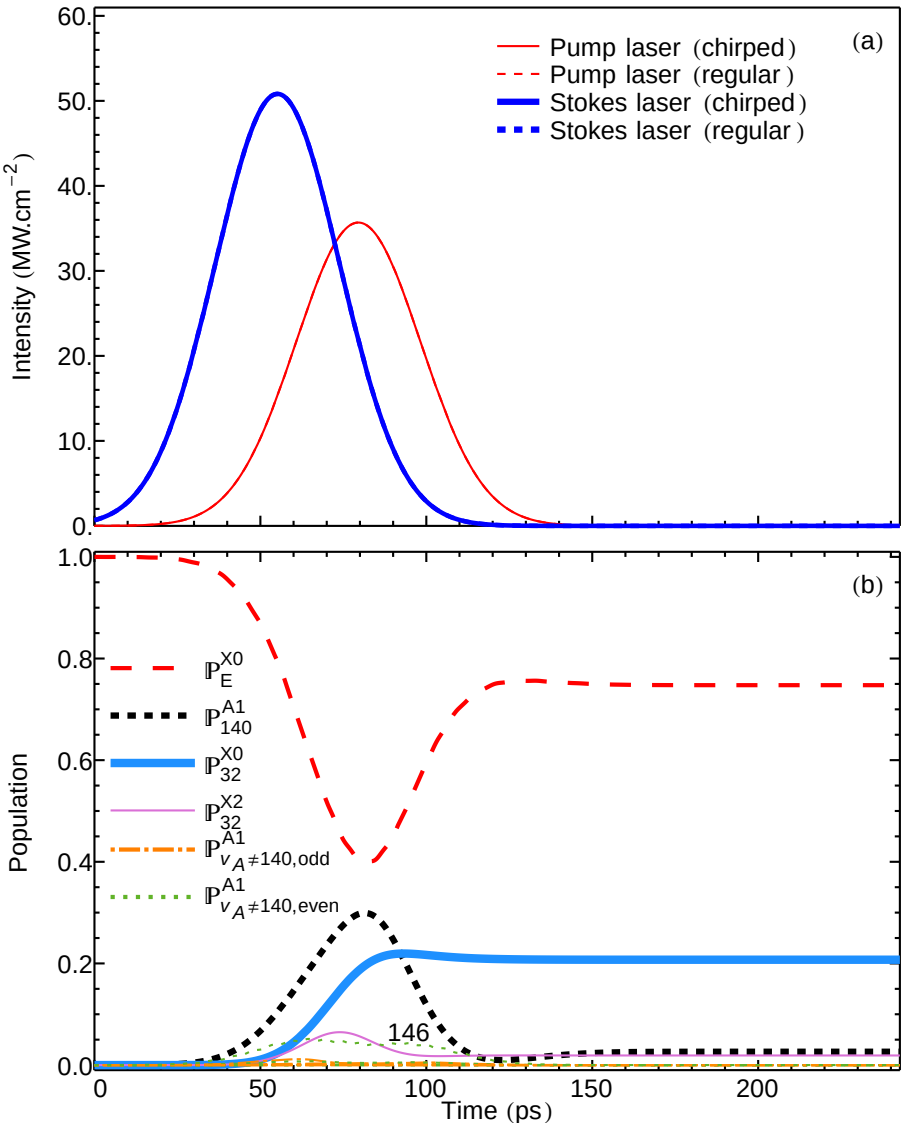

Figure 6.36: (Color online) Populations with optimized parameters for case 11—BNCu. The broad spectral bandwidth of the lasers involve the intermediate states not resonant with the laser, but with a strong TDMME. The graph clearly shows the transient population into the state $|A, v_A = 146, 1\rangle$, which prevents the realization of an adiabatic state favorable to the population transfer.

6.4.13 Case 12—BNCc: counter-intuitive sequence of chirped lasers with broad spectral bandwidth, exclusive of SO coupling

Appendix G details the numerical search for the optimal parameters for this case. Compared to case 11—BNCu, chirping the lasers helps to remove population from the continuum. The final population in $|X, v_X = 32, 0\rangle$ is smaller here than in case 11 (20.7%). One benefit of chirping the lasers is the higher probability that the scattering atoms were photoassociated, *i.e.* formed a molecule. Indeed the probability to find the system elsewhere than in the continuum is 88.1%. Table 6.3 gives the probabilities at the end of the process for this case.

State	$\mathbb{P}_{\text{final}}(\%)$
$\lvert\chi_E^{X0}\rangle$	11.9
$\lvert X, v_X = 32, J = 0\rangle$	10.7
$\lvert X, 32, 2\rangle$	1.9
$\lvert A, v_A = 146, 1\rangle$	16.3
$\lvert A, 144, 1\rangle$	5.7
$\lvert A, 143, 1\rangle$	6.1
$\lvert A, 142, 1\rangle$	0.4
$\lvert A, 141, 1\rangle$	37.3
$\lvert A, 140, 1\rangle$	9.7

Table 6.3: Population in the various states involved in case 12—BNCc at the end of the process.

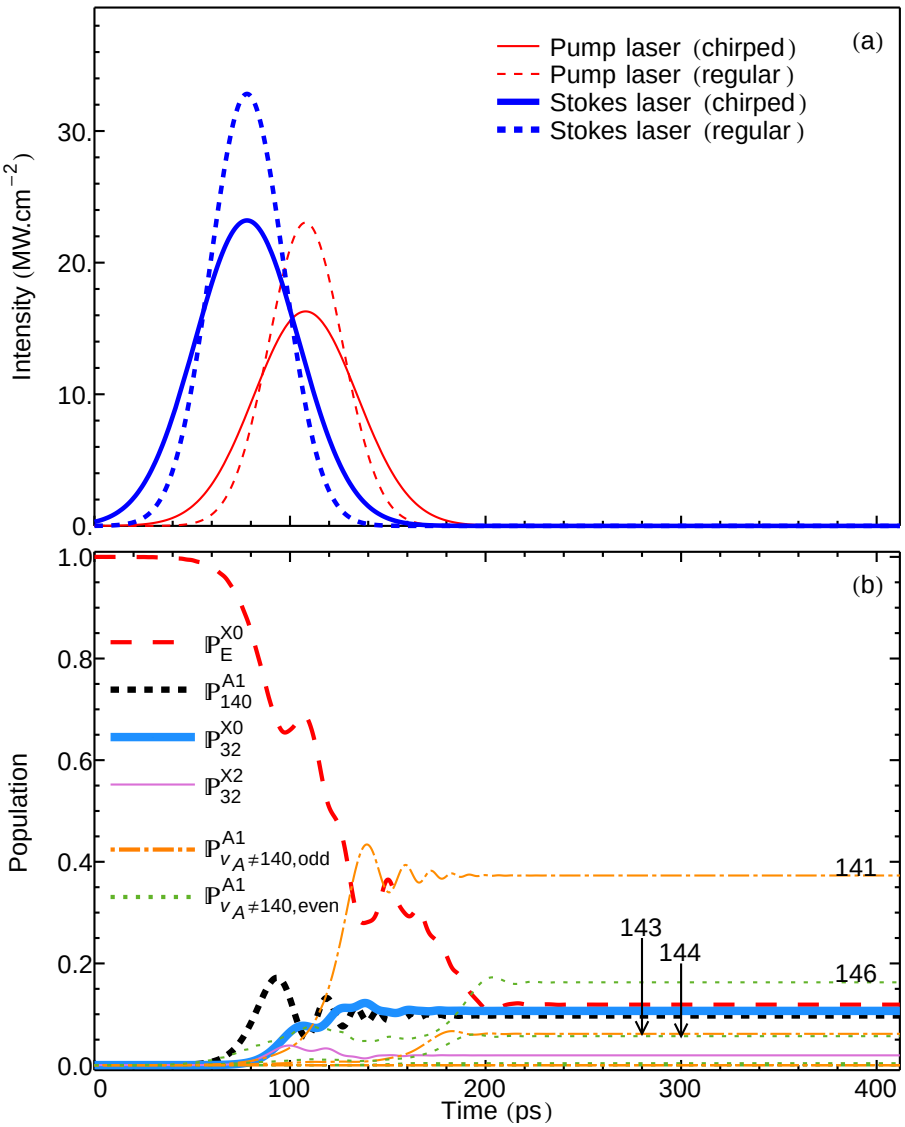

Figure 6.37: (Color online) Populations with optimized parameters for case 12—BNCc. The populations are nicely spread over the high-lying states of the $A^1\Sigma^+$ state, with $|A, v_A = 141, 1\rangle$ being the most populated state. Only 10.7% of population reaches the $|X, v_X = 32, J = 0\rangle$. Chirping the lasers in the counter-intuitive sequence depletes the continuum much more than in the unchirped case 11—BNCu.

6.4.14 Case 13—BSIu: intuitive sequence of unchirped lasers with broad spectral bandwidth, inclusive of SO coupling

I obtained the population transfer in Fig. **6.38** by using the minimal π-pulse intensities possible, at zero detuning at first. Similarly to case 9—BNIu, (Sec. 6.4.10, p. 185) the vibrational state with the highest free-bound transition dipole moment matrix element intervenes significantly in the transfer. Also, the broader bandwidth of the laser now lets population arrive into $|X, 2, 32\rangle$.

For the same reasons as in case 9—BNIu, the influence of the detuning of the pump laser on the population transfer is important. The inclusion of spin-orbit coupling effects has not changed the fact mentioned in Sec. 6.4.10: here too there exists a non-zero value of the detuning of the pump laser that drastically enhances the population in the final state. The ideal detuning is now $-2.8 \times 10^{-6}\, E_h$ and yields a final population in $|X, 0, 32\rangle$ of 68.8% for the minimal π-pulse intensity of the laser. Figure **6.39** shows the variation of the most important final populations as a function of the detuning of the pump pulse.

With the optimal detuning, the final population depends also on the intensity. The qualitative behavior of figure **6.40** is identical to that of Fig. **6.30**. The quantitative difference originate from the difference in the free-bound transition dipole moment matrix elements, already evoked in Sec. 6.4.5: the minimal π-pulse intensity is smaller in the present case, the maximum final population is smaller also, and the next optimal intensity value is also smaller. As in case 9—BNIu, I chose both intensities such that the peak Rabi frequencies of each lasers are equal. The maxima do not reach 100%, and the oscillations are dampened as the intensity increases because of the presence of the neighboring states, as explained in Sec. 6.4.5.

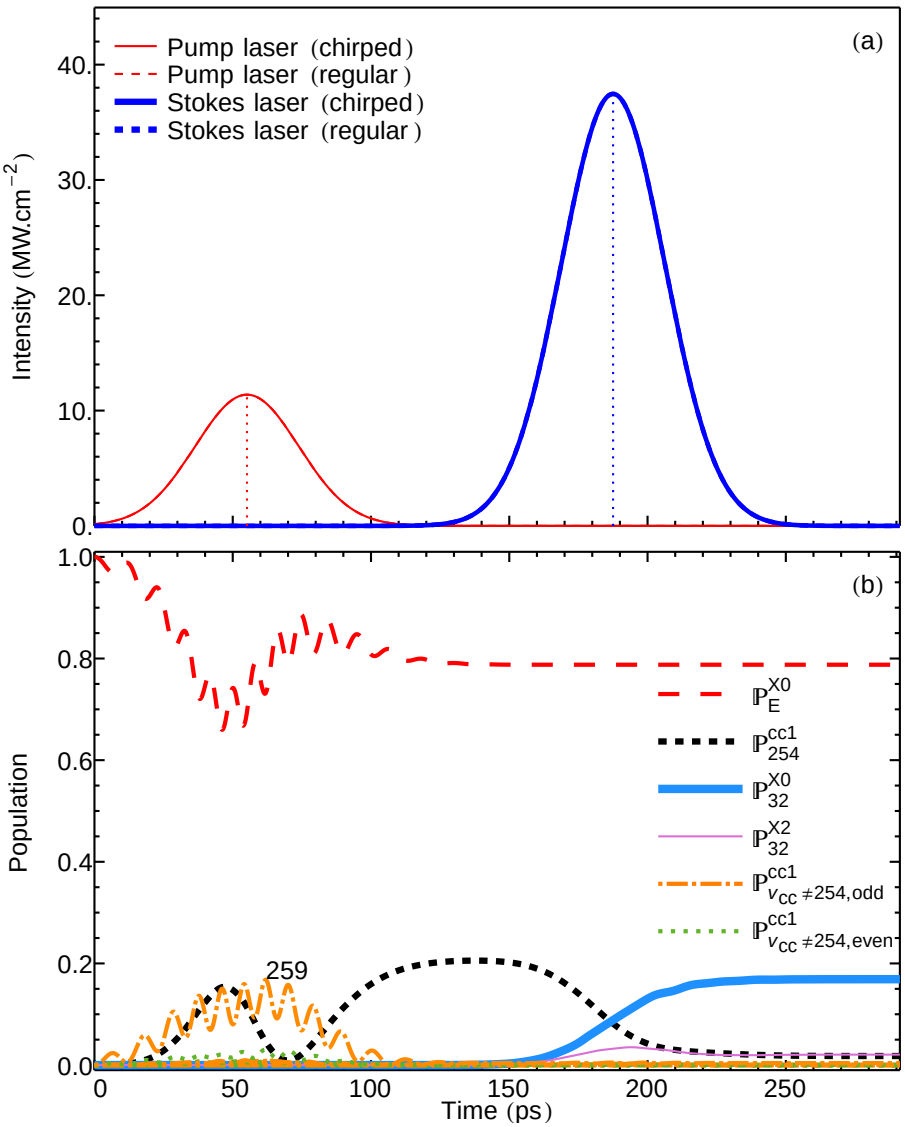

Figure 6.38: (Color online) Population transfer for intuitive sequence of unchirped lasers with broad spectral bandwidth (10 GHz), inclusive of spin-orbit coupling, case 13—BSIu. The strong free-bound transition dipole moment matrix element between the continuum and $|\Phi^{cc}_{v_{cc}=259}\rangle$ prevents the π-pulse from fully achieving photoassociation into $|\Phi^{cc}_{v_{cc}=254}\rangle$. Notice also the small amount of population that transits through $v_{cc} = 258$ (green dots between 0 ps and 100 ps

For consistency's sake, figure 6.41 shows the robustness of the process with respect to the pulse delay. To conclude this section, Fig. 6.42 shows the population transfer for the optimal parameters discussed above. The state $|X, 0, 32\rangle$ receives 68.8% of the total population, 8.3% go into the $|X, 2, 32\rangle$ state, 7.2%

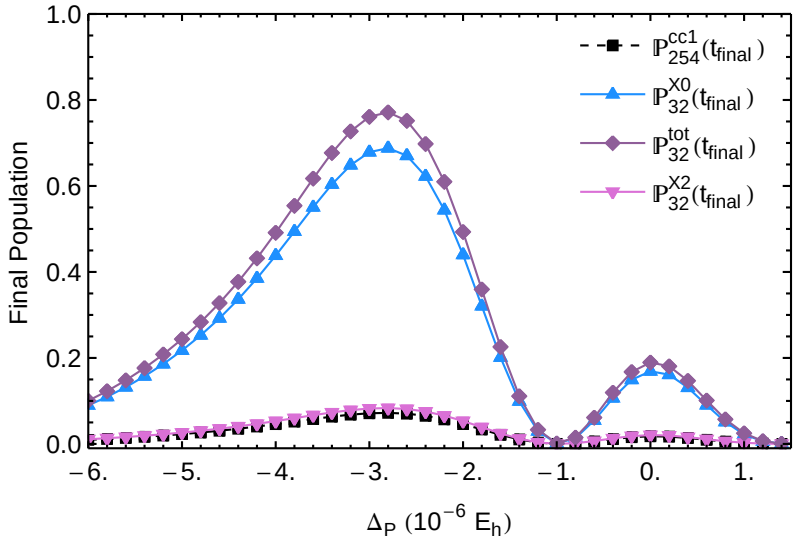

Figure 6.39: (Color online) Dependence of the final population on the detuning of the pump pulse for case 13—BSIu. The final population in the final state is greatly enhanced for a detuning of $\Delta_P = -2.8 \times 10^{-6}\, E_h$.

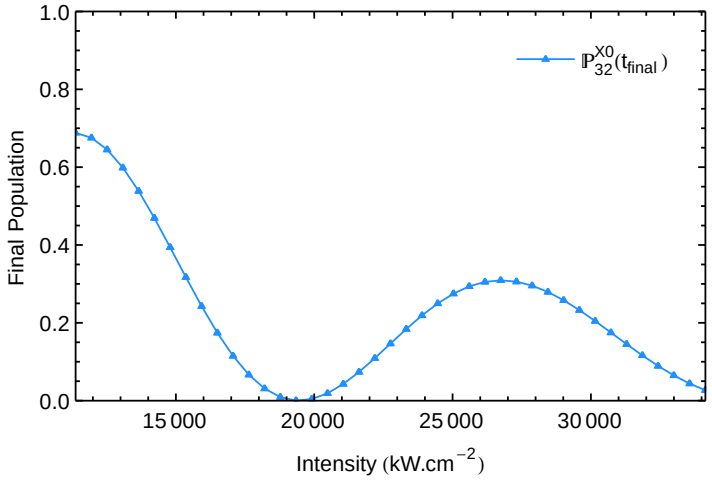

Figure 6.40: (Color online) Dependence of final population on the intensity of the pump pulse for case 13—BSIu. The final population in the final state is maximal for the minimal π-pulse intensity.

of the population is trapped in the intermediate state $|\Phi^{cc}_{\nu_{cc}=254}\rangle$, and 14.9% remains in the continuum state. The neighbors of $|\Phi^{cc}_{\nu_{cc}=254}\rangle$ in energy share the remaining 0.8% of population.

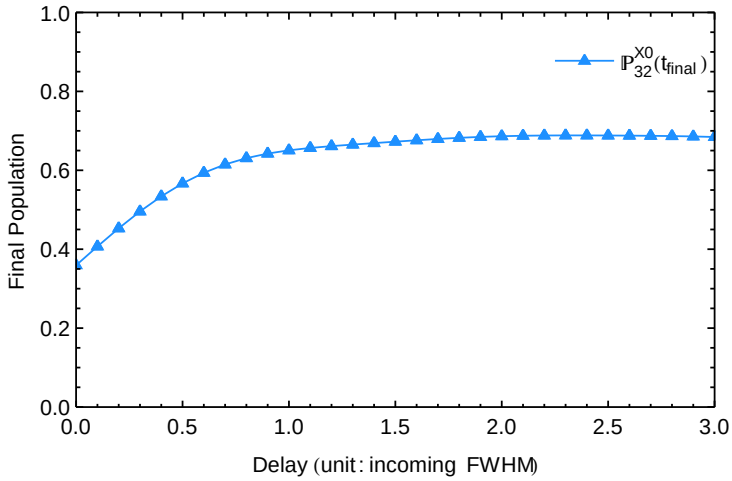

Figure 6.41: (Color online) Dependence of final population on the pulse delay for case 13—BSIu. The final population is comparatively high when the pulse delay is at least 1.5 FWHM of the laser.

6.4.15 Case 14—BSIc: intuitive sequence of chirped lasers with broad spectral bandwidth, inclusive of SO coupling

I show the details of the numerical search for the optimal parameters for this case in Appendix G. Figure 6.43 shows the population transfer with parameters that maximize the final population in $|X, v_X = 32, J = 0\rangle$. All the states that take a significant part in the transfer are also labeled. Chirping the laser distributes the total population over many more intermediate states than in the unchirped case. At the end of the process, there is only a 0.4% probability that the scattering atoms did not form a molecule. The wave function of the system consists of 2 distinct wave packets: one in the $X^1\Sigma^+$ state, and the other in the spin-orbit coupled-channel excited state. The final probability to find the system in the wave packet belonging to the coupled-channel excited state is 59.3%, while the total probability to find the system in the $X^1\Sigma^+$ state is 40.2%. The 0.1% remainder of the population is shared between the unlabeled states that belong to the spin-orbit coupled-channel excited state.

The process takes 200 ps more than the unchirped case 13—BSIu for pop-

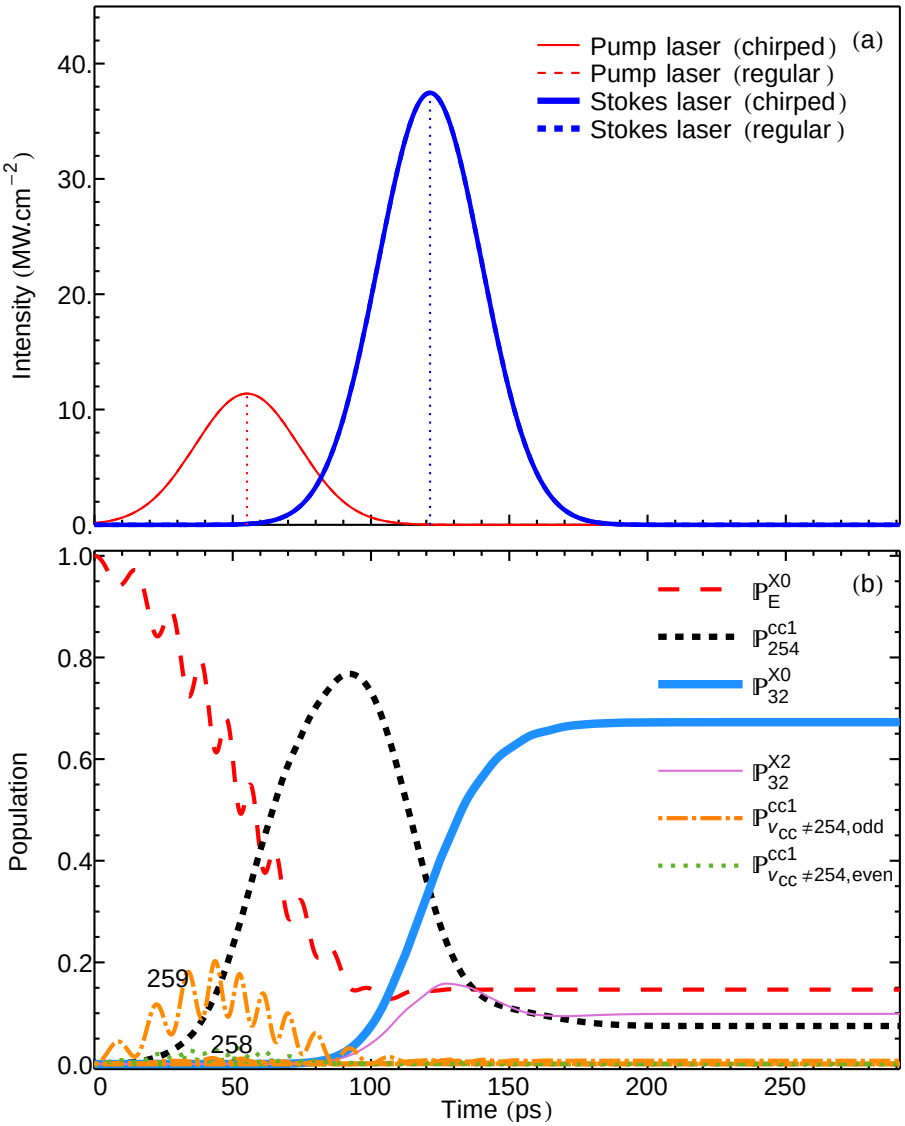

Figure 6.42: (Color online) Population transfer for intuitive sequence of unchirped lasers with broad spectral bandwidth (10GHz), inclusive of spin-orbit coupling, case 13—BSIu with optimized parameters.

ulation to accumulate in $|X, v_X = 32, J = 0\rangle$. The total final population in the $X^1\Sigma^+$ state is 40.2%, while it is 77.5% in case 13—BSIu. Moreover, in the present case, the necessary laser intensities are much higher than in case 13. Therefore, if the goal is the transfer of population into $|X, v_X = 32, J = 0\rangle$ the parameters in case 13 are more favorable; if the goal is the spectroscopy of the high-lying coupled-channel vibrational states, experimentalists should favor the procedure of case 14. Table 6.4 gives the probabilities at the end of the process for this case.

State	$\mathbb{P}_{\text{final}}(\%)$
$\|\chi_E^{X0}\rangle$	0.4
$\|X, v_X = 32, J = 0\rangle$	36.3
$\|X, 32, 2\rangle$	3.9
$\|\Phi^{cc}_{v_{cc}=259}\rangle$	13.7
$\|\Phi^{cc}_{258}\rangle$	5.2
$\|\Phi^{cc}_{257}\rangle$	9.2
$\|\Phi^{cc}_{256}\rangle$	3.1
$\|\Phi^{cc}_{255}\rangle$	12.6
$\|\Phi^{cc}_{254}\rangle$	14.1
$\|\Phi^{cc}_{253}\rangle$	1.4

Table 6.4: Population in the various states involved in case 14—BSIc at the end of the process. The lasers being first resonant with $|\Phi^{cc}_{254}\rangle$ and then with $|\Phi^{cc}_{255}\rangle$, these states are the most populatedat the end of the process. A significant amount of population accumulates in $|\Phi^{cc}_{259}\rangle$ because it has the largest fbTDMME.

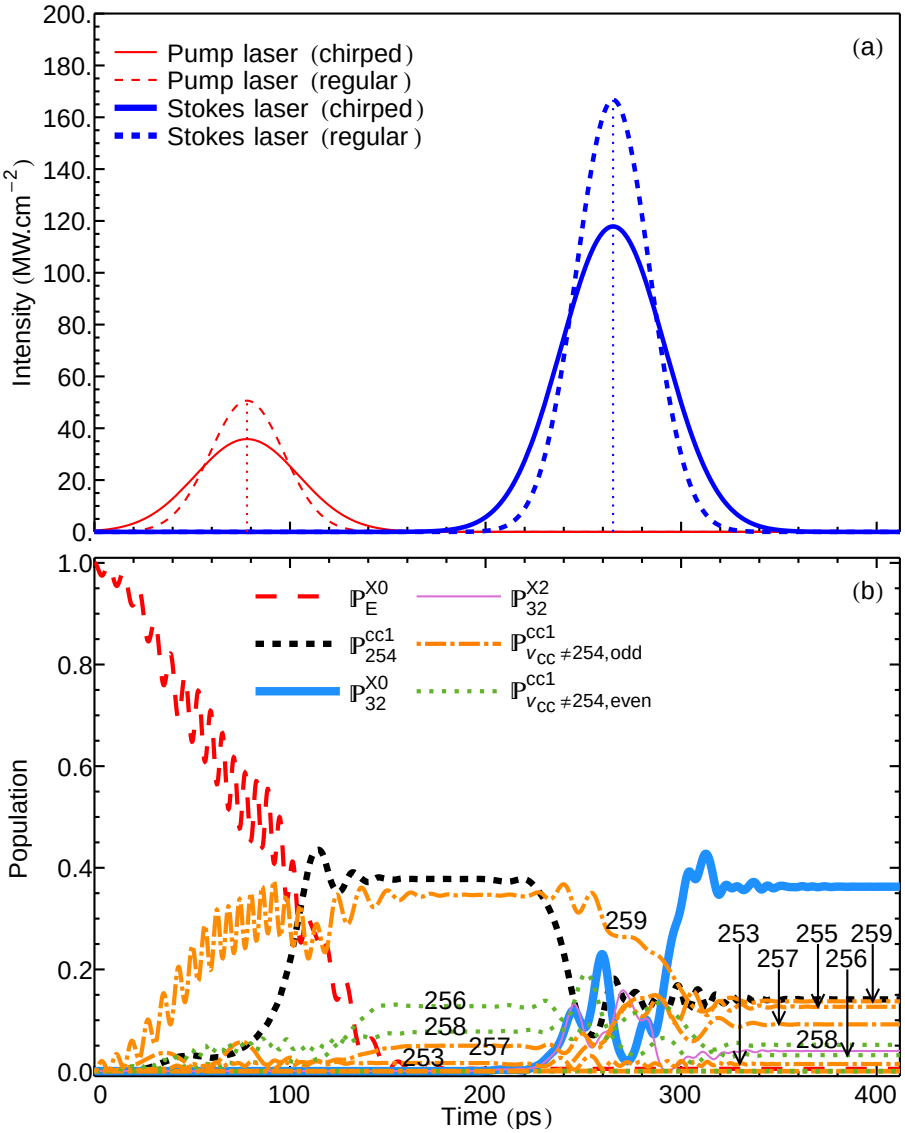

Figure 6.43: (Color online) Populations with optimized parameters for case 14—BSIc.

6.4.16 Case 15—BSCu: counter-intuitive sequence of unchirped lasers with broad spectral bandwidth, inclusive of SO coupling

As for the previous section, the details for the numerical search of the parameters that maximize the final population in $|X, v_X = 32, J = 0\rangle$ appear in Appendix G. Figure 6.45 shows the resulting population for the present case. Ba-

sically one switches to the counter-intuitive laser sequence in hope of creating and following an adiabatic state that carries all population from the initial state to the chosen final state., without populating significantly the intermediate state. The present scheme does not achieve this goal. Similarly to case 11—BNCu, broadening the spectral width of the laser increases the effect of the intermediate bound state with the largest fbTDMME, $|\Phi^{cc}_{v_{cc}=259}\rangle$. In particular, the influence of $|\Phi^{cc}_{v_{cc}=259}\rangle$ prevents the occurence of an adiabatic state suitable for STIRAP. The conditions of case 15—BSCu yield less population in $|X, v_X = 32, J = 0\rangle$ than the conditions of either case 13—BSIu or case 14—BSIc. Let's examine what happens when we chirp the lasers with a counter intuitive sequence.

6.4.17 Case 16—BSCc: counter-intuitive sequence of chirped lasers with broad spectral bandwidth, inclusive of SO coupling

Figure 6.45 shows the populations as a function of time. The numerical search for optimal parameters appears in Appendix G, as for the other cases. Compared to the previous 3 situations, case 16—BSCc yields the *smallest* final population in $|X, v_X = 32, J = 0\rangle$. However, the continuum is completely depleted: all of the scattering atoms are photoassociated. The final populations in the intermediate states are higher in the present case than for the intuitive sequence with chirped pulses (case 14—BSIc). A very clear distribution of the population among the intermediate state, much clearer than in case 14—BSIc, makes the process more suitable to populate the high lying coupled-channel vibrational states. Also the necessary laser intensities are much lower than in case 14. Thus, the set up of case 16 appears well adapted to the spectroscopic

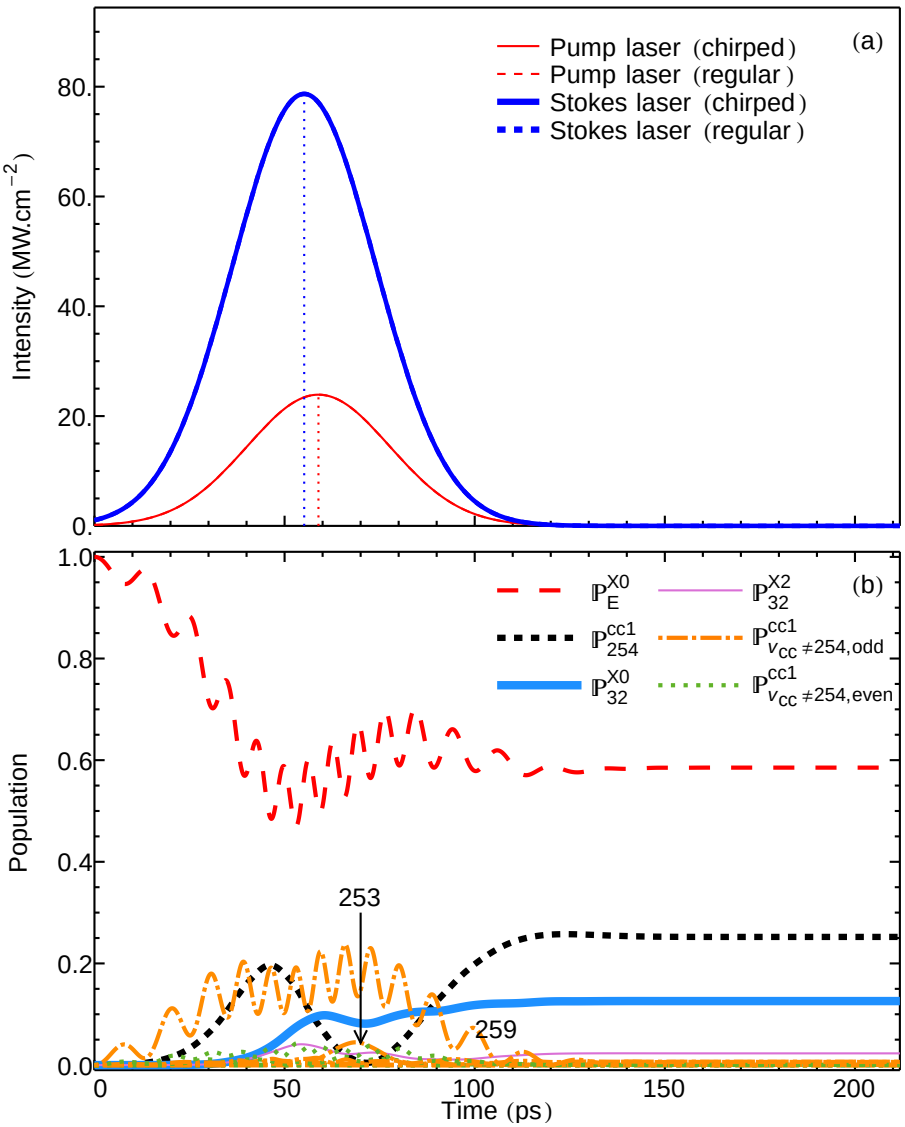

Figure 6.44: (Color online) Populations with optimized parameters for case 15—BSCu.

study of the states $|\Phi_{v_{cc}}^{cc}\rangle, v_{cc} = 253, ..., 259$.

Table 6.5 compares the final populations between the present case and case case 14—BSIc, where the lasers were in the intuitive sequence. notice that

State	$\mathbb{P}_{\text{final}}^{\text{counter}}(\%)$	$\mathbb{P}_{\text{final}}^{\text{intuitive}}(\%)$
$\lvert\chi_E^{X0}\rangle$	0	0.4
$\lvert X, v_X = 32, J = 0\rangle$	6.6	36.3
$\lvert X, 32, 2\rangle$	4.1	3.9
$\lvert\Phi_{v_{cc}=259}^{cc}\rangle$	37.7	13.7
$\lvert\Phi_{258}^{cc}\rangle$	10.1	5.2
$\lvert\Phi_{257}^{cc}\rangle$	7.6	9.2
$\lvert\Phi_{256}^{cc}\rangle$	21.7	3.1
$\lvert\Phi_{255}^{cc}\rangle$	1.3	12.6
$\lvert\Phi_{254}^{cc}\rangle$	10.8	14.1
$\lvert\Phi_{253}^{cc}\rangle$	0.1	1.4

Table 6.5: Population in the various states involved in case 16—BSCc at the end of the process, and comparison with case 14—BSIc where the lasers are in the intuitive sequence. Notice how the population in $\lvert X, v_X = 32, J = 0\rangle$ is much smaller for lasers in the counter-intuitive sequence.

6.4.18 Consequences of broader spectral bandwidths

From Sec. 6.4.10 to Sec. 6.4.17, I examined the effect on the overall process of using shorter laser pulses in the time domain, *i.e.* pulses with a broader spectral bandwidth than the cases studied in Sec. 6.4.1 to Sec. 6.4.8. What's the takeaway? First with broader spectral bandwidth, the states close in energy to the ones chosen influence the process more. In particular, the on-resonance requirement valid for continuous wave lasers or laser pulses with very narrow spectral bandwidth no longer optimizes the population transfer. For unchirped pulses, a numerical search near the resonance provides the value for optimal detunings. For chirped pulses, the GRHYP provides a pair of values for the pump and Stokes detuning that can serve as a starting point for the numerical

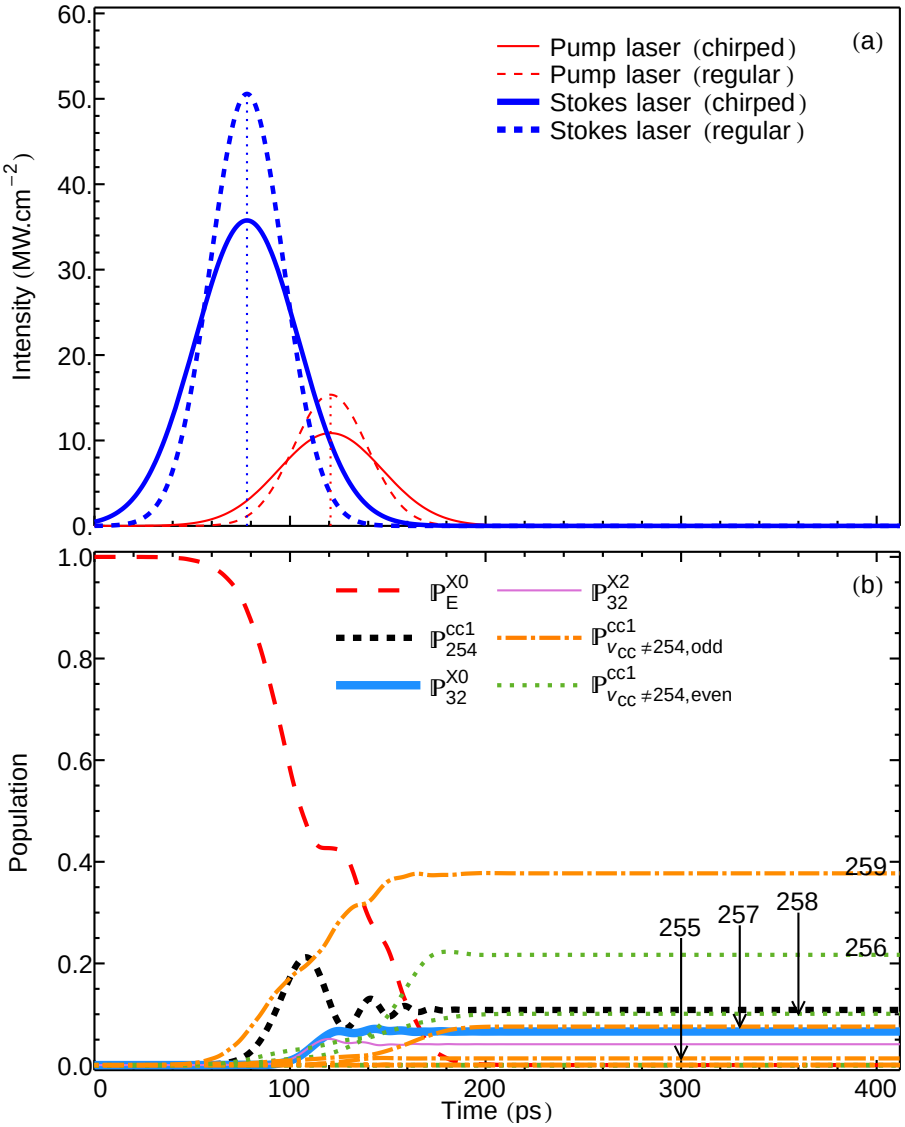

Figure 6.45: (Color online) Populations with optimized parameters for case 16—BSCc.

search of ideal detunings.

Next, a broader spectral bandwidth makes the overall process much more sensitive to changes in the laser intensities. The laser intensities act as an undiscriminating magnifying lens on the whole system: when one increases the laser intensity in the hope of increasing the final population in the final state, instead the transient population in the states with the largest fbTDMME increases, effectively acting as a leak on the total wave function of the system

and preventing an actual increase of the final population in the final state.

Last, no set up with broadband pulses provides an adiabatic state suitable for population transfer as we found in the case of narrow spectral bandwidth pulses.

To close this section, using laser pulses with smaller temporal bandwidth appears as a good way to populate very high lying vibrational states of the spin-orbit coupled-channel excited electronic state. The π-pulse sequence of case 13—BSIu was the setup that transferred most of the population to the $X^1\Sigma^+$ ground electronic state—67.5% in $|X, v_X = 32, 0\rangle$—and that process was over in 200 ps.

This chapter has reached its final point. It is now time to draw the overall conclusions of this work.

Chapter 7

Conclusion

"Would you tell me, please, which way I ought to go from here ?"
"That depends a good deal on where you want to get to," said the Cat.

—Lewis Carroll, *Alice in Wonderland*

7.1 Summary

The purpose of this work was to find a procedure that yields heteronuclear, polar, diatomic molecules in a low-lying vibrational state of the $X^1\Sigma^+$ ground electronic state, from a pair of scattering atoms at ultracold temperature, using two laser pulses. In Section 6.4, I showed that certain laser configurations yield indeed a final population in the state $|X^1\Sigma^+, v_X = 32, J = 0\rangle$ greater than 95%. A π-pulse sequence always works, and chirping the lasers increases the robustness of such sequence when the laser intensity changes.

To obtain the results of chapters 5 & 6, I constructed highly accurate potential energy curves, valid at all internuclear separation and based on published experimental data (see Sec. 2.5.1).

Using a basis expansion technique, I obtained spin-orbit coupled-channel wave function of the $A^1\Sigma^+ - -b^3\Pi_0$ manifold (Sec. 4.4). I validated this method by comparing the coupled-channel energy levels I calculated with experimental results (see Fig. **F.19** p. 258).

We validated the calculation of the transition dipole moment matrix elements necessary to this work by comparing the corresponding photoassociation rates for NaCs to those obtained experimentally for similar molecules and

reported in the literature (see Sec. 6.2, p. 146).

After careful examination of the results in Sec. 6.4, I concluded that the overall speed of the transfer is limited: when the temporal bandwidth of the laser is decreased, the spectral bandwidth increases bringing more intermediate states in the process, in turn lowering its efficiency. Nevertheless, faster lasers populate a small selection of the very high-lying states of the excited coupled-channel manifold: such procedure appears well suited for the photoassociation spectroscopy of these high-lying states.

Let's see what avenues may be explored now.

7.2 Outlook

Like any research project, several new directions of research are now open. For example, one could include the effect of spontaneous emission in the model, and assess the consequences on the population transfer and in particular the population of the final state.

Another possible line of research lies in the treatment of the initial state. I used a single-channel formalism with only one scattering wave function. Should a $X^1\Sigma^+ - -a^3\Sigma^+$ coupled-channel formalism be used to treat the continuum, the derivation would start essentially at Eq. (4.17).

Although I included the dominant spin-orbit effect in the problem, there are indirect spin-orbit coupling effects between the $A^1\Sigma^+$ state and the $\Omega = 1, 2$ components of the $b^3\Pi$. Furthermore, if one uses a coupled-channel formalism for the continuum, then the $B^1\Pi$ and $c^3\Sigma^+$ electronic states must be involved in the calculation, along with the relevant spin-orbit coupling function, which to my knowledge is unknown at the time of this writing.

As I limited my work to two chirped laser pulses of identical Full Width at

Half Maximum and identical chirp rates, one may envision the study of procedures that use lasers with *different* FWHM and/or *different* chirp rates.

The Generalized Resonance Hypothesis (GRHYP, Sec. 6.4.2.1, p. 159) worked rather well to predict adapted detunings for the cases involving chirped lasers with narrow spectral bandwidth. How can the GRHYP be improved to work with broader lasers?

The last outstanding question is how to get from the $|X^1\Sigma^+, v_X = 32, J = 0\rangle$ state to the lowest state of all, $|X^1\Sigma^+, v_X = 0, J = 0\rangle$?

Thank you, dear reader, for bearing with me until this very last sentence.

Bibliography

[1] M. H. Anderson, J. R. Ensher, M. R. Matthews, C. E. Wieman, and E. A. Cornell, *Observation of Bose-Einstein condensation in a dilute atomic vapor*, Science, **269**(5221), 198 (1995).

[2] J. Doyle, B. Friedrich, R. Krems, and F. Masnou-Seeuws, *Editorial: Quo vadis, cold molecules?*, The European Physical Journal D - Atomic, Molecular, Optical and Plasma Physics, **31**(2), 149 (2004).

[3] L. D. Carr, D. DeMille, R. V. Krems, and J. Ye, *Cold and ultracold molecules: science, technology and applications*, New Journal of Physics, **11**(5), 055049 (2009).

[4] R. V. Krems, *Cold controlled chemistry*, Physical Chemistry Chemical Physics, **10**, 4079 (2008).

[5] J. J. Hudson, B. E. Sauer, M. R. Tarbutt, and E. A. Hinds, *Measurement of the Electron Electric Dipole Moment Using YbF Molecules*, Physical Review Letters, **89**, 023003 (2002).

[6] D. DeMille, *Quantum Computation with Trapped Polar Molecules*, Physical Review Letters, **88**(6), 067901 (2002).

[7] P. Rabl, D. DeMille, J. M. Doyle, M. D. Lukin, R. J. Schoelkopf, and P. Zoller, *Hybrid Quantum Processors: Molecular Ensembles as Quantum Memory for Solid State Circuits*, Physical Review Letters, **97**, 033003 (2006).

[8] L. Bomble, P. Pellegrini, P. Ghesquière, and M. Desouter-Lecomte, *Toward scalable information processing with ultracold polar molecules in an electric field: A numerical investigation*, Physical Review A, **82**, 062323 (2010).

[9] G. Pupillo, A. Griessner, A. Micheli, M. Ortner, D.-W. Wang, and P. Zoller, *Cold Atoms and Molecules in Self-Assembled Dipolar Lattices*, Physical Review Letters, **100**, 050402 (2008).

[10] J. Zaharova, M. Tamanis, R. Ferber, A. N. Drozdova, E. A. Pazyuk, and A. V. Stolyarov, *Solution of the fully-mixed-state problem: Direct deperturbation analysis of the $A^1\Sigma^+$–$b^3\Pi$ complex in a NaCs dimer*, Physical Review A, **79**(1), 012508 (2009).

[11] E. Luc-Koenig and F. Masnou-Seeuws, *Cold Molecules: Theory, Experiment, Applications*, chapter 7: Prospects for Control of Ultracold Molecule Formation via Photassociation with Chirped Laser Pulses, 245–290, CRC Press (2009).

[12] E. Luc-Koenig, M. Vatasescu, R. Kosloff, and F. Masnou-Seeuws, *Making Ultracold Molecules with Chirped Laser Pulses*, in E. Dalimier, editor, *Spectral Line Shapes 2004*, volume 1 of *Proceedings of the 17$^{\text{th}}$ International Conference on Spectral Line Shapes*, 329–336, Frontier Group (2004).

[13] C. P. Koch, E. Luc-Koenig, and F. Masnou-Seeuws, *Making ultracold molecules in a two-color pump-dump photoassociation scheme using chirped pulses*, Physical Review A, **73**(3), 033408 (2006).

[14] K. Winkler, F. Lang, G. Thalhammer, P. v. d. Straten, R. Grimm, and J. H. Denschlag, *Coherent Optical Transfer of Feshbach Molecules to a Lower Vibrational State*, Physical Review Letters, **98**(4), 043201 (2007).

[15] S. Ospelkaus, A. Pe'er, K.-K. Ni, J. J. Zirbel, B. Neyenhuis, S. Kotochigova, P. S. Julienne, J. Ye, and D. S. Jin, *Efficient state transfer in an ultracold dense gas of heteronuclear molecules*, Nature Physics, **4**(8), 622 (2008).

[16] K. Bergmann, H. Theuer, and B. W. Shore, *Coherent population transfer among quantum states of atoms and molecules*, Reviews of Modern Physics, **70**(3), 1003 (1998).

[17] K. Bergmann and B. W. Shore, *Molecular Dynamics and Spectroscopy by Stimulated Emission Pumping*, volume 4 of *Advanced Series in Physical Chemistry*, chapter 9: Coherent Population Transfer, 315–373, World Scientific (1995).

[18] A. J. Kerman, J. M. Sage, S. Sainis, T. Bergeman, and D. DeMille, *Production of Ultracold, Polar RbCs* Molecules via Photoassociation*, Physical Review Letters, **92**(3), 033004 (2004).

[19] M. Aymar and O. Dulieu, *Calculation of accurate permanent dipole moments of the lowest $^{1,3}\Sigma^+$ states of heteronuclear alkali dimers using extended basis sets*, The Journal of Chemical Physics, **122**(20), 204302 (2005).

[20] P. S. Żuchowski and J. M. Hutson, *Reactions of ultracold alkali-metal dimers*, Physical Review A, **81**(6), 060703 (2010).

[21] O. Docenko, M. Tamanis, J. Zaharova, R. Ferber, A. Pashov, H. Knöckel, and E. Tiemann, *The coupling of the $X^1\Sigma^+$ and $a^3\Sigma^+$ states of the atom pair Na+Cs and modelling cold collisions*, Journal of Physics B: Atomic, Molecular and Optical Physics, **39**(19), S929 (2006).

[22] C. Haimberger, J. Kleinert, O. Dulieu, and N. P. Bigelow, *Processes in the formation of ultracold NaCs*, Journal of Physics B: Atomic, Molecular and Optical Physics, **39**(19), S957 (2006).

[23] B. E. A. Saleh and M. C. Teich, *Fundamentals of photonics*, Wiley-Interscience, Hoboken, N.J., 2nd. edition (2007).

[24] B. H. Bransden and C. J. Joachain, *Physics of atoms and molecules*, Prentice Hall, Harlow ; Munich [u.a.] (2010).

[25] M. H. Nayfeh and M. K. Brussel, *Electricity and Magnetism*, Wiley, New York (1985).

[26] D. A. Steck, *Cesium D Line Data* (2009). Version 2.1.2.

[27] J. R. R. Tolkien, *The Lord of The Rings*, Houghton Mifflin, Boston (1967).

[28] A. Messiah, *Quantum mechanics*, North-Holland Pub. Co. ; John Wiley, Amsterdam; New York (1966).

[29] C. Cohen-Tannoudji, B. Diu, and F. Laloë, *Quantum mechanics*, Wiley, New York (1977).

[30] B. W. Shore, *The theory of coherent atomic excitation*, John Wiley and Sons, Inc., New York (1990).

[31] U. Gaubatz, P. Rudecki, S. Schiemann, and K. Bergmann, *Population transfer between molecular vibrational levels by stimulated Raman scattering with partially overlapping laser fields. A new concept and experimental results*, The Journal of Chemical Physics, **92**(9), 5363 (1990).

[32] M. P. Fewell, B. W. Shore, and K. Bergmann, *Coherent Population Transfer among Three States: Full Algebraic Solutions and the Relevance of Non Adiabatic Processes to Transfer by Delayed Pulses*, Australian Journal of Physics, **50**(2), 281 (1997).

[33] J. H. Van Vleck, *The Coupling of Angular Momentum Vectors in Molecules*, Reviews of Modern Physics, **23**, 213 (1951).

[34] H. Lefebvre-Brion and R. W. Field, *The spectra and dynamics of diatomic molecules*, Elsevier Academic Press, Amsterdam; Boston (2004).

[35] H. Katô, *Energy Levels and Line Intensities of Diatomic Molecules. Application to Alkali Metal Molecules*, Bulletin of the Chemical Society of Japan, **66**(11), 3203 (1993).

[36] J. F. Ogilvie, *The vibrational and rotational spectrometry of diatomic molecules*, Academic Press (1998).

[37] R. J. LeRoy, *Molecular Spectroscopy, Specialist periodical reports*, volume 1, chapter 3 : Energy Levels of a diatomic near dissociation, 113–176 (1973).

[38] S. J. Umanski and A. I. Voronin, *Asymptotic Calculation of Some Exchange Integrals*, Theoretica Chimica Acta, **12**(2), 166 (1968).

[39] H. Margenau, *Van der waals forces*, Reviews of Modern Physics, **11**(1), 1 (1939).

[40] K. M. Jones, E. Tiesinga, P. D. Lett, and P. S. Julienne, *Ultracold photoassociation spectroscopy: long-range molecules and atomic scattering*, Reviews of Modern Physics, **78**, 483 (2006).

[41] B. Bussery, Y. Achkar, and M. Aubert-Fécon, *Long-Range Molecular States Dissociating To The Three or Four Lowest Asymptotes for the Ten Heteronuclear Diatomic Alkali Molecules*, Chemical Physics, **116**, 319 (1987).

[42] M. Marinescu and H. R. Sadeghpour, *Long range potentials for two-species alkali-metal atoms*, Physical Review A, **59**(1), 390 (1999).

[43] I. G. Kaplan, *Intermolecular interactions : physical picture, computational methods, model potentials*, Wiley, Hoboken, NJ (2006).

[44] M. Aymar and O. Dulieu, *Calculations of transition and permanent dipole moments of heteronuclear alkali dimers NaK, NaRb and NaCs*, Molecular Physics, **105**(11-12), 1733 (2007).

[45] R. J. LeRoy, *LEVEL 8.0: A Computer Program for Solving the Radial Schrödinger Equation for Bound and Quasibound Levels*, Research Report CP-661, University of Waterloo Chemical Physics (2007).

[46] J. Kim, Y. Lee, and A. Stolyarov, *Quasi-relativistic treatment of the low-lying {KCs} states*, Journal of Molecular Spectroscopy, **256**(1), 57 (2009). PRAHA2008, The 20th International Conference on High Resolution Molecular Spectroscopy.

[47] C. Haimberger, J. Kleinert, P. Zabawa, A. Wakim, and N. P. Bigelow, *Formation of ultracold, highly polar $X^1\Sigma^+$ NaCs molecules*, New Journal of Physics, **11**(5), 055042 (2009).

[48] J. Kleinert, C. Haimberger, P. J. Zabawa, and N. P. Bigelow, *Trapping of Ultracold Polar Molecules with a Thin-Wire Electrostatic Trap*, Physical Review Letters, **99**, 143002 (2007).

[49] P. Zabawa, A. Wakim, A. Neukirch, C. Haimberger, N. P. Bigelow, A. V. Stolyarov, E. A. Pazyuk, M. Tamanis, and R. Ferber, *Near-dissociation photoassociative production of deeply bound NaCs molecules*, Physical Review A, **82**, 040501 (2010).

[50] P. F. Bernath, *Spectra of atoms and molecules*, Oxford University Press, New York, 2nd edition (2005).

[51] J. M. Brown and A. Carrington, *Rotational spectroscopy of diatomic molecules*, Cambridge University Press, Cambridge; New York (2003).

[52] M. E. Rose, *Elementary theory of angular momentum*, Wiley, New York (1957).

[53] M. A. Morrison and G. A. Parker, *A Guide to Rotations in Quantum Mechanics*, Australian Journal of Physics, **40**(4), 465 (1987).

[54] M. D. Sturge, *Statistical and thermal physics : fundamentals and applications*, A.K. Peters, Natick, Mass. (2003).

[55] G. Herzberg, *Molecular Spectra and Molecular Structure I*, volume I. Spectra of Diatomic Molecules, Van Nostrand Reinhold Company, 2nd edition (1950).

[56] A. R. Edmonds, *Angular momentum in quantum mechanics.*, Princeton University Press, Princeton, N.J. (1957).

[57] J. H. Van Vleck, *On σ-Type Doubling and Electron Spin in the Spectra of Diatomic Molecules*, Physical Review, **33**, 467 (1929).

[58] D. Bohm, *Quantum Theory*, Prentice-Hall, Inc., 1 edition (1951).

[59] M. Born and R. Oppenheimer, *Zur Quantentheorie der Molekeln*, Annalen der Physik, **389**, 457 (1927).

[60] J. O. Hornkohl and C. Parigger, *Angular momentum states of the diatomic molecule*, American Journal of Physics, **64**(5), 623 (1996).

[61] R. T. Pack and J. O. Hirschfelder, *Energy Corrections to the Born–Oppenheimer Approximation. The Best Adiabatic Approximation*, The Journal of Chemical Physics, **52**(2), 521 (1970).

[62] C. Eckart, *The Kinetic Energy of Polyatomic Molecules*, Physical Review, **46**, 383 (1934).

[63] U. Fano, *Description of States in Quantum Mechanics by Density Matrix and Operator Techniques*, Reviews of Modern Physics, **29**, 74 (1957).

[64] K. Blum, *Density matrix theory and applications*, Plenum Press, New York (1981).

[65] S. Stenholm, *Foundations of laser spectroscopy*, Wiley, New York (1984).

[66] J. Vala, O. Dulieu, F. Masnou-Seeuws, P. Pillet, and R. Kosloff, *Coherent control of cold-molecule formation through photoassociation using a chirped-pulsed-laser field*, Physical Review A, **63**, 013412 (2000).

[67] D. J. Heinzen, *Ultracold Atomic Interactions*, in M. Inguscio, S. Stringari, and C. E. Wieman, editors, *Bose-Einstein condensation in atomic gases*, 351–390, International School of Physics "Enrico Fermi" and Societ italiana di fisica., IOS Press, Amsterdam; Washington, DC (1998).

[68] W. C. Stwalley and H. Wang, *Photoassociation of Ultracold Atoms: A New Spectroscopic Technique*, Journal of Molecular Spectroscopy, **195**(2), 194 (1999).

[69] C. Drag, *Photoassociation d'atomes de cesium froids. Formation et caractérisation d'un nuage froid de molécules diatomiques de cesium.*, Ph.D. thesis, [S.l.] (2000).

[70] P. S. Julienne, *Cold molecules : theory, experiment, applications*, chapter 6: Molecular States Near a Collision Threshold, 221–243, CRC Press, Boca Raton (2009).

[71] C. P. Koch, R. Kosloff, E. Luc-Koenig, F. Masnou-Seeuws, and A. Crubellier, *Photoassociation with chirped laser pulses: calculation of the absolute number of molecules per pulse*, Journal of Physics B: Atomic, Molecular and Optical Physics, **39**(19), S1017 (2006).

[72] H. Friedrich, *Theoretical atomic physics*, Springer-Verlag, Berlin; New York, 3rd edition (2005).

[73] B. E. Londoño, J. E. Mahecha, E. Luc-Koenig, and A. Crubellier, *Resonant coupling effects on the photoassociation of ultracold Rb and Cs atoms*, Physical Review A, **80**, 032511 (2009).

[74] R. Stoer, Josef; Bulirsch, *Introduction to numerical analysis*, Springer-Verlag, New York (1992).

[75] C. Haimberger, J. Kleinert, M. Bhattacharya, and N. P. Bigelow, *Formation and detection of ultracold ground-state polar molecules*, Physical Review A, **70**, 021402 (2004).

[76] S. Azizi, M. Aymar, and O. Dulieu, *Prospects for the formation of ultracold ground state polar molecules from mixed alkali atom pairs*, The European Physical Journal D: Atomic, Molecular, Optical and Plasma Physics, **31**(2), 195 (2004).

[77] J. L. Bohn and P. S. Julienne, *Semianalytic theory of laser-assisted resonant cold collisions*, Physical Review A, **60**, 414 (1999).

[78] P. Pillet, A. Crubellier, A. Bleton, O. Dulieu, P. Nosbaum, I. Mourachko, and F. Masnou-Seeuws, *Photoassociation in a gas of cold alkali atoms: I. Perturbative quantum approach*, Journal of Physics B: Atomic, Molecular and Optical Physics, **30**(12), 2801 (1997).

[79] S. Dutta, J. Lorenz, A. Altaf, D. S. Elliott, and Y. P. Chen, *Photoassociation of ultracold LiRb* molecules: Observation of high efficiency and unitarity-limited rate saturation*, Physical Review A, **89**, 020702 (2014).

[80] H. Wang and W. C. Stwalley, *Ultracold photoassociative spectroscopy of heteronuclear alkali-metal diatomic molecules*, The Journal of Chemical Physics, **108**(14), 5767 (1998).

[81] N. V. Vitanov, M. Fleischhauer, B. W. Shore, and K. Bergmann, *Coherent manipulation of atoms and molecules by sequential laser pulses*, volume 46 of *Advances In Atomic, Molecular, and Optical Physics*, 55 – 190, Academic Press (2001).

[82] E. Luc-Koenig, R. Kosloff, F. Masnou-Seeuws, and M. Vatasescu, *Photoassociation of cold atoms with chirped laser pulses: Time-dependent calculations and analysis of the adiabatic transfer within a two-state model*, Physical Review A, **70**, 033414 (2004).

[83] J. R. Taylor, *An introduction to error analysis : the study of uncertainties in physical measurements*, University Science Books, Sausalito, Calif. (1997).

Appendix A

More on chirped laser pulses

Introduction

This appendix is an extract of a term paper I wrote for Modern Optics class, and covers some theoretical points regarding chirped laser pulses.

I will first define mathematically what chirped pulse are, by comparing Transform Limited Gaussian pulses to Chirped Gaussian pulses. Then I examine how linear filters are used to chirp laser pulses.

Notation. In this appendix, I will refer to a time-dependent signal by a script capital, as $\mathcal{A}(t)$, and to the corresponding frequency-dependent Fourier transform by a regular *non*-script capital, as $A(\nu)$.

A.1 Definitions

A.1.1 What is a chirped pulse ?

An optical pulse centered at the frequency $\omega_0 = 2\pi\nu_0$, with complex envelope $\mathcal{A}(t)$, has the mathematical form

$$U(t) = \mathcal{A}(t)\exp(\mathbf{i}\,\omega_0 t). \qquad \textbf{(A.1)}$$

Such pulse can be rewritten in terms of the phase and modulus of the complex envelope as

$$U(t) = |\mathcal{A}(t)|\exp(\mathbf{i}\,\phi(t))\exp(\mathbf{i}\,\omega_0 t) = |\mathcal{A}(t)|\exp(\mathbf{i}\,(\phi(t)+\omega_0 t)). \qquad \textbf{(A.2)}$$

The instantaneous frequency ω_i of the pulse is the time derivative of the total phase of $U(t)$

$$\omega_i(t) = \omega_0 + \frac{d}{dt}\phi(t). \qquad \textbf{(A.3)}$$

By definition, a pulse is ***chirped*** when the instantaneous frequency ω_i depends on time, or equivalently when the phase of the complex envelope is not stationary. Therefore a chirped pulse has a time-varying instantaneous frequency. If the range of frequencies the pulse spans is in the visible range, the pulse changes color as time passes. An example of a chirped pulse is plotted in Fig. 2.3.

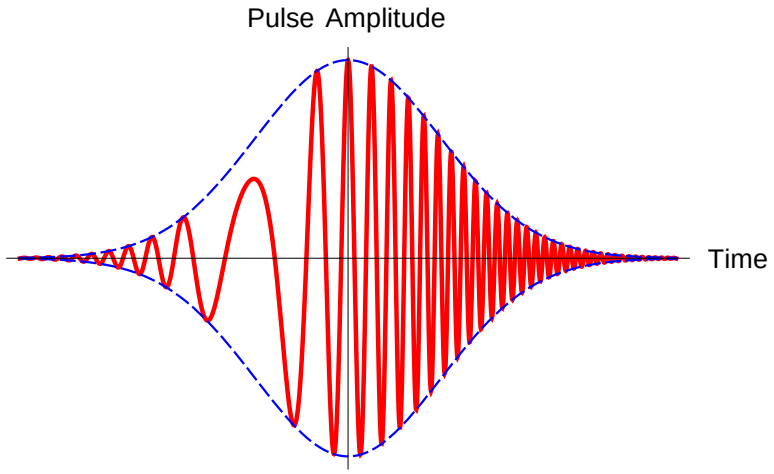

Figure A.1: Linearly up-chirped Gaussian pulse. The functional form used to draw this plot is $U(t) = \mathbf{e}^{-t^2}\cos(10\pi t + 21t^2)$.

A.1.2 Linear chirps

A pulse is *linearly chirped* when its instantaneous frequency ω_i depends linearly on time, i.e. when there exists a real constant α such that

$$\omega_i = \omega_0 + \alpha t. \tag{A.4}$$

For linear chirps, the phase of the pulse's complex envelope must depend quadratically on time

$$\phi(t) = \alpha \frac{t^2}{2}. \tag{A.5}$$

Linear chirped pulses are *up-chirped* for $\alpha > 0$ and *down-chirped* for $\alpha < 0$.

Two kinds of pulses are worth examining: the Transform limited Gaussian pulse and the Chirped Gaussian pulse.

A.1.3 Transform Limited Gaussian pulses

A temporal envelope $\mathcal{A}(t)$ with constant phase and Gaussian amplitude

$$\mathcal{A}(t) = A_0 \exp\left(-\frac{t^2}{\tau^2}\right), \qquad A_0 \in \mathbb{C} \tag{A.6}$$

defines a *Transform-Limited Gaussian* (TLG) pulse. The temporal intensity of a TLG pulse is itself Gaussian:

$$I(t) = |\mathcal{A}(t)|^2 = |A_0|^2 \exp\left(-2\frac{t^2}{\tau^2}\right). \tag{A.7}$$

The intensity defined by Eq. (A.7) has full width[a] at $1/e$ equal to $\tau\sqrt{2}$. The corresponding Full Width at Half Maximum[b,c] (FWHM) is $\Delta\tau = \tau\sqrt{2\ln 2}$.

The spectral intensity $S(\nu)$ is the square modulus of the Fourier transform of the pulse:

$$S(\nu) = |A(\nu)|^2 = A(\nu)A^*(\nu), \quad \text{with} \tag{A.8a}$$

$$A(\nu) = A_0\tau\sqrt{\pi}\exp\left(-\pi^2\tau^2(\nu-\nu_0)^2\right), \quad \text{[TLG pulse Fourier transform]} \tag{A.8b}$$

$$S(\nu) = |A_0|^2\tau^2\pi\exp\left(-2\pi^2\tau^2(\nu-\nu_0)^2\right) \tag{A.8c}$$

where ν_0 is the pulse's initial frequency. The spectral width, defined as the FWHM of the spectral intensity, is thus

$$\Delta\nu = \frac{\sqrt{2\ln 2}}{\pi}\frac{1}{\tau} = \frac{2\ln 2}{\pi}\frac{1}{\Delta\tau} \Leftrightarrow \Delta\omega = \frac{4\ln 2}{\Delta\tau} \tag{A.9}$$

A.1.4 Chirped Gaussian Pulse

Mathematically, multiplying a TLG pulse by a phase factor with a time dependent phase suffices to define a Chirped Gaussian (CG) pulse:

$$\mathcal{A}(t) = A_0\exp\left(-\frac{t^2}{\tau^2}\right)\exp(\mathbf{i}\,\phi(t)), \qquad A_0 \in \mathbb{C}. \tag{A.10}$$

The pulse is linearly chirped if the phase is quadratic in time $\phi(t) = at^2/2\tau^2, a \in \mathbb{R}$. If the *chirp parameter* a is zero, the CG pulse reduces to the TLG pulse. The general form of a linearly CG pulse is thus

$$\mathcal{A}(t) = A_0\exp\left(-(1-\mathbf{i}\,a)\frac{t^2}{\tau^2}\right) \qquad A_0 \in \mathbb{C}, \tag{A.11}$$

[a] The full width δ at $1/e$ of a Gaussian $f(t)$ centered at t_0 is such that $f(t_0 \pm \frac{\delta}{2}) = f(t_0)/e$.
[b] The FWHM of a Gaussian function $f(t)$ centered at t_0 is such that $f(t_0 \pm \frac{\Delta\tau}{2}) = f(t_0)/2$.
[c] The FWHM of the temporal envelope $\mathcal{A}(t)$ is $\Delta t = 2\tau\sqrt{\ln 2}$

from which we can calculate the Fourier transform

$$A(\nu) = A_0 \tau \sqrt{\frac{\pi}{1 - \mathbf{i}\, a}} \exp\left(-\frac{\pi^2 \tau^2 (\nu - \nu_0)^2}{1 - \mathbf{i}\, a} \right). \tag{A.12}$$

The spectral intensity of the linear CG pulse is thus

$$S(\nu) = |A_0|^2 \tau^2 \frac{\pi}{\sqrt{1 + a^2}} \exp\left(-2 \frac{\pi^2 \tau^2 (\nu - \nu_0)^2}{1 + a^2} \right), \tag{A.13}$$

and the spectral width is

$$\Delta\nu = \frac{\sqrt{2 \ln 2}}{\pi} \frac{\sqrt{1 + a^2}}{\tau} = \frac{2 \ln 2}{\pi} \frac{\sqrt{1 + a^2}}{\Delta\tau} \Leftrightarrow \Delta\omega = \frac{4 \ln 2}{\Delta\tau} \sqrt{1 + a^2}. \tag{A.14}$$

Note that the Parseval-Plancherel theorem remains satisfied: whether the chirped pulse is considered in the temporal or the spectral domain, the pulse carries the same total energy per unit area:

$$\begin{aligned} \int_{-\infty}^{+\infty} I(t)\, \mathrm{d}t = \int_{-\infty}^{+\infty} |\mathcal{A}(t)|^2\, \mathrm{d}t &= \int_{-\infty}^{+\infty} |A(\nu)|^2\, \mathrm{d}\nu \\ &= \int_{-\infty}^{+\infty} S(\nu)\, \mathrm{d}\nu \\ &= |A_0|^2 \tau \sqrt{\frac{\pi}{2}} \end{aligned}$$

A.1.5 Summary

Knowing the basics of chirped pulses, I now turn to *how* pulses are chirped. I will consider the use of filters to chirp optical pulses, and shall examine the effect of a chirping filter on the two pulses described in the preceding section.

A.2 How to chirp a pulse?

A.2.1 Filtering in Theory

Within the framework of the theory of linear systems, a linear filter amounts to its transfer function $\mathscr{H}(\nu)$. Multipying the transfer function by the Fourier transform $A_1(\nu)$ of the input signal yields the Fourier transform $A_2(\nu)$ of the ouput signal:

$$A_2(\nu) = \mathscr{H}(\nu) A_1(\nu). \tag{A.15}$$

A chirp filter has to impart a time-dependent phase to the signal, i.e. a frequency-dependent phase on the signal's Fourier transform. Therefore a chirp filter has the transfer function

$$\mathscr{H}(\nu - \nu_0) = \exp\left(-\mathbf{i}\, b\pi^2(\nu - \nu_0)^2\right). \tag{A.16}$$

A.2.2 Chirping a Transform-Limited Gaussian Pulse

Let's examine the effect of the chirp filter on a TLG pulse with temporal width τ_1 and amplitude A_{10}. Remembering the Fourier transform of the input pulse from Eq. (A.8b)

$$A_1(\nu) = A_{10}\tau_1\sqrt{\pi}\exp\left(-\pi^2\tau_1^2(\nu - \nu_0)^2\right), \tag{A.17}$$

the chirp filter defined in Eq. (A.16) multiplies $A_1(\nu)$ and yields

$$A_2(\nu) = A_{10}\tau_1\sqrt{\pi}\exp\left(-\pi^2\tau_1^2(\nu - \nu_0)^2\right)\exp\left(-\mathbf{i}\, b\pi^2(\nu - \nu_0)^2\right) \tag{A.18a}$$

$$= A_{10}\tau_1\sqrt{\pi}\exp\left(-\pi^2(\nu - \nu_0)^2(\tau_1^2 + \mathbf{i}\, b)\right). \tag{A.18b}$$

To extract the amplitude A_{20}, the temporal width τ_2, and the chirp parameter a_2 of the output signal $A_2(\nu)$, we need to recast $A_2(\nu)$ as the Fourier transform of a chirped pulse, given by Eq. (A.12)

$$A_2(\nu) = A_{20}\tau_2\sqrt{\frac{\pi}{1-\mathbf{i}\,a_2}}\exp\left(-\frac{\pi^2\tau_2^2(\nu-\nu_0)^2}{1-\mathbf{i}\,a_2}\right). \tag{A.19}$$

Equating the real and imaginary parts of Eqs. A.18b and A.19, and noticing that the equations must hold for all ν, yields τ_2, a_2, and A_{20}:

$$\boxed{\begin{aligned} a_2 &= \frac{b}{\tau_1^2}, && \text{(A.20a)}\\ \tau_2 &= \tau_1\sqrt{1+a_2^2}, && \text{(A.20b)}\\ A_{20} &= \frac{A_{10}}{\sqrt{1-\mathbf{i}\,a_2}}. && \text{(A.20c)} \end{aligned}}$$

The spectral width of the chirped pulse described by Eq. (A.19) is obtained from Eqs. A.14 and A.20b,

$$\Delta\nu_2 = \frac{\sqrt{2\ln 2}}{\pi}\frac{\sqrt{1+a_2^2}}{\tau_2} = \frac{\sqrt{2\ln 2}}{\pi\tau_1} = \Delta\nu_1. \tag{A.21}$$

Therefore the chirp filter has the following effects on the TLG pulse:

- the pulse acquires a chirp parameter $a_2 = b/\tau_1^2$,
- the temporal width of the pulse is increased by a factor $\sqrt{1+a_2^2} > 1$, i.e. the pulse is temporally stretched,
- the *spectral width* of the pulse *remains unchanged*,
- the peak *intensity* is divided by $\sqrt{1+a_2^2}$, i.e. chirping decreases the peak intensity of the pulse.

Although the peak intensity decreases, the total energy contained in the TLG pulse is conserved, since the pulse is also temporally stretched.

Appendix B

The many faces of adiabaticity in physics

The word "adiabatic" comes from the greek *a* ("not") + *dia* ("through") + *batos* ("passable"). Something adiabatic is therefore, etymologically, something that prevents another from passing through. An *excellent* illustration of an adiabatic entity is given in [27, Book 2, end of chap. V].

B.1 Thermodynamics and Statistical Mechanics

In thermodynamics, a process is called adiabatic if it does not let any heat pass into or out of the system. If the process is *reversible*, the change in heat dQ is directly related to the change in entropy dS by $dS = dQ/T$. Thus if this reversible process is adiabatic, no heat is exchanged, and the entropy stays constant.

From a statistical mechanics point of view, since the entropy of the system stays constant during this reversible adiabatic process, the multiplicity of the macrostate of the system stays the same. Thus although the microstate of the system may change throughout the process, the macrostate is unaffected by the reversible adiabatic process, keeping the entropy of the system constant.

B.2 Quantum Mechanics

Messiah [28, chap. xvii, vol. II] discusses extensively the adiabatic theorem in Quantum Mechanics. Messiah proves the adiabatic theorem by considering that the Hamiltonian of the system is *explicitly time dependent*, *and changes*

slowly with time. The essential result of the adiabatic theorem is that ***if the system starts in an eigenstate*** $|\psi(t_0)\rangle$ ***of the Hamiltonian*** $\widehat{\mathscr{H}}(t_0)$ ***at*** $t = t_0$***, and if*** $\widehat{\mathscr{H}}(t)$ ***changes slowly with time, then at*** $t = t_1 > t_0$***, the system will be in the eigenstate*** $|\psi(t_1)\rangle$ ***that derives from*** $|\psi(t_0)\rangle$ ***by continuity***. This statement is best illustrated in the context of STImulated Raman Adiabatic Passage (STIRAP), which I discuss in Sec. 2.3.

Although Messiah proves the adiabatic theorem when the total hamiltonian depends explicitly on time t and changes slowly with t, nothing in the theorem prevents its application to a hamiltonian that changes slowly when *any* one of its variable changes. Thus, I can consider the time independent Hamiltonian of a diatomic molecule, which does depend on the internuclear separation R, and consider that said hamiltonian varies slowly as R changes.

If $\widehat{\mathscr{H}}$ changes slowly from R_i to R_{i+1}, the state of the electrons at R_{i+1} derives from the state of the electrons at R_i by continuity. In this sense, Hund's cases states are *adiabatic*: they obey the adiabatic theorem where R, rather than time t, is the key variable.

Since Hund's cases always diagonalize $\widehat{\mathscr{H}_e}$, and all Hund's cases are adiabatic in the sense of the adiabatic theorem, by extension, models that describe molecular dynamics where $\widehat{\mathscr{H}_e}$ is diagonal are called adiabatic. On the contrary, when the model does not diagonalize $\widehat{\mathscr{H}_e}$, then the model is *non-adiabatic*. Non-adiabatic models (*i.e.* not diagonalizing $\widehat{\mathscr{H}_e}$) that diagonalize $\widehat{\mathscr{T}_n}(R)$ are sometimes called *diabatic* models [34].

Appendix C

Optimal Pulse Delay

In this appendix I translate mathematically the condition for optimal pulse delay expressed at the end of §V.B (p. 1011) in [16]:

> "For optimum delay, the mixing angle should reach an angle of $\pi/4$ when Ω_{eff} reaches its maximum value."

where $\Omega_{\text{eff}}(t) = \sqrt{\Omega_P^2(t) + \Omega_S^2(t)}$. The expressions for the Gaussian Rabi pulses are:

$$\Omega_P(t) = \Omega_P^0 \exp\left(-4\ln 2\left(\frac{t-t_P}{\Delta\tau_P}\right)^2\right) = \Omega_P^0 \exp\left(-\frac{(t-t_P)^2}{2\sigma_P^2}\right) \tag{C.1a}$$

$$\Omega_S(t) = \Omega_S^0 \exp\left(-4\ln 2\left(\frac{t-t_S}{\Delta\tau_S}\right)^2\right) = \Omega_S^0 \exp\left(-\frac{(t-t_S)^2}{2\sigma_S^2}\right) \tag{C.1b}$$

I restrict the derivation below to Rabi pulses of identical width and height [31]: $\sigma_P = \sigma_S = \sigma$, $\Omega_P^0 = \Omega_S^0 = \Omega$. First, let's find the extrema of

$$\Omega_{\text{eff}}(t) = \Omega_0\left(\exp\left(-\frac{(t-t_P)^2}{\sigma^2}\right) + \exp\left(-\frac{(t-t_S)^2}{\sigma^2}\right)\right)^{1/2} = \Omega_0\sqrt{u(t)}$$

The extrema of $\Omega_{\text{eff}}(t)$ are such that $\frac{\mathrm{d}u}{\mathrm{d}t} = 0$:

$$\frac{\mathrm{d}u}{\mathrm{d}t} = -\frac{2}{\sigma^2}\left((t-t_P)\exp\left(-\frac{(t-t_P)^2}{\sigma^2}\right) + (t-t_S)\exp\left(-\frac{(t-t_S)^2}{\sigma^2}\right)\right)$$

The roots $\frac{\mathrm{d}u}{\mathrm{d}t}$ are the solution of a transcendental equation. However, $t_{1/2} = \frac{t_S+t_P}{2}$ is an analytic root of $\mathrm{d}u/\mathrm{d}t$, since $t_{1/2} - t_P = \eta/2 = -(t_{1/2} - t_S)$. The nature of the extremum of Ω_{eff} at $t = t_{1/2}$ is given by the sign of $\left.\frac{\mathrm{d}\Omega_{\text{eff}}}{\mathrm{d}t}\right|_{t=t_{1/2}}$. Using the

shorthand $u(t)$ defined above,

$$\frac{\mathrm{d}^2}{\mathrm{d}t^2}\Omega_{\mathrm{eff}} = \frac{\Omega_0}{2}\left(\ddot{u}u - \frac{\dot{u}^2}{2}\right)u^{-3/2} \tag{C.2}$$

$$\left.\frac{\mathrm{d}^2\Omega_{\mathrm{eff}}}{\mathrm{d}t^2}\right|_{t=t_{1/2}} = \frac{\Omega_0}{2}\left(\left.\frac{\mathrm{d}^2u}{\mathrm{d}t^2}\right|_{t=t_{1/2}} u(t_{1/2}) - \frac{0^2}{2}\right)(u(t_{1/2}))^{-3/2} \tag{C.3}$$

$$= \frac{\Omega_0}{2}\left(\left.\frac{\mathrm{d}^2u}{\mathrm{d}t^2}\right|_{t=t_{1/2}} \times \frac{1}{\sqrt{u(t_{1/2})}}\right) \tag{C.4}$$

The above equation shows that $\left.\frac{\mathrm{d}^2u}{\mathrm{d}t^2}\right|_{t=t_{1/2}}$ determines the sign of $\left.\frac{\mathrm{d}\Omega_{\mathrm{eff}}}{\mathrm{d}t}\right|_{t=t_{1/2}}$. Let's calculate the second derivative of u with respect to time t:

$$\frac{\mathrm{d}^2u}{\mathrm{d}t^2} = -\frac{2}{\sigma^2}\left[\left(1 - 2\frac{(t-t_P)^2}{\sigma^2}\right)\exp\left(-\frac{(t-t_P)^2}{\sigma^2}\right) + \left(1 - 2\frac{(t-t_S)^2}{\sigma^2}\right)\exp\left(-\frac{(t-t_S)^2}{\sigma^2}\right)\right] \tag{C.5a}$$

$$\ddot{u}(t_{1/2}) = -\frac{2}{\sigma^2}\exp\left(-\frac{(t_P-t_S)^2}{4\sigma^2}\right)\left[\left(1 - 2\frac{(t_S-t_P)^2}{4\sigma^2}\right) + \left(1 - 2\frac{(t_P-t_S)^2}{4\sigma^2}\right)\right] \tag{C.5b}$$

$$\ddot{u}(t_{1/2}) = -\frac{4}{\sigma^2}\exp\left(-\frac{\eta^2}{4\sigma^2}\right)\left[\left(1 - \frac{\eta^2}{2\sigma^2}\right)\right] \tag{C.5c}$$

The effective Rabi frequency Ω_{eff} reaches a maximum at $t = t_{1/2}$ if and only if $\left.\frac{\mathrm{d}\Omega_{\mathrm{eff}}}{\mathrm{d}t}\right|_{t=t_{1/2}} \leq 0$, *i.e.*

$$\ddot{u}(t_{1/2}) \leq 0 \tag{C.6a}$$

$$\Leftrightarrow 0 \leq 1 - \frac{\eta^2}{2\sigma^2} \tag{C.6b}$$

$$\Leftrightarrow \eta^2 \leq 2\sigma^2 \tag{C.6c}$$

$$\Leftrightarrow |\eta| \leq \sigma\sqrt{2} \tag{C.6d}$$

Thus the optimal pulse delay is $|\eta| = \sigma\sqrt{2}$. Since $\frac{1}{2\sigma^2} = \frac{4\ln 2}{\Delta\tau^2}$, then in terms of the pulse FWHM $\Delta\tau$

$$\boxed{\eta = t_S - t_P = -\frac{\Delta\tau}{2\sqrt{\ln 2}} \approx -0.6\Delta\tau} \tag{C.7}$$

as reported in [31]. It is important to remember that $\Delta\tau$ is the FWHM of the Rabi pulse *amplitude*. The optimal pulse delay must be negative, since STIRAP can only occur in the counterintuitive sequence, when the Stokes pulse *precedes* the pump pulse.

Appendix D

Getting the derivative of the spin-orbit mixing angle from its tangent

It is easy to obtain the tangent of γ from Eq. (4.57):

$$\tan\gamma = \frac{\sin\gamma}{\cos\gamma} = \frac{V_A - V_{1/2}}{\sqrt{2}\xi}.$$

Defining $u(R) = \dfrac{V_A - V_{1/2}}{\sqrt{2}\xi}$, then $\gamma = \arctan u$. Remembering now that

$$\frac{\mathrm{d}}{\mathrm{d}R}\arctan u = \frac{u'}{1+u^2} \quad ,$$

one gets

$$\frac{\mathrm{d}\gamma}{\mathrm{d}R} = \frac{\mathrm{d}}{\mathrm{d}R}\arctan u = \frac{1}{1+\left(\frac{V_A - V_{1/2}}{\sqrt{2}\xi}\right)^2}\,\frac{\mathrm{d}}{\mathrm{d}R}\left(\frac{V_A - V_{1/2}}{\sqrt{2}\xi}\right),$$

which is an expression for $\mathrm{d}\gamma/\mathrm{d}R$ that does not require calculating γ explicitly. Substituting the definition for $V_{1/2}$ from Eq. (4.55) leads to

$$\frac{\mathrm{d}\gamma}{\mathrm{d}R} = \frac{1}{1+\left(\frac{V_A - V_{b0}}{2\sqrt{2}\xi} + \sqrt{\left(\frac{V_A - V_{b0}}{2\sqrt{2}\xi}\right)^2 + 1}\right)^2}\,\frac{\mathrm{d}}{\mathrm{d}R}\left(\frac{V_A - V_{b0}}{2\sqrt{2}\xi} + \sqrt{\left(\frac{V_A - V_{b0}}{2\sqrt{2}\xi}\right)^2 + 1}\right),$$

showing that the derivative of the mixing angle can be expressed solely in terms of the Hund's case (a) potentials and the relevant spin-orbit coupling terms. This latter expression was used to obtain the three graphs of Fig. 4.3.

Appendix E

Checking hermicity of the kinetic energy operator

All operators defined in Eqs. (4.54a) are hermitian. This property is obvious for all operators that do not involve a derivative with respect to R: $\mathbf{R}$, $\mathbf{D}$, and $\mathbf{H}^{\text{el}}$. A hermitian operator remains hermitian under a unitary transformation. Thus the change of basis defined by $\mathbf{U}$ conserves the hermicity of $\mathbf{R}$, $\mathbf{D}$, and $\mathbf{H}^{\text{el}}$ whether they are expressed in basis $\mathcal{A}$ or $\mathcal{H}$.

Although the hermicity of the kinetic energy operator $\widehat{\mathscr{T}}$ is trivial, the hermicity of the kinetic energy matrix $\mathbf{T}$ is not necessarily obvious after performing a unitary transformation, even though such transformation cannot affect hermicity. Let's prove that $\mathbf{T}$ of Eq. (4.54a) and Eq. (4.61) is indeed hermitian, no matter what basis it is expressed in.

First consider matrix elements of the form

$$\left\langle v'_\alpha \left| -\frac{\hbar^2}{2\mu}\frac{\mathrm{d}^2}{\mathrm{d}R^2} \right| v_\alpha \right\rangle,$$

where α denotes any of the electronic states, and $|v_\alpha\rangle$ is any vibrational state belonging to the electronic state $|\Phi_\alpha^{el}\rangle$. The vibrational state $|v_\alpha\rangle$ satisfies the time-independent Schrödinger equation (TISE):

$$-\frac{\hbar^2}{2\mu}\frac{\mathrm{d}^2}{\mathrm{d}R^2}|v_\alpha\rangle + V_\alpha^{\text{total}}|v_\alpha\rangle = E_{v_\alpha}|v_\alpha\rangle,$$

where V_α^{total} is the sum of the rotational energy and all other potential energies.

Then

$$\left\langle v'_\alpha \left| -\frac{\hbar^2}{2\mu}\frac{\mathrm{d}^2}{\mathrm{d}R^2} \right| v_\alpha \right\rangle = E_{v_\alpha}\delta_{v'_\alpha v_\alpha} - \left\langle v'_\alpha \left| V_\alpha^{\text{total}} \right| v_\alpha \right\rangle \tag{E.1a}$$

$$= E_{v'_\alpha}\delta_{v_\alpha v'_\alpha} - \left\langle v_\alpha \left| V_\alpha^{\text{total}} \right| v'_\alpha \right\rangle \tag{E.1b}$$

$$= \left\langle v_\alpha \left| -\frac{\hbar^2}{2\mu}\frac{\mathrm{d}^2}{\mathrm{d}R^2} \right| v'_\alpha \right\rangle, \tag{E.1c}$$

since V_α^{total} is purely multiplicative and $\delta_{v_\alpha v'_\alpha} = \delta_{v'_\alpha v_\alpha}$. Matrix elements of the type described in the previous equation occur both in the $\mathcal{A}$ and $\mathcal{H}$ basis. Equations E.1 show that $\mathbf{T}_\mathcal{A}$ and the parts of $\mathbf{T}_\mathcal{H}$ that contain $\mathrm{d}^2/\mathrm{d}R^2$ are indeed hermitian.

The function $\mathrm{d}\gamma/\mathrm{d}R$ is purely multiplicative, therefore

$$\left\langle v'_\alpha \left| \left(\frac{\mathrm{d}\gamma}{\mathrm{d}R}\right)^2 \right| v_\alpha \right\rangle = \left\langle v_\alpha \left| \left(\frac{\mathrm{d}\gamma}{\mathrm{d}R}\right)^2 \right| v'_\alpha \right\rangle,$$

so all diagonal blocks of $\mathbf{T}_\mathcal{H}$ are hermitian.

Let's focus now on the off-diagonal blocks of $\mathbf{T}_\mathcal{H}$. To finish proving that $\mathbf{T}_\mathcal{H}$ is hermitian, I need to prove that

$$\left\langle v_{3/2} \left| \frac{\mathrm{d}^2\gamma}{\mathrm{d}R^2} + 2\frac{\mathrm{d}\gamma}{\mathrm{d}R}\frac{\partial}{\partial R} \right| v_{1/2} \right\rangle = \left\langle v_{1/2} \left| -\frac{\mathrm{d}^2\gamma}{\mathrm{d}R^2} - 2\frac{\mathrm{d}\gamma}{\mathrm{d}R}\frac{\partial}{\partial R} \right| v_{3/2} \right\rangle. \tag{E.2}$$

Let's recall the rule of integration by parts for the product of three well-behaved functions f, g, and h:

$$\int_a^b fgh'\,\mathrm{d}R = [fgh]_a^b - \int_a^b f'gh\,\mathrm{d}R - \int_a^b fg'h\,\mathrm{d}R,$$

and apply this expression to

$$f(R) = \langle R | v_{3/2} \rangle = \psi_{v_{3/2}}(R) = \psi_{v_{3/2}},$$
$$g(R) = \frac{\mathrm{d}\gamma}{\mathrm{d}R},$$
$$h(r) = \langle R | v_{1/2} \rangle = \psi_{v_{1/2}}(R) = \psi_{v_{1/2}}.$$

Starting from part of the matrix element on the left hand side of Eq. (E.2):

$$\left\langle v_{3/2} \left| \frac{\mathrm{d}\gamma}{\mathrm{d}R} \frac{\partial}{\partial R} \right| v_{1/2} \right\rangle = \int_0^{+\infty} \psi_{v_{3/2}} \frac{\mathrm{d}\gamma}{\mathrm{d}R} \left(\psi_{v_{1/2}}\right)' \mathrm{d}R \tag{E.3a}$$
$$= \left[\psi_{v_{3/2}} \frac{\mathrm{d}\gamma}{\mathrm{d}R} \psi_{v_{1/2}} \right]_{R=0}^{R=+\infty} - \int_0^{+\infty} \left(\psi_{v_{3/2}}\right)' \frac{\mathrm{d}\gamma}{\mathrm{d}R} \psi_{v_{1/2}} \mathrm{d}R$$
$$- \int_0^{+\infty} \psi_{v_{3/2}} \left(\frac{\mathrm{d}\gamma}{\mathrm{d}R}\right)' \psi_{v_{1/2}} \mathrm{d}R, \tag{E.3b}$$

where the quantity between square brackets is zero, since the wave functions vanish at $R = 0$ and $R = +\infty$. Permuting the order of the products in the remaining integrals yields

$$\left\langle v_{3/2} \left| \frac{\mathrm{d}\gamma}{\mathrm{d}R} \frac{\partial}{\partial R} \right| v_{1/2} \right\rangle = -\int_0^{+\infty} \psi_{v_{1/2}} \frac{\mathrm{d}\gamma}{\mathrm{d}R} \left(\psi_{v_{3/2}}\right)' \mathrm{d}R - \int_0^{+\infty} \psi_{v_{1/2}} \left(\frac{\mathrm{d}\gamma}{\mathrm{d}R}\right)' \psi_{v_{3/2}} \mathrm{d}R \tag{E.3c}$$
$$= -\left\langle v_{1/2} \left| \frac{\mathrm{d}\gamma}{\mathrm{d}R} \frac{\partial}{\partial R} \right| v_{3/2} \right\rangle - \left\langle v_{1/2} \left| \frac{\mathrm{d}^2\gamma}{\mathrm{d}R^2} \right| v_{3/2} \right\rangle \tag{E.3d}$$

Let's now combine Eq. (E.3d) with Eq. (E.2)

$$\left\langle v_{3/2} \left| \frac{\mathrm{d}^2\gamma}{\mathrm{d}R^2} + 2\frac{\mathrm{d}\gamma}{\mathrm{d}R} \frac{\partial}{\partial R} \right| v_{1/2} \right\rangle = \left\langle v_{3/2} \left| \frac{\mathrm{d}^2\gamma}{\mathrm{d}R^2} \right| v_{1/2} \right\rangle + 2\left\langle v_{3/2} \left| \frac{\mathrm{d}\gamma}{\mathrm{d}R} \frac{\partial}{\partial R} \right| v_{1/2} \right\rangle \tag{E.4a}$$

$$\left\langle v_{3/2} \left| \frac{\mathrm{d}^2\gamma}{\mathrm{d}R^2} + 2\frac{\mathrm{d}\gamma}{\mathrm{d}R}\frac{\partial}{\partial R} \right| v_{1/2} \right\rangle = \left\langle v_{1/2} \left| \frac{\mathrm{d}^2\gamma}{\mathrm{d}R^2} \right| v_{3/2} \right\rangle - 2\left\langle v_{1/2} \left| \frac{\mathrm{d}\gamma}{\mathrm{d}R}\frac{\partial}{\partial R} \right| v_{3/2} \right\rangle$$
$$- 2\left\langle v_{1/2} \left| \frac{\mathrm{d}^2\gamma}{\mathrm{d}R^2} \right| v_{3/2} \right\rangle \quad \text{(E.4b)}$$
$$= \left\langle v_{1/2} \left| -\frac{\mathrm{d}^2\gamma}{\mathrm{d}R^2} - 2\frac{\mathrm{d}\gamma}{\mathrm{d}R}\frac{\partial}{\partial R} \right| v_{3/2} \right\rangle, \quad \text{(E.4c)}$$

which completes the proof that $\mathbf{T}_{\mathcal{H}}$ is hermitian, as it should.

First, verifying that $\mathbf{T}_{\mathcal{H}}$ is hermitian allows to check whether I did any algebraic mistake when passing from basis $\mathcal{A}$ to basis $\mathcal{H}$. Second, notice that the $V_{1/2}$ state holds 146 rovibrational states, and the $V_{3/2}$ holds 114. If I did not remember that $\mathbf{T}$ must be hermitian, I would have had to calculate $(146+114)^2 = 67\,600$ matrix elements. Thanks to hermicity, I now only have to calculate

$146 \times (146+1)/2 = 10731$ elements of the form $\left\langle v'_{1/2} \left| \left(\frac{\mathrm{d}\gamma}{\mathrm{d}R}\right)^2 - \frac{\hbar^2}{2\mu}\frac{\partial^2}{\partial R^2} \right| v_{1/2} \right\rangle$,

$114 \times (114+1)/2 = 6555$ $\left\langle v'_{3/2} \left| \left(\frac{\mathrm{d}\gamma}{\mathrm{d}R}\right)^2 - \frac{\hbar^2}{2\mu}\frac{\partial^2}{\partial R^2} \right| v_{3/2} \right\rangle$,

$114 \times 146 = 16644$ $\left\langle v_{3/2} \left| \frac{\mathrm{d}^2\gamma}{\mathrm{d}R^2} + 2\frac{\mathrm{d}\gamma}{\mathrm{d}R}\frac{\partial}{\partial R} \right| v_{1/2} \right\rangle$,

that is 33930 matrix elements, about half what I was about to calculate before I remembered (and checked!) the hermicity of $\mathbf{T}$.

Appendix F

Examining the coupled-channels wave functions

F.1 Introduction

In this appendix I verify the validity of the solutions to the coupled-channels problem I set out to solve, and I show the closeness of the calculated coupled-channels rovibrational energies with the results published in [10].

F.2 Validity of the coupled-channels solutions

Let's recall equations (4.71) from Sec. 4.4.2.4 on p. 114, and use them to define the operators $\hat{h}_{11}$, $\hat{h}_{12}$, $\hat{h}_{21}$, and $\hat{h}_{22}$, such that

$$\left[-\frac{\hbar^2}{2\mu}\left(\frac{\mathrm{d}^2}{\mathrm{d}R^2}-\left(\frac{\mathrm{d}\gamma}{\mathrm{d}R}\right)^2\right)+V_{1/2}(R)+4\frac{\hbar^2}{2\mu R^2}\right]\psi_{v_{cc}}^{[1/2]}(R) + \frac{\hbar^2}{2\mu}\left[\frac{\mathrm{d}^2\gamma}{\mathrm{d}R^2}+2\frac{\mathrm{d}\gamma}{\mathrm{d}R}\frac{\mathrm{d}}{\mathrm{d}R}\right]\psi_{v_{cc}}^{[3/2]}(R)=\mathrm{E}_{v_{cc}}^{cc}\psi_{v_{cc}}^{[1/2]}(R), \quad \text{(F.1a)}$$

$$-\frac{\hbar^2}{2\mu}\left[\frac{\mathrm{d}^2\gamma}{\mathrm{d}R^2}+2\frac{\mathrm{d}\gamma}{\mathrm{d}R}\frac{\mathrm{d}}{\mathrm{d}R}\right]\psi_{v_{cc}}^{[1/2]}(R) + \left[-\frac{\hbar^2}{2\mu}\left(\frac{\mathrm{d}^2}{\mathrm{d}R^2}-\left(\frac{\mathrm{d}\gamma}{\mathrm{d}R}\right)^2\right)+V_{3/2}(R)+4\frac{\hbar^2}{2\mu R^2}\right]\psi_{v_{cc}}^{[3/2]}(R)=\mathrm{E}_{v_{cc}}^{cc}\psi_{v_{cc}}^{[3/2]}(R). \quad \text{(F.1b)}$$

$$\Leftrightarrow \quad \hat{h}_{11}\,\psi_{v_{cc}}^{[1/2]}+\hat{h}_{12}\,\psi_{v_{cc}}^{[3/2]}=\mathrm{E}_{v_{cc}}^{cc}\psi_{v_{cc}}^{[1/2]}, \quad \text{(F.2a)}$$

$$\hat{h}_{21}\,\psi_{v_{cc}}^{[1/2]}+\hat{h}_{22}\,\psi_{v_{cc}}^{[3/2]}=\mathrm{E}_{v_{cc}}^{cc}\psi_{v_{cc}}^{[3/2]}. \quad \text{(F.2b)}$$

$\gamma(R)$ is defined by Eq. (4.57) p. 103, and the coupled channel eigenket $|\Phi_{v_{cc}}^{cc}\rangle$ is defined in Eq. (4.70) p. 115. By plotting on the same

graph the left and right hand side of Eqs. (F.2a-F.2b), I can assess whether $|\Phi^{cc}_{v_{cc}}\rangle$ is actually an eigenstate of the coupled-channel Time-Independent Schrödinger Equation with eigenenergy $E^{cc}_{v_{cc}}$. If the left hand side of the equations superimposes on the right hand side, then $|\Phi^{cc}_{v_{cc}}\rangle$ *is indeed* a coupled-channel eigenstate with energy $E^{cc}_{v_{cc}}$.

Figures F.1–F.9 below show plots of Eqs. (F.2a) and (F.2b). On each figure, panel (a) is always a plot of Eq. (F.2a), and panel (b) is always a plot of Eq. (F.2b). The red (*resp*.gray) solid line always represents the left hand side of Eq. (F.2a) (*resp*.Eq. (F.2b)), while the dotted blue (resp. dashed green) line represents the right hand side of Eq. (F.2a) (resp. Eq. (F.2b)). The legend on each figure is a reminder of this convention. The black horizontal line is the horizontal axis, drawn to guide the eye.

Notice that on all figures, the continuous and the discontinuous lines always superimpose nicely, no matter the vibrational energy. To reinforce the graphical agreement of figures F.1–F.9, I plot in figures F.10–F.18 the absolute difference between the left hand side and the right hand side of Eqs. (F.2a-F.2b). I calculated the absolute error using error propagation techniques from Taylor [83], given the uncertainty in the various terms that appear on the left and right hand side of Eq. (F.1).

I also compare in Fig. F.19 the vibrational transition energies[a] $E^{cc}_{v_{cc}} - E^{J_X=0}_{v_X=0}$ obtained from my calculation, to the experimental results reported in the second column of Tbl. III in [10]. The difference between my results and those of [10] is at least $0.017\,cm^{-1}$ for $v_{cc} = 42$ and at most $2.018\,cm^{-1}$ for $v_{cc} = 40$. Zaharova *et al*. [10] include more physical effects in the model they use to analyse their experimental data (see Sec. III of [10]) than I do in my model. This is the most probable cause for the discrepancy.

[a] Remember: for the coupled-channel calculation, the rotational quantum number J_{cc} is 1.

The graphical match of the wave functions, further supported by the smallness of the difference between each side of Eqs. (F.2a-F.2b) strongly suggests that *I correctly encoded the machinery to solve the coupled equations Eq. (F.1) (or equivalently and Eq. (F.2))* and *the method I chose to solve these equations produce results in agreement with the experimental results* published in [10].

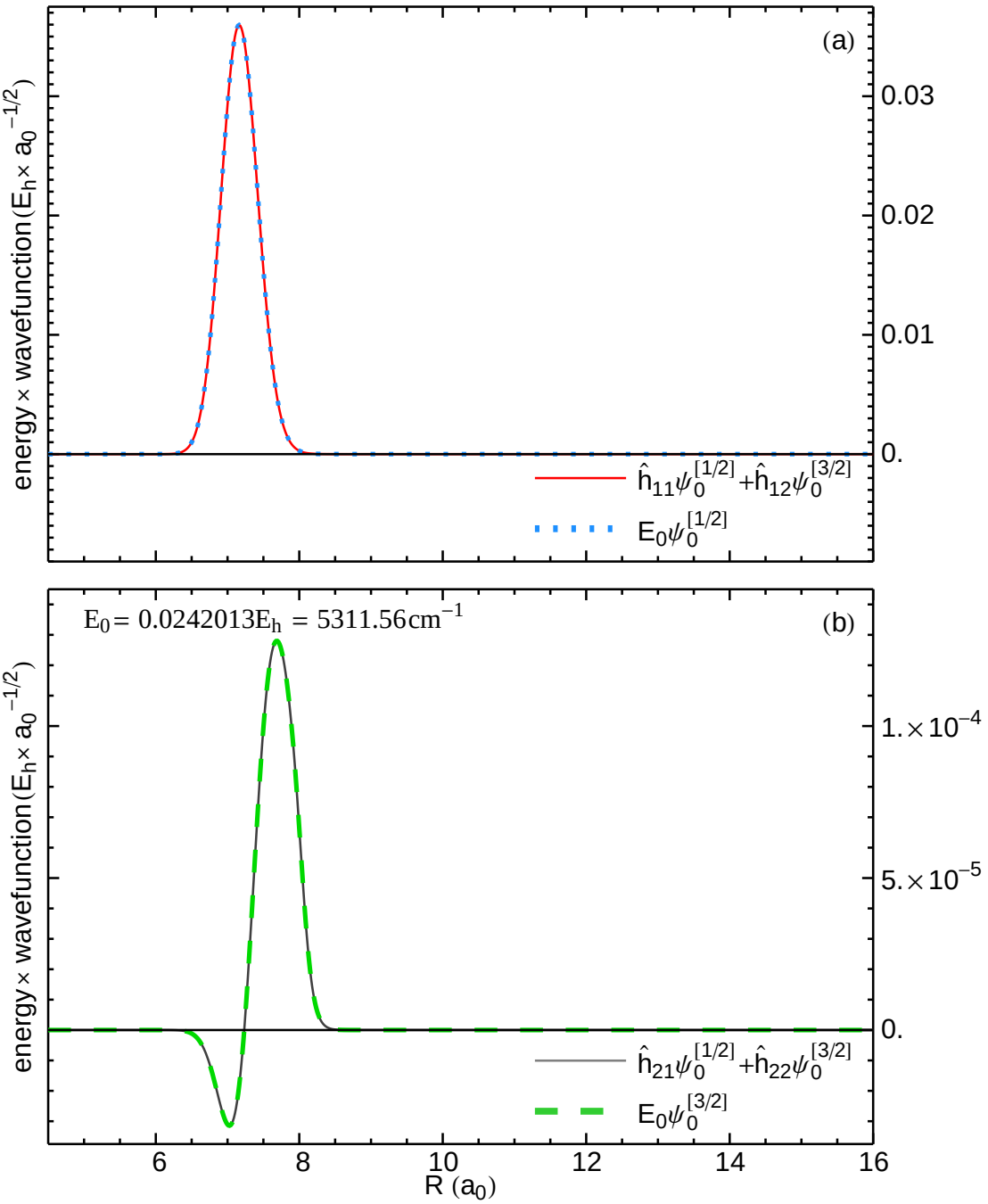

Figure F.1: (Color online) Graphical check of the validity of the coupled-channel wave function $v_{cc} = 0$ calculated with the basis expansion method. (**a**)—Left and right hand side of the coupled-channel Time-Independent Schrödinger Equation for the $V_{1/2}$ channel. (**b**)—Same as (a) for the $V_{3/2}$ channel. Note how the continuous and discontinuous lines superimpose, showing the Time-Independent Schrödinger Equation is verified.

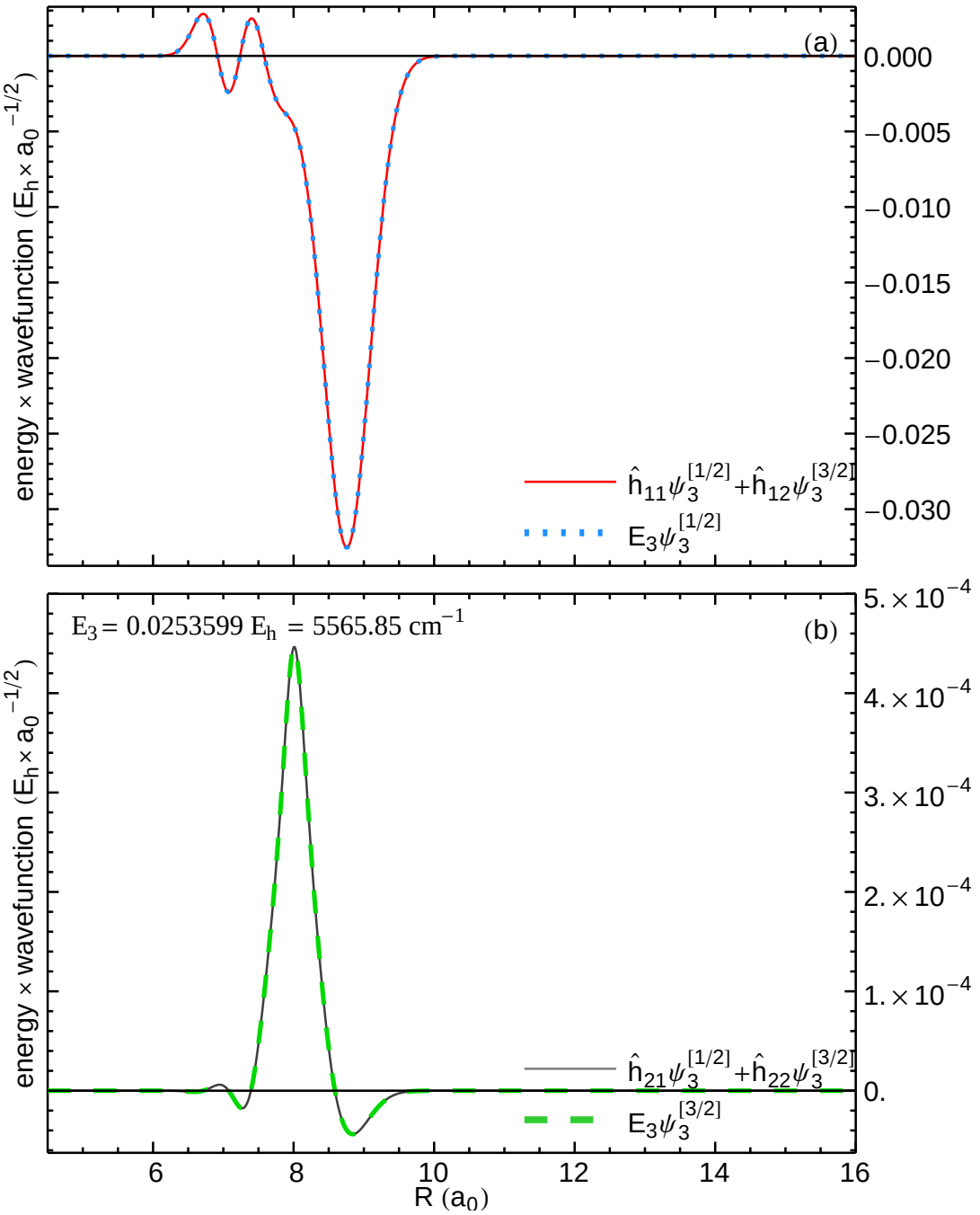

Figure F.2: (Color online) Validity of the coupled-channel wave function $v_{cc} = 3$ calculated with the basis expansion method.

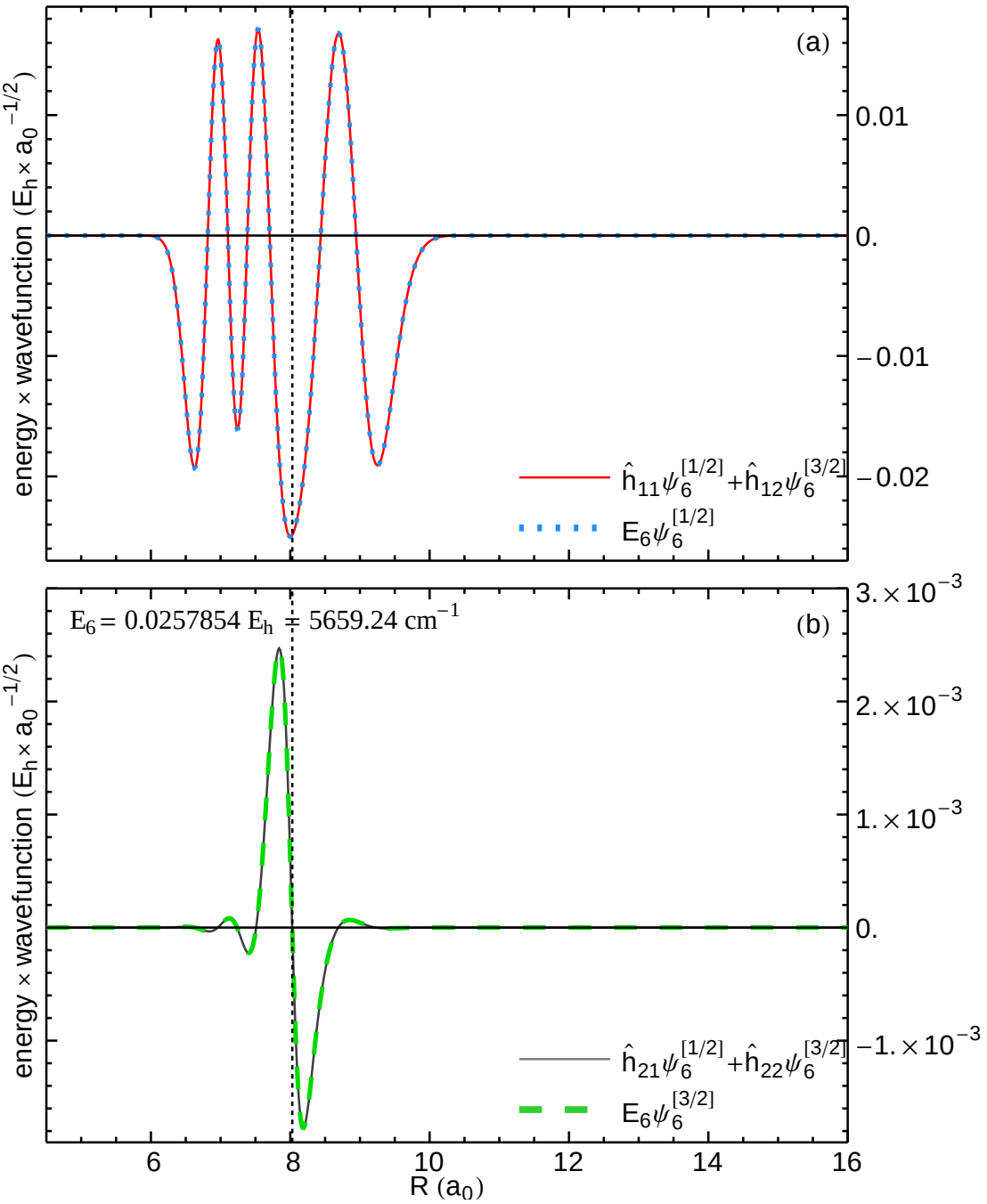

Figure F.3: (Color online) Validity of the coupled-channel wave function $v_{cc} = 6$ calculated with the basis expansion method. The vertical dashed line marks the position of the avoided crossing of the potentials.

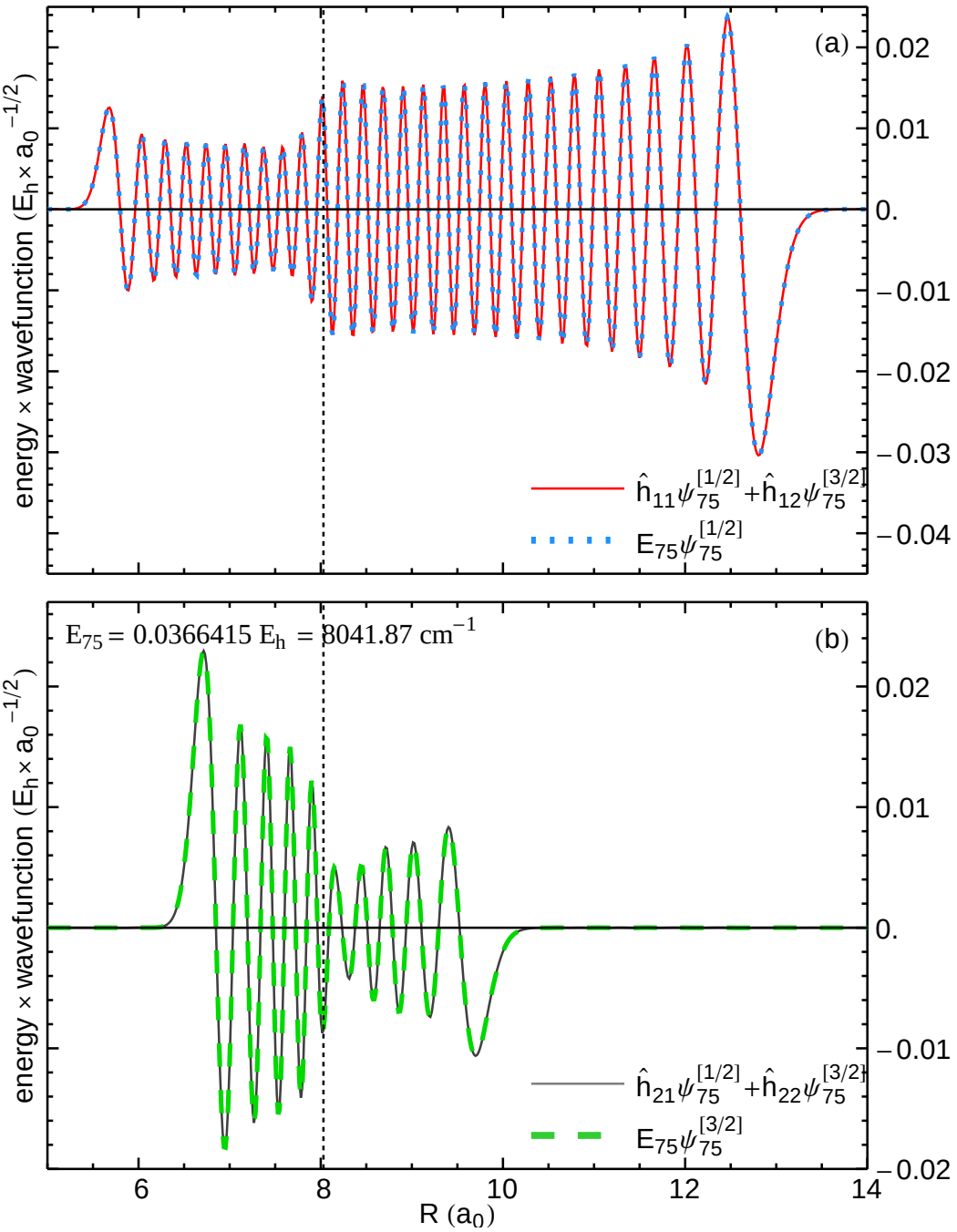

Figure F.4: (Color online) Validity of the coupled-channel wave function $v_{cc} = 75$ calculated with the basis expansion method. Vertical dashes: avoided crossing of the potentials.

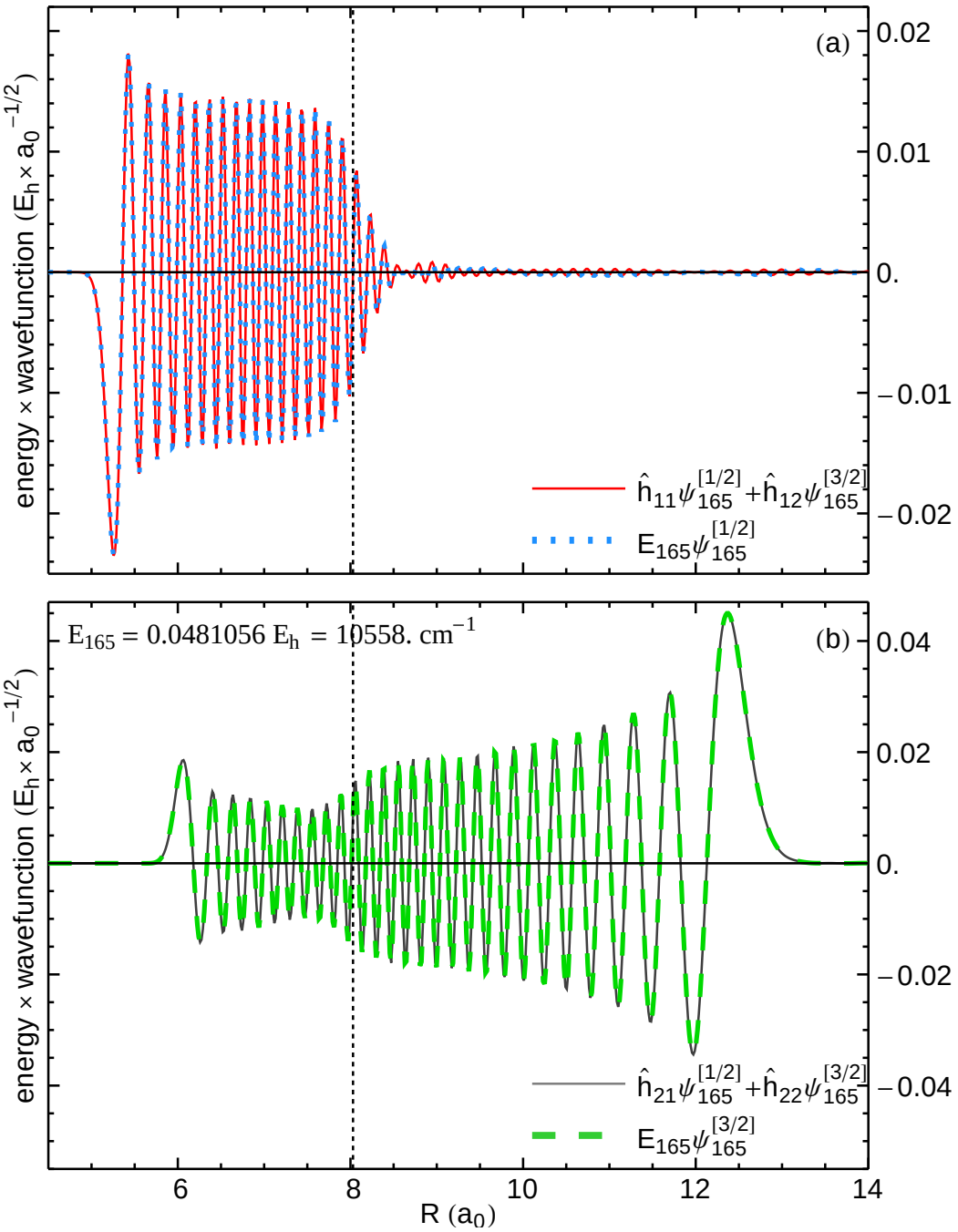

Figure F.5: (Color online) Validity of the coupled-channel wave function $v_{cc} = 165$ calculated with the basis expansion method. Vertical dashes: avoided crossing of the potentials.

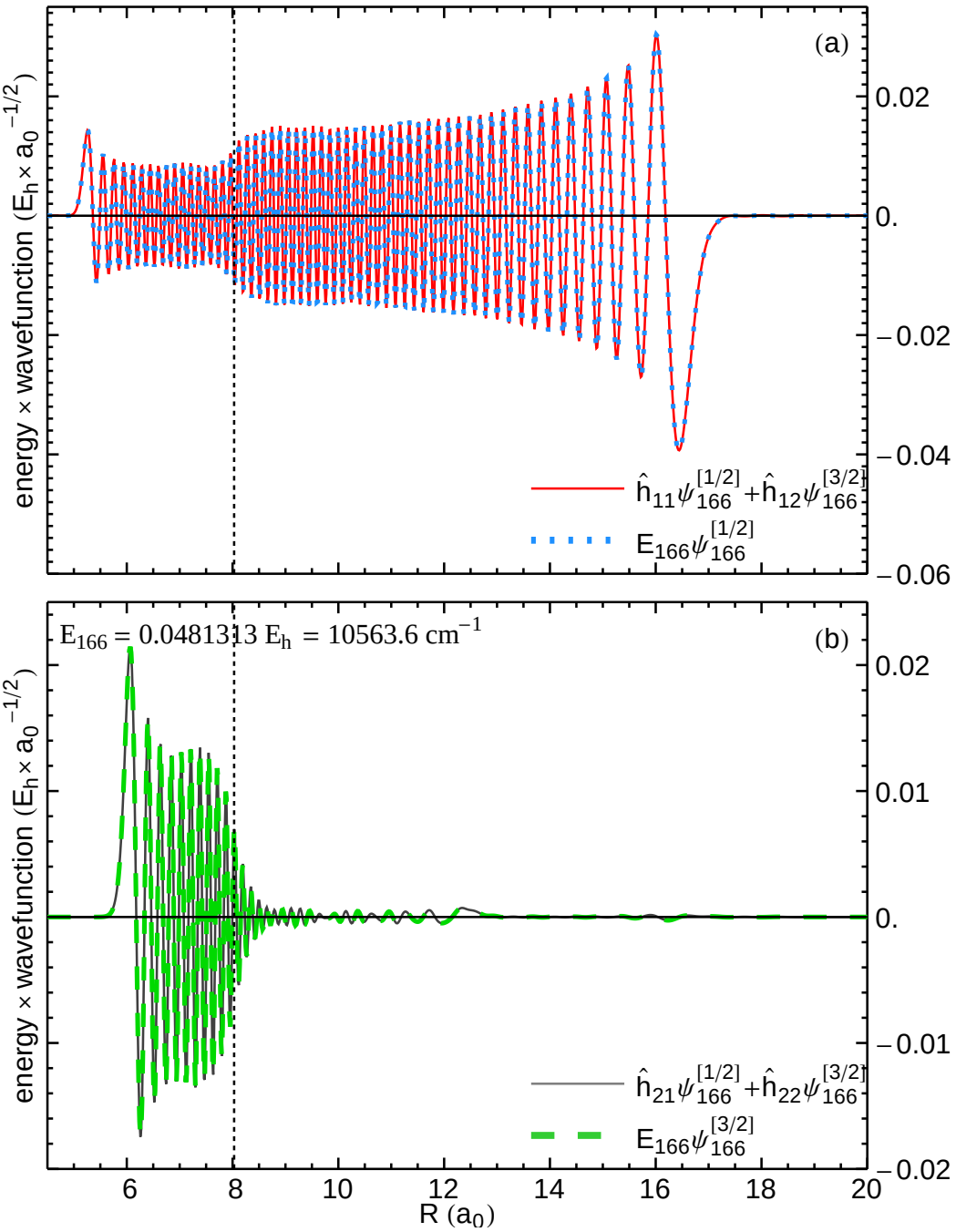

Figure F.6: (Color online) Validity of the coupled-channel wave function $v_{cc} = 166$ calculated with the basis expansion method. Vertical dashes: avoided crossing of the potentials.

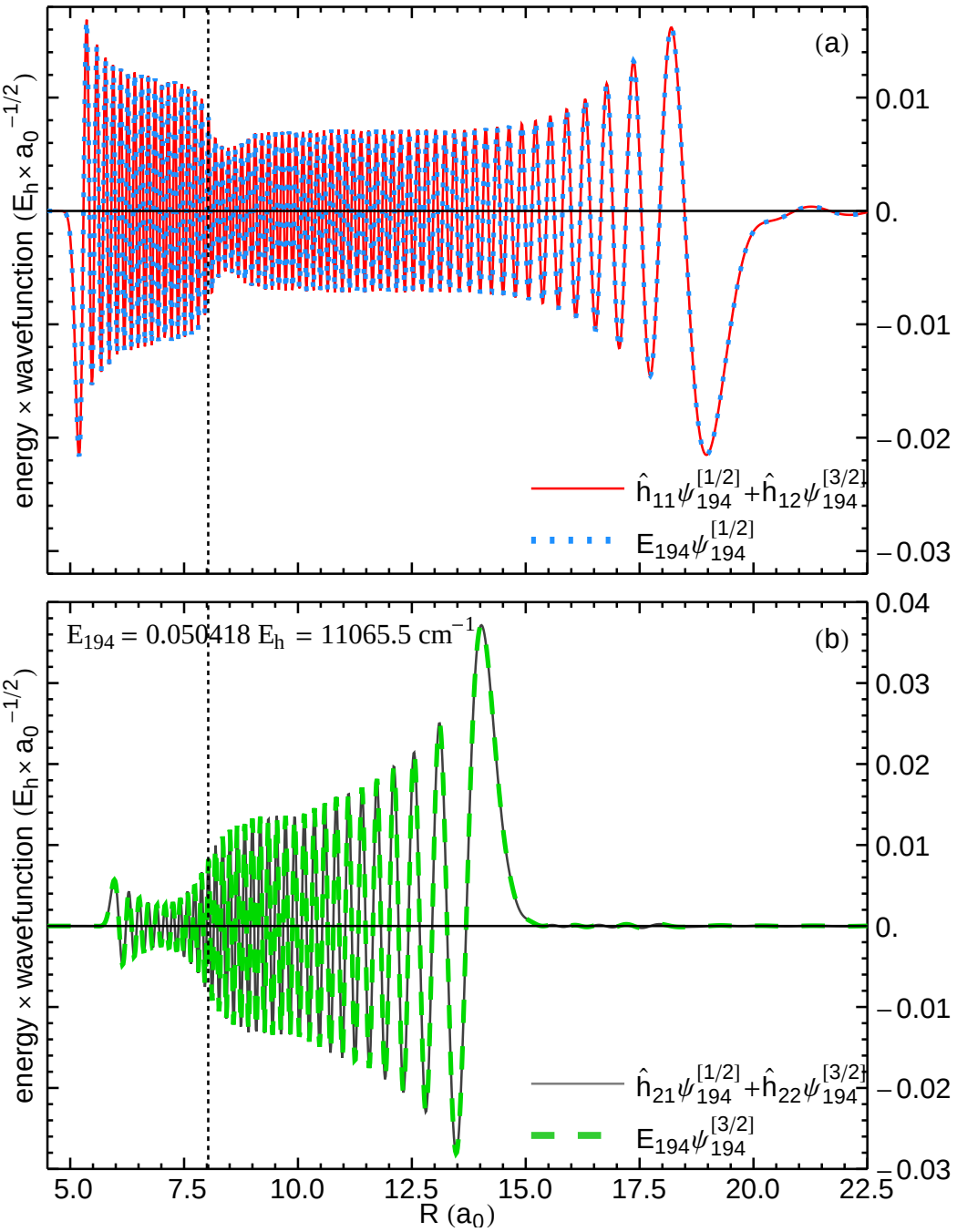

Figure F.7: (Color online) Validity of the coupled-channel wave function $v_{cc} = 194$ calculated with the basis expansion method. Vertical dashes: avoided crossing of the potentials.

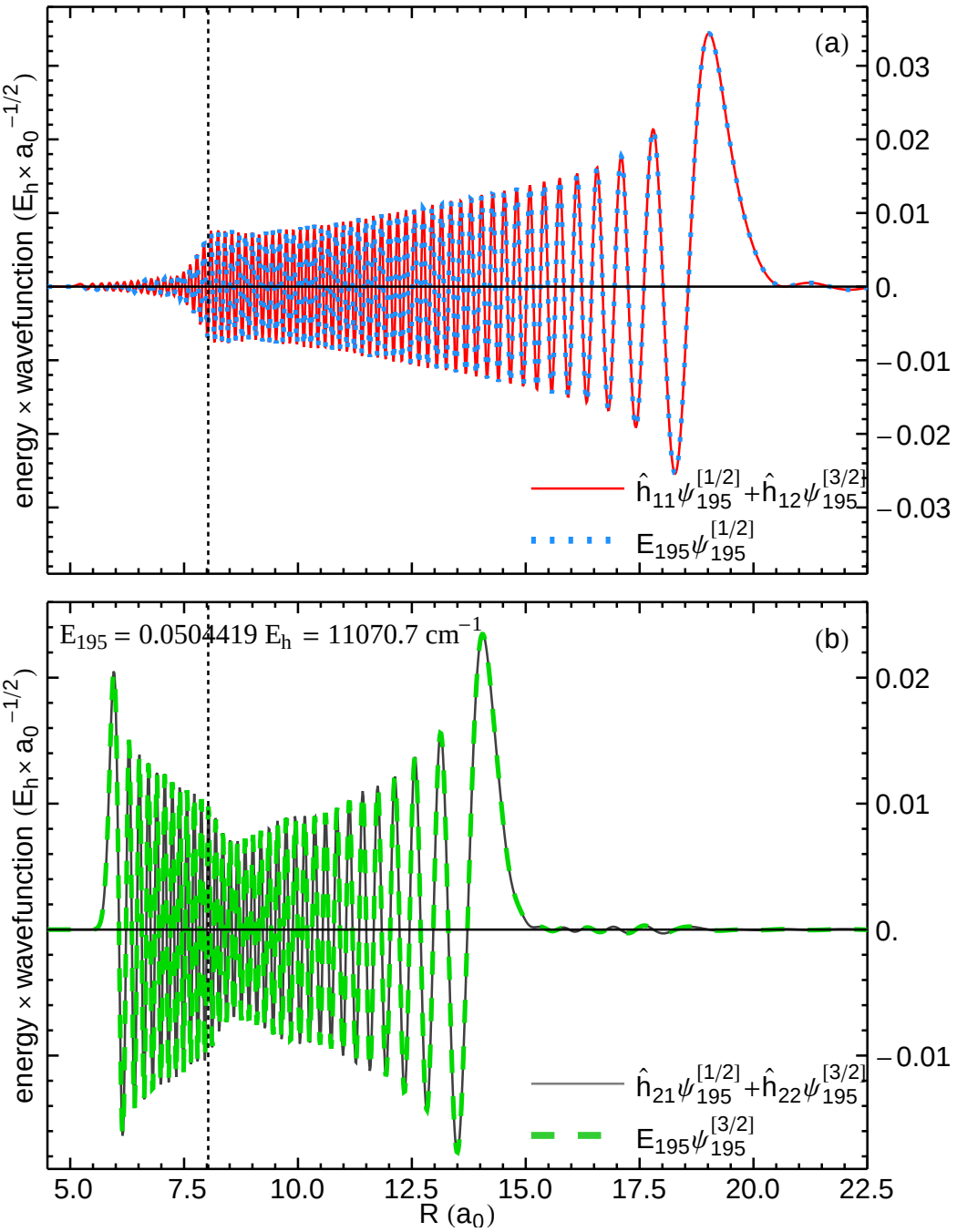

Figure F.8: (Color online) Validity of the coupled-channel wave function $v_{cc} = 195$ calculated with the basis expansion method. Vertical dashes: avoided crossing of the potentials.

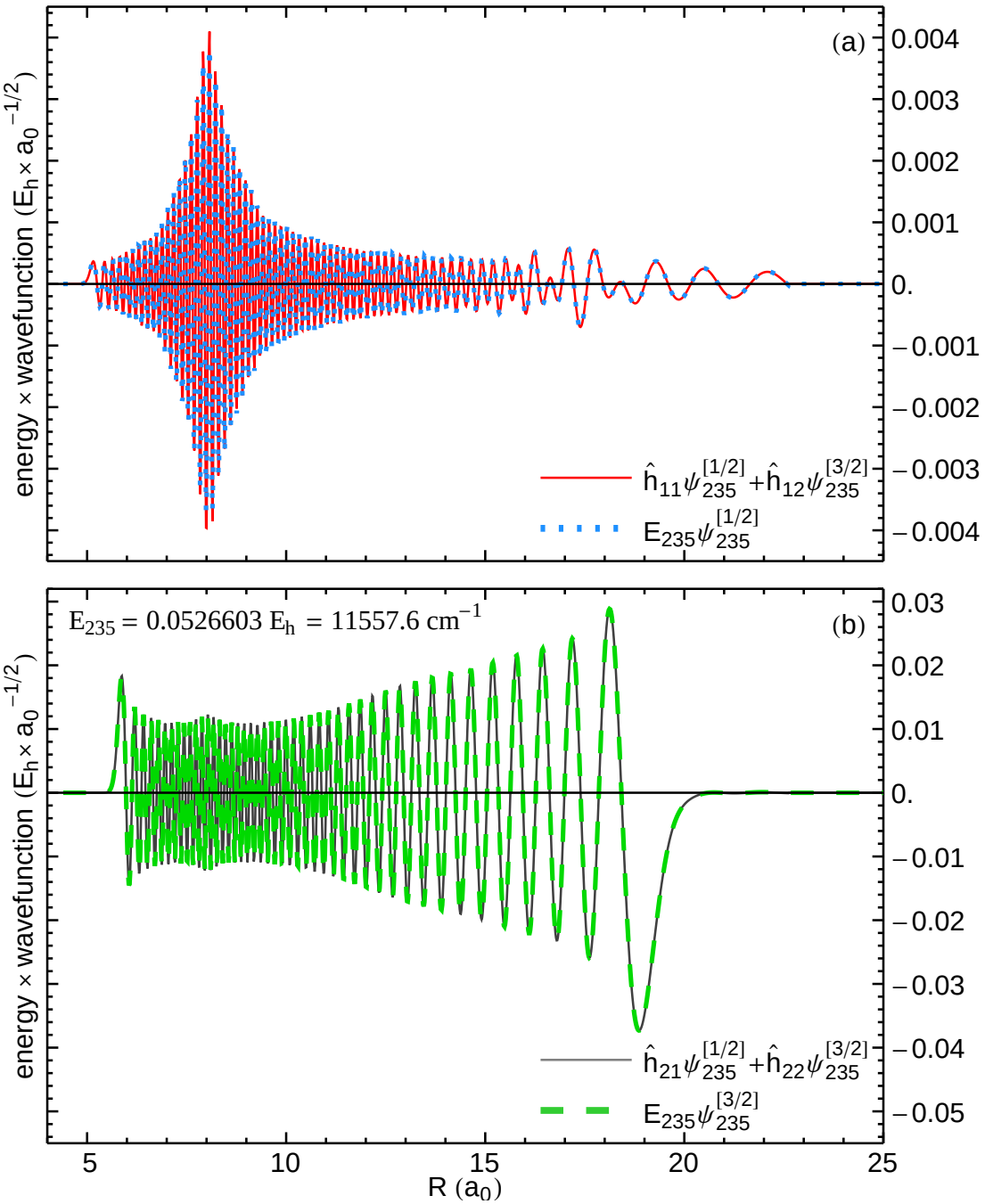

Figure F.9: (Color online) Validity of the coupled-channel wave function $v_{cc} = 235$ calculated with the basis expansion method.

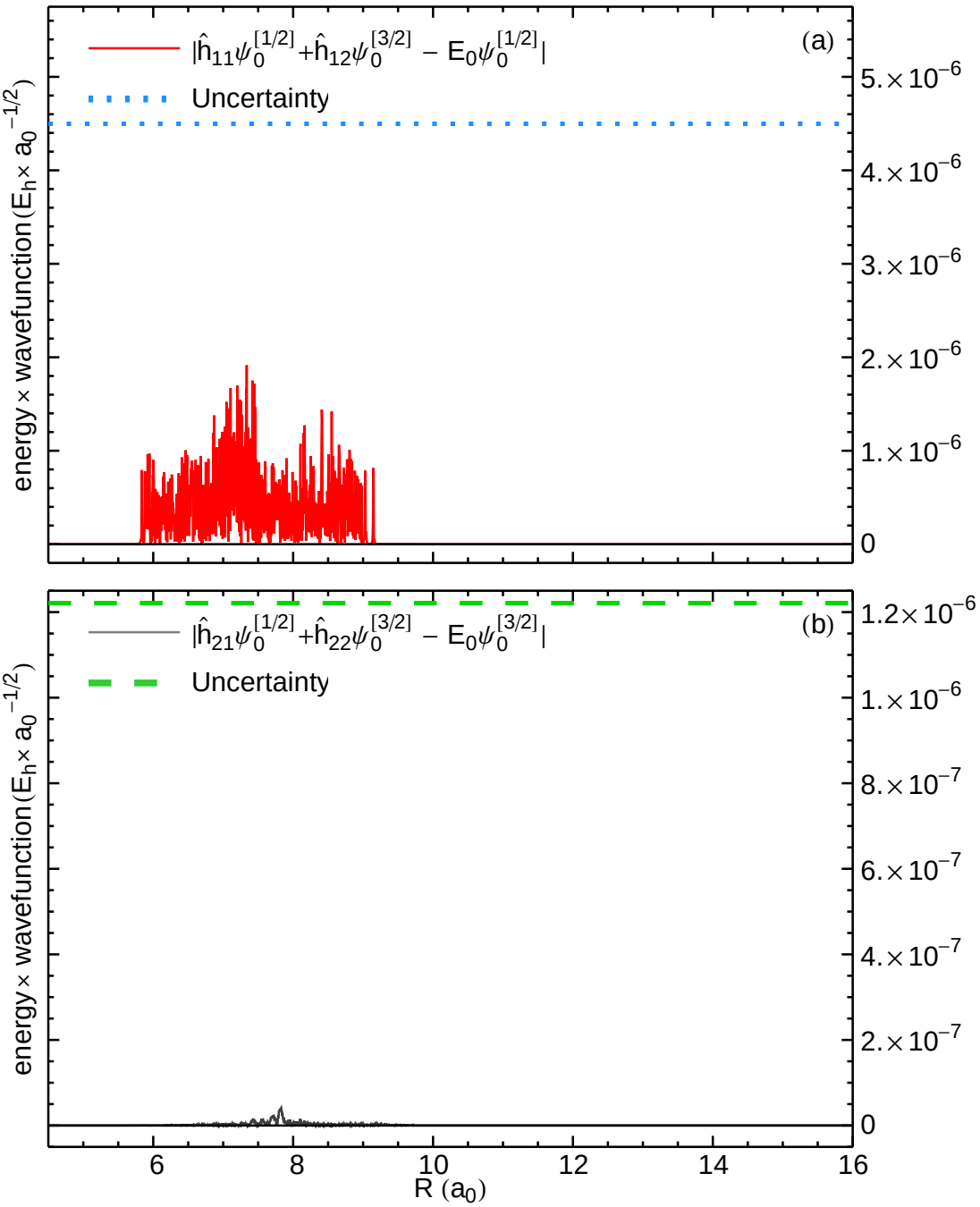

Figure F.10: (Color online) **Solid lines**—Absolute difference between the left hand side and right hand side of Eq. (F.2a) (panel (**a**)) and Eq. (F.2b) (panel (**b**)) for $v_{cc} = 0$. **Dashed lines**—*a priori* uncertainty estimate on the difference, based on the precision of the terms in Eqs. (F.2). Notice that in panel (**b**) the actual difference is ten times smaller than the estimate.

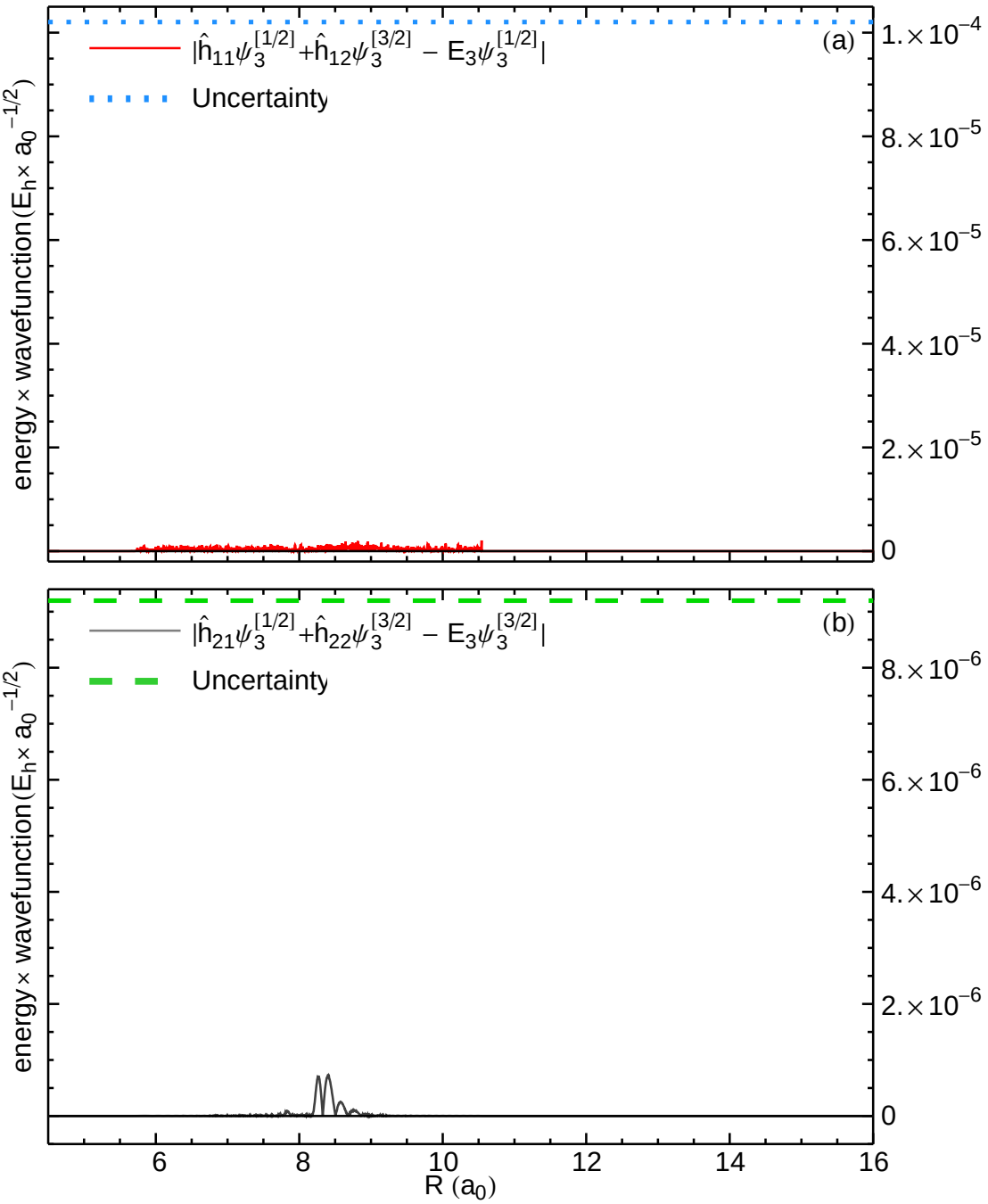

Figure F.11: (Color online) **Solid lines**—Absolute difference between the left hand side and right hand side of Eq. (F.2a) (panel (**a**)) and Eq. (F.2b) (panel (**b**)) for $v_{cc} = 3$. The actual difference is much smaller than the estimate (dashed lines).

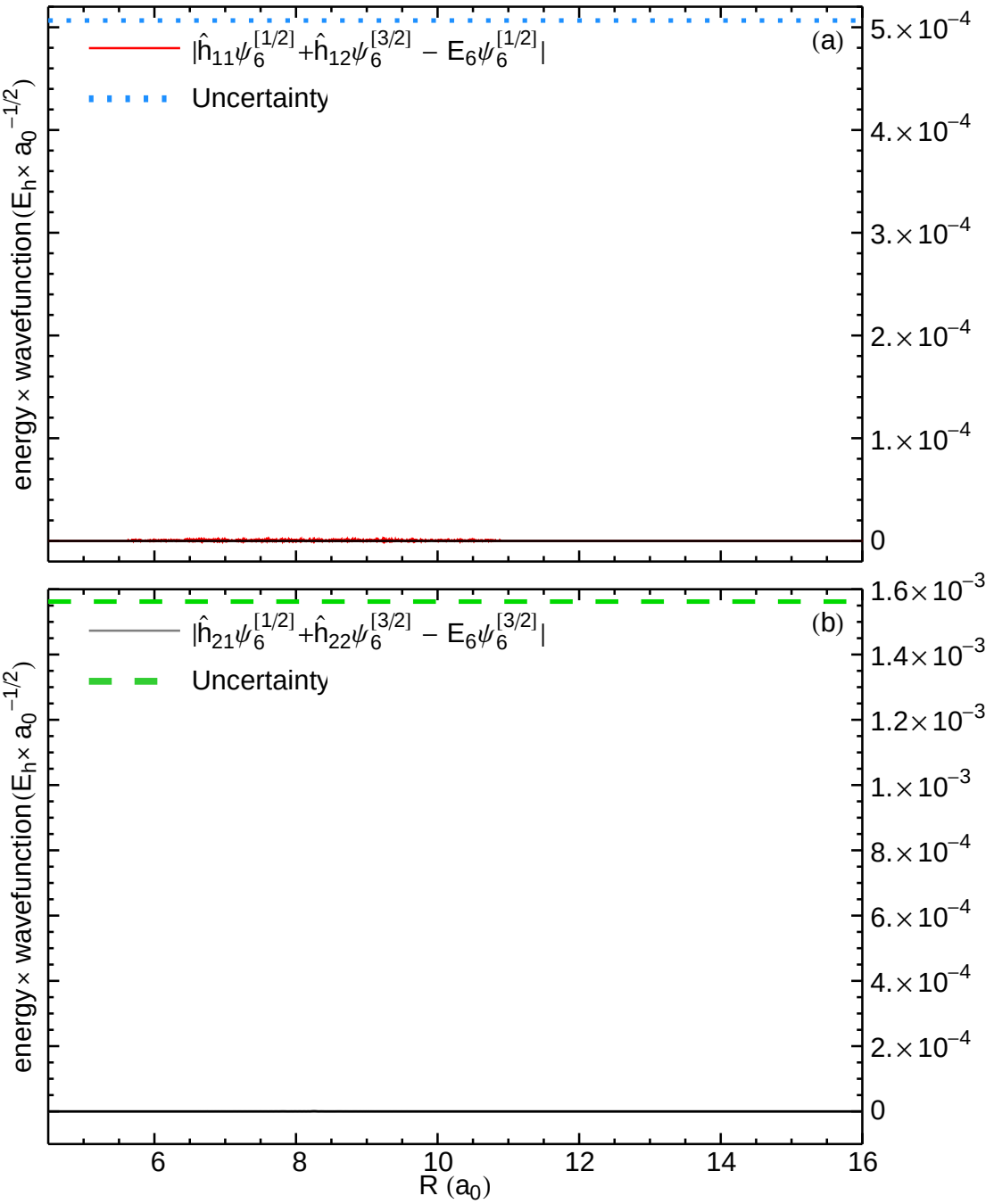

Figure F.12: (Color online) **Solid lines**—Absolute difference between the left hand side and right hand side of Eq. (F.2a) (panel (**a**)) and Eq. (F.2b) (panel (**b**)) for $v_{cc} = 6$. The actual difference is much smaller than the estimate (dashed lines); in particular in panel (**b**), the actual difference is crushed onto the horizontal axis.

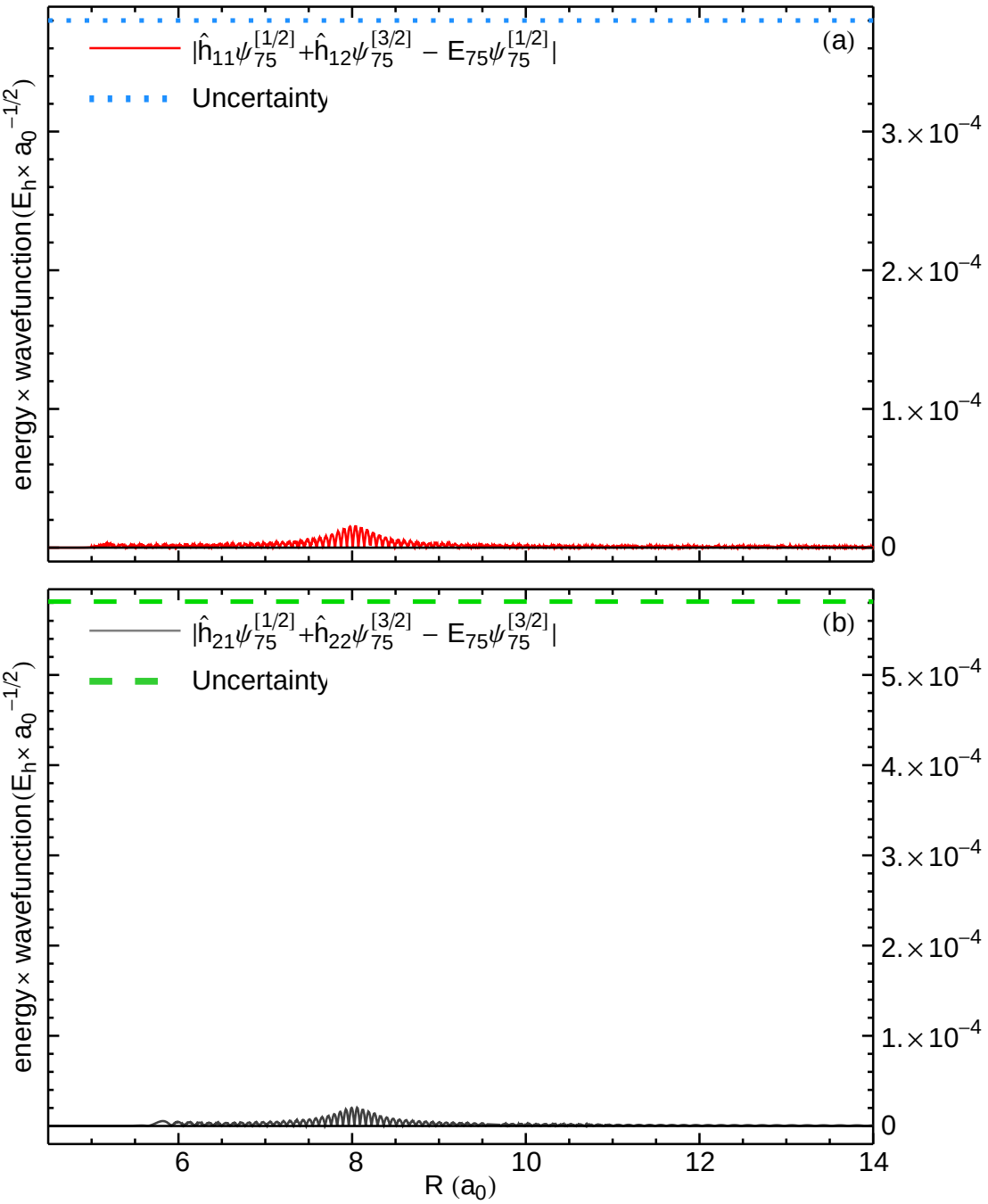

Figure F.13: (Color online) **Solid lines**—Absolute difference between the left hand side and right hand side of Eq. (F.2a) (panel (**a**)) and Eq. (F.2b) (panel (**b**)) for $v_{cc} = 75$.

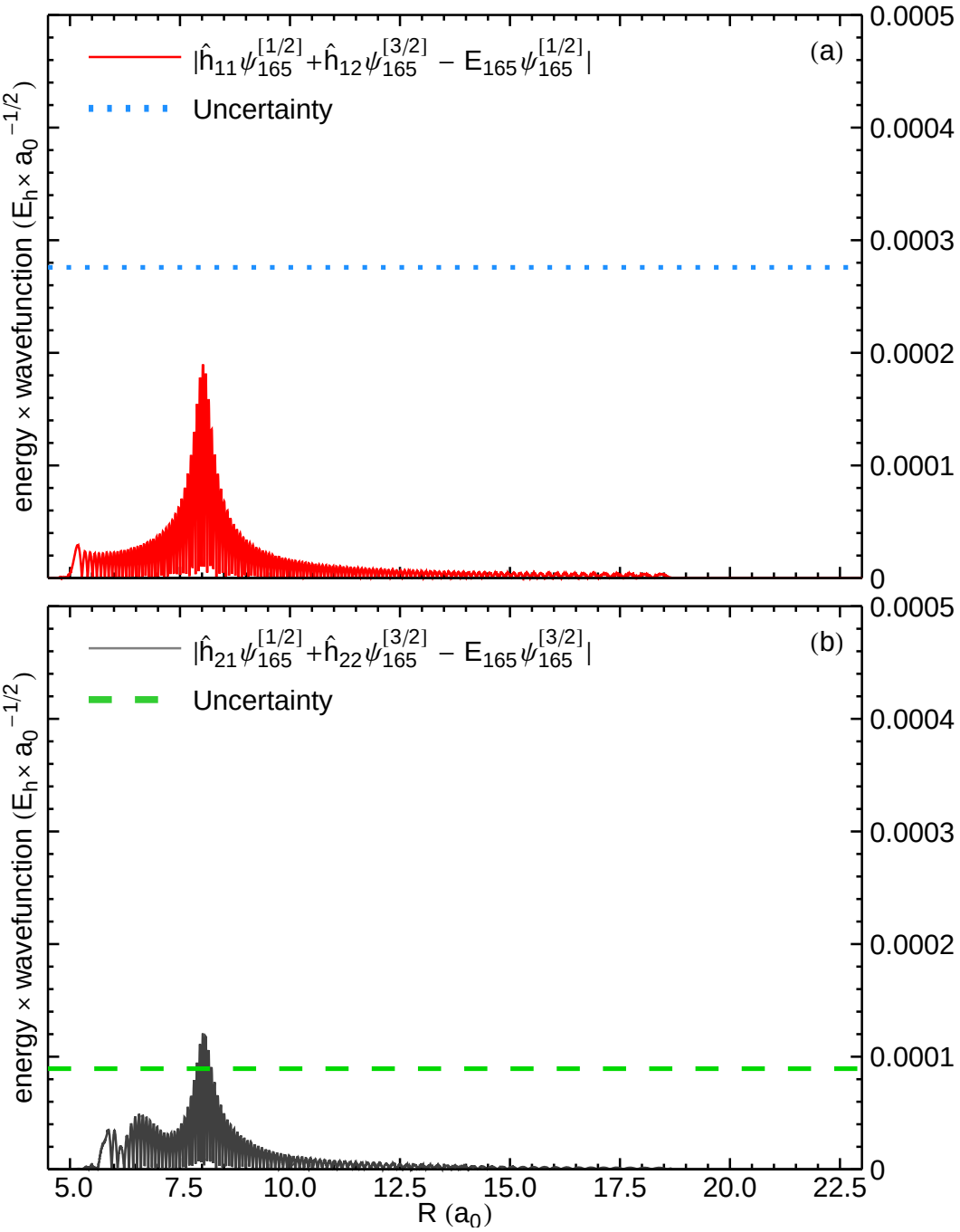

Figure F.14: (Color online) **Solid lines**—Absolute difference between the left hand side and right hand side of Eq. (F.2a) (panel (**a**)) and Eq. (F.2b) (panel (**b**)) for $v_{cc} = 165$.

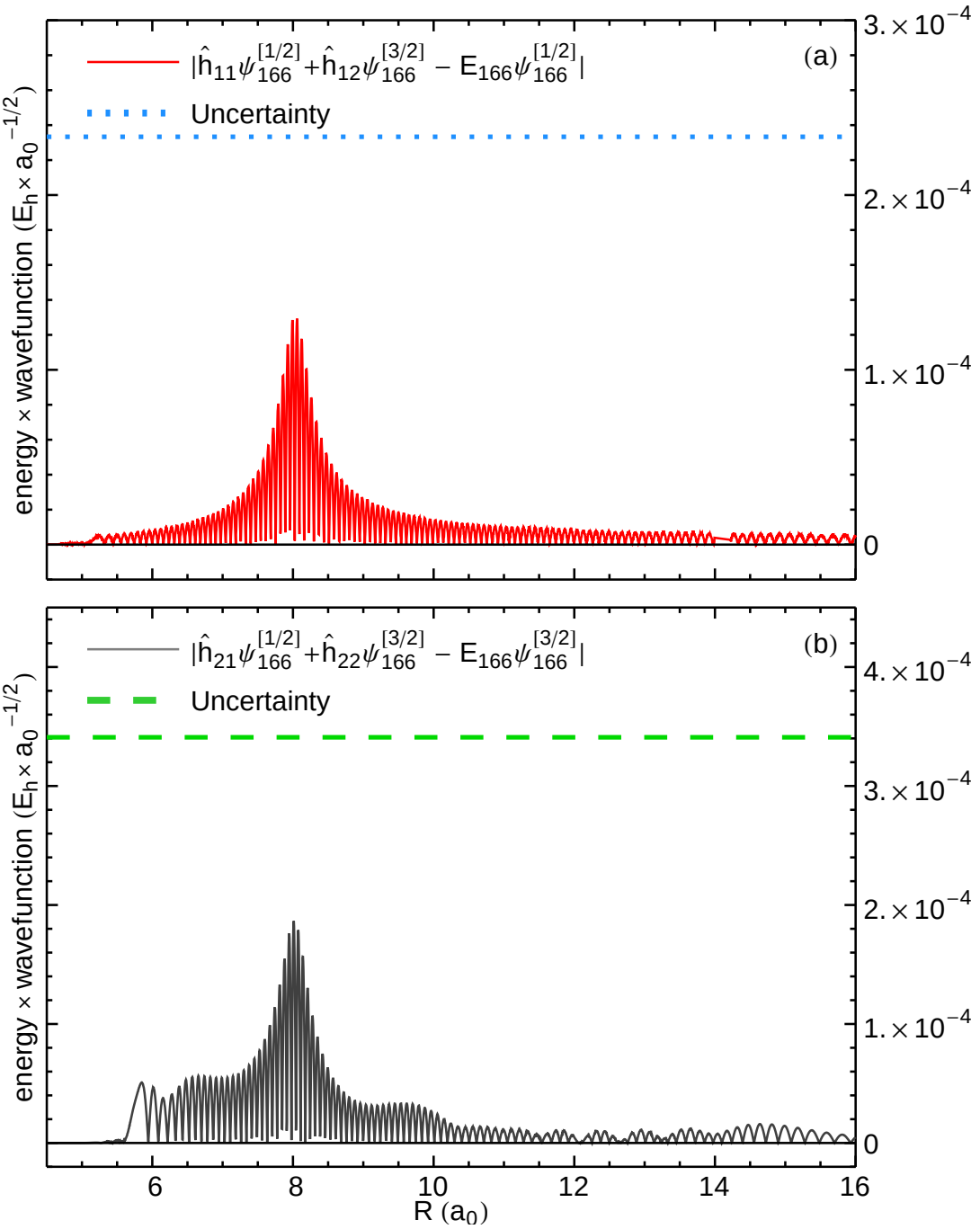

Figure F.15: (Color online) **Solid lines**—Absolute difference between the left hand side and right hand side of Eq. (F.2a) (panel (**a**)) and Eq. (F.2b) (panel (**b**)) for $v_{cc} = 166$.

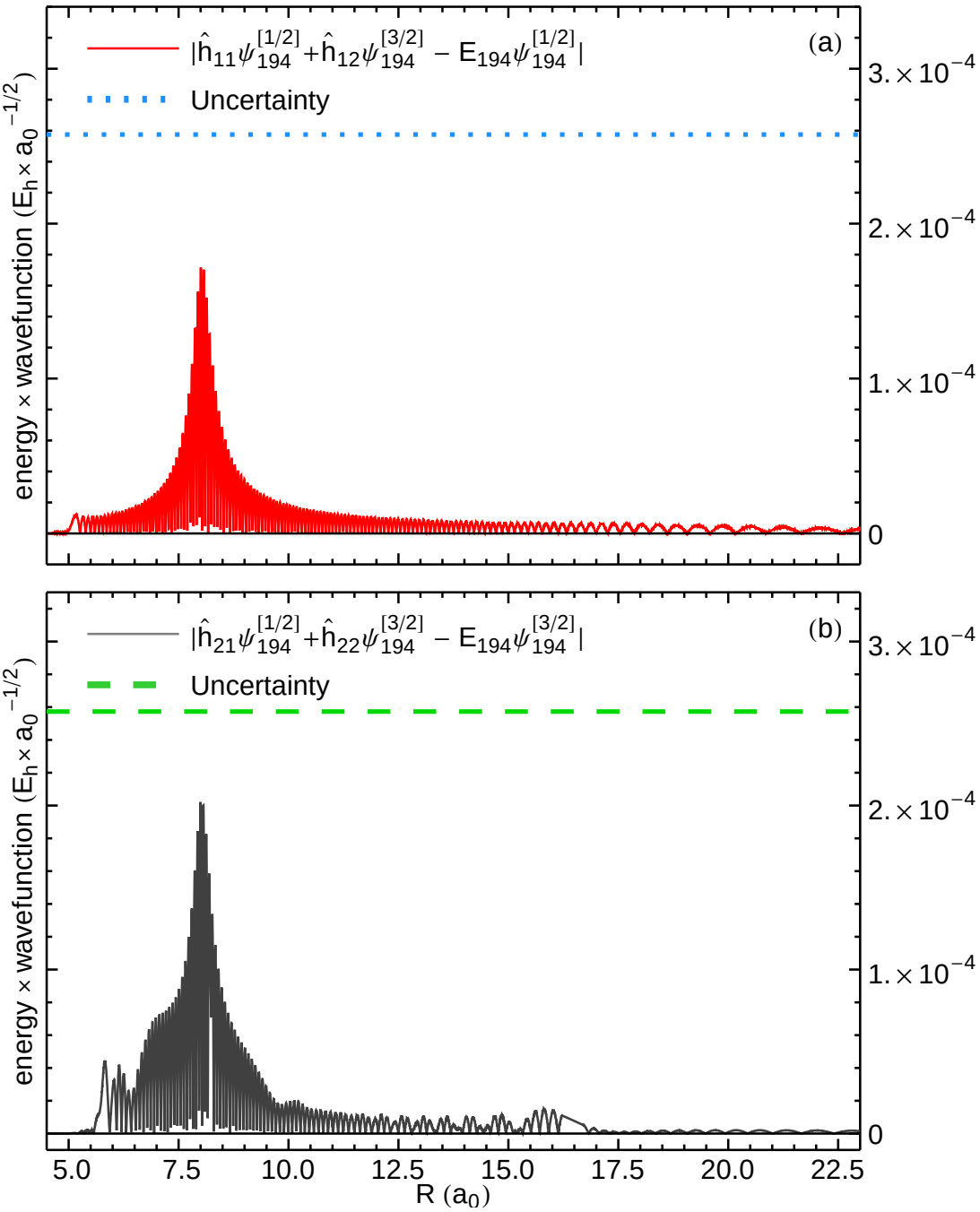

Figure F.16: (Color online) **Solid lines**—Absolute difference between the left hand side and right hand side of Eq. (F.2a) (panel (**a**)) and Eq. (F.2b) (panel (**b**)) for $v_{cc} = 194$.

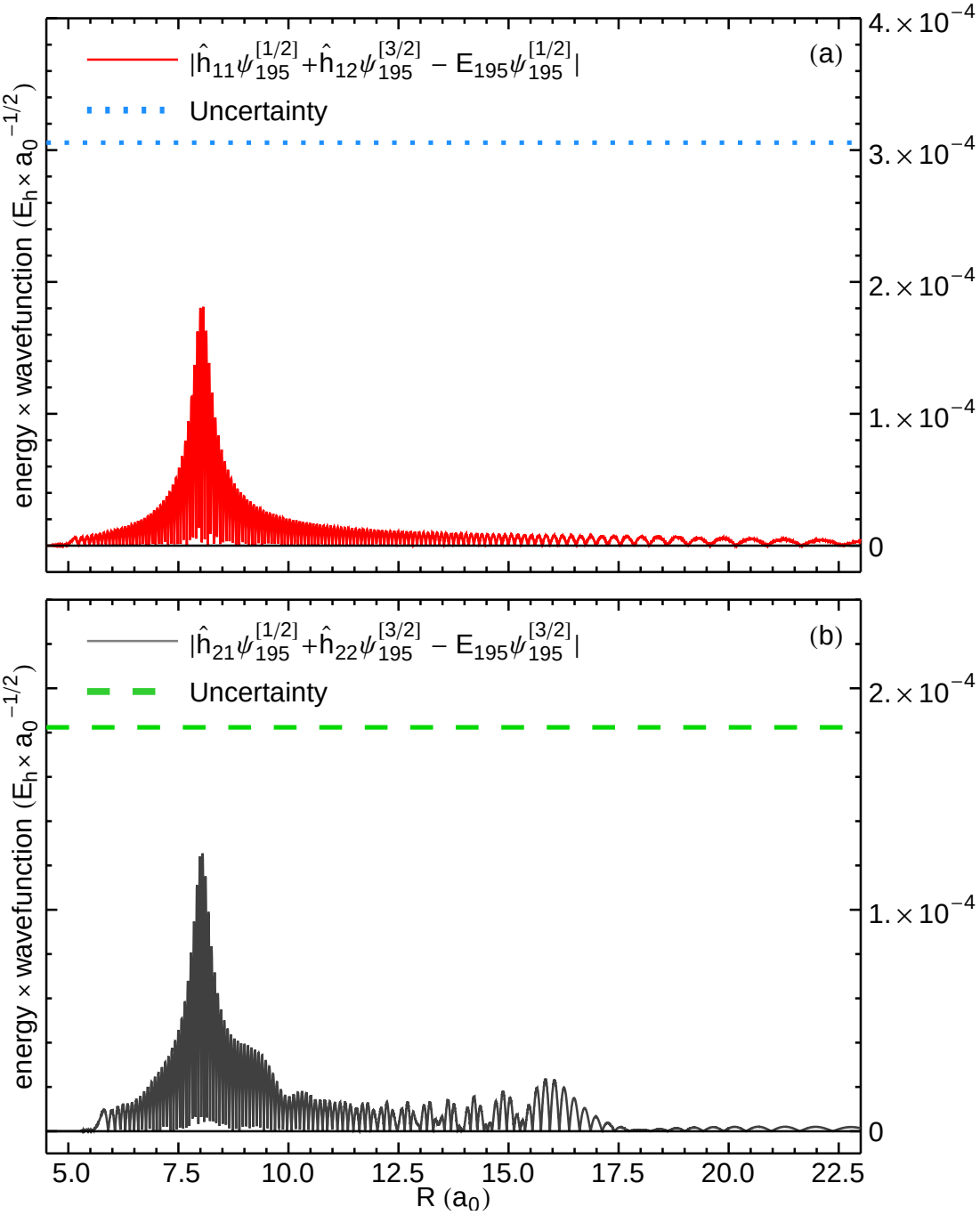

Figure F.17: (Color online) **Solid lines**—Absolute difference between the left hand side and right hand side of Eq. (F.2a) (panel (**a**)) and Eq. (F.2b) (panel (**b**)) for $v_{cc} = 195$.

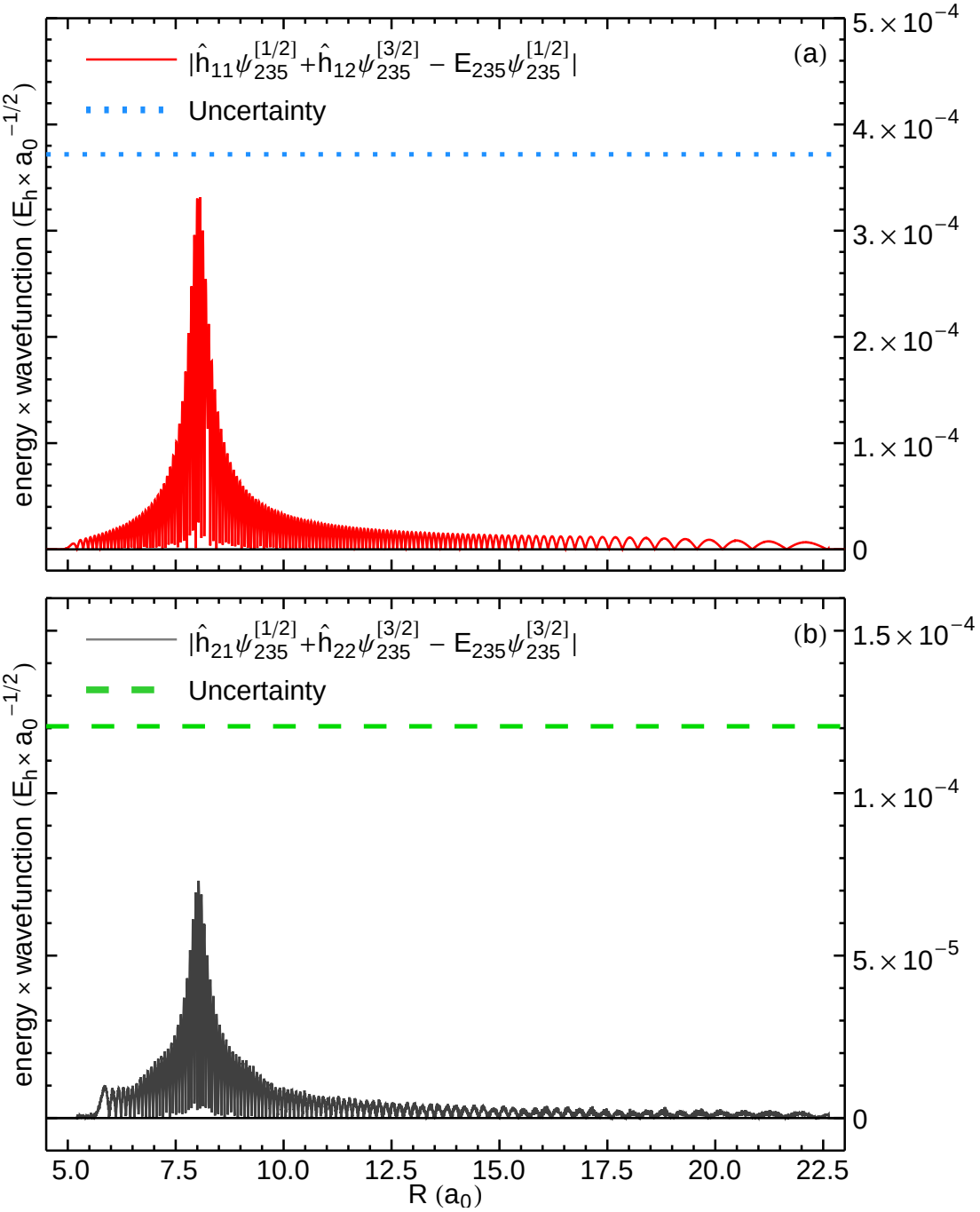

Figure F.18: (Color online) **Solid lines**—Absolute difference between the left hand side and right hand side of Eq. (F.2a) (panel (**a**)) and Eq. (F.2b) (panel (**b**)) for $v_{cc} = 235$.

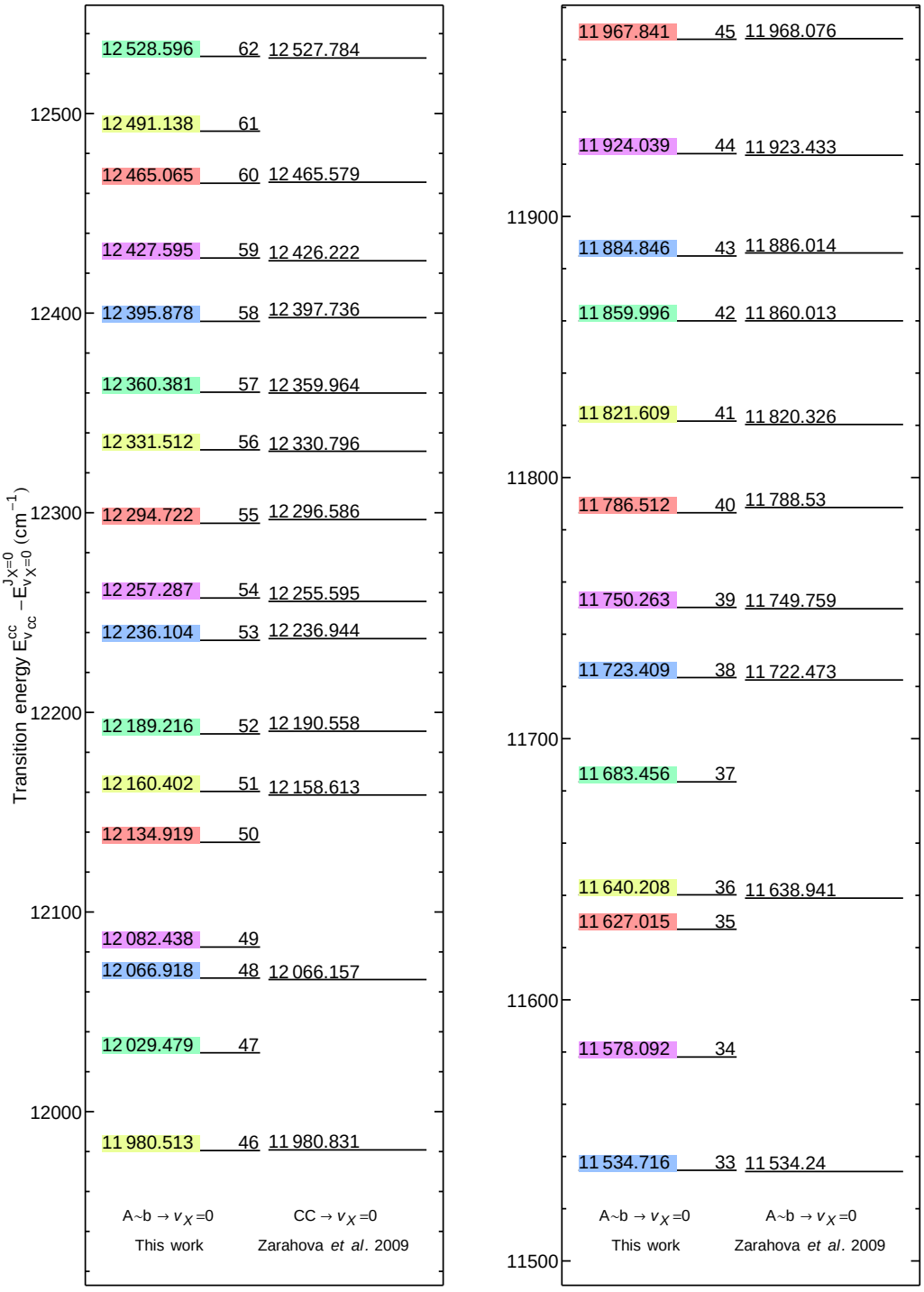

Figure F.19: (Color online) Energy level diagram comparing the transition energy $E^{cc}_{v_{cc}} - E^{J=0}_{v_X=0}$ reported in Tbl. III of [10] (right column) to the values calculated from the coupled-channel results of this work (left, colored column). The integer number in the middle is the coupled-channel vibrational index v_{cc}. The absolute error is at most 2.018 cm^{-1} for $v_{cc} = 40$.

Appendix G

Parameters for populations plots of chapter 6

This appendix gives tables of the laser parameters that lead the optimized populations for the 16 cases of Sec. 6.4. For certain cases, the details of the numerical search for the optimized parameters is also given.

G.1 case 1—bNIu

	Unit	Pump pulse		Stokes pulse
Intensity	$kW.cm^{-2}$	37.17735239		52.94266239
Bandwidth				
spectral	GHz	0.5		0.5
temporal	ps	882.5424006		882.5424006
Time delay	ps		2647.63	
Chirp rates	GHz/ps	0		0
	cm^{-1}/ps	0		0
Transition energy	E_h	0.05258941688		0.06222832894
	eV	1.43103081		1.693318945
	cm^{-1}	11542.04288		13657.53955
Detuning	E_h	0		0
	eV	0		0
	cm^{-1}	0		0

Table G.1: Parameters for optimized population transfer in case 1—bNIu.

G.2 case 2—bNIc

	Unit	Pump pulse		Stokes pulse
Intensity	$kW.cm^{-2}$	594.729		846.928
Bandwidth				
spectral	GHz	0.5		0.5
temporal	ps	1248.103		1248.103
Time delay	ps		561.65	
Chirp rates	GHz/ps	1.77985×10^{-3}		=
	cm^{-1}/ps	5.93695×10^{-5}		=
Transition	E_h	0.05258941688		0.06222832894
energy	eV	1.43103081		1.693318945
	cm^{-1}	11542.04288		13657.53955
Detuning	E_h	$8.440532615 \times 10^{-7}$		$1.147912436 \times 10^{-6}$
	eV	$2.2296785729 \times 10^{-5}$		$3.123628592 \times 10^{-5}$
	cm^{-1}	0.1852482784		0.2519376586

Table G.2: Parameters for optimized population transfer in case 2—bNIc. The temporal bandwidth of the effective lasers differs from case 1—bNIu due to the chirping. The chirp rates of the lasers are equal.

G.3 case 3—bNCu

	Unit	Pump pulse		Stokes pulse
Intensity	$kW.cm^{-2}$	594.838		847.083
Bandwidth				
spectral	GHz	0.5		0.5
temporal	ps	882.5424006		882.5424006
Time delay	ps		-749.562	
Chirp rates	GHz/ps	0		0
	cm^{-1}/ps	0		0
Transition energy	E_h	0.05258941688		0.06222832894
	eV	1.43103081		1.693318945
	cm^{-1}	11542.04288		13657.53955
Detuning	E_h	0		0
	eV	0		0
	cm^{-1}	0		0

Table G.3: Parameters for optimized population transfer in case 3—bNCu. The pulse delay is negative since the laser sequence is counter-intuitive.

G.4 case 4—bNCc

	Unit	Pump pulse		Stokes pulse
Intensity	$kW.cm^{-2}$	594.734		846.936
Bandwidth				
spectral	GHz	0.5		0.5
temporal	ps	1248.103		1248.103
Time delay	ps		-344.79	
Chirp rates	GHz/ps	1.77985×10^{-3}		=
	cm^{-1}/ps	5.93695×10^{-5}		=
Transition	E_h	0.05258941688		0.06222832894
energy	eV	1.43103081		1.693318945
	cm^{-1}	11542.04288		13657.53955
Detuning	E_h	$8.440532615 \times 10^{-7}$		$1.147912436 \times 10^{-6}$
	eV	$2.2296785729 \times 10^{-5}$		$3.123628592 \times 10^{-5}$
	cm^{-1}	0.1852482784		0.2519376586

Table G.4: Parameters for optimized population transfer in case 4—bNCc. The temporal bandwidth of the effective lasers differs from case 1—bNIu due to the chirping. The chirp rates of the lasers are equal. The pulse delay is negative since the laser sequence is counter-intuitive.

G.5 case 5—bSIu

	Unit	Pump pulse		Stokes pulse
Intensity	$kW.cm^{-2}$	28.446		93.650
Bandwidth				
spectral	GHz	0.5		0.5
temporal	ps	882.5424006		882.5424006
Time delay	ps		2647.63	
Chirp rates	GHz/ps	1.77985×10^{-3}		=
	cm^{-1}/ps	5.93695×10^{-5}		=
Transition energy	E_h	0.05344353723		0.06308244928
	eV	1.454272606		1.716560742
	cm^{-1}	11729.5		13844.9973
Detuning	E_h	0		0
	eV	0		0
	cm^{-1}	0		0

Table G.5: Parameters for optimized population transfer in case 5—bSIu.

G.6 case 6—bSIc

	Unit	Pump pulse		Stokes pulse
Intensity	$kW.cm^{-2}$	711.150		2341.251
Bandwidth				
spectral	GHz	0.5		0.5
temporal	ps	1248.103		1248.103
Time delay	ps		750.16	
Chirp rates	GHz/ps	1.77985×10^{-3}		=
	cm^{-1}/ps	5.9369×10^{-5}		=
Transition energy	E_h	0.05344353723		0.06308244928
	eV	1.454272606		1.716560742
	cm^{-1}	11729.5		13844.9973
Detuning	E_h	$8.440532615 \times 10^{-7}$		1.2499×10^{-6}
	eV	$2.2296785729 \times 10^{-5}$		3.401155×10^{-5}
	cm^{-1}	0.1852482784		0.274322

Table G.6: Parameters for optimized population transfer in case 6—bSIc. The temporal bandwidth of the effective lasers differs from case 5—bSIu due to the chirping. The chirp rates of the lasers are equal.

G.7 case 7—bSCu

	Unit	Pump pulse		Stokes pulse
Intensity	$kW.cm^{-2}$	469.36		1545.23
Bandwidth				
spectral	GHz	0.5		0.5
temporal	ps	882.5424006		882.5424006
Time delay	ps		-337.30	
Chirp rates	GHz/ps	0		=
	cm^{-1}/ps	0		=
Transition energy	E_h	0.05344353723		0.06308244928
	eV	1.454272606		1.716560742
	cm^{-1}	11729.5		13844.9973
Detuning	E_h	0		0
	eV	0		0
	cm^{-1}	0		0

Table G.7: Parameters for optimized population transfer in case 7—bSCu. The pulse delay is negative since the laser sequence is counter-intuitive.

G.8 case 8—bSCc

	Unit	Pump pulse		Stokes pulse
Intensity	$kW.cm^{-2}$	455.14		1498.4
Bandwidth				
spectral	GHz	0.5		0.5
temporal	ps	1248.103		1248.103
Time delay	ps		-449.74	
Chirp rates	GHz/ps	1.77985×10^{-3}		=
	cm^{-1}/ps	5.9369×10^{-5}		=
Transition energy	E_h	0.05344353723		0.06308244928
	eV	1.454272606		1.716560742
	cm^{-1}	11729.5		13844.9973
Detuning	E_h	$8.440532615 \times 10^{-7}$		1.0874×10^{-6}
	eV	2.22968×10^{-5}		2.9589×10^{-5}
	cm^{-1}	0.1852482784		0.23865

Table G.8: Parameters for optimized population transfer in case 6—bSIc. The temporal bandwidth of the effective lasers differs from case 5—bSIu due to the chirping. The chirp rates of the lasers are equal.

G.9 case 9—BNIu

	Unit	Pump pulse		Stokes pulse
Intensity	$MW.cm^{-2}$	14.868		21.173
Bandwidth				
spectral	GHz	10		10
temporal	ps	44.127		44.127
Time delay	ps		-24.36	
Chirp rates	GHz/ps	0		=
	cm^{-1}/ps	0		=
Transition energy	E_h	0.05258941688		0.06222832894
	eV	1.43103081		1.693318945
	cm^{-1}	11542.04288		13657.53955
Detuning	E_h	-10^{-6}		0
	eV	-2.72114×10^{-5}		0
	cm^{-1}	-0.21947		0

Table G.9: Parameters for optimized population transfer in case 9—BNIu.

G.10 case 10—BNIc

	Unit	Pump pulse		Stokes pulse
Intensity	$\mathrm{MW.cm^{-2}}$	14.868		21.173
Bandwidth				
spectral	GHz	10		10
temporal	ps	62.405		62.405
Time delay	ps		187.2155	
Chirp rates	GHz/ps	0.7119		=
	$\mathrm{cm^{-1}/ps}$	0.02375		=
Transition energy	E_h	0.05258941688		0.06222832894
	eV	1.43103081		1.693318945
	$\mathrm{cm^{-1}}$	11542.04288		13657.53955
Detuning	E_h	1.6881×10^{-6}		5.73956×10^{-5}
	eV	4.59357×10^{-4}		1.56181×10^{-3}
	$\mathrm{cm^{-1}}$	3.70496		12.59688

Table G.10: Parameters for optimized population transfer in case 10—BNIc.

G.11 case 11—BNCu

	Unit	Pump pulse		Stokes pulse
Intensity	$MW.cm^{-2}$	35.683		50.815
Bandwidth				
spectral	GHz	10		10
temporal	ps	44.127		44.127
Time delay	ps		-24.36	
Chirp rates	GHz/ps	0		=
	cm^{-1}/ps	0		=
Transition	E_h	0.05258941688		0.06222832894
energy	eV	1.43103081		1.693318945
	cm^{-1}	11542.04288		13657.53955
Detuning	E_h	-6×10^{-7}		0
	eV	-1.632×10^{-5}		0
	cm^{-1}	-0.13168		0

Table G.11: Parameters for optimized population transfer in case 11—BNCu.

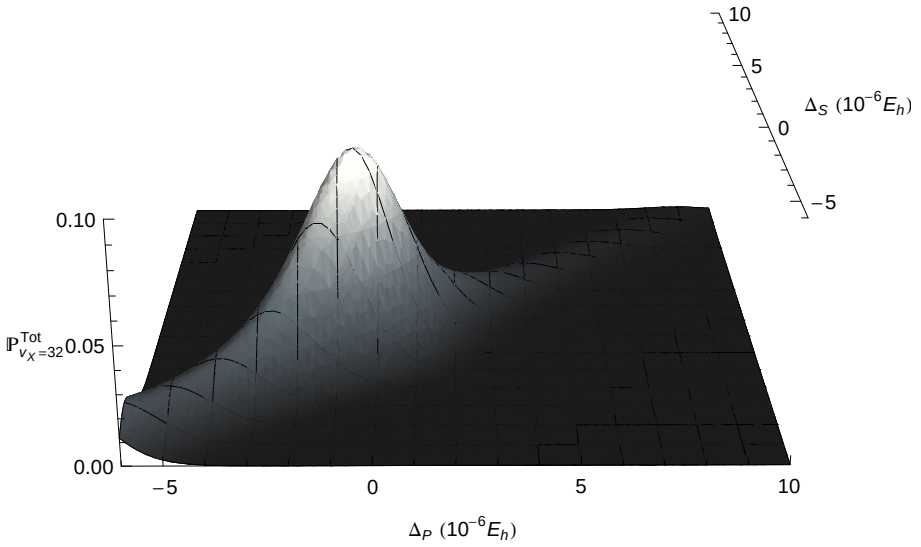

Figure G.1: Numerical search for optimal detunings in case 11—BNCu.

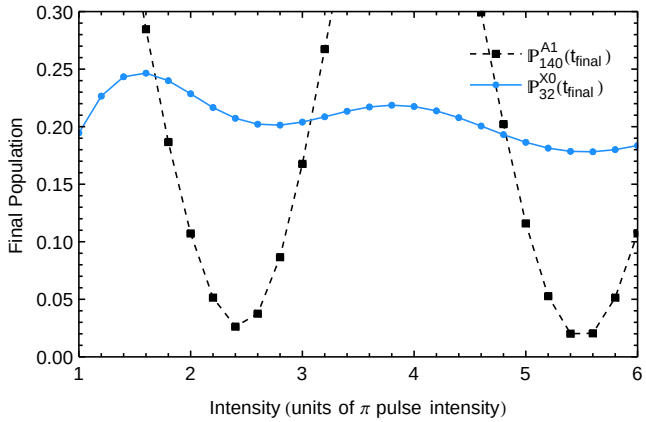

Figure G.2: Numerical search for optimal laser intensities in case 11—BNCu, for the optimal detuning from Fig. G.1.

G.12 case 12—BNCc

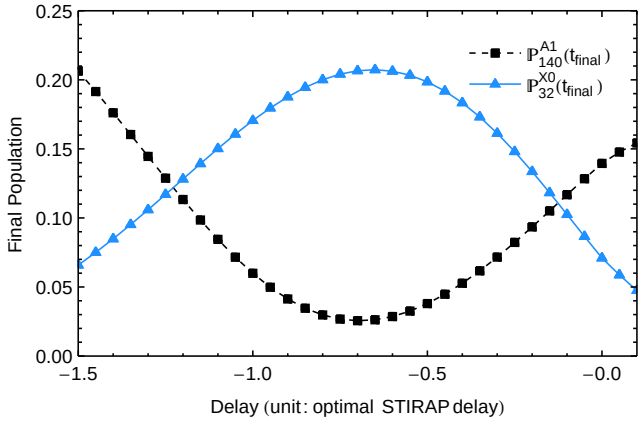

Figure G.3: Numerical search for the optimal value of the pulse delay for the optimal detuning of Fig. G.1 and the optimal intensities Fig. G.2, case 11—BNCu.

	Unit	Pump pulse		Stokes pulse
Intensity	$MW.cm^{-2}$	23.045		32.818
Bandwidth				
spectral	GHz	10		10
temporal	ps	62.405		62.405
Time delay	ps		-29.9825	
Chirp rates	GHz/ps	0.7119		=
	cm^{-1}/ps	0.02375		=
Transition	E_h	0.05258941688		0.06222832894
energy	eV	1.43103081		1.693318945
	cm^{-1}	11542.04288		13657.53955
Detuning	E_h	1.46×10^{-5}		1.76×10^{-5}
	eV	3.9728×10^{-4}		4.7892×10^{-4}
	cm^{-1}	3.20433		3.8627

Table G.12: Parameters for optimized population transfer in case 12—BNCc.

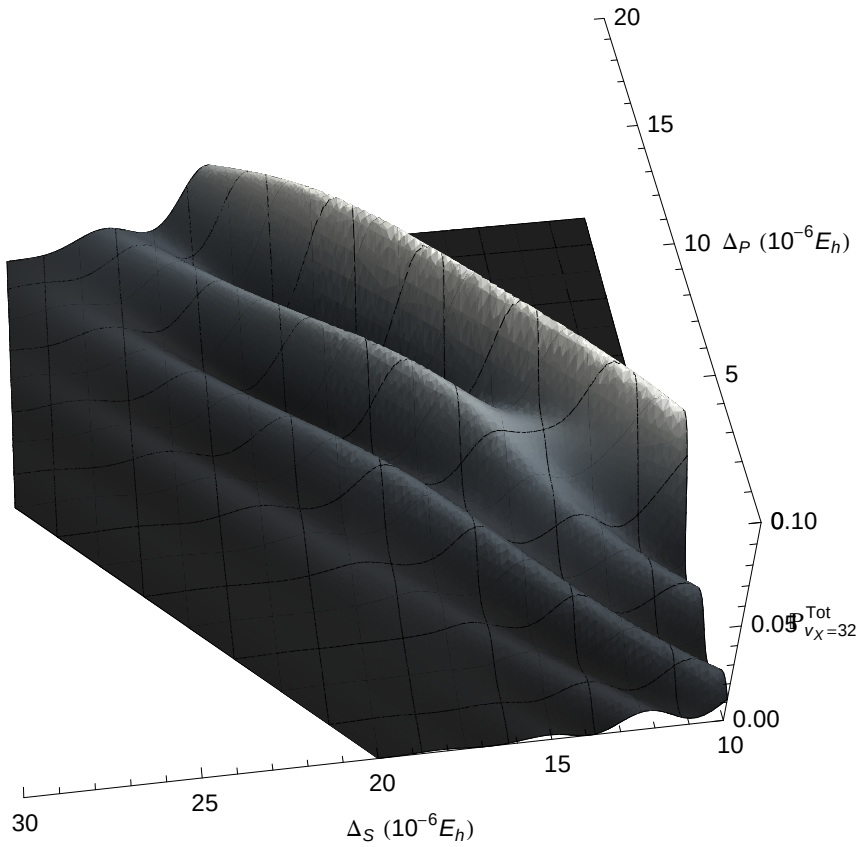

Figure G.4: Numerical search for optimal detunings in case 12—BNCc.

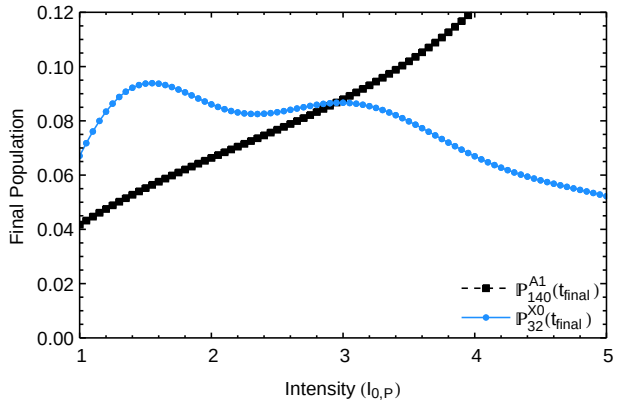

Figure G.5: Numerical search for optimal laser intensities in case 12—BNCc, for the optimal detuning from Fig. G.4.

G.13 case 13—BSIu

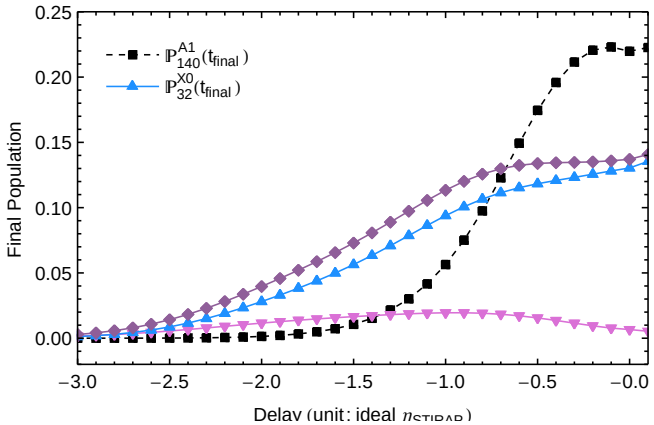

Figure G.6: Numerical search for the optimal value of the pulse delay for the optimal detuning of Fig. G.4 and the optimal intensities Fig. G.5, case 12—BNCc.

	Unit	Pump pulse		Stokes pulse
Intensity	$MW.cm^{-2}$	11.378		37.460
Bandwidth				
spectral	GHz	10		10
temporal	ps	44.127		44.127
Time delay	ps		66.191	
Chirp rates	GHz/ps	0		=
	cm^{-1}/ps	0		=
Transition energy	E_h	0.05344353723		0.06308244928
	eV	1.454272606		1.716560742
	cm^{-1}	11729.5		13844.9973
Detuning	E_h	-2.8×10^{-6}		0
	eV	7.6191×10^{-5}		0
	cm^{-1}	-0.61453		0

Table G.13: Parameters for optimized population transfer in case 13—BSIu.

G.14 case 14—BSIc

	Unit	Pump pulse		Stokes pulse
Intensity	$MW.cm^{-2}$	50.634		166.697
Bandwidth				
spectral	GHz	10		10
temporal	ps	62.405		62.405
Time delay	ps		187.21	
Chirp rates	GHz/ps	0.712		=
	cm^{-1}/ps	0.2375		=
Transition energy	E_h	0.05344353723		0.06308244928
	eV	1.454272606		1.716560742
	cm^{-1}	11729.5		13844.9973
Detuning	E_h	8.9×10^{-6}		5.13×10^{-5}
	eV	2.4218×10^{-4}		1.396×10^{-3}
	cm^{-1}	11.259		0

Table G.14: Parameters for optimized population transfer in case 14—BSIc. The temporal bandwidth of the effective lasers differs from case 14—BSIu due to the chirping. The chirp rates of the lasers are equal.

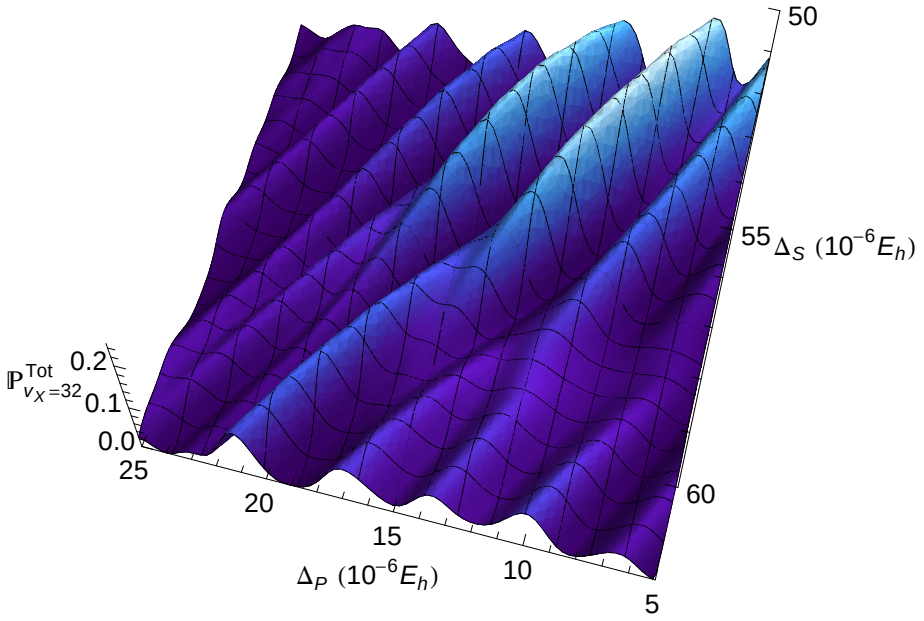

Figure G.7: Numerical search for optimal detunings in case 14—BSIc.

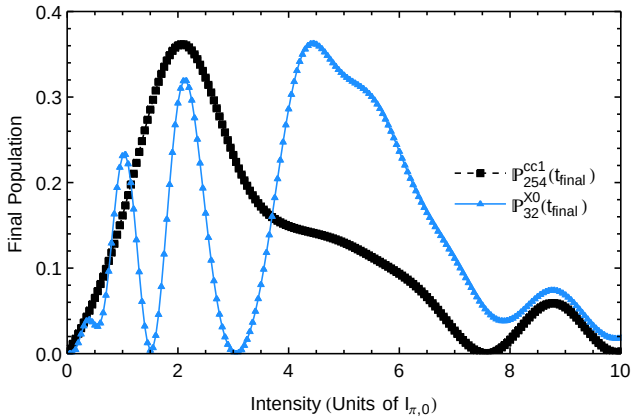

Figure G.8: Numerical search for optimal laser intensities in case 14—BSIc, for the optimal detuning from Fig. G.7.

G.15 case 15—BSCu

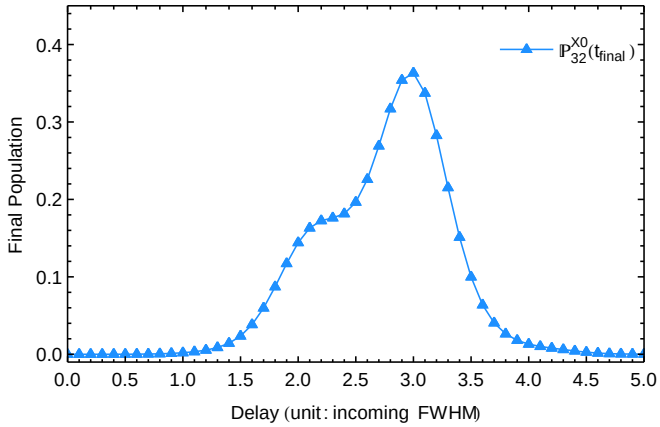

Figure G.9: Numerical search for the optimal value of the pulse delay for the optimal detuning of Fig. G.7 and the optimal intensities Fig. G.8, case 14—BSIc.

	Unit	Pump pulse		Stokes pulse
Intensity	$MW.cm^{-2}$	23.899		78.68
Bandwidth				
spectral	GHz	10		10
temporal	ps	44.127		44.127
Time delay	ps		-3.748	
Chirp rates	GHz/ps	0		=
	cm^{-1}/ps	0		=
Transition energy	E_h	0.05344353723		0.06308244928
	eV	1.454272606		1.716560742
	cm^{-1}	11729.5		13844.9973
Detuning	E_h	-1.75×10^{-6}		-2.5×10^{-7}
	eV	-4.762×10^{-5}		-6.80285×10^{-6}
	cm^{-1}	−0.38408		-0.054869

Table G.15: Parameters for optimized population transfer in case 15—BSCu.

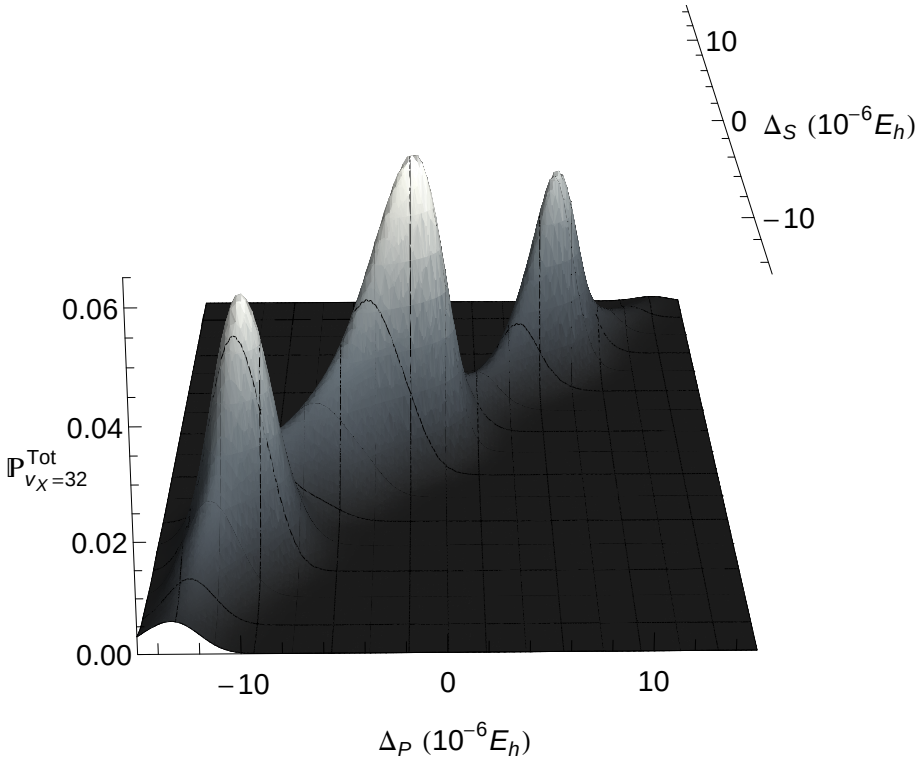

Figure G.10: Numerical search for optimal detunings in case 15—BSCu.

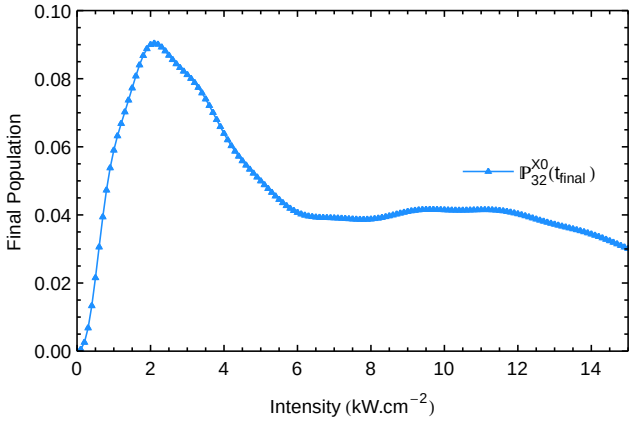

Figure G.11: Numerical search for optimal laser intensities in case 15—BSCu, for the optimal detuning from Fig. G.1.

G.16 case 16—BSCc

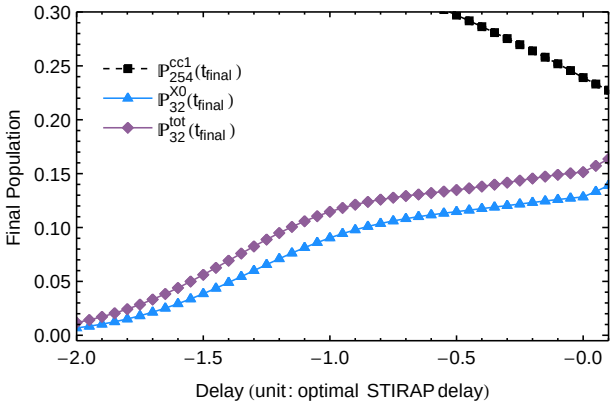

Figure G.12: Numerical search for the optimal value of the pulse delay for the optimal detuning of Fig. G.1 and the optimal intensities Fig. G.2, case 15—BSCu.

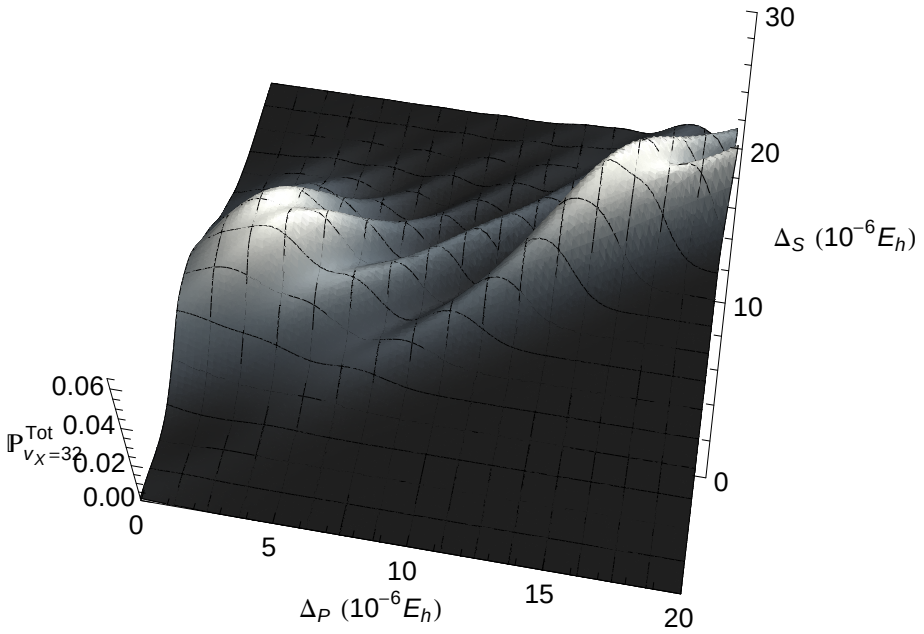

Figure G.13: Numerical search for optimal detunings in case 16—BSCc.

	Unit	Pump pulse		Stokes pulse
Intensity	$\mathrm{MW.cm^{-2}}$	15.360		50.571
Bandwidth				
spectral	GHz	10		10
temporal	ps	62.405		62.405
Time delay	ps		-42.725	
Chirp rates	GHz/ps	0.712		=
	$\mathrm{cm^{-1}/ps}$	0.2375		=
Transition energy	E_h	0.05344353723		0.06308244928
	eV	1.454272606		1.716560742
	$\mathrm{cm^{-1}}$	11729.5		13844.9973
Detuning	E_h	1.575×10^{-5}		2.15×10^{-5}
	eV	4.28579×10^{-4}		5.85045×10^{-4}
	$\mathrm{cm^{-1}}$	3.45672		4.7187

Table G.16: Parameters for optimized population transfer in case 14—BSIc. The temporal bandwidth of the effective lasers differs from case 14—BSIu due to the chirping. The chirp rates of the lasers are equal.

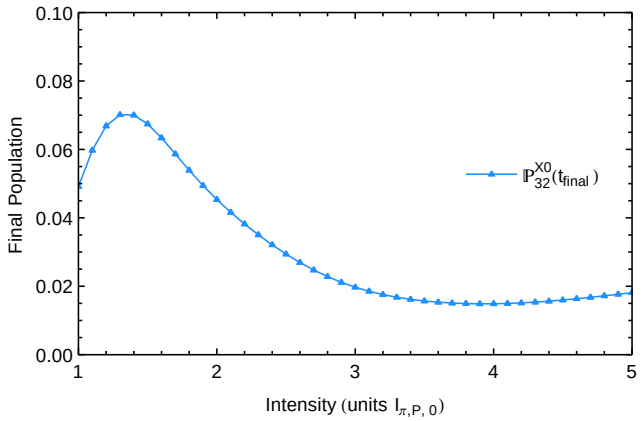

Figure G.14: Numerical search for optimal laser intensities in case 16—BSCc, for the optimal detuning from Fig. G.13.

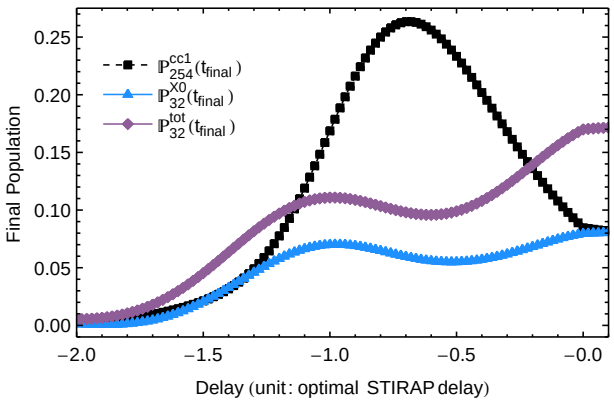

Figure G.15: Numerical search for the optimal value of the pulse delay for the optimal detuning of Fig. G.13 and the optimal intensities Fig. G.14, case 16—BSCc.